

Probing QCD matter via fluctuations, correlations, and flow in heavy-ion collisions at the LHC

By

SWATI SAHA

PHYS11201805003

National Institute of Science Education and Research

*A thesis submitted
to the Board of Studies in
Physical Sciences*

*In partial fulfillment of requirements
For the Degree of*

DOCTOR OF PHILOSOPHY

of

HOMI BHABHA NATIONAL INSTITUTE



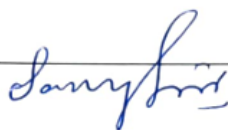
October, 2025

Homi Bhabha National Institute

Recommendations of the Viva Voce Committee

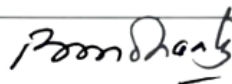
As members of the Viva Voce Committee, we certify that we have read the dissertation prepared by **Swati Saha** entitled **“Probing QCD matter via fluctuations, correlations, and flow in heavy-ion collisions at the LHC”** and recommend that it may be accepted as fulfilling the thesis requirement for the award of Degree of Doctor of Philosophy.

Chairman - Prof. Sanjay Kumar Swain



Date: 19/12/2025

Guide / Convener - Prof. Bedangadas Mohanty



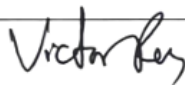
Date: 19/12/2025

Examiner - Dr. Sabyasachi Ghosh



Date: 19/12/2025

Member 1 - Dr. Victor Roy



Date: 19.12.2025

Member 2 - Dr. Najmul Haque



Date: 19.12.2025

Member 3 - Dr. Md Nasim



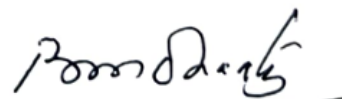
Date: 19.12.2025

Final approval and acceptance of this thesis is contingent upon the candidate's submission of the final copies of the thesis to HBNI.

I hereby certify that I have read this thesis prepared under my direction and recommend that it may be accepted as fulfilling the thesis requirement.

Date : December 19,
2025

Place : Jatni



(Guide)

19/12/2025

STATEMENT BY THE AUTHOR

This dissertation has been submitted in partial fulfillment of requirements for an advanced degree at Homi Bhabha National Institute (HBNI) and is deposited in the library to be made available to borrowers under rules of the HBNI.

Brief quotations from this dissertation are allowable without special permission, provided that accurate acknowledgement of source is made. Requests for permission for extended quotation from or reproduction of this manuscript in whole or in part may be granted by the Competent Authority of HBNI when in his or her judgment the proposed use of the material is in the interests of scholarship. In all other instances, however, permission must be obtained from the author.

Date : December 19, 2025

Place : Jatni

Swati Saha

(SWATI SAHA)

DECLARATION

I hereby declare that the investigation presented in the thesis has been carried out by me. The work is original and has not been submitted earlier as a whole or in part for a degree/diploma at this or any other Institution/University.

Date : December 19, 2025

Place : Jatni

Swati Saha

(SWATI SAHA)

CERTIFICATION OF ACADEMIC INTEGRITY

Undertaking by the student

1. I **Swati Saha**, HBNI Enrolment No. **PHYS11201805003** hereby undertake that the thesis titled “**Probing QCD matter via fluctuations, correlations, and flow in heavy-ion collisions at the LHC**” is prepared by me and is the original work undertaken by me.
2. I also hereby undertake that this document has been duly checked through a plagiarism detection tool and the document is found to be plagiarism free as per the guidelines of the Institute/UGC.
3. I am aware and undertake that if plagiarism is detected in my thesis at any stage in the future, suitable penalty will be imposed as applicable as per the guidelines of the Institute/UGC.

Swati Saha 19/12/25

Signature of the Student with date

Endorsed by the thesis supervisor

I certify that the thesis written by the student is plagiarism free as mentioned above.

Prof. Bedangadas Mohanty
19/12/2025

Signature of the thesis supervisor with date

Name : Prof. Bedangadas Mohanty
Designation : Senior Professor
Department / Centre : School of Physical Sciences
Name of the CI / OCC : National Institute of Science Education and Research

List of Publications arising from the thesis

Journal

Published

1. ALICE Collaboration, "*Skewness and kurtosis of mean transverse momentum fluctuations at the LHC energies*", arXiv:2308.16217 [nucl-ex], *Phys. Lett. B* 850 (2024) 138541.
Arxiv link: <https://arxiv.org/abs/2308.16217>.
Journal link: <https://doi.org/10.1016/j.physletb.2024.138541>.
Primary authors: **Swati Saha**, Sourav Kundu, Bedangadas Mohanty.
2. ALICE Collaboration, "*Measurement of correlations among net-charge, net-proton, and net-kaon multiplicity distributions in Pb-Pb collisions at $\sqrt{s_{NN}} = 5.02$ TeV*", arXiv:2503.18743 [nucl-ex], *JHEP* 08 (2025) 210.
Arxiv link: <https://arxiv.org/abs/2503.18743>.
Journal link: [https://doi.org/10.1007/JHEP08\(2025\)210](https://doi.org/10.1007/JHEP08(2025)210).
Primary authors: **Swati Saha**, Bedangadas Mohanty.
3. **Swati Saha**, Ranbir Singh, Bedangadas Mohanty, " *p_T -differential radial flow in blast-wave model*", arXiv:2505.19697 [nucl-ex], *Phys. Rev. C* 112, 024902 (2025).

Arxiv link: <https://arxiv.org/abs/2505.19697>.

Journal link: <https://link.aps.org/doi/10.1103/83zq-kdjg>.

Accepted

1. ALICE Collaboration, "*Long-range transverse momentum correlations and radial flow in Pb–Pb collisions at the LHC*", arXiv:2504.04796 [nucl-ex].

Arxiv link: <https://arxiv.org/abs/2504.04796>.

Accepted by *Physical Review Letters* with *Editor's Suggestion*.

Primary authors: **Swati Saha**, Ranbir Singh, Bedangadas Mohanty.

Other publications

- Rajiv V. Gavai, Bedangadas Mohanty, Jaydev Singh Rao, **Swati Saha**, "*Cumulants and ordering of their ratios in 2D Potts models: Lessons for QCD?*", arXiv:2312.12130 [hep-lat].

Arxiv link: <https://arxiv.org/abs/2312.12130>.

Internal analysis notes

1. "*Higher-order event-by-event mean- p_T fluctuations in pp and A–A collisions with ALICE (2022)*". ALICE Internal Note link: <https://alice-notes.web.cern.ch/node/1231>. Primary contributors: Swati Saha, Sourav Kundu, Bedangadas Mohanty.
2. "*Correlations of net-charge, net-kaon and net-proton in Pb–Pb at $\sqrt{s_{NN}} = 5.02$ TeV (2023)*". ALICE Internal Note link: <https://alice-notes.web.cern.ch/node/1425>. Primary contributors: Swati Saha, Bedangadas Mohanty.
3. "*Measurement of $v_0(p_T)$ in Pb–Pb collisions at $\sqrt{s_{NN}} = 5.02$ TeV (2024)*". ALICE Internal Note link: <https://alice-notes.web.cern.ch/node/1513>. Primary contributors: Swati Saha, Bedangadas Mohanty.

Conference proceedings

1. Swati Saha. “Skewness of event-by-event $\langle p_T \rangle$ distribution of charged particles at LHC energies with ALICE”. *PoS ICHEP2022* (2022), p. 1157. URL: <https://pos.sissa.it/414/1157>.
2. Swati Saha. “Skewness of event-by-event $\langle p_T \rangle$ distribution of charged particles at LHC energies with ALICE”. *DAE Symp. Nucl. Phys.* 66 (2023), pp. 940–941.
3. Swati Saha. “Correlations among net-charge, net-kaon and net-proton at LHC energies with ALICE”. *DAE Symp. Nucl. Phys.* 67 (2024), pp. 1009–1010.
4. Swati Saha. “Investigating baryon-strangeness and charge-strangeness correlations in Pb–Pb collisions at $\sqrt{s_{NN}} = 5.02$ TeV with ALICE”. *PoS ICHEP2024* (2025), p. 598. arXiv: [2409.10939 \[nucl-ex\]](#).
5. Swati Saha. “Study of baryon-strangeness and charge-strangeness correlations in Pb–Pb collisions at $\sqrt{s_{NN}} = 5.02$ TeV with ALICE”. *EPJ Web Conf.* 316 (2025), p. 06010. arXiv: [2411.07002 \[nucl-ex\]](#).
6. “Investigating the effect of magnetic field on baryon-charge correlations in Pb–Pb collisions at $\sqrt{s_{NN}} = 5.02$ TeV with ALICE”. In: *Springer Nature*. Contribution to XXVI DAE-BRNS High Energy Physics Symposium 2024.
7. “EPJ Featured Talk: First direct measurement of radial flow in heavy-ion collisions with ALICE”. In: *EPJ Web of Conferences*. Contribution to Quark Matter 2025.

Conference/Workshop presentations

1. Hot QCD Matter 2025 (Series 3), IIT Bhilai, India [September 4–6, 2025], Oral presentation: *Radial flow via $v_0(p_T)$ in heavy-ion collisions at LHC energies*.
2. The 40th Young Physicists’ Colloquium (YPC 2025), Saha Institute of Nuclear Physics, Kolkata, India [August 21–22, 2025], Oral presentation: *Radial flow using $v_0(p_T)$ in heavy-ion collisions at LHC energies*.

3. XXXI Conference on ultra-relativistic nucleus-nucleus collisions, Quark Matter 2025, Frankfurt, Germany [April 6–12, 2025], Oral presentation: *EPJ Featured Talk: First direct measurement of radial flow in heavy-ion collisions with ALICE.*
4. 10th Asian Triangle Heavy-Ion Conference (ATHIC 2025), IISER Berhampur, India [January 13–16, 2025], Oral presentation: *Fluctuations and correlations of net-conserved quantities at LHC energies with ALICE.*
5. XXVI DAE-BRNS High Energy Physics Symposium 2024, Banaras Hindu University, Varanasi, India [December 19–23, 2024], Oral presentation: *Investigating the effect of magnetic field on baryon-charge correlations in Pb–Pb collisions at $\sqrt{s_{NN}} = 5.02$ TeV with ALICE.*
6. 42nd International Conference on High Energy Physics (ICHEP2024), Prague, Czech Republic [July 17–24, 2024], Oral presentation: *Study of baryon-strangeness and charge-strangeness correlations in Pb–Pb collisions at 5.02 TeV with ALICE*
7. 21st International Conference on Strangeness in Quark Matter (SQM-2024), Strasbourg, France [June 3–7, 2024], Oral presentation: *Study of baryon-strangeness and charge-strangeness correlations in Pb–Pb collisions at 5.02 TeV with ALICE*
8. 67th DAE Nuclear Symposium on Nuclear Physics, IIT Indore, India [December 9–13, 2023], Oral presentation: *Correlations among net-charge, net-kaon and net-proton at LHC energies with ALICE.*
9. Aspects of the QCD Phase Diagram, IISER Bhopal, India [November 18–20, 2023], Oral presentation: *Study of cumulants and its ordering in 2D Pott’s model.*
10. XXXth Conference on ultra-relativistic nucleus-nucleus collisions, Quark Matter 2023, Houston, Texas, USA [September 3–9, 2023], Poster presentation (online): *Correlations of net-charge, net-kaon and net-proton in Pb–Pb at $\sqrt{s_{NN}} = 5.02$ TeV with ALICE.*
11. International Conference on Physics and Astrophysics of Quark Gluon Plasma (ICPAQGP-2023), Puri, India [February 7–10, 2023], Poster presentation: *Probing the initial conditions of heavy-ion collisions by measurements of fluctuations and correlations with ALICE.*

12. XXV DAE-BRNS HEP SYMPOSIUM, IISER Mohali, India [December 12–16, 2022], Oral presentation: *Study of Ising model and three state Pott's model cumulants in 2D lattice.*
13. 66th DAE Symposium on Nuclear Physics, Guwahati, India [December 1–5, 2022], Poster presentation: *Skewness of event-by-event $\langle p_T \rangle$ distribution of charged particles at LHC energies with ALICE.*
14. 28th International Nuclear Physics Conference (INPC2022), Cape Town, South Africa [September 11–16, 2022], Oral presentation: *Higher-order event-by-event mean- p_T fluctuations in pp and A–A collisions with ALICE.*
15. XI International Conference on New Frontiers in Physics (ICNFP2022), Kolymbari, Crete, Greece [August 30–September 12, 2022], Oral presentation (online): *Higher-order event-by-event mean- p_T fluctuations in pp and A–A collisions with ALICE.*
16. XLI International Conference on High Energy Physics (ICHEP2022), Bologna, Italy [July 6–13, 2022], Poster presentation (online): *Higher-order event-by-event mean- p_T fluctuations in pp and A–A collisions with ALICE.*
17. 20th International Conference on Strangeness in Quark Matter (SQM2022), Seoul, South Korea [June 13–17, 2022], Poster presentation (online): *Higher-order event-by-event mean- p_T fluctuations in pp and A–A collisions with ALICE.*
18. XXIXth International Conference on Ultra-relativistic Nucleus-Nucleus Collisions, Quark Matter 2022, Krakow, Poland [April 4–10, 2022], Poster presentation (online): *Higher-order event-by-event mean- p_T fluctuations in pp and A–A collisions with ALICE.*

Date : December 19, 2025

Place : Jatni

(SWATI SAHA)

DEDICATED TO

*My beloved parents, my supervisor, and Lord Shiva,
whose guidance and blessings have been my greatest support.*

ACKNOWLEDGEMENTS

I would like to express my heartfelt gratitude to my supervisor, Prof. Bedangadas Mohanty, for his unwavering guidance, constant encouragement, and profound insights throughout this journey. His deep understanding of physics and his passion for research have been a continuous source of inspiration. I feel truly privileged in having him as my supervisor for the past six years, beginning from my Master's studies. During moments of self-doubt, his faith in me has always been a source of strength, motivating me to move forward with confidence. I greatly admire his scientific rigor, methodical approach to problem-solving, and exceptional commitment to excellence. Observing his unparalleled dedication and wholehearted devotion to his work has continually inspired me. His constructive feedback and thoughtful guidance have helped me grow as a researcher and as a person. I remain sincerely indebted to him for welcoming me into his group, for the invaluable opportunities and learning experiences offered, and for everything I have been able to accomplish under his guidance.

I am grateful to Dr. Ranbir Singh and Dr. Varchaswi Kashyap for always being there to guide and assist me, both academically and personally, even amidst their busy professional commitments. Their encouragement, patience, and kindness have made my time in the group truly enjoyable and inspiring, that I will always cherish. They have always been approachable, ready to clarify my doubts, and generous with their time and advice. Beyond academics, their support during challenging times has given me confidence and motivation, and I feel truly fortunate to have had such mentors.

I am deeply grateful to Prof. Rajiv V. Gavai for his invaluable guidance and profound knowledge, which have greatly enriched my understanding during our collaborative project. I am also deeply thankful for the opportunity he extended to me to present our work at

the Aspects of QCD conference, a truly valuable experience. His generosity in sharing wisdom and providing constructive feedback has inspired me to strive for excellence. I am fortunate to have benefited from his expertise and kindness, which have greatly supported my growth and learning.

I am sincerely thankful to Prof. Jean Yves Ollitrault for inspiring me to pursue the measurement of $v_0(p_T)$, and for his exceptional support throughout my research work. Whenever I reached out—whether by email or Zoom meeting—he was always willing to patiently clarify my doubts and enhance my understanding. His guidance has been instrumental in shaping my theoretical foundation for two key analyses presented in this thesis. I am grateful for his generosity in sharing his profound knowledge, which has greatly enriched my research.

I would also like to warmly acknowledge Prof. Chun Shen, Prof. Bjoern Schenke, and Prof. Derek Teaney for generously providing the theoretical calculations of $v_0(p_T)$. Their knowledge, helpful insights, and openness to discussions have been extremely valuable. Thanks to my doctoral committee members Dr. Sanjay Kumar Swain, Dr. Victor Roy, Dr. Najmul Haque, and Dr. Md Nasim, for their invaluable suggestions and insightful comments on my thesis work. Thanks to Dr. Ante Bilandzic, Dr. Stefan Thomas Heckel, Dr. Dong Jo Kim, Dr. Ramni Gupta, Dr. Mesut Arslanok, Dr. Anar Rustamov, Dr. Igor Altsybeev, Dr. Anthony Robert Timmins for carefully reviewing my analysis and corresponding analysis note, and paper drafts within the collaboration as Analysis Review Committee (ARC) members and Internal Review Committee (IRC) members. I would also like to thank Dr. Ante Bilandzic, Dr. Tapan Nayak, Dr. Mesut Arslanok, and Dr. Sumit Basu for their valuable suggestions as Physics Analysis Group Convenors. I am especially thankful to Dr. Ante Bilandzic for always being supportive, approachable, and generous with his time, and for providing constructive feedback on my analyses. I would

als like to thank Dr. Francesco Prino, Dr. Zaida Conesa Del Valle, and Dr. Ralf Averbeck for reviewing my papers and providing their valuable comments as Editorial Board (EB) members of ALICE.

I also deeply appreciate Dr. Marco Van Leeuwen, Dr. Kai Schweda, Dr. Tapan Nayak, Dr. Luciano Musa, and Dr. Jurgen Schukraft for their insightful discussions and valuable feedback on my analysis during collaboration meetings and their visits to NISER. My sincere thanks to Dr. You Zhou for inviting me to NBI, Copenhagen and for graciously hosting me during my visit. I am grateful for his guidance and support throughout my stay, which made the experience both productive and memorable. I also wish to sincerely thank Dr. Sabyasachi Ghosh for giving me the opportunity to present my work as a plenary talk at the Hot QCD Matter conference, and for his warm hospitality during my visit.

I owe my sincere thanks to Dr. Sourav Kundu for his invaluable mentorship during the early stages of my research journey. When I first joined the group, he guided me through my very first project with great patience and encouragement, helping me learn the ALICE coding framework. I would like to thank Dr. Debashish Mallick, Dr. Ashish Pandav, Dr. Dukhishyam Mallick, Dr. Ashutosh Dash, who have been always beside me to resolve any doubt irrespective of coding or theory. Their practical insights and friendly guidance have made learning in the group an engaging and enriching experience. I extend my heartfelt regards to Dr. Mouli Choudhury for taking care of me just like an elder sister. I am sincerely thankful to Dr. Prottay Das for guiding me through the Lego train submission of analysis codes in ALICE, without which calculating the systematic uncertainties of the measurements would have been immensely cumbersome. He has been there for me on numerous occasions, both academically and personally, providing valuable support and advice. I could not have asked for better seniors than them; their constant support and encouragement have made my time in the group truly memorable.

My heartfelt thanks to Mr. Sudipta Das for his immense support, encouragement, and the warmth he brought into every interaction with him. His kindness, patience, and unwavering positivity have been a true source of strength and comfort throughout my time at NISER. He has always been there to listen with empathy, guide me with patience, and lift my spirits, often going above and beyond to help without a second thought. I am also grateful for his academic support—he never hesitated to assist me whenever I approached him, even though his expertise lies outside heavy-ion physics. He has truly been someone I could always rely on, making me feel safe and supported whenever I needed it most. My kind regards to Mr. Sawan Sawan, Ms. Sarjeeta Gami, Mr. Bappaditya Mondal, Ms. Dipanwita Mondal, Mr. Subhadeep Mandal, Mr. Saptarshi Datta, Mr. Yash Parakh and all students from our lab for their friendliness and support, which have made my time in the group both enjoyable and memorable. I would also acknowledge Dr. Raveendrababu Karnam, Dr. Shuddha Shankar Dasgupta, and Dr. Ganesh Jagannath Tambave for their kindness and encouragement, which have been truly uplifting. I sincerely thank Dr. Tribhuvan Parida for patiently guiding me to learn the intricacies of hydro simulations. His support and clear explanations made a complex topic much easier to understand and have greatly helped me in applying these simulations to my research.

This thesis is the realization of a dream long cherished by my parents. I owe everything I am to them. I am profoundly grateful to my father, whose blessings and values have continued to guide me. Though he has been away for nearly 14 years, his blessings, values, and quiet strength have stayed with me throughout this journey. There were many moments when I wished he could see how far I had come, but even in his absence, I felt his presence guiding me. His memory has been my silent encouragement. To my mother, whose unwavering faith has always lifted and inspired me, I owe an immeasurable debt of gratitude. She has been the pillar of my life—her patience, encouragement, and

unconditional love have given me strength in every difficult moment. She believed in me when I doubted myself and quietly sacrificed so much to allow me to follow my dreams. Her love has been my shelter and her resilience my greatest lesson. Without her constant support and care, this journey would have been far more difficult or never possible. My little sister has always cheered me on, no matter what. Her optimism and constant belief in me always kept me going, and her presence made difficult times easier and happy moments brighter. Her laughter and warmth have brought joy to this journey in ways that only she could. I am also grateful to my close friends, whose companionship and kindness have made this journey both enjoyable and meaningful. Above all, I humbly thank the Almighty for His divine grace and guidance, which lifted me from the darkest moments of my life and led me toward light, strength, and purpose. May He bless me with wisdom, courage, and perseverance throughout my life.

Contents

Contents	xxv
Synopsis	xxix
List of Figures	xliv
List of Tables	lxv
List of Abbreviations	lxvii
1 Introduction	1
1.1 The Standard Model of elementary particles	2
1.2 Quantum Chromodynamics and Quark–gluon plasma	4
1.3 QCD phase diagram	9
1.4 Relativistic heavy-ion collisions and their evolution	12
1.4.1 Kinematic variables and key observables	14
1.5 Experimental probes of QGP	18
1.5.1 Hard probes	19
1.5.2 Soft probes	23
1.6 Thesis physics motivation	31
1.6.1 Higher-order fluctuations of mean transverse momentum	32
1.6.2 Radial Flow through novel observable $v_0(p_T)$	33

1.6.3	Fluctuations and correlations of conserved charges	34
1.7	Organization of thesis	35
2	A Large Ion Collider Experiment	47
2.1	The Large Hadron Collider	48
2.2	ALICE detector	51
2.2.1	Inner Tracking System	54
2.2.2	Time Projection Chamber	55
2.2.3	Time-Of-Flight	58
2.2.4	V0	60
2.2.5	Trigger and data acquisition	62
2.3	ALICE offline analysis	63
2.3.1	Monte Carlo data generation	64
3	Experimental data and analysis methodology	67
3.1	Datasets	68
3.2	Event selection	68
3.3	Track selection	69
3.4	Particle identification	70
3.5	Centrality determination	73
3.6	Statistical uncertainty estimation	75
3.7	Systematic uncertainty estimation	76
4	Higher-order fluctuations of mean transverse momentum	81
4.1	Introduction	82
4.2	Observable	84
4.3	Analysis details	87
4.4	Results and discussions	94
4.4.1	Standardized skewness	94
4.4.2	Intensive skewness	97
4.4.3	Kurtosis	99
4.5	Summary	101
A.1	Simplification of multi-particle p_T correlators	105
A.1.1	2-particle p_T correlator, $\langle \Delta p_i \Delta p_j \rangle$	105

A.1.2	3-particle p_T correlator, $\langle \Delta p_i \Delta p_j \Delta p_k \rangle$	107
A.1.3	4-particle p_T correlator, $\langle \Delta p_i \Delta p_j \Delta p_k \Delta p_l \rangle$	109
5	Radial flow using $v_0(p_T)$	115
5.1	Introduction and motivation	116
5.2	Observable and methodology	118
5.3	Hydrodynamic predictions	119
5.4	Analysis details	122
5.4.1	Purity of selected particles	122
5.4.2	Effect of pseudorapidity-gap variation	124
5.4.3	Monte Carlo closure of $v_0(p_T)$	125
5.4.4	Systematic uncertainty	126
5.5	Results and discussions	127
5.5.1	$v_0(p_T)$ measurements	127
5.5.2	Sensitivity to transport and thermodynamic properties	134
5.5.3	Blast-wave modelling of $v_0(p_T)$	138
5.5.4	Extraction of blast-wave model parameters	145
5.6	Summary	155
6	Measurement of correlations among conserved charges	163
6.1	Introduction	164
6.1.1	Theoretical motivation	164
6.1.2	Experimental proxies for conserved charges	166
6.1.3	Review of previous studies	167
6.1.4	Non-critical effects influencing cumulant measurements	169
6.2	Observable	170
6.3	Analysis details	171
6.3.1	Purity of identified samples	171
6.3.2	Centrality bin-width correction	171
6.3.3	Detector efficiencies and correction of cumulants	173
6.3.4	Monte Carlo closure test for efficiency correction procedure	180
6.3.5	Systematic uncertainties	182
6.3.6	Brief review of theoretical models used for comparison	182

	HIJING and EPOS model	183
	Thermal-FIST model	184
	Modeling of resonance decays	185
6.4	Results and discussions	186
6.4.1	Effect of Q, B, S conservation	190
6.4.2	Estimation of CE correlation volume	192
6.4.3	Effect of resonance decays	195
6.4.4	Collision energy dependence	196
6.4.5	Testing the LQCD predictions with magnetic field	198
6.5	Summary	202
6.6	Outlook	203
7	Conclusions	209

Synopsis

The study of strongly interacting matter under extreme temperature and energy density is one of the central goals of relativistic heavy-ion collision experiments. Under such conditions, quantum chromodynamics (QCD), the fundamental theory of strong interactions, predicts the formation of a deconfined state of quarks and gluons, known as the quark–gluon plasma (QGP) [1–6]. This state of matter, believed to have existed in the early universe shortly after the Big Bang, can now be recreated under laboratory conditions through ultra-relativistic collisions of heavy nuclei [4, 7, 8]. The ALICE experiment [9, 10] at the Large Hadron Collider (LHC) is uniquely designed to investigate the properties of this QCD medium by measuring a wide range of observables sensitive to its thermodynamic and transport properties. A comprehensive understanding of the QGP can be obtained by studying event-by-event fluctuations of various quantities, such as temperature, particle multiplicity, net-conserved charge, and mean transverse momentum [11–13].

Among these, event-by-event fluctuations of mean transverse momentum, denoted as $\langle p_T \rangle$, serve as valuable probes of the dynamical processes occurring in heavy-ion collisions. These fluctuations can reflect temperature variations in the system, which are essential for

exploring the nature of the QCD phase transition [14]. A non-monotonic behavior of $\langle p_T \rangle$ fluctuations as a function of centrality or collision energy was proposed as a possible signature of QGP formation [13]. The space-time evolution of the medium created in heavy-ion collisions is described using relativistic hydrodynamics, which treats the QGP as a nearly perfect fluid exhibiting local thermal equilibrium and collective expansion [15, 16]. This hydrodynamic behavior governs the momentum distributions of the final-state particles. As a result, $\langle p_T \rangle$ fluctuations can carry important information about the degree of thermalization and the collective behavior of the system.

However, these fluctuations are not solely determined by the bulk properties of the medium itself. They are influenced by initial-state effects, such as event-by-event fluctuations in the geometry of the overlap region between the colliding nuclei. These include event-by-event variations in the initial size, shape, and orientation of the system, as well as in the number of participating nucleons. The presence of hard processes, such as jets, originating from high-momentum parton scatterings in the early stages of the collision, can introduce large amounts of transverse momentum into localized regions of an event, thereby modifying the event-wise average $\langle p_T \rangle$ and its fluctuations. Furthermore, final-state effects, including contributions from resonance decays and hadronic rescatterings, can also alter the observed $\langle p_T \rangle$ fluctuations.

Measurements of $\langle p_T \rangle$ fluctuations, characterized by the second-order cumulant of $\langle p_T \rangle$ distribution, have been reported at both RHIC and LHC energies [17, 18]. These studies reveal that for the most central collisions, the magnitude of $\langle p_T \rangle$ fluctuations remains relatively constant across a wide range of collision energies and system sizes. Contrary to earlier expectations, no evidence of a non-monotonic dependence on collision energy, suggested as a potential signature of the QCD phase transition, has been observed at RHIC. The fluctuations are generally found to be larger in small systems, such as in peripheral

collisions, and decrease systematically with increasing system size. This trend follows a power-law behavior with event multiplicity, that aligns with expectations from independent particle production, where the collision can be approximated as a superposition of multiple independent nucleon–nucleon interactions. However, in the most central heavy-ion collisions, a significant suppression of fluctuations is observed, suggesting the presence of collective dynamics or thermalization effects that go beyond simple superposition models.

In this thesis, we present the first measurements of higher-order fluctuations of $\langle p_T \rangle$ as a function of system size in Pb–Pb and Xe–Xe collisions at a centre-of-mass energy per nucleon–nucleon collision of $\sqrt{s_{NN}} = 5.02$ TeV and 5.44 TeV, respectively. These higher-order fluctuations, specifically the third and fourth moments of the $\langle p_T \rangle$ distribution, are referred to as skewness and kurtosis. While the second moment (variance) describes the overall spread of fluctuations, skewness captures the asymmetry of the distribution, and kurtosis characterizes how sharply peaked or flat the distribution is when compared to a Gaussian distribution. To quantify these moments, we use multi-particle transverse momentum correlators involving combinations of two, three, and four particles within each event. Two different measures of skewness are investigated. The first is standardized skewness, which measures the asymmetry relative to the width of the distribution. The second is intensive skewness, which is constructed to be independent of the number of particles produced in an event, and is therefore useful for comparing systems of different sizes.

Our measurements in both collision systems show that standardized skewness decreases with increasing system size, while intensive skewness remains positive and exceeds expectations from independent particle production. These findings are consistent with predictions from relativistic hydrodynamic model studies for semicentral to central collisions [19]. In such models, the evolution of the medium is initiated by the geometry and energy density

profile of the overlapping nuclei shortly after collision, and proceeds according to the laws of energy–momentum conservation, governed by the QCD equation of state and the transport properties of the QGP, such as shear and bulk viscosities. Moreover, by comparing our data with hydrodynamic model calculations that use various initial conditions, we observe that these higher-order moments are sensitive to fluctuations present in the earliest stages of the collision. In the most central collisions, we find a significant increase in skewness with event multiplicity, and kurtosis approaches values expected from Gaussian fluctuations. This behavior is also reproduced in hydrodynamic simulations as a generic consequence of local thermal equilibrium, and therefore points to the onset of thermalization in the system [20, 21].

To provide a baseline for interpreting results from heavy-ion collisions, similar measurements were also carried out in proton proton (pp) collisions at a centre of mass energy of $\sqrt{s} = 5.02$ TeV. When compared at similar multiplicities, the trends observed in pp collisions are qualitatively similar to those in heavy-ion collisions. Simulations using the PYTHIA8 event generator [22], incorporating a mechanism called color reconnection [23] that mimic collective behavior in small systems, qualitatively reproduce the experimental multiplicity dependence. This indicates that in addition to initial-state effects and hydrodynamic collective expansion, final-state interactions also play an important role in shaping the observed fluctuations.

The collective expansion of the QGP medium, leaving imprints in the momentum distributions of final-state particles, can also be explored through flow measurements. This expansion gives rise to two main types of flow: anisotropic flow, which reflects momentum-space anisotropies originating from the initial geometric asymmetries in the collision zone, and radial flow, which corresponds to the isotropic outward motion of particles driven by the system’s overall pressure buildup. Radial flow is typically inferred from transverse

momentum (p_T) spectra using simultaneous fits to pion, kaon, and proton distributions within the blast-wave model, a simplified hydrodynamic framework [24, 25]. However, this approach yields only a single effective value of the radial flow parameter known as the transverse radial expansion velocity ($\langle\beta_T\rangle$), masking finer details such as species-specific behavior or p_T -dependent modifications.

A recently proposed observable [26, 27], $v_0(p_T)$, addresses this limitation by allowing for a p_T -differential study. The observable, defined as the normalized covariance between the fraction of particles in a p_T -bin and the event-wise $\langle p_T \rangle$, is evaluated using a pseudorapidity (η) gap to suppresses short-range "nonflow" effects like resonance decays and jets. As a result, it captures genuine long-range p_T correlations arising from the collective radial expansion of the medium.

In this thesis, we report the first measurement of $v_0(p_T)$ for inclusive charged particles, pions, kaons, and protons, across different centrality intervals in Pb–Pb collisions at $\sqrt{s_{NN}} = 5.02$ TeV. It is found that $v_0(p_T)$ is negative at low p_T and positive at higher p_T , which results from the influence of $\langle p_T \rangle$ fluctuations on the spectral shape. An upward fluctuation in event-by-event $\langle p_T \rangle$ (i.e., $\langle p_T \rangle$ in an event $> \langle p_T \rangle$ averaged over all events) increases the number of high- p_T particles and reduces low- p_T ones, while a downward fluctuation has the opposite effect. This interplay determines the sign of $v_0(p_T)$, which typically changes near the $\langle p_T \rangle$ value of the corresponding particle species. The measurements further reveal a clear mass ordering at low p_T : $v_0(p_T)_{\text{pion}} > v_0(p_T)_{\text{kaon}} > v_0(p_T)_{\text{proton}}$, reflecting the stronger radial push experienced by heavier particles. At higher p_T ($p_T > 3$ GeV/c), protons exhibit a larger $v_0(p_T)$ than pions and kaons, suggesting possible contributions from quark recombination mechanisms in hadron production. These observed trends are consistent with those seen in anisotropic flow measurements [28].

Comparisons with hydrodynamic models highlight the sensitivity of $v_0(p_T)$ to the bulk

transport properties of the QGP medium. While hydrodynamic models using IP-Glasma initial conditions combined with hydrodynamic evolution (MUSIC) and a hadronic phase (UrQMD), describe the data well for $p_T \lesssim 2$ GeV/ c , they increasingly deviate at higher p_T . Importantly, changing model parameters such as bulk viscosity (ζ/s) and the equation of state (EOS) in the hydrodynamic model reveals that $v_0(p_T)$ is particularly sensitive to ζ/s and the squared speed of sound (c_s^2), while being less affected by shear viscosity (η/s) [29, 30]. This unique sensitivity makes $v_0(p_T)$ a promising new diagnostic tool for probing isotropic expansion and constraining the EOS of strongly interacting matter. In contrast, the HIJING model [31, 32], which does not incorporate collective expansion or hydrodynamic behavior but instead focuses on initial-state parton dynamics and jet production, significantly deviates from the experimental data in central Pb–Pb collisions. This discrepancy underscores that the observed $v_0(p_T)$ signal is dominated by final-state collective effects rather than non-flow contributions from initial-state processes. Overall, this measurement introduces $v_0(p_T)$ as a novel tool to study the bulk properties of the QGP, offering a p_T -differential perspective on radial flow that complements traditional measurements of azimuthal anisotropy.

To further understand the relation between $v_0(p_T)$ and the traditionally obtained radial velocity, $\langle\beta_T\rangle$, we employed a Boltzmann-Gibbs blast-wave model [33] that provides a simplified, hydrodynamically motivated description of the kinetic freeze-out stage, the moment when particles in the medium stop interacting and start moving freely toward the detectors. It assumes that this hot and dense medium is locally thermalized and expands collectively outward, similar to a fireball explosion. In this framework, the transverse momentum spectra of final-state particles are governed primarily by two parameters: the radial flow velocity, which reflects the collective expansion strength, and the kinetic freeze-out temperature, which characterizes the thermal conditions at decoupling. To investigate how

event-by-event variations in these parameters influence the shape of the $v_0(p_T)$ distribution, Gaussian fluctuations in both $\langle\beta_T\rangle$ and the freeze-out temperature are introduced in the model. It is found that the model qualitatively reproduces the key features of the $v_0(p_T)$ distributions observed in recent ALICE data. While an increase in the $\langle\beta_T\rangle$ enhances the characteristic mass ordering in $v_0(p_T)$, indicating a stronger collective push imparted to heavier particles, change in freeze-out temperature only controls the slope of $v_0(p_T)$. The width of the fluctuations primarily governs the overall magnitude of $v_0(p_T)$. To quantitatively extract these parameters, we used Bayesian parameter estimation to fit the model to ALICE measurements of identified hadrons. The results show that $\langle\beta_T\rangle$ decreases, and the kinetic freeze-out temperature increases from central to peripheral collisions, consistent with reduced collective expansion and earlier freeze-out in smaller systems. Such an anti-correlation between radial flow velocity and freeze-out temperature is consistent with earlier findings based on particle spectra [25]. The fluctuation widths of these parameters also increase toward peripheral collisions, indicating enhanced event-by-event variability. Model predictions based on the best-fit parameters describe the experimental data well, especially at low p_T . Together, these findings provide new insights into the nature of collective expansion and freeze-out dynamics, highlighting the role of flow strength, thermal motion, and their fluctuations in shaping $v_0(p_T)$ across different collision centralities.

Apart from studying the collective behavior and properties of the QGP, it is equally important to understand how this early-universe state transformed into the ordinary matter we observe today. Ordinary matter consists of hadrons such as baryons and mesons, in which quarks and gluons are confined. This transformation is closely related to the phase structure of strongly interacting matter, which is described by the QCD phase diagram [34]. The conjectured QCD phase diagram shows how matter behaves at different temperatures (T) and baryon chemical potentials (μ_B), highlighting the conditions under which the

transition between QGP and hadronic matter takes place. The baryon chemical potential reflects the imbalance between baryons and anti-baryons in the system. At the high energies achieved at the LHC, where μ_B is close to zero [35], first-principle lattice QCD (LQCD) calculations predict that the transition from hadronic matter to QGP occurs smoothly, as a crossover [36]. For larger values of μ_B , theory suggests that a first-order phase transition may occur [37]. This first-order transition line is expected to end at a critical point, where the system exhibits large fluctuations [34, 38–42].

Fluctuations and correlations among conserved charges, such as net-electric charge (Q), net-baryon number (B), and net-strangeness (S), are important tools for exploring the QCD phase structure [11–13]. These net- quantities represent the difference between the number of particles and antiparticles carrying a given conserved charge. They are directly connected to the underlying thermodynamic susceptibilities predicted by QCD, which can be calculated using LQCD and measured experimentally in heavy-ion collisions [43–47]. In experiments, these susceptibilities are accessed through the cumulants (σ) of event-by-event distributions of the corresponding net-conserved charges. Due to the limitation in detecting all baryons and strange hadrons on an event-by-event basis in experiments, net-proton (difference between number of protons and antiprotons, p) and net-kaon (difference between number of positively- and negatively-charged kaons, K) numbers are commonly used as proxies for net-baryon and net-strangeness, respectively. In addition to LQCD, fluctuation and correlation observables can be studied using the Hadron Resonance Gas (HRG) model, which serves as the basis of the statistical hadronization approach [48]. This approach assumes that the system is in thermal equilibrium at the time of chemical freeze-out, the moment when inelastic collisions cease and the relative abundances of different hadron species are fixed. The hadron abundances are determined using system's partition function governed by temperature and chemical potential, and can successfully

describe particle yields observed in experiments [49]. By comparing measured cumulants of conserved charges with model predictions, one can extract freeze-out parameters and explore their connection to the QCD phase transition [50].

In this thesis, we report the correlations among the net-charged particle, net-proton, and net-kaon ($C_{p,K}$, $C_{Q,K}$, and $C_{Q,p}$) as a function of centrality in Pb–Pb collisions at $\sqrt{s_{NN}} = 5.02$ TeV. These observables provide experimental insight into the correlations between conserved quantum numbers in QCD: baryon-strangeness (BS), charge-strangeness (QS), and charge-baryon (QB) correlations, respectively. They are constructed as ratios of second-order cumulants from event-by-event distributions of net-particle numbers. Since the ratios form intensive quantities, they are largely independent of the system volume and therefore show only a weak dependence on collision centrality. All three correlations exhibit significant deviations from the Poisson baseline, which represents the expectation for uncorrelated particle production. The observed deviations point to the presence of genuine dynamical correlations arising from physical processes such as resonance decays and charge conservation within a finite spatial volume [51, 52]. The measurements are compared to predictions from various hadronization models. Among them, the HRG model incorporating localized charge conservation provides the best description of the data. The size of this localized volume is quantitatively estimated through a chi-squared comparison between the model predictions and the experimental results. These LHC measurements are also compared to similar results at RHIC energies [53], revealing a stronger deviation from the Poisson baseline at higher collision energies. This trend is consistent with enhanced particle production and stronger correlations in the more densely interacting medium created at the LHC.

Additionally, certain combinations of cumulants are studied, that have been theoretically proposed as sensitive probes of the intense magnetic field (on the order of $\sim 10^4$ T) [54],

generated in collisions with non-zero impact parameter by the fast-moving spectator protons [55, 56]. Among these, a specific scaled ratio involving correlations between net-proton and net-electric charge shows a stronger deviation from unity in peripheral collisions. This trend is qualitatively consistent with predictions from LQCD and the observed deviations are not fully captured by HRG model calculations that do not include magnetic field effects. This suggests that additional physics mechanisms, such as the initial magnetic field, incomplete resonance decay contributions, or other medium-induced effects, may be influencing the results. These findings show the need for more detailed studies to better understand how magnetic fields influence the observed fluctuations and correlations.

This thesis presents a comprehensive experimental investigation of the properties of strongly interacting matter created in ultra-relativistic heavy-ion collisions at the LHC, using data from the ALICE experiment. The work introduces and analyzes novel observables, including higher-order moments (skewness and kurtosis) of event-by-event mean transverse momentum fluctuations, and the first measurement of a transverse momentum differential radial flow observable, $v_0(p_T)$, which captures long-range collective correlations. In addition, the thesis reports on centrality-dependent correlations among net-proton, net-kaon, and net-charge multiplicities to probe the interplay of conserved quantum numbers and the freeze-out conditions of the QCD medium. The results reveal signatures of thermalization, species-dependent collective expansion, and sensitivity to the QCD equation of state—especially the bulk viscosity and speed of sound—through comparison with hydrodynamic and statistical models. Together, these measurements provide new insights into the initial-state geometry, the transport properties of the quark–gluon plasma, and the QCD phase structure, advancing our understanding of QCD matter under extreme conditions.

The thesis is organized as follows: Chapter 1 provides a concise introduction to QCD and the formation of the quark–gluon plasma in heavy-ion collisions, emphasizing the im-

portance of studying fluctuations and collective phenomena to probe its properties. Chapter 2 provides an overview of the ALICE detector at the LHC and details the datasets analyzed from Pb–Pb, Xe–Xe, and pp collisions. Chapter 3 discusses the analysis methods common to all such as event and track selection, centrality determination, etc. Chapter 4 presents comprehensive measurements of event-by-event transverse momentum fluctuations, including higher-order moments such as skewness and kurtosis, alongside comparisons with theoretical models. Chapter 5 introduces the novel observable $v_0(p_T)$, offering new insights into radial flow and the bulk transport properties of the QGP. Chapter 6 investigates correlations among net-proton, net-kaon, and net-charge distributions, aiming to understand the QCD phase structure and freeze-out conditions. Finally, Chapter 7 summarizes the key findings and discusses their implications for advancing our understanding of QGP properties and the behavior of strongly interacting matter under extreme conditions.

Bibliography

- [1] Edward V. Shuryak. “Quark-Gluon Plasma and Hadronic Production of Leptons, Photons and Psions”. *Phys. Lett. B* 78 (1978), p. 150.
- [2] Edward V. Shuryak. “Quantum Chromodynamics and the Theory of Superdense Matter”. *Phys. Rept.* 61 (1980), pp. 71–158.
- [3] Wit Busza, Krishna Rajagopal, and Wilke van der Schee. “Heavy Ion Collisions: The Big Picture, and the Big Questions”. *Ann. Rev. Nucl. Part. Sci.* 68 (2018), pp. 339–376. arXiv: [1802.04801 \[hep-ph\]](#).
- [4] J. Schukraft. “Ultra-relativistic heavy-ion collisions: Searching for the quark-gluon plasma”. *Nucl. Phys. A* 553 (1993), pp. 31–44.
- [5] Ulrich W. Heinz. “The Strongly coupled quark-gluon plasma created at RHIC”. *J. Phys. A* 42 (2009). Ed. by David Neilson and Gaetano Senatore, p. 214003. arXiv: [0810.5529 \[nucl-th\]](#).

- [6] Shreyasi Acharya et al. “The ALICE experiment: a journey through QCD”. *Eur. Phys. J. C* 84.8 (2024), p. 813. arXiv: [2211.04384 \[nucl-ex\]](#).
- [7] R. S. Bhalerao and Rajiv V. Gavai. “Heavy Ions at LHC: A Quest for Quark-Gluon Plasma”. In: *Physics at the Large Hadron Collider*. Ed. by Amitava Datta et al. 2009, pp. 105–130. arXiv: [0812.1619 \[hep-ph\]](#).
- [8] D. Boyanovsky, H. J. de Vega, and D. J. Schwarz. “Phase transitions in the early and the present universe”. *Ann. Rev. Nucl. Part. Sci.* 56 (2006), pp. 441–500. arXiv: [hep-ph/0602002](#).
- [9] K. Aamodt et al. “The ALICE experiment at the CERN LHC”. *JINST* 3 (2008), S08002.
- [10] Betty Bezverkhny Abelev et al. “Performance of the ALICE Experiment at the CERN LHC”. *Int. J. Mod. Phys. A* 29 (2014), p. 1430044. arXiv: [1402.4476 \[nucl-ex\]](#).
- [11] Edward V. Shuryak. “Event per event analysis of heavy ion collisions and thermodynamical fluctuations”. *Phys. Lett. B* 423 (1998), pp. 9–14. arXiv: [hep-ph/9704456](#).
- [12] Misha A. Stephanov, K. Rajagopal, and Edward V. Shuryak. “Event-by-event fluctuations in heavy ion collisions and the QCD critical point”. *Phys. Rev. D* 60 (1999), p. 114028. arXiv: [hep-ph/9903292](#).
- [13] Henning Heiselberg. “Event-by-event physics in relativistic heavy ion collisions”. *Phys. Rept.* 351 (2001), pp. 161–194. arXiv: [nucl-th/0003046](#).
- [14] Leo Stodolsky. “Temperature fluctuations in multiparticle production”. *Phys. Rev. Lett.* 75 (1995), pp. 1044–1045.
- [15] Ulrich Heinz, Chun Shen, and Huichao Song. “The viscosity of quark-gluon plasma at RHIC and the LHC”. *AIP Conf. Proc.* 1441.1 (2012). Ed. by Stephen G. Steadman and George S. F. Stephans, pp. 766–770. arXiv: [1108.5323 \[nucl-th\]](#).
- [16] Charles Gale, Sangyong Jeon, and Bjoern Schenke. “Hydrodynamic Modeling of Heavy-Ion Collisions”. *Int. J. Mod. Phys. A* 28 (2013), p. 1340011. arXiv: [1301.5893 \[nucl-th\]](#).
- [17] J. Adams et al. “Incident energy dependence of pt correlations at RHIC”. *Phys. Rev. C* 72 (2005), p. 044902. arXiv: [nucl-ex/0504031](#).

- [18] Betty Bezverkhny Abelev et al. “Event-by-event mean p_T fluctuations in pp and Pb-Pb collisions at the LHC”. *Eur. Phys. J. C* 74.10 (2014), p. 3077. arXiv: [1407.5530 \[nucl-ex\]](#).
- [19] Giuliano Giacalone et al. “Skewness of mean transverse momentum fluctuations in heavy-ion collisions”. *Phys. Rev. C* 103.2 (2021), p. 024910. arXiv: [2004.09799 \[nucl-th\]](#).
- [20] Rupam Samanta et al. “Thermalization at the femtoscale seen in high-energy Pb+Pb collisions”. *Phys. Rev. C* 109.5 (2024), p. L051902. arXiv: [2303.15323 \[nucl-th\]](#).
- [21] Rupam Samanta et al. “Non-Gaussian transverse momentum fluctuations from impact parameter fluctuations”. *Phys. Rev. C* 108.2 (2023), p. 024908. arXiv: [2306.09294 \[nucl-th\]](#).
- [22] Torbjörn Sjöstrand et al. “An introduction to PYTHIA 8.2”. *Comput. Phys. Commun.* 191 (2015), pp. 159–177. arXiv: [1410.3012 \[hep-ph\]](#).
- [23] Torbjorn Sjostrand and Maria van Zijl. “A Multiple Interaction Model for the Event Structure in Hadron Collisions”. *Phys. Rev. D* 36 (1987), p. 2019.
- [24] L. Adamczyk et al. “Bulk Properties of the Medium Produced in Relativistic Heavy-Ion Collisions from the Beam Energy Scan Program”. *Phys. Rev. C* 96.4 (2017), p. 044904. arXiv: [1701.07065 \[nucl-ex\]](#).
- [25] Shreyasi Acharya et al. “Production of charged pions, kaons, and (anti-)protons in Pb-Pb and inelastic pp collisions at $\sqrt{s_{NN}} = 5.02$ TeV”. *Phys. Rev. C* 101.4 (2020), p. 044907. arXiv: [1910.07678 \[nucl-ex\]](#).
- [26] Björn Schenke, Chun Shen, and Derek Teaney. “Transverse momentum fluctuations and their correlation with elliptic flow in nuclear collision”. *Phys. Rev. C* 102.3 (2020), p. 034905. arXiv: [2004.00690 \[nucl-th\]](#).
- [27] Tribhuban Parida, Rupam Samanta, and Jean-Yves Ollitrault. “Probing collectivity in heavy-ion collisions with fluctuations of the p_T spectrum”. *Phys. Lett. B* 857 (2024), p. 138985. arXiv: [2407.17313 \[nucl-th\]](#).
- [28] Shreyasi Acharya et al. “Anisotropic flow and flow fluctuations of identified hadrons in Pb–Pb collisions at $\sqrt{s_{NN}} = 5.02$ TeV”. *JHEP* 05 (2023), p. 243. arXiv: [2206.04587 \[nucl-ex\]](#).

- [29] Heikki Mäntysaari et al. “Probing nuclear structure of heavy ions at energies available at the CERN Large Hadron Collider”. *Phys. Rev. C* 110.5 (2024), p. 054913. arXiv: [2409.19064 \[nucl-th\]](#).
- [30] Jiaxuan Gong, Hendrik Roch, and Chun Shen. “A Gaussian Process Generative Model for QCD Equation of State” (Oct. 2024). arXiv: [2410.22160 \[nucl-th\]](#).
- [31] Xin-Nian Wang and Miklos Gyulassy. “HIJING: A Monte Carlo model for multiple jet production in p p, p A and A A collisions”. *Phys. Rev. D* 44 (1991), pp. 3501–3516.
- [32] V. Topor Pop et al. “Baryon junction loops and the baryon-meson anomaly at high energies”. *Phys. Rev. C* 70 (2004), p. 064906. arXiv: [nucl-th/0407095](#).
- [33] Ekkard Schnedermann, Josef Sollfrank, and Ulrich W. Heinz. “Thermal phenomenology of hadrons from 200-A/GeV S+S collisions”. *Phys. Rev. C* 48 (1993), pp. 2462–2475. arXiv: [nucl-th/9307020](#).
- [34] M. A. Stephanov. “QCD phase diagram: An Overview”. *PoS LAT2006* (2006). Ed. by Tom Blum et al., p. 024. arXiv: [hep-lat/0701002](#).
- [35] Shreyasi Acharya et al. “Measurements of Chemical Potentials in Pb-Pb Collisions at $\sqrt{s_{NN}}=5.02$ TeV”. *Phys. Rev. Lett.* 133.9 (2024), p. 092301. arXiv: [2311.13332 \[nucl-ex\]](#).
- [36] Y. Aoki et al. “The Order of the quantum chromodynamics transition predicted by the standard model of particle physics”. *Nature* 443 (2006), pp. 675–678. arXiv: [hep-lat/0611014](#).
- [37] Shinji Ejiri. “Canonical partition function and finite density phase transition in lattice QCD”. *Phys. Rev. D* 78 (2008), p. 074507. arXiv: [0804.3227 \[hep-lat\]](#).
- [38] M. Asakawa and K. Yazaki. “Chiral Restoration at Finite Density and Temperature”. *Nucl. Phys. A* 504 (1989), pp. 668–684.
- [39] Juergen Berges, Dirk-Uwe Jungnickel, and Christof Wetterich. “The Chiral phase transition at high baryon density from nonperturbative flow equations”. *Eur. Phys. J. C* 13 (2000), pp. 323–329. arXiv: [hep-ph/9811347](#).
- [40] M. A. Stephanov. “Non-Gaussian fluctuations near the QCD critical point”. *Phys. Rev. Lett.* 102 (2009), p. 032301. arXiv: [0809.3450 \[hep-ph\]](#).

- [41] Xiaofeng Luo and Nu Xu. “Search for the QCD Critical Point with Fluctuations of Conserved Quantities in Relativistic Heavy-Ion Collisions at RHIC : An Overview”. *Nucl. Sci. Tech.* 28.8 (2017), p. 112. arXiv: [1701.02105 \[nucl-ex\]](#).
- [42] A. Pandav, D. Mallick, and B. Mohanty. “Search for the QCD critical point in high energy nuclear collisions”. *Prog. Part. Nucl. Phys.* 125 (2022), p. 103960. arXiv: [2203.07817 \[nucl-ex\]](#).
- [43] Sourendu Gupta et al. “Scale for the Phase Diagram of Quantum Chromodynamics”. *Science* 332 (2011), pp. 1525–1528. arXiv: [1105.3934 \[hep-ph\]](#).
- [44] A. Bazavov et al. “Fluctuations and Correlations of net baryon number, electric charge, and strangeness: A comparison of lattice QCD results with the hadron resonance gas model”. *Phys. Rev. D* 86 (2012), p. 034509. arXiv: [1203.0784 \[hep-lat\]](#).
- [45] Heng-Tong Ding, Frithjof Karsch, and Swagato Mukherjee. “Thermodynamics of strong-interaction matter from Lattice QCD”. *Int. J. Mod. Phys. E* 24.10 (2015), p. 1530007. arXiv: [1504.05274 \[hep-lat\]](#).
- [46] H. T. Ding et al. “Chiral Phase Transition Temperature in (2+1)-Flavor QCD”. *Phys. Rev. Lett.* 123.6 (2019), p. 062002. arXiv: [1903.04801 \[hep-lat\]](#).
- [47] Szabolcs Borsanyi et al. “Higher order fluctuations and correlations of conserved charges from lattice QCD”. *JHEP* 10 (2018), p. 205. arXiv: [1805.04445 \[hep-lat\]](#).
- [48] R. Venugopalan and M. Prakash. “Thermal properties of interacting hadrons”. *Nucl. Phys. A* 546 (1992), pp. 718–760.
- [49] Anton Andronic et al. “Decoding the phase structure of QCD via particle production at high energy”. *Nature* 561.7723 (2018), pp. 321–330. arXiv: [1710.09425 \[nucl-th\]](#).
- [50] B. Friman et al. “Fluctuations as probe of the QCD phase transition and freeze-out in heavy ion collisions at LHC and RHIC”. *Eur. Phys. J. C* 71 (2011), p. 1694. arXiv: [1103.3511 \[hep-ph\]](#).
- [51] D. K. Mishra et al. “Effect of resonance decay on conserved number fluctuations in a hadron resonance gas model”. *Phys. Rev. C* 94.1 (2016), p. 014905. arXiv: [1607.01875 \[hep-ph\]](#).

- [52] Peter Braun-Munzinger, Anar Rustamov, and Johanna Stachel. “The role of the local conservation laws in fluctuations of conserved charges” (July 2019). arXiv: [1907.03032 \[nucl-th\]](#).
- [53] Jaroslav Adam et al. “Collision-energy dependence of second-order off-diagonal and diagonal cumulants of net-charge, net-proton, and net-kaon multiplicity distributions in Au + Au collisions”. *Phys. Rev. C* 100.1 (2019). [Erratum: *Phys.Rev.C* 105, 029901 (2022)], p. 014902. arXiv: [1903.05370 \[nucl-ex\]](#).
- [54] V. Skokov, A. Yu. Illarionov, and V. Toneev. “Estimate of the magnetic field strength in heavy-ion collisions”. *Int. J. Mod. Phys. A* 24 (2009), pp. 5925–5932. arXiv: [0907.1396 \[nucl-th\]](#).
- [55] H. T. Ding et al. “Fluctuations and correlations of net baryon number, electric charge and strangeness in a background magnetic field”. *Eur. Phys. J. A* 57.6 (2021), p. 202. arXiv: [2104.06843 \[hep-lat\]](#).
- [56] Heng-Tong Ding et al. “Baryon Electric Charge Correlation as a Magnetometer of QCD”. *Phys. Rev. Lett.* 132.20 (2024), p. 201903. arXiv: [2312.08860 \[hep-lat\]](#).

List of Figures

- 1.1 A schematic overview of the Standard Model is shown, illustrating all known fundamental particles. The diagram groups quarks and leptons into three generations, and presents the bosons mediating forces, including the Higgs particle. Particle symbols, masses, charges, and spins are indicated for each, reflecting the organization of matter and interactions in contemporary particle physics. The figure is taken from Ref. [6]. 3
- 1.2 Evolution of the strong coupling constant α_s as a function of momentum transfer Q , determined from several processes including deep inelastic scattering (green triangles), e^+e^- annihilation (red circles), hadron collisions (blue diamonds), and heavy quarkonia (magenta squares). The solid curve and yellow band represent the QCD prediction and its uncertainty. The figure is taken from Ref. [16]. 7
- 1.3 Equation of state of QCD matter as a function of temperature from lattice QCD results, showing normalized pressure ($3p/T^4$), energy density (ϵ/T^4), and entropy density ($3s/T^4$). The yellow band indicates the region near the critical temperature T_c , with the hadron resonance gas (HRG) model shown for comparison at low T_c . The dotted line at the top represents the Stefan–Boltzmann (non-interacting gas) limit for comparison. The figure is taken from Ref. [26]. 10

1.4	Illustration of a conjectured phase diagram of QCD matter in temperature vs. baryon chemical potential μ_B plane, with distinct colors separating different phases of QCD matter—hadron gas, quark–gluon plasma, and the predicted color-superconducting phase. The figure is taken from Ref. [30].	11
1.5	Schematic illustration of the various stages in a relativistic heavy-ion collision. The temporal sequence moves from the initial state of Lorentz-contracted nuclei, through pre-equilibrium dynamics and QGP formation, followed by hadronization and hadronic rescattering, to final kinetic freeze-out and detection in the ALICE experiment. The figure is taken from Ref. [43].	13
1.6	Nuclear modification factor R_{AA} for central PbPb (SPS), AuAu (RHIC), and PbPb (LHC) collisions as a function of p_T , comparing results from WA98, PHENIX, STAR, CMS, and ALICE experiments. The data are shown alongside theoretical predictions for various parton energy loss scenarios in the quark–gluon plasma, illustrating strong jet quenching effects at RHIC and LHC energies. The figure is taken from Ref. [50].	20
1.7	Transverse momentum dependence of inclusive J/ψ nuclear modification factor R_{AA} in Pb–Pb collisions at $\sqrt{s_{NN}} = 5.02$ TeV and 2.76 TeV, measured by ALICE in the rapidity range $2.5 < y < 4$. Bottom panel shows the ratio of R_{AA} between 5.02 TeV and 2.76 TeV. The shaded band correspond to calculations from a transport model. Error bars and boxes indicate statistical and systematic uncertainties, respectively. The figure is taken from Ref. [52].	22
1.8	Transverse momentum dependence of the nuclear modification factor R_{AA} for $\Upsilon(1S)$, $\Upsilon(2S)$, and $\Upsilon(3S)$ mesons measured by the CMS experiment in Pb–Pb collisions at $\sqrt{s_{NN}} = 5.02$ TeV for rapidity $ y < 2.4$ and 0–90% centrality. The plot demonstrates strong and sequential suppression of the excited bottomonium states relative to the ground state. Statistical and systematic uncertainties are indicated by error bars and boxes, respectively. The figure is taken from Ref. [54].	22

- 1.9 Hyperon-to-pion ratios (Ξ/π and Ω/π) as a function of the mean number of participating nucleons ($\langle N_{\text{part}} \rangle$) in various collision systems and energies. Results are shown for Pb–Pb collisions at $\sqrt{s_{\text{NN}}} = 2.76$ TeV (ALICE), pp collisions at $\sqrt{s} = 7$ TeV and 900 GeV (ALICE), and Au–Au and pp collisions at $\sqrt{s_{\text{NN}}} = 200$ GeV (STAR). The increasing ratios with system size and event multiplicity clearly illustrate the enhancement of multi-strange baryon production. The solid and dashed lines indicate theoretical predictions from thermal models [57, 58]. Error bars represent statistical and systematic uncertainties. The figure is taken from Ref. [59]. 24
- 1.10 Illustration of anisotropic flow development in a non-central heavy-ion collision. Panel (a) shows the almond-shaped overlap region in the plane perpendicular to the beam axis. Panel (b) and (c) depicts the initial spatial asymmetry in coordinate space translating into anisotropy in momentum space of emitted particles. The figure is taken from Ref. [65]. 25
- 1.11 Shear viscosity to entropy density ratio (η/s) as a function of the temperature normalized to the critical temperature (T/T_c) for conventional substances like water and helium at different pressures, compared with the quark–gluon plasma created in heavy-ion collisions. The dashed line indicates the lower bound ($1/4\pi$) predicted by AdS/CFT calculations. The figure is adapted from Ref. [78]. 27
- 1.12 Centrality dependence of anisotropic flow coefficients $v_2\{2\}$, $v_2\{4\}$, $v_3\{2\}$, and $v_4\{2\}$, measured using multi-particle correlations (where the number in curly braces $\{m\}$ denotes the order of the m -particle correlation) in Pb–Pb collisions at $\sqrt{s_{\text{NN}}} = 2.76$ and 5.02 TeV. The experimental data points are compared with corresponding hydrodynamic model predictions indicated by the lines. The lower panel presents the ratio of model predictions to data for both energies, demonstrating agreement within $\pm 10\%$ across centralities. The figure is adapted from Ref. [78]. 27
- 1.13 Transverse momentum dependence of the elliptic flow coefficient, v_2 for identified particle species—pions, kaons, protons, ϕ mesons, K_s^0 , and Λ —measured in Pb–Pb collisions at $\sqrt{s_{\text{NN}}} = 5.02$ TeV with ALICE. Results are displayed for various collision centralities, highlighting the evolution of collective flow strength and particle-type dependence from central to peripheral events. The figure is taken from Ref. [79]. 28

1.14	The ratios of net-proton cumulants C_3/C_2 (left) and C_4/C_2 (right) plotted against the collision energy $\sqrt{s_{NN}}$ in Au+Au collisions at 0–5% centrality, for given kinematic acceptance on y and p_T . Solid lines show polynomial fits (5th order for C_3/C_2 and 4th order for C_4/C_2) to the data points, while dashed lines represent the Poisson baseline for comparison. Below each main plot, the derivative of the fit is shown to highlight the nonmonotonic behavior, with significance levels of 1.0σ for C_3/C_2 and 3.1σ for C_4/C_2 . Error bars combine both statistical and systematic uncertainties. The figure is adapted from Ref. [37].	30
1.15	Left: Relative fluctuations of the event-average p_T , shown as the normalized two-particle correlator for Pb–Pb collisions at $\sqrt{s_{NN}} = 2.76$ TeV (ALICE, red circles) and Au–Au collisions at 0.2 TeV (STAR, blue squares), plotted versus charged-particle multiplicity density $dN_{ch}/d\eta$. The dashed line corresponds to the independent particle production baseline (given by fit with $y \propto x^{-b}$). Right: ALICE data are compared to hydrodynamic model predictions for both 2.76 and 5.02 TeV. Lower panels display data/fit ratios and model/data comparisons. The figures are adapted from Refs. [78] and [90].	32
2.1	A schematic overview of the CERN accelerator complex, showing the chain of particle accelerators and transfer lines. The diagram highlights major facilities such as the LHC, SPS, PS, Booster, and LEIR, alongside specialized experiments and beamlines for protons, ions, antiprotons, electrons, muons, and neutrons. Color-coded paths indicate different particle types and the evolution of the complex from initial acceleration to high-energy collision points for experiments like ALICE, ATLAS, CMS, and LHCb, as well as other dedicated facilities with years marking their commencement. The figure is taken from Ref. [4].	49
2.2	Total integrated luminosities for different triggers: (left) pp collisions at $\sqrt{s} = 5.02$ TeV, (right) Pb–Pb collisions at $\sqrt{s_{NN}} = 5.02$ TeV, taken in the year 2015. The figures are taken from Refs. [5, 6].	51
2.3	Schematic illustration of the ALICE detector highlighting its subsystems with numbered labels. The figure is taken from Ref. [9].	53
2.4	Schematic representation of the ITS layer arrangement as implemented in the ALICE simulation and reconstruction software. The figure is taken from Ref. [10].	55

2.5	Schematic representation of the ALICE TPC, showing its key components: the central high-voltage electrode, inner and outer field cages, endplates, readout wire chambers, and the CO ₂ insulation gap. The coordinate axes (x, y, z) illustrate the detector's orientation relative to the beam direction. The figure is taken from Ref. [11].	56
2.6	Left: Specific energy loss resolution, $\sigma_{dE/dx}$ of the ALICE TPC as a function of the number of TPC clusters associated with a single track. Right: Relative transverse momentum resolution of the ALICE TPC as a function of particle transverse momentum. The figures are taken from Ref. [11].	57
2.7	Schematic representation of the ALICE TOF detector mechanical structure. The left panel illustrates the arrangement of TOF supermodules (highlighted in color) mounted on the cylindrical spaceframe that provides mechanical support, with the “babyframe” and “backframe” also indicated. The right panel shows a detailed representation of a single 9.3 m long supermodule, which houses five MRPC modules and custom electronics crates for readout. The figure is taken from Ref. [12].	58
2.8	Performance of the ALICE TOF detector. The figures are taken from Ref. [13].	59
2.9	The schematic layout illustrates the segmentation scheme of the V0 detector arrays in ALICE. The figure is taken from Ref. [14].	61
2.10	Centrality resolution as a function of centrality percentile for Pb–Pb collisions at $\sqrt{s_{NN}} = 2.76$ TeV, comparing performance across different ALICE detectors: ZDC vs ZEM, TPC, SPD, and VZERO. The figure is taken from Ref. [14]. . .	62
3.1	Particle identification performance in ALICE for Pb–Pb collisions at $\sqrt{s_{NN}} = 5.02$ TeV. (Left) TPC specific energy loss (dE/dx) versus momentum over charge (p/z), showing clear separation of particle species (π , K, p, d, t, ^3He). (Right) TOF measured velocity (β) versus momentum, with visible bands for electrons, pions, kaons, protons, and deuterons. These distributions demonstrate the capability of the ALICE detectors to discriminate between different charged hadrons over a broad momentum range. The figures are taken from Refs. [6, 7].	71

- 3.2 Diagram illustrating the geometry of a relativistic heavy-ion collision with nonzero impact parameter. Lorentz contraction flattens the nuclei along their direction of motion (as indicated by arrows), making them appear disk-like. Nucleons within the overlapping region are classified as participants; those outside (beyond dashed lines) are spectators. The impact parameter quantifies the distance between the centers of the colliding nuclei in the transverse plane. 73
- 3.3 The V0 scintillators' amplitude distribution for Pb–Pb collisions at $\sqrt{s_{\text{NN}}} = 5.02$ TeV. The line represents the NBD-Glauber fit to the data, while the inset provides a closer view of the most peripheral collisions. In the bottom panel, the ratio of experimental data to fit is shown. The figure is taken from Ref. [12]. 75
- 3.4 Illustration of bootstrap sampling: multiple new datasets (bootstrap samples) are generated by randomly sampling with replacement from the original dataset. Each bootstrap sample may contain repeated or omitted data points, enabling robust statistical inference about the original population. The figure is taken from Ref. [14]. 76
- 4.1 Correlation between the event-by-event mean transverse momentum $\langle p_{\text{T}} \rangle$ and initial-state properties in Pb+Pb collisions at $\sqrt{s_{\text{NN}}} = 5.02$ TeV: (left) anticorrelation with the initial transverse size R of the fireball, and (right) positive correlation with the initial energy E_i , as obtained from T_RENTO+V-USPHYDRO (referred as T_RENTO+V-USPHYDRO in figure) simulations. The figure is adapted from Ref. [2]. 83
- 4.2 Centrality dependence of the intensive skewness of event-by-event mean transverse momentum distributions for hydrodynamic models in Pb+Pb (open circles) and Xe+Xe (filled circles) collisions at $\sqrt{s_{\text{NN}}} = 5.02$ TeV and 5.44 TeV, respectively, compared to the independent particle emission baseline (dotted line). Error bars represent statistical uncertainties. The figure is taken from Ref. [3]. 84

- 4.3 The probability distributions of $\langle p_T \rangle$, measured for different centrality intervals in Pb–Pb collisions at $\sqrt{s_{NN}} = 5.02$ TeV. True distributions (red open circles) are compared to reference distributions (black stars) along with their corresponding Gaussian fits (dashed red lines for data, solid black lines for reference distributions (see text for details) for each centrality interval. The lower panels show the ratio between the measured distribution and the corresponding fit. The figure is taken from Ref. [8]. 88
- 4.4 Comparison between reconstructed and generated (truth) results for standardized skewness (left), intensive skewness (middle), and kurtosis (right) of $\langle p_T \rangle$ fluctuations in Pb–Pb collisions at $\sqrt{s_{NN}} = 5.02$ TeV using the HIJING event generator. The top row presents the measured quantities as a function of centrality, while the bottom row displays the ratio of reconstructed to generated quantities, which is fitted with a zeroth-order polynomial (red solid line). The blue dashed line at unity is shown for reference that would represent 100% closure, and the obtained closure values are also denoted. The vertical bars represent only statistical uncertainties. 89
- 4.5 Comparison between reconstructed and generated (truth) results for standardized skewness (left), intensive skewness (middle), and kurtosis (right) of $\langle p_T \rangle$ fluctuations in Xe–Xe collisions at $\sqrt{s_{NN}} = 5.44$ TeV using the HIJING event generator. The top row presents the measured quantities as a function of centrality, while the bottom row displays the ratio of reconstructed to generated quantities, which is fitted with a zeroth-order polynomial (red solid line). The blue dashed line at unity is shown for reference that would represent 100% closure, and the obtained closure values are also denoted. The vertical bars represent only statistical uncertainties. 91

- 4.6 Comparison between reconstructed and generated (truth) results for standardized skewness (left), intensive skewness (middle), and kurtosis (right) of $\langle p_T \rangle$ fluctuations in pp collisions at $\sqrt{s} = 5.02$ TeV using the PYTHIA event generator. The top row presents the measured quantities as a function of V0M multiplicity percentile, while the bottom row displays the ratio of reconstructed to generated quantities, which is fitted with a zeroth-order polynomial (red solid line). The blue dashed line at unity is shown for reference that would represent 100% closure, and the obtained closure values are also denoted. The vertical bars represent only statistical uncertainties. 92
- 4.7 Correlation between the mean accepted charged-particle multiplicity $\langle N_{\text{acc}} \rangle$ for the kinematic region $0.2 < p_T < 3.0$ GeV/c and $|\eta| < 0.8$ and the midrapidity charged-particle density $\langle dN_{\text{ch}}/d\eta \rangle_{|\eta| < 0.5}$ for Pb–Pb collisions at $\sqrt{s_{\text{NN}}} = 5.02$ TeV. Central values and the values shifted up and down by their uncertainty are fitted with a first-order polynomial to enable conversion between centrality intervals and multiplicity density for system comparisons. . 93
- 4.8 Correlation between the mean accepted charged-particle multiplicity $\langle N_{\text{acc}} \rangle$ for the kinematic region $0.2 < p_T < 3.0$ GeV/c and $|\eta| < 0.8$ and the midrapidity charged-particle density $\langle dN_{\text{ch}}/d\eta \rangle_{|\eta| < 0.5}$ for Xe–Xe collisions at $\sqrt{s_{\text{NN}}} = 5.44$ TeV. Central values and the values shifted up and down by their uncertainty are fitted with a first-order polynomial to enable conversion between centrality intervals and multiplicity density for system comparisons. . 93
- 4.9 Standardized skewness $\gamma_{\langle p_T \rangle}$ of the event-averaged transverse momentum distribution is shown as a function of the cubic root of midrapidity charged-particle density, $\langle dN_{\text{ch}}/d\eta \rangle_{|\eta| < 0.5}^{1/3}$ in Pb–Pb collisions at $\sqrt{s_{\text{NN}}} = 5.02$ TeV, Xe–Xe collisions at $\sqrt{s_{\text{NN}}} = 5.44$ TeV and pp collisions at $\sqrt{s} = 5.02$ TeV. Colored bands represent predictions from event generators (PYTHIA8, HIJING) and hydrodynamic simulations (V-USPHYDRO, and MC-Glauber+MUSIC). Statistical and systematic uncertainties are represented by vertical bars and shaded boxes, respectively. The figure is taken from Ref. [8]. 95

- 4.10 Intensive skewness $\Gamma_{\langle p_T \rangle}$ of the event-averaged transverse momentum distribution is shown as a function of the cubic root of midrapidity charged-particle density, $\langle dN_{\text{ch}}/d\eta \rangle_{|\eta| < 0.5}^{1/3}$ in Pb–Pb collisions at $\sqrt{s_{\text{NN}}} = 5.02$ TeV, Xe–Xe collisions at $\sqrt{s_{\text{NN}}} = 5.44$ TeV and pp collisions at $\sqrt{s} = 5.02$ TeV. Colored bands represent predictions from event generators (PYTHIA8, HIJING) and hydrodynamic simulations (V-USPHYDRO, and MC-Glauber+MUSIC). Statistical and systematic uncertainties are represented by vertical bars and shaded boxes, respectively. Independent baseline calculations for each system are also displayed (dotted lines) for reference. The figure is taken from Ref. [8]. 98
- 4.11 Kurtosis $\kappa_{\langle p_T \rangle}$ of the event-averaged transverse momentum distribution is shown as a function of the cubic root of midrapidity charged-particle density, $\langle dN_{\text{ch}}/d\eta \rangle_{|\eta| < 0.5}^{1/3}$ in Pb–Pb collisions at $\sqrt{s_{\text{NN}}} = 5.02$ TeV, Xe–Xe collisions at $\sqrt{s_{\text{NN}}} = 5.44$ TeV and pp collisions at $\sqrt{s} = 5.02$ TeV. Colored bands represent predictions from event generators (PYTHIA8, HIJING) and hydrodynamic simulation (MC-Glauber+MUSIC). The dashed curve marks the Gaussian expectation for reference. Vertical lines depict statistical uncertainties, with boxes illustrating the systematic error range for each data point. The figure is taken from Ref. [8]. 100
- 5.1 Blast-wave model predictions for the transverse momentum (p_T) spectra of pions, kaons, and protons, shown for two scenarios: without radial flow ($\langle \beta_T \rangle = 0$, dashed blue line) and with significant radial flow ($\langle \beta_T \rangle = 0.5$, solid orange line). 117
- 5.2 Schematic illustration of the sub-event method with a pseudorapidity gap ($\Delta\eta = 0.4$). Regions A ($-0.8 < \eta < -0.2$) and B ($0.2 < \eta < 0.8$) are separated to suppress nonflow effects from short-range correlations in the measurement. 118
- 5.3 Illustration of how fluctuations in event-wise mean transverse momentum $[p_T]$ influence the shape of the p_T spectrum. Events with $[p_T] < \langle [p_T] \rangle$ (blue dashed line) and $[p_T] > \langle [p_T] \rangle$ (green dashed line) show opposite changes in particle yields at low and high p_T , resulting in negative and positive correlations in $v_0(p_T)$ respectively. 120

5.4	Transverse momentum dependence of $v_0(p_T)$ for inclusive charged particles (h^\pm), pions ($\pi^+ + \pi^-$), kaons ($K^+ + K^-$), and protons ($p + \bar{p}$) in Pb–Pb collisions at $\sqrt{s_{NN}} = 5.02$ TeV for the 30–40% centrality interval. The figure is taken from Ref. [4].	121
5.5	Purity as a function of transverse momentum (p_T) for identified pions (top left), kaons (top right), and protons (bottom) in Pb–Pb collisions at $\sqrt{s_{NN}} = 5.02$ TeV. Results are shown separately for particles and antiparticles, selected within the acceptance $ \eta < 0.8$ and $0.2 < p_T < 6.0$ GeV/c. The values, greater than 0.9 for kaons and close to 1 for pions, and protons, indicate high sample purity for all particle species across the measured p_T intervals. Average purity values for each species are also noted in the panels.	123
5.6	Dependence of $v_0(p_T)$ on the pseudorapidity gap ($\Delta\eta$) for inclusive charged particles in Pb–Pb collisions at $\sqrt{s_{NN}} = 5.02$ TeV, shown for three centrality intervals: 10–20%, 30–40%, and 60–70%. Top panels display $v_0(p_T)$ for various $\Delta\eta$ values, while bottom panels present the ratio with respect to zero gap ($\Delta\eta = 0$), illustrating the suppression of nonflow effects with the inclusion of η -gap, across different centralities. The figure is taken from Ref. [18].	124
5.7	Comparison of $v_0(p_T)$ obtained from generated events and corresponding reconstructed ones for inclusive charged particles in Pb–Pb collisions at $\sqrt{s_{NN}} = 5.02$ TeV, simulated with HIJING and ALICE detector modeling. Results are shown for three centrality intervals (10–20%, 30–40%, and 60–70%). The close agreement between generated and reconstructed values across all centrality classes demonstrates that detector effects do not significantly bias the measurement of $v_0(p_T)$. The figure is taken from Ref. [18].	125
5.8	Systematic uncertainties (absolute value) in the measurement of $v_0(p_T)$ for inclusive charged particles as a function of p_T in three centrality classes (10–20%, 30–40%, and 60–70%). The contributions from individual sources, including centrality estimation, pileup rejection, tracking quality cuts (fit of TPC χ^2 , ITS χ^2 , filter bit selection that controls DCA, TPC crossed rows), primary vertex position (V_z), minimum pseudorapidity-gap (η_{\min}), and the total combined uncertainty, are shown separately.	127

- 5.9 Systematic uncertainties (absolute value) in the measurement of $v_0(p_T)$ for pions as a function of p_T in three centrality classes (10–20%, 30–40%, and 60–70%). The contributions from individual sources, including centrality estimation, pileup rejection, tracking quality cuts (fit of TPC χ^2 , ITS χ^2 , filter bit selection that controls DCA, TPC crossed rows), primary vertex position (V_z), particle identification (PID), minimum pseudorapidity-gap (η_{\min}), and the total combined uncertainty, are shown separately. 128
- 5.10 Systematic uncertainties (absolute value) in the measurement of $v_0(p_T)$ for kaons as a function of p_T in three centrality classes (10–20%, 30–40%, and 60–70%). The contributions from individual sources, including centrality estimation, pileup rejection, tracking quality cuts (fit of TPC χ^2 , ITS χ^2 , filter bit selection that controls DCA, TPC crossed rows), primary vertex position (V_z), particle identification (PID), minimum pseudorapidity-gap (η_{\min}), and the total combined uncertainty, are shown separately. 128
- 5.11 Systematic uncertainties (absolute value) in the measurement of $v_0(p_T)$ for protons as a function of p_T in three centrality classes (10–20%, 30–40%, and 60–70%). The contributions from individual sources, including centrality estimation, pileup rejection, tracking quality cuts (fit of TPC χ^2 , ITS χ^2 , filter bit selection that controls DCA, TPC crossed rows), primary vertex position (V_z), particle identification (PID), minimum pseudorapidity-gap (η_{\min}), and the total combined uncertainty, are shown separately. 129
- 5.12 Transverse momentum dependence of $v_0(p_T)$ for inclusive charged particles in Pb–Pb collisions at $\sqrt{s_{NN}} = 5.02$ TeV. The measurements for three centrality intervals 10–20% (top-left), 30–40% (top-right), and 60–70% (bottom-left) are compared to expectations from HIJING [19] and IP-Glasma+MUSIC+UrQMD [23] models. The bottom right panel presents the normalized ratio $v_0(p_T)/v_0$ as a function of p_T for the three centrality intervals. Statistical uncertainties are shown as bars and systematic uncertainties as boxes. The figure is taken from Ref. [18]. 130

- 5.13 Transverse momentum dependence of $v_0(p_T)$ for pions (π^\pm), kaons (K^\pm), and protons ($p(\bar{p})$) in Pb–Pb collisions at $\sqrt{s_{NN}} = 5.02$ TeV. Measurements for three centrality intervals, 10–20% (left), 30–40% (middle), and 60–70% (right), are compared with HIJING [19] and IP-Glasma+MUSIC+UrQMD [23] models. Statistical uncertainties are shown as bars and systematic uncertainties as boxes. The lower panels present the normalized difference between data and models, $(\text{Data-Model})/\sigma$. The figure is taken from Ref. [18]. 132
- 5.14 The $v_0(p_T)$ values for pions (π^\pm), kaons (K^\pm), and protons ($p(\bar{p})$) are scaled by the number of constituent quarks (n_q), and displayed as a function of transverse kinetic energy per constituent quark, $(m_T - m_0)/n_q$, measured in Pb–Pb collisions at $\sqrt{s_{NN}} = 5.02$ TeV. The results are presented for three centrality intervals: 10–20% (left), 30–40% (middle), and 60–70% (right). The solid curve shows a smooth cubic fit to the pion data, providing a clear representation of the overall trend. The figure is taken from Ref. [18]. 133
- 5.15 Transverse momentum dependence of $v_0(p_T)$ of inclusive charged particles in 10–20% central Pb–Pb collisions at $\sqrt{s_{NN}} = 5.02$ TeV, compared to IP-Glasma+MUSIC+UrQMD [23] calculations for variations in transport coefficients, η/s and ζ/s . Statistical (systematic) uncertainties are represented by vertical bars (boxes). The statistical uncertainties are also smaller than the marker size and thus not visible. The figure is taken from Ref. [18]. 135
- 5.16 Transverse momentum dependence of $v_0(p_T)$ of inclusive charged particles in 10–20% central Pb–Pb collisions at $\sqrt{s_{NN}} = 5.02$ TeV, compared to IP-Glasma+MUSIC+UrQMD [23] calculations for different equations of state (EOS). Statistical (systematic) uncertainties are represented by vertical bars (boxes). The statistical uncertainties are also smaller than the marker size and thus not visible. The figure is taken from Ref. [18]. 136
- 5.17 Squared speed of sound (c_s^2) as a function of temperature (T) for three QCD equations of state: EOS1 (green dashed line), EOS2 (blue dash-dotted line), and the lattice QCD-based HotQCD EOS (solid black line). The conformal limit ($c_s^2 = 1/3$) is indicated by the dotted orange line. This figure is taken from Ref. [17]. 137

- 5.18 Centrality dependence of the slope term of $v_0(p_T)$ scaled with $\sqrt{N_{\text{ch}}}$ for $0.2 < p_T < 3.0$ GeV/c, comparing predictions from EOS1 (red dashed line), EOS2 (green dash-dotted line), and the lattice QCD-based HotQCD EOS (solid black line). Shaded bands indicate model uncertainties. This figure is taken from Ref. [17]. 138
- 5.19 Transverse momentum dependence of $v_0(p_T)$ of inclusive charged particles in 10–20% central Pb–Pb collisions at $\sqrt{s_{\text{NN}}} = 5.02$ TeV, compared to IP-Glasma+MUSIC+UrQMD [23] calculations for initial conditions (IC) with (w) and without (w/o) sub-nucleonic fluctuations (right). Statistical (systematic) uncertainties are represented by vertical bars (boxes). The statistical uncertainties are also smaller than the marker size and thus not visible. The figure is taken from Ref. [18]. 139
- 5.20 Transverse momentum dependence of $v_0(p_T)$ for pions (left), kaons (middle), and protons (right), obtained from the blast-wave model incorporating Gaussian fluctuations in the transverse expansion velocity at the surface. The kinetic freeze-out temperature (T_{kin}) and the fluctuation width of the surface velocity $\sigma(\beta_s)$ are fixed at 0.094 GeV and 0.006, respectively, while the mean surface velocity β_s is varied in the range [0.697, 0.927]. The figure is taken from Ref. [35]. 141
- 5.21 Transverse momentum dependence of $v_0(p_T)$ for pions (left), kaons (middle), and protons (right), obtained from the blast-wave model incorporating Gaussian fluctuations in the transverse expansion velocity at the surface. $v_0(p_T)$ of pions (left), kaons (middle), and protons (right) in blast-wave model for Gaussian-fluctuations of transverse expansion velocity at the surface. The kinetic freeze-out temperature (T_{kin}) and mean value of fluctuations β_s are kept fixed at 0.094 GeV and 0.897, respectively, while the width $\sigma(\beta_s)$ is varied in the range [0.003, 0.015] [35]. 142

- 5.22 Transverse momentum dependence of $v_0(p_T)$ for pions (left), kaons (middle), and protons (right), obtained from the blast-wave model incorporating Gaussian fluctuations in the transverse expansion velocity at the surface. $v_0(p_T)$ of pions (left), kaons (middle), and protons (right) in blast-wave model for Gaussian-fluctuations of kinetic freeze-out temperature. The transverse expansion velocity at the surface (β_s) and width of fluctuations $\sigma(T_{\text{kin}})$ are kept fixed at 0.897 and 0.003 GeV, respectively, while the mean value T_{kin} is varied in the range [0.064, 0.114] GeV [35]. 143
- 5.23 Transverse momentum dependence of $v_0(p_T)$ for pions (left), kaons (middle), and protons (right) obtained from the blast-wave model incorporating Gaussian fluctuations in the transverse expansion velocity at the surface. $v_0(p_T)$ of pions (left), kaons (middle), and protons (right) in blast-wave model for Gaussian-fluctuations of kinetic freeze-out temperature. The transverse expansion velocity at the surface (β_s) and mean value of fluctuations T_{kin} are kept fixed at 0.897 and 0.094 GeV, respectively, while the width $\sigma(T_{\text{kin}})$ is varied in the range [0.003, 0.010] GeV [35]. 144
- 5.24 The posterior distributions and parameter correlations for $n, \beta_s, T_{\text{kin}}, \sigma(\beta_s)$, and $\sigma(T_{\text{kin}})$ using $v_0(p_T)$ measurements of pions, kaons, and protons for centrality classes 10–20%. The diagonal panels display the marginalized probability distributions of individual parameters, while the off-diagonal panels show the 2D joint distributions with contour levels indicating confidence regions. The plot suggests correlations between some parameters, highlighting the uncertainties in their estimations. The figure is taken from Ref. [35]. 148
- 5.25 The posterior distributions and parameter correlations for $n, \beta_s, T_{\text{kin}}, \sigma(\beta_s)$, and $\sigma(T_{\text{kin}})$ using $v_0(p_T)$ measurements of pions, kaons, and protons for centrality classes 30–40%. The diagonal panels display the marginalized probability distributions of individual parameters, while the off-diagonal panels show the 2D joint distributions with contour levels indicating confidence regions. The plot suggests correlations between some parameters, highlighting the uncertainties in their estimations [35]. 149

- 5.26 The posterior distributions and parameter correlations for n , β_s , T_{kin} , $\sigma(\beta_s)$, and $\sigma(T_{\text{kin}})$ using $v_0(p_T)$ measurements of pions, kaons, and protons for centrality classes 60–70%. The diagonal panels display the marginalized probability distributions of individual parameters, while the off-diagonal panels show the 2D joint distributions with contour levels indicating confidence regions. The plot suggests correlations between some parameters, highlighting the uncertainties in their estimations [35]. 150
- 5.27 Transverse momentum dependence of $v_0(p_T)$ of pions (left), kaons (middle), and protons (right) in Pb–Pb collisions at $\sqrt{s_{\text{NN}}} = 5.02$ TeV for centrality interval 10–20%. The measurements of ALICE (red marker) are compared to blast-wave predictions obtained with the best-fit parameters. The bottom panels show the residual, $n\sigma = (\text{data} - \text{model})/\text{error}_{\text{data}}$. The figure is taken from Ref. [35]. 151
- 5.28 Transverse momentum dependence of $v_0(p_T)$ of pions (left), kaons (middle), and protons (right) in Pb–Pb collisions at $\sqrt{s_{\text{NN}}} = 5.02$ TeV for centrality interval 30–40%. The measurements of ALICE (red marker) are compared to blast-wave predictions obtained with the best-fit parameters. The bottom panels show the residual, $n\sigma = (\text{data} - \text{model})/\text{error}_{\text{data}}$ [35]. 152
- 5.29 Transverse momentum dependence of $v_0(p_T)$ of pions (left), kaons (middle), and protons (right) in Pb–Pb collisions at $\sqrt{s_{\text{NN}}} = 5.02$ TeV for centrality interval 60–70%. The measurements of ALICE (red marker) are compared to blast-wave predictions obtained with the best-fit parameters. The bottom panels show the residual, $n\sigma = (\text{data} - \text{model})/\text{error}_{\text{data}}$ [35]. 152
- 5.30 Comparison of the extracted surface radial flow velocity (β_s , left) and kinetic freeze-out temperature (T_{kin} , right) as a function of centrality. The results from this analysis, obtained via blast-wave model fits to $v_0(p_T)$ measurements, are shown together with values previously determined from blast-wave fits to p_T spectra reported in Ref. [3]. Vertical bars indicate the uncertainties estimated from fit for each point. The figure is taken from Ref. [35]. 155

6.1	The correlations, $C_{p,K}$ (top), $C_{Q,K}$ (middle), and $C_{Q,p}$ (bottom) as a function of centre-of-mass energy per nucleon pair, $\sqrt{s_{NN}}$ for Au+Au collisions. The markers correspond to data points from the STAR experiment while the colored bands are from UrQMD model calculations. The results from the HRG model are shown as red dot-dashed curves, while the Poisson expectation is indicated by black dashed lines. Statistical uncertainties are represented by bars, and systematic uncertainties are illustrated using shaded boxes. This figure is taken from Ref. [8].	168
6.2	The p_T dependence of purities of pions (top-left), kaons (top-right), and protons (bottom) up to 2 GeV/c in Pb–Pb collisions at $\sqrt{s_{NN}} = 5.02$ TeV. The black markers represent particle (π^+ , K^+ , and p) while red markers represent anti-particle (π^- , K^- , and \bar{p}), and the integrated purity values for the respective particle are given in the legend.	172
6.3	The centrality dependence of second-order cumulants of net-charge, net-kaon and net-proton in Pb–Pb collisions at $\sqrt{s_{NN}} = 5.02$ TeV. The different colored markers represent different centrality bin width.	174
6.4	Comparison of centrality bin width (CBW) corrected and uncorrected results of second-order cumulants of net-charge, net-kaon and net-proton as a function of centrality in Pb–Pb collisions at $\sqrt{s_{NN}} = 5.02$ TeV.	175
6.5	Two-dimensional event-by-event distributions correlating generated and reconstructed net-particle numbers in Pb–Pb collisions at $\sqrt{s_{NN}} = 5.02$ TeV, obtained using the HIJING event generator. From left to right, the panels correspond to net-pion, net-kaon, and net-proton multiplicities.	176
6.6	The p_T dependence of efficiency for pions, π^+ (left) and π^- (right), across different centrality intervals in Pb–Pb collisions at $\sqrt{s_{NN}} = 5.02$ TeV. The bottom panel shows the ratio of efficiencies in a given centrality interval relative to those in the 0–90% interval.	177
6.7	The p_T dependence of efficiency for pions, K^+ (left) and K^- (right), across different centrality intervals in Pb–Pb collisions at $\sqrt{s_{NN}} = 5.02$ TeV. The bottom panel shows the ratio of efficiencies in a given centrality interval relative to those in the 0–90% interval.	177

- 6.8 The p_T dependence of efficiency for pions, p (left) and \bar{p} (right), across different centrality intervals in Pb–Pb collisions at $\sqrt{s_{NN}} = 5.02$ TeV. The bottom panel shows the ratio of efficiencies in a given centrality interval relative to those in the 0–90% interval. 178
- 6.9 Results of the Monte Carlo closure test for efficiency correction procedures in Pb–Pb collisions at $\sqrt{s_{NN}} = 5.02$ TeV. Shown are the second-order diagonal and off-diagonal cumulants for net-charge, net-kaon, and net-proton distributions as a function of collision centrality. The generated cumulants (red markers) are compared to reconstructed values before (blue markers) and after (black markers) efficiency correction. The efficiency-corrected cumulants closely match the generated results, demonstrating the validity of the correction method within statistical uncertainties. 181
- 6.10 The second-order diagonal cumulants, κ_α^2 , and off-diagonal cumulants, $\kappa_{\alpha,\beta}^{11}$, for net-pion, net-kaon, net-proton, and net-electric charge distributions measured in Pb–Pb collisions at $\sqrt{s_{NN}} = 5.02$ TeV. Results are displayed as a function of centrality for two distinct p_T ranges, referred to as Set 1 and Set 2 (refer to text for details). Statistical uncertainties are indicated by vertical error bars, while systematic uncertainties are shown as open boxes. The figure is taken from Ref. [22]. 187
- 6.11 The cumulant ratios $C_{Q,p}$ (top panel), $C_{Q,K}$ (middle panel), and $C_{p,K}$ (bottom panel) in Pb–Pb collisions at $\sqrt{s_{NN}} = 5.02$ TeV is shown as a function of centrality, with left and right columns corresponding to two distinct p_T intervals, referred to as Set 1 and Set 2, respectively. Model predictions from HIJING [17], EPOS LHC [23], and Thermal-FIST [24] are shown as colored lines. The Thermal-FIST calculations are presented within both the grand canonical (GCE) and canonical ensemble (CE) frameworks. The CE calculations impose exact conservation of electric charge, baryon number, and strangeness within a correlation volume defined as $V_c = 3dV/dy$. Statistical uncertainties are represented by vertical bars, systematic uncertainties by open boxes, and the dashed line indicates the Poisson baseline expectation. The figure is taken from Ref. [22]. 189

- 6.12 The centrality dependence of $C_{p,K}$ (top-left), $C_{Q,p}$ (top-right), and $C_{Q,K}$ (bottom) is presented for Pb–Pb collisions at $\sqrt{s_{NN}} = 5.02$ TeV for Set 1 p_T acceptance (π^\pm , K^\pm : $0.2 < p_T < 2.0$ GeV/ c , and $p(\bar{p})$: $0.4 < p_T < 2.0$ GeV/ c). The colored lines represent predictions from the Thermal-FIST (TheFIST) model in the canonical ensemble (CE), calculated with a correlation volume of $V_c = 3dV/dy$, under various conservation scenarios for Q, B, and S. Statistical uncertainties are displayed as vertical bars, while systematic uncertainties are indicated by boxes. These figures are taken from Ref. [43]. 191
- 6.13 The centrality dependence of $C_{p,K}$, $C_{Q,p}$, and $C_{Q,K}$ is displayed for Pb–Pb collisions at $\sqrt{s_{NN}} = 5.02$ TeV is presented in the left, middle, and right panels, respectively. Model predictions from Thermal-FIST (TheFIST) [24], calculated within the canonical ensemble (CE) framework with exact conservation of Q, B, and S in a correlation volume (V_c), are superimposed as colored lines for different values of V_c . Vertical bars denote statistical errors, whereas systematic uncertainties are indicated by boxes. The figure is taken from Ref. [22]. . . . 193
- 6.14 Dependence of the combined chi-squared, χ^2_{combined} on the correlation volume V_c for Set 1 p_T acceptance (π^\pm , K^\pm : $0.2 < p_T < 2.0$ GeV/ c , and $p(\bar{p})$: $0.4 < p_T < 2.0$ GeV/ c). Panel (a) presents the χ^2_{combined} distributions from fits of the observables $C_{p,K}$, $C_{Q,p}$, and $C_{Q,K}$ to the model. Panel (b) presents the χ^2 distributions obtained when the data are shifted upward by their systematic uncertainties, while panel (c) shows the corresponding case for a downward shift. The minima of χ^2_{combined} distributions in each case, which correspond to the best-fit values of V_c , are obtained by fitting the distributions with a fourth-order polynomial. The resulting minima and their associated uncertainties are marked in each panel. 194

- 6.15 Dependence of the combined chi-squared, χ^2_{combined} on the correlation volume V_c for Set 2 p_T acceptance (π^\pm , K^\pm , $p(\bar{p})$: $0.4 < p_T < 1.6$ GeV/ c). Panel (a) presents the χ^2_{combined} distributions from fits of the observables $C_{p,K}$, $C_{Q,p}$, and $C_{Q,K}$ to the model. Panel (b) presents the χ^2 distributions obtained when the data are shifted upward by their systematic uncertainties, while panel (c) shows the corresponding case for a downward shift. The minima of χ^2_{combined} distributions in each case, which correspond to the best-fit values of V_c , are obtained by fitting the distributions with a fourth-order polynomial. The resulting minima and their associated uncertainties are marked in each panel. 195
- 6.16 The centrality dependence of $C_{p,K}$, $C_{Q,p}$, and $C_{Q,K}$ is displayed in the left, middle, and right panels, respectively, for Pb–Pb collisions at $\sqrt{s_{NN}} = 5.02$ TeV. The curves correspond to predictions from the Thermal-FIST (TheFIST) [24] framework within the canonical ensemble (CE), shown both with (w) and without (w/o) the inclusion of resonance decays. Statistical uncertainties are indicated by vertical error bars, while systematic uncertainties are shown as open boxes. The figure is taken from Ref. [22]. 196
- 6.17 The collision-energy dependence of $C_{p,K}$ (left), $C_{Q,p}$ (middle), and $C_{Q,K}$ (right). Results for central and peripheral Au+Au collisions at lower beam energies ($\sqrt{s_{NN}} = 7.7\text{--}200$ GeV) from the STAR experiment [8] are compared to that of Pb–Pb collisions at LHC energies ($\sqrt{s_{NN}} = 5.02$ TeV). The dashed line marks the expectation from an uncorrelated (Poisson) baseline. Vertical error bars indicate statistical uncertainties, whereas the systematic effects are shown as surrounding boxes. The figure is taken from Ref. [22]. 197
- 6.18 Lattice QCD simulation results with non-zero magnetic field: $(2\chi_{Q,S}^{11} - \chi_{B,S}^{11})/\chi_S^2$ (left) and $(2\chi_{B,Q}^{11} - \chi_{B,S}^{11})/\chi_B^2$ (right) shown as a function of eB . Different colored markers correspond to various temperatures spanning the range $140 < T < 281$ MeV. The figure is taken from Ref. [47]. 198

- 6.19 The dependence of $[\chi_{Q,B}^{11}/\chi_Q^2(eB)]/[\chi_{Q,B}^{11}/\chi_Q^2(eB=0)]$ on the strength of the magnetic field eB at the pseudocritical temperature, T_{pc} , as obtained from lattice QCD simulations. The black curve indicates the prediction from the HRG model, while the dashed-purple line represents an experimentally accessible proxy $[\sigma_{Q,p}^{11}/\sigma_Q^2(eB)]/[\sigma_{Q,B}^{11}/\sigma_Q^2(eB=0)]$. The yellow band denotes the QCD continuum estimate, with results for different lattice spacings indicated by blue ($N_\tau = 8$) and red ($N_\tau = 12$) bands. The inset illustrates the ratios of the HRG and proxy results to those from lattice QCD. The figure is taken from Ref. [48]. 199
- 6.20 The ratios $(2\kappa_{Q,K}^{11} - \kappa_{p,K}^{11})/\kappa_K^2$ (left) and $(2\kappa_{Q,p}^{11} - \kappa_{p,K}^{11})/\kappa_K^2$ (right) measured as a function of centrality in Pb–Pb collisions at $\sqrt{s_{NN}} = 5.02$ TeV. The colored band shows the expectations from the Thermal-FIST (TheFIST) [24] framework within the canonical ensemble (CE), obtained using a correlation volume of $V_c = 2.6, dV/dy$. Statistical errors are indicated by vertical lines, and systematic uncertainties are displayed as boxes. The figure is taken from Ref. [22]. 200
- 6.21 Variation of the normalized ratio $(\kappa_{Q,p}^{11}/\kappa_Q^2)/(\kappa_{Q,p}^{11}/\kappa_Q^2)^{0-5\%}$ as a function of collision centrality in Pb–Pb collisions at $\sqrt{s_{NN}} = 5.02$ TeV. Results are shown for two p_T acceptances: Set 1 and Set 2 (refer to text for details) in left and right panels, respectively. The shaded bands correspond to predictions from the Thermal-FIST (TheFIST) [24] framework within the canonical ensemble (CE), evaluated for different choices of correlation volume V_c . Statistical errors are indicated by vertical bars, while systematic uncertainties are depicted as boxes. The figure is taken from Ref. [22]. 201

List of Tables

4.1	Summary of the main sources and ranges of systematic uncertainties associated with the standardized skewness $\gamma_{\langle p_T \rangle}$, intensive skewness $\Gamma_{\langle p_T \rangle}$, and kurtosis $\kappa_{\langle p_T \rangle}$, measured in Pb–Pb, Xe–Xe, and pp collisions at different collision energies. The uncertainties are evaluated by varying experimental conditions and analysis selections independently. Ranges are given where uncertainties depend on centrality or multiplicity.	90
4.2	The values of $\langle dN_{\text{ch}}/d\eta \rangle_{ \eta < 0.5}$ for different multiplicity classes in pp, $\sqrt{s} = 5.02$ TeV taken from [13].	94
5.1	Summary of the key findings from the blast-wave model investigation of $v_0(p_T)$ by the variation of mean values for transverse expansion velocity (β_s), kinetic freeze-out temperature (T_{kin}), and their fluctuations ($\sigma(\beta_s)$ and $\sigma(T_{\text{kin}})$). . . .	145
5.2	Uniform prior ranges used for the blast-wave model parameters in the Bayesian analysis of $v_0(p_T)$ for pions, kaons, and protons [35].	147
5.3	Extracted blast-wave parameters and their event-by-event fluctuation width for different centrality intervals [35].	153
6.1	Ratios of QCD thermodynamic susceptibilities (second-order) to corresponding HRG model results for different temperatures. The table is taken from Ref. [2].	167

6.2	Systematic uncertainty contributions to $C_{p,K}$, $C_{Q,K}$, and $C_{Q,p}$ in Pb–Pb collisions at $\sqrt{s_{NN}} = 5.02$ TeV. For each source, the range indicates the lowest and highest uncertainty values observed over all centrality intervals [22].	183
-----	--	-----

List of Abbreviations

AGS	Alternating Gradient Synchrotron
ALICE	A Large Ion Collider Experiment
ATLAS	A Toroidal LHC ApparatuS
CERN	Conseil Européen pour la Recherche Nucléaire, The European Organization for Nuclear Research
CMS	Compact Muon Solenoid
FAIR	Facility for Antiproton and Ion Research
LHC	Large Hadron Collider
NICA	Nuclotron-based Ion Collider fAcility
PHENIX	Pioneering High Energy Nuclear Interaction eXperiment
RHIC	Relativistic Heavy Ion Collider
SPS	Super Proton Synchrotron
STAR	Solenoidal Tracker at RHIC

Introduction

Contents

1.1	The Standard Model of elementary particles	2
1.2	Quantum Chromodynamics and Quark–gluon plasma	4
1.3	QCD phase diagram	9
1.4	Relativistic heavy-ion collisions and their evolution	12
1.5	Experimental probes of QGP	18
1.6	Thesis physics motivation	31
1.7	Organization of thesis	35

The study of strongly interacting matter under extreme conditions is an important area of modern nuclear physics, with relativistic heavy-ion collisions at the LHC offering valuable opportunities to investigate the quark–gluon plasma, referred as QGP. Over the past two decades, extensive experimental and theoretical investigations have revealed that the QGP exhibits properties consistent with a nearly perfect fluid, characterized by collective flow, complex correlations, and are sensitive to underlying thermodynamic properties of the system. Despite these advances, many aspects of the QGP remain the subject

of active research, including, among others, the detailed nature of its radial expansion, correlations among conserved quantum numbers, and the role of higher-order fluctuations in momentum distributions. This thesis contributes to addressing selected open questions by presenting three complementary analyses within the ALICE experiment: (i) measurements of a novel observable $v_0(p_T)$, aimed at probing radial flow through long-range transverse momentum correlations; (ii) a study of correlations among net-charge, net-proton, and net-kaon multiplicity distributions, which are related to thermodynamic susceptibilities in Quantum Chromodynamics, QCD (using lattice QCD); and (iii) an exploration of skewness and kurtosis of event-by-event mean transverse momentum fluctuations, offering insights into the hydrodynamic response of the QGP. Together, these studies add to the collective effort to deepen our understanding of how collective behavior and fluctuations manifest in strongly interacting matter.

To understand the behavior of strongly interacting matter and the formation of the QGP, it is first necessary to review the underlying theoretical framework that describes fundamental particles and their interactions: the Standard Model of particle physics. The chapter starts with a brief overview of the Standard Model, focusing on QCD, the theory of the strong interaction. It then introduces the QGP, discusses the QCD phase diagram, and reviews the stages of relativistic heavy-ion collisions along with key experimental probes. It also summarizes important kinematic variables used in data analysis and outlines the thesis motivation and organization.

1.1 The Standard Model of elementary particles

The Standard Model (SM) constitutes the prevailing theoretical framework in contemporary particle physics, describing the classification and interactions of all known fundamental

particles through the formalism of quantum field theory [1–5]. It is built upon the gauge symmetry group $SU(3)_C \times SU(2)_L \times U(1)_Y$, which integrates the strong, weak, and electromagnetic forces within a unified mathematical structure. The subscripts correspond to key physical attributes: C denotes the color charge involved in the strong interaction described by QCD; L indicates that the $SU(2)$ component acts on left-handed fermions, governing the weak interaction; and Y represents the weak hypercharge associated with the $U(1)$ group, which combines with $SU(2)_L$ to form the electroweak interaction after spontaneous symmetry breaking. This gauge structure encapsulates the classification of elementary particles into quarks, leptons, and gauge bosons, as illustrated in Fig. 1.1 and

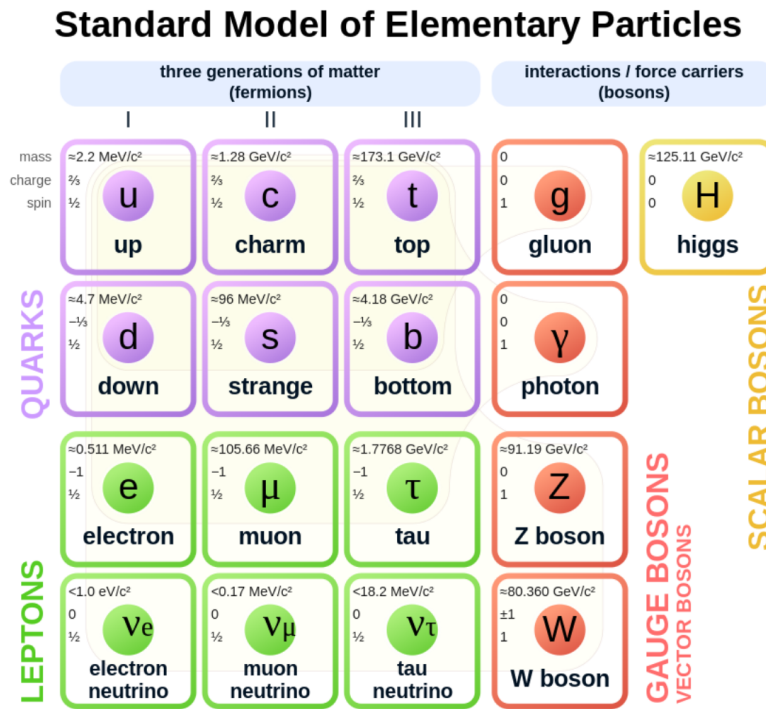


FIGURE 1.1: A schematic overview of the Standard Model is shown, illustrating all known fundamental particles. The diagram groups quarks and leptons into three generations, and presents the bosons mediating forces, including the Higgs particle. Particle symbols, masses, charges, and spins are indicated for each, reflecting the organization of matter and interactions in contemporary particle physics. The figure is taken from Ref. [6].

prescribes their interaction dynamics through quantum field theory. There are six flavors of quarks—up, down, charm, strange, top, and bottom—each carrying a fractional electric charge and a color charge. Leptons include the electron, muon, tau, and their corresponding neutrinos; unlike quarks, leptons do not experience the strong force and carry integer electric charges or are electrically neutral in the case of neutrinos.

Bosons, on the other hand, are particles with integer spin values. Among them, gauge bosons that include the photon, gluons, and the weak W^\pm and Z bosons, act as force carriers mediating the fundamental interactions. The Higgs boson, a scalar particle with spin 0, is unique in imparting mass to other particles through Higgs mechanism. The Higgs mechanism induces spontaneous symmetry breaking, generating masses for the W and Z bosons, as well as the fermions, while leaving the photon massless [7–9]. This dual classification and the interactions they mediate form the backbone of the quantum field theoretical description within the SM, allowing precise predictions of particle behavior confirmed by numerous experiments to date. However, despite its experimental successes, including the discovery of the Higgs boson [10, 11], the Standard Model remains incomplete, as it does not incorporate gravity, nor does it explain phenomena such as neutrino oscillations [12] or dark matter [13]. Nevertheless, it remains the foundational model for understanding particle physics and continues to guide both theoretical and experimental research.

1.2 Quantum Chromodynamics and Quark–gluon plasma

Central to the SM is the QCD, the fundamental theoretical framework that governs the interaction between quarks and gluons [5, 14, 15]. It also elucidates the strong nuclear force, which is responsible for binding quarks into hadrons such as protons, neutrons, and

mesons. This framework is a non-Abelian gauge theory constructed on the $SU(3)$ symmetry group, in which the concept of color charge serves a role similar to that of electric charge in quantum electrodynamics (QED). Within the QCD theory, quarks are assigned one of three types of this color charges, labeled as red, green, and blue, and they interact by exchanging gluons, the force carrier of QCD. Unlike photons in electromagnetism that carry no charge, gluons themselves carry color charge and exist in eight distinct types (each represented by specific combinations of color and anticolor charges such as red-antired, red-antigreen, red-antiblu, etc.), allowing them to interact with each other as well as with quarks. This makes QCD a highly non-linear theory with complex dynamics.

Even though quarks and gluons carry color charge, hadrons composed from these quarks are color-neutral. In particular, baryons are formed by three quarks, each of a different color, combining to yield an overall colorless state. Protons and neutrons, the primary constituents of ordinary matter, belong to this category. Similarly, mesons consist of a quark and an antiquark paired so that their color and anticolor charges cancel out, also resulting in color neutrality. Together, baryons and mesons comprise the class of hadrons, all of which participate in the strong interaction governed by QCD.

QCD stands out in the SM through three key features that essentially characterize the strong interaction. Two of these features pertain to the behavior of the strong force's interaction strength, while the third focuses on the spontaneous breaking of chiral flavor symmetry. The interaction strength in QCD is quantified by the strong coupling constant, often denoted as α_s . This coupling parameter determines the probability amplitude for quarks and gluons to interact. Unlike the electromagnetic coupling in QED, which remains nearly constant across different energy scales, α_s varies significantly with the squared

momentum transfer Q^2 involved in the interaction. Formally, α_s is expressed as

$$\alpha_s(Q^2) = \frac{12\pi}{(11N_c - 12N_f) \log(Q^2/\Lambda_{\text{QCD}}^2)}, \quad (1.1)$$

where N_c represents the number of distinct color charges in QCD, while N_f refers to the total number of quark flavors participating in the process or interaction. The parameter Λ_{QCD} , known as the QCD scale parameter, defines the characteristic energy scale at which the strong interaction transitions from perturbative to non-perturbative regimes. The value of Λ_{QCD} typically lies within the range of 100 to 500 MeV. The behavior of α_s predicted by QCD as a function of Q is depicted in Fig. 1.2 alongside experimental measurements, demonstrating excellent agreement over a wide range of energy scales—from the lowest accessible energies to the highest probed by experiments.

In the high-energy regime ($Q \gg \Lambda_{\text{QCD}}$), Eq. (1.1) reveals that the α_s decreases logarithmically with increasing momentum transfer. This property, known as *asymptotic freedom* [14–16], is a direct consequence of the self-interaction of gluons, which produce an antiscreening effect. It implies that quarks and gluons behave as if they were nearly free particles when probed at very short distances or equivalently at large Q^2 . This remarkable feature enables reliable perturbative calculations in high-energy particle collisions and underpins much of QCD’s predictive power at short distances. It underlies the success of perturbative QCD calculations in describing hard processes such as jet production, deep inelastic scattering, and high- p_T hadron production in collider experiments.

In contrast, at low energies ($Q \lesssim \Lambda_{\text{QCD}}$), the strong coupling constant becomes large, rendering perturbative expansions invalid. This non-perturbative regime manifests in the phenomenon of *color confinement* [17], wherein isolated quarks or gluons cannot be observed as free particles due to the increasing strength of their interaction at larger distances. As quarks are pulled apart, the force between them grows stronger instead of

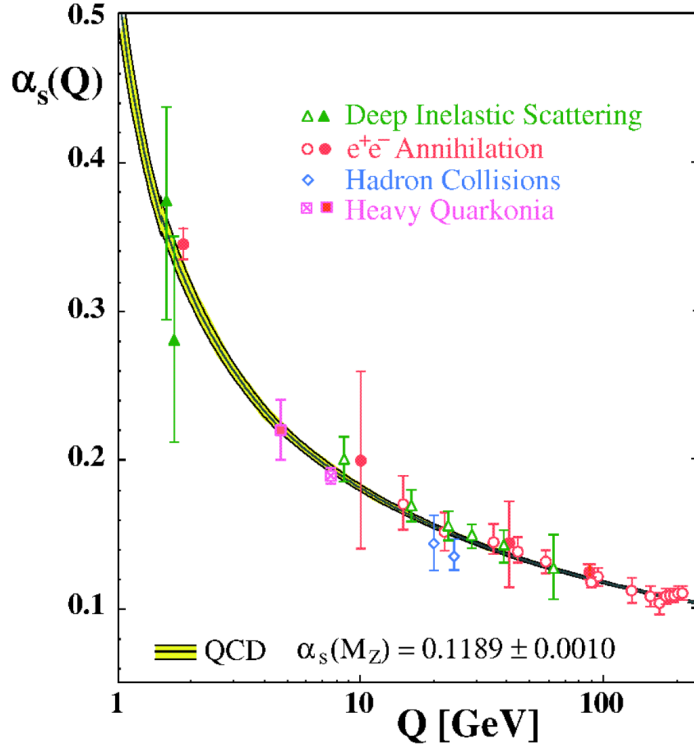


FIGURE 1.2: Evolution of the strong coupling constant α_s as a function of momentum transfer Q , determined from several processes including deep inelastic scattering (green triangles), e^+e^- annihilation (red circles), hadron collisions (blue diamonds), and heavy quarkonia (magenta squares). The solid curve and yellow band represent the QCD prediction and its uncertainty. The figure is taken from Ref. [16].

diminishing, effectively confining them within hadrons. This behavior is encapsulated in the effective QCD potential

$$V(r) = -\frac{4}{3} \frac{\alpha_s}{r} + kr \quad (1.2)$$

where the first term dominates at short distances and produces a Coulomb-like attraction, while the second term, which grows linearly with quark separation r , corresponds to a constant confining "string tension" k . This linear component reflects the formation of a color flux tube between quarks, preventing their separation without generating new quark-antiquark pairs. Confinement is well supported by lattice QCD ¹ (LQCD) simulations and

¹Lattice QCD is a non-perturbative computational framework for solving QCD by discretizing space-time

experimental evidence for confinement comes from the absence of free quark detection and from observations in high-energy collisions, where quarks and gluons produced in the early stages rapidly hadronize into colorless states.

The third important feature of QCD is the spontaneous breaking of chiral flavor symmetry [18, 19]. In the chiral limit, where the light-quark masses are taken to be negligible, the QCD Lagrangian exhibits a symmetry between left- and right-handed quark components. However, this chiral symmetry is not reflected by the physical QCD vacuum². Instead, the vacuum spontaneously breaks this symmetry, creating a nonzero quark condensate $\langle q\bar{q} \rangle$. This breaking leads to the emergence of nearly massless pseudoscalar mesons, such as pions and kaons, which act as the Nambu-Goldstone bosons for this broken symmetry. Although the quark masses are small but not zero, they explicitly break chiral symmetry, giving these mesons their small but finite mass. This phenomenon explains why hadrons have substantial masses despite the lightness of their constituent quarks and governs their low-energy interactions.

Building on the property of asymptotic freedom, QCD predicts that matter subjected to extremely high temperatures or energy densities will undergo a transition into a new phase where quarks and gluons are no longer confined within hadrons [14, 15, 20]. In such extreme conditions, realized for instance in the early universe microseconds after the Big Bang [21, 22], the strong coupling becomes sufficiently weak allowing quarks and gluons to propagate over extended distances. This leads to the formation of a deconfined medium

into a finite lattice of points. Quark fields are defined on lattice sites and gluon fields on the links between sites, preserving local gauge symmetry. Numerical Monte Carlo simulations in Euclidean space-time enable the evaluation of QCD observables from first principles, overcoming the challenges of strong coupling and nonlinearity in low-energy regimes.

²The physical QCD vacuum refers to the true ground state of the QCD theory. It is a complex, non-perturbative state characterized by nonzero quark and gluon condensates. Unlike the vacuum in QED, which can be thought of as empty space with no particles, QCD vacuum exhibits a rich structure due to strong quantum fluctuations, that underpin the essential features of strong interactions.

known as the quark–gluon plasma or QGP [23]. In this state, color charges are liberated, and quarks and gluons behave as effective quasiparticles rather than being bound into hadrons. Importantly, LQCD calculations (at baryon chemical potential $\mu_B \approx 0$) further show that the transition into the QGP is accompanied by a restoration of (approximate) chiral symmetry, fundamentally altering the mass generation mechanism and hadronic interactions [24, 25].

The equation of state (EoS) of strongly interacting matter plays a central role in understanding the properties and dynamics of the QGP. It defines the relationship between thermodynamic quantities such as pressure, energy density, and temperature, characterizing how QCD matter responds to extreme conditions. LQCD calculations provide a first-principles determination of the EoS, revealing that at low temperatures the pressure and energy density remain small, consistent with a hadron gas, while near a critical temperature $T_c \approx 154 \pm 9$ MeV, these quantities rapidly increase, signaling the transition to the QGP phase [26, 27]. This behavior is illustrated in Fig. 1.3, where the normalized pressure, energy density, and entropy density sharply rise above T_c , reflecting the rapid increase of thermodynamic activity with the liberation of color degrees of freedom. Understanding of the EoS is crucial for mapping the QCD phase diagram, which organizes the different phases of QCD matter as a function of temperature and baryon chemical potential, illustrating the conditions under which quark confinement and chiral symmetry breaking are lifted.

1.3 QCD phase diagram

Following the earlier discussion on the QGP and QCD EoS, the QCD phase diagram serves as a conjectured map of the different phases of strongly interacting matter as a function of temperature T and baryon chemical potential μ_B [28]. Figure 1.4 shows that

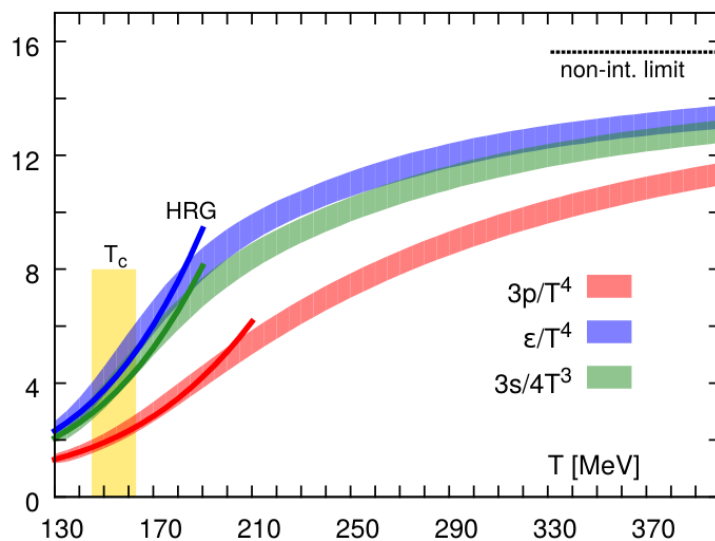


FIGURE 1.3: Equation of state of QCD matter as a function of temperature from lattice QCD results, showing normalized pressure ($3p/T^4$), energy density (ϵ/T^4), and entropy density ($3s/4T^3$). The yellow band indicates the region near the critical temperature T_c , with the hadron resonance gas (HRG) model shown for comparison at low T_c . The dotted line at the top represents the Stefan–Boltzmann (non-interacting gas) limit for comparison. The figure is taken from Ref. [26].

at low T and low μ_B , matter exists in a hadron gas phase where quarks and gluons are confined within color-neutral hadrons and chiral symmetry is spontaneously broken. At vanishing μ_B , when the temperature rises above the T_c , LQCD predicts a smooth crossover transition to the deconfined QGP phase, characterized by the liberation of color charges and approximate restoration of chiral symmetry [29]. This T_c , often referred to as the crossover temperature, reflects a smooth change of system from one phase to another: the free energy and all its derivatives with respect to some thermodynamic variable remain continuous. At larger values of μ_B , LQCD becomes limited by the sign problem, and the phase structure is inferred from effective models. These studies suggest that the smooth crossover may turn into a first-order phase transition at high baryon density [31], with the first-order line terminating at a second-order critical point [28, 32, 33]. At a first-order phase transition,

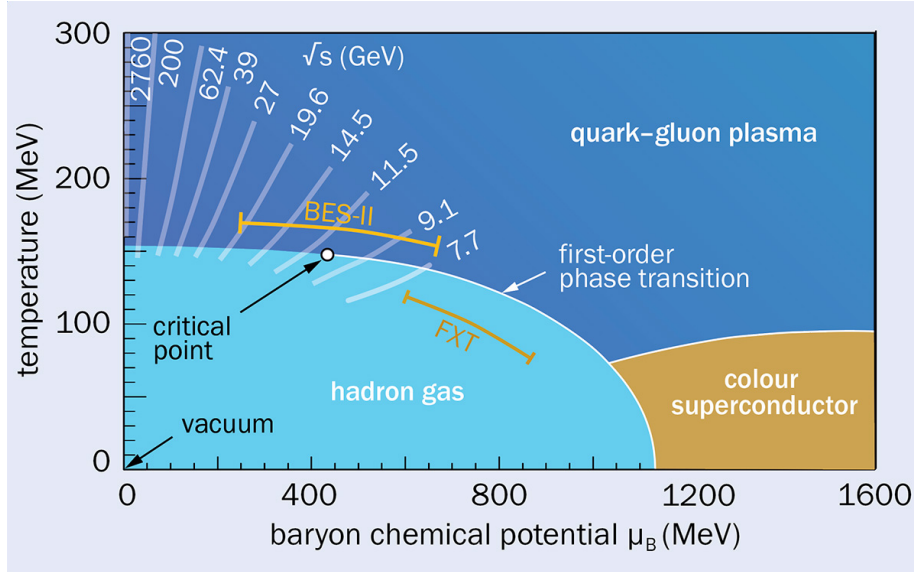


FIGURE 1.4: Illustration of a conjectured phase diagram of QCD matter in temperature vs. baryon chemical potential μ_B plane, with distinct colors separating different phases of QCD matter—hadron gas, quark-gluon plasma, and the predicted color-superconducting phase. The figure is taken from Ref. [30].

the free energy itself remains continuous, but its first derivatives are discontinuous leading to coexistence of two distinct phases [34, 35]. On the other hand, the critical point is a second-order phase transition characterized by the continuous change of the free energy and its first derivatives. However, at the critical point, second or higher-order derivatives of the free energy (such as specific heat or susceptibilities) diverge, reflecting critical fluctuations. This unique behavior defines the universality class of the phase transition and is the key signature sought in experiment and theory [34, 35]. The search for this QCD critical point is a central goal of current relativistic heavy-ion collision experiments. At very high μ_B and low T , QCD predicts color-superconducting phases where quarks form Cooper pairs near the Fermi surface, a state relevant for the dense cores of neutron stars though inaccessible in current collider experiments [36].

The experimental exploration of the QCD phase diagram is pursued using ultrarela-

tivistic heavy-ion collisions at facilities such as the Large Hadron Collider (LHC) and the Relativistic Heavy Ion Collider (RHIC). The LHC operates at the highest available collision energies, probing the QCD phase diagram at very high T and $\mu_B \approx 0$ and providing detailed insight into the QGP in the crossover region. In contrast, the RHIC spans a wide range of collision energies, enabling the study of both low and moderate baryon densities. RHIC's Beam Energy Scan program aims to explore experimentally the region around the conjectured critical point and possible first-order phase transition by varying the μ_B [37–40].

1.4 Relativistic heavy-ion collisions and their evolution

Relativistic heavy-ion collisions provide a unique experimental avenue to create and study matter under the extreme conditions of temperature and density where the QGP exists [23, 41]. This concept was first proposed in the 1970s, shortly after the formulation of QCD theory that laid the foundation for dedicated experimental programs aimed at recreating and exploring QGP properties under controlled laboratory conditions. Early experimental programs were initiated at facilities such as the Bevalac at Berkeley and later at Brookhaven's AGS and CERN's SPS, evolving into the dedicated relativistic heavy-ion programs at the RHIC and the LHC. By colliding nuclei at nearly the speed of light, these experiments reproduce conditions similar to those in the early Universe microseconds after the Big Bang [42], and has since become a cornerstone in exploring the strong interaction and QGP.

The evolving system proceeds through a sequence of stages, each governed by distinct physical processes and characteristic timescales. At the earliest instant, the overlap of two highly Lorentz-contracted nuclei results in an instantaneous deposition of energy in a small

volume. The spatial distribution of the deposited energy and entropy is predominantly influenced by the number and arrangement of participant nucleons and partons within the nuclei. Due to nucleon position fluctuations, this energy density is not uniform but exhibits a highly irregular and "lumpy" structure with localized hotspots, as shown in Fig. 1.5. Following this, the system enters a short-lived pre-equilibrium phase, characterized by rapid

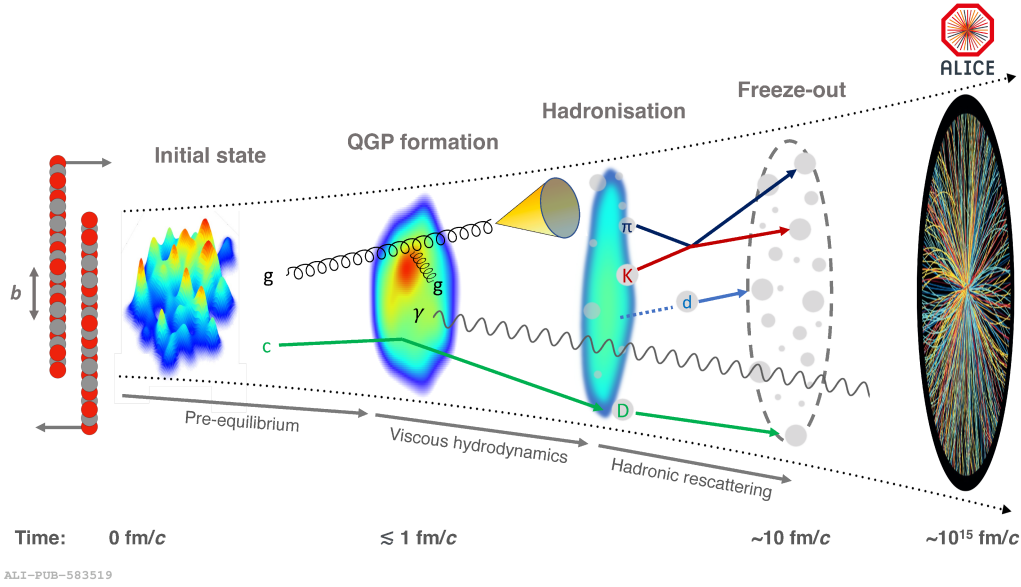


FIGURE 1.5: Schematic illustration of the various stages in a relativistic heavy-ion collision. The temporal sequence moves from the initial state of Lorentz-contracted nuclei, through pre-equilibrium dynamics and QGP formation, followed by hadronization and hadronic rescattering, to final kinetic freeze-out and detection in the ALICE experiment. The figure is taken from Ref. [43].

gluon production and intense color field interactions. Within approximately 1 femtosecond, interactions among constituents drive the system towards local thermalization. Beyond this point, the medium—often referred to as a "fireball"—can be effectively described by relativistic hydrodynamics [44], signaling the onset of the QGP phase. During the QGP phase, the fireball expands and cools while developing collective flow [45] and dynamically evolving in its thermodynamic properties. As the temperature drops to the critical value T_c , which depends on μ_B , the medium undergoes a transition to a hadron gas composed of

color-neutral hadrons such as pions, kaons, and protons. This transition process is known as hadronization, and the matter often referred to as hadronic matter. The hadronic matter continues to evolve and interact until inelastic scattering processes cease at the chemical freeze-out. At this point, the particle abundances are fixed and no longer change, except through subsequent resonance decays. Beyond chemical freeze-out, hadrons still undergo elastic scatterings which maintain kinetic thermalization of the momentum distributions until the system further expands and its density decreases. Finally, at the kinetic freeze-out, these elastic interactions cease, and hadrons decouple from the medium, streaming freely to the detection systems. These free-streaming hadrons retain the imprints of the medium's space-time evolution and thermodynamic history, making them essential experimental probes for studying the properties of the created medium.

1.4.1 Kinematic variables and key observables

In high-energy nuclear collisions, the description of the final-state hadrons is carried out using a set of well-defined kinematic variables [46]. These variables provide a consistent framework for characterizing particle motion and form the basis for both theoretical modeling and experimental analyses. By studying the energy and momentum distributions of outgoing hadrons, valuable insights into the properties of the created system can be obtained. In addition to variables defined at the single-particle level, global event observables characterize the overall properties of the collision. Together, these kinematic and event-level observables enable a detailed understanding of the system's formation, evolution, and underlying physics across different collision energies and experimental conditions.

The motion of each particle can be expressed through its four-momentum,

$$p^\mu = (E, p_x, p_y, p_z), \quad (1.3)$$

where E denotes the energy and (p_x, p_y, p_z) are the Cartesian components of the momentum. From this, several derived quantities particularly relevant to collider experiments are constructed:

- **Transverse momentum (p_T):**

The momentum component orthogonal to the beam axis is defined as

$$p_T = \sqrt{p_x^2 + p_y^2}. \quad (1.4)$$

This variable plays a central role in heavy-ion physics because it is unaffected by longitudinal boosts and is directly sensitive to the collective expansion of the medium.

- **Azimuthal angle (φ):**

The azimuthal angle φ is conventionally defined as the angle between the particle's transverse momentum vector and the x-axis in the plane perpendicular to the beam axis. Mathematically, it is expressed as:

$$\varphi = \tan^{-1} \left(\frac{p_y}{p_x} \right). \quad (1.5)$$

- **Rapidity (y):**

For a particle with energy E and longitudinal momentum p_z , the rapidity is given by

$$y = \frac{1}{2} \ln \left(\frac{E + p_z}{E - p_z} \right). \quad (1.6)$$

Rapidity provides a convenient description of particle production since differences in rapidity remain invariant under Lorentz boosts along the collision axis, making it particularly useful when comparing results across different collision energies.

- **Pseudorapidity (η):**

In experimental analyses, especially where the particle mass is not determined, a

related angular variable is often employed:

$$\eta = \frac{1}{2} \ln \left(\frac{|p| + p_z}{|p| - p_z} \right) = -\ln \left[\tan \left(\frac{\theta}{2} \right) \right], \quad (1.7)$$

where θ is the polar angle relative to the beam axis, and $|p| = \sqrt{p_x^2 + p_y^2 + p_z^2}$. At ultrarelativistic energies, η closely approximates the rapidity, allowing a straightforward description of detector coverage and event multiplicity distributions.

- **Transverse Mass (m_T):**

Defined as the combination of a particle's rest mass and transverse momentum, the transverse mass is expressed by:

$$m_T = \sqrt{m^2 + p_T^2}, \quad (1.8)$$

where m is the particle's rest mass. This variable is insightful for investigating collective flow effects and spectral shapes across different particle species.

- **Invariant mass:**

For a system of particles, the invariant mass is constructed from the sum of their four-momenta:

$$M^2 = \left(\sum_i E_i \right)^2 - \left| \sum_i \vec{p}_i \right|^2. \quad (1.9)$$

The quantity is invariant under Lorentz transformations. This fundamental property makes the invariant mass a powerful tool for reconstructing short-lived resonances and studying multi-particle decay channels.

- **Collision centrality:**

Centrality quantifies the degree of overlap between the two nuclei during collision and is closely linked to the impact parameter—the transverse distance between their centers at closest approach. Although the impact parameter cannot be measured

directly, centrality classes are experimentally determined using signals sensitive to collision geometry, primarily the charged-particle multiplicity or energy deposited in forward detectors. This classification enables categorizing events from the most central (head-on) to the most peripheral (glancing) collisions. Central collisions produce larger volumes of hot and dense QCD matter, making centrality a crucial variable for understanding how the initial geometric configuration affects the evolution and observable signatures of the system. Conversely, more peripheral collisions, characterized by smaller overlap regions, generate less dense matter and serve as important references for delineating medium effects from baseline particle production. A more detailed discussion of collision geometry, centrality determination, and the experimental methods employed in ALICE is provided in Chapter 3.

- **Multiplicity:**

Multiplicity refers to the total number of particles produced and detected within a defined kinematic acceptance in each collision event. It is a key observable that reflects the system size and entropy generated in the collision. Charged-particle multiplicity distributions give insight into the overall particle production mechanisms and the energy density achieved. Higher multiplicities are typically associated with more central collisions, where the nuclear overlap region is larger, thus producing more particles. Multiplicity measurements thus serve as essential input for event classification.

- **Invariant yield:**

The invariant yield $E \frac{d^3N}{dp^3}$ represents the particle production rate in a Lorentz-invariant differential form, typically given by

$$E \frac{d^3N}{dp^3} = \frac{1}{2\pi p_T} \frac{d^2N}{dp_T dy} \quad (1.10)$$

where N is the particle count within a specific kinematic bin. It serves as a fundamental observable quantifying particle production normalized to remove frame-dependent effects, allowing direct comparison between different experimental systems and collision energies.

- **Centre-of-mass energy (\sqrt{s}):**

The center-of-mass energy is a fundamental quantity in high-energy nuclear and particle collisions. It defines the total available energy in the rest frame of the composite system, setting the energy scale for all particle production and dynamics emerging from the collision. For symmetric collider experiments (such as those at the LHC), where two beams with equal energy E collide head-on, the Mandelstam variable s , defined as the square of the total four-momentum of the incoming particles, is given by:

$$s = (p_1 + p_2)^2 = (E_1 + E_2)^2 - (\vec{p}_1 + \vec{p}_2)^2. \quad (1.11)$$

For two identical beams colliding head-on (as in a collider), $E_1 = E_2 = E$ and momenta being equal in magnitude and opposite in direction ($\vec{p}_1 = -\vec{p}_2$), Eq. 1.11 simplifies to $\sqrt{s} = 2E$. Thus, for collisions at $\sqrt{s} = 5.02$ TeV, each incoming beam carries an energy of $E = 2.51$ TeV. In heavy-ion experiments, it is standard practice to specify the center-of-mass energy per nucleon pair, denoted as $\sqrt{s_{NN}}$, facilitating direct comparison of collision dynamics across different beam species and systems.

1.5 Experimental probes of QGP

The formation of QGP in heavy-ion collisions are confirmed and studied through indirect experimental signatures. A variety of probes have been developed that provide complementary insights into the properties and evolution of this deconfined state of matter. These are

broadly categorized into hard probes, which involve high-momentum particles produced in primary scatterings, and soft probes, which reflect the bulk properties and collective behavior of the medium.

1.5.1 Hard probes

Hard probes emerge from high-momentum transfer processes occurring in the earliest stages of the collision. Their great advantage lies in being produced before the QGP forms and subsequently interacting with the medium as calibrated external probes. These include high- p_T partons that evolve into jets, as well as heavy-flavor quarks.

- **Jet quenching:**

Jets arise as narrow streams of hadrons originating from the fragmentation and hadronization of energetic quarks and gluons produced in the initial hard scatterings of high-energy nuclear collisions. When these energetic partons created in heavy-ion collisions propagate through the QGP, they interact strongly with the medium constituents, losing energy and momentum predominantly through medium-induced gluon radiation as well as elastic scatterings with the plasma particles [47]. This energy degradation, known as jet quenching, results in both a suppression of high- p_T hadron yields when compared with proton–proton collisions.

The magnitude of this suppression is usually expressed in terms of the nuclear modification factor R_{AA} , which is defined as

$$R_{AA}(p_T) = \frac{d^2 N_{AA}/(dp_T dy)}{\langle T_{AA} \rangle d^2 \sigma_{pp}/(dp_T dy)}, \quad (1.12)$$

where the numerator corresponds to high- p_T hadron yields measured in nucleus–nucleus collision events, while the denominator is obtained from the corresponding

production cross section in proton-proton collisions σ_{pp} , scaled by the average nuclear overlap function T_{AA} . The overlap function itself is determined from the number of binary nucleon–nucleon collisions, N_{coll} , calculated using the Glauber model of nuclear collision geometry [48], divided by the inelastic nucleon–nucleon cross section $\sigma_{NN}^{\text{inel}}$ [49]. If a heavy-ion collision were merely a sum of independent proton-proton interactions, one would expect $R_{AA} = 1$. Instead, observed values well below unity provide direct evidence for strong energy dissipation of hard partons inside the QGP. Experimental results obtained at both RHIC and the LHC have demonstrated jet quenching signatures in central heavy-ion collisions. The R_{AA} as a function of p_T measured in central heavy-ion collisions at different collision energies and experiments, is shown in Fig. 1.6. The data points illustrate the strong suppression

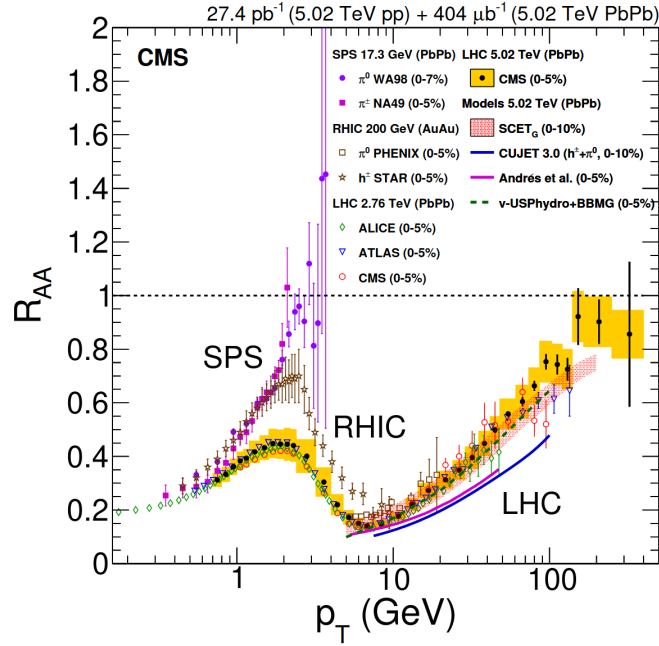


FIGURE 1.6: Nuclear modification factor R_{AA} for central PbPb (SPS), AuAu (RHIC), and PbPb (LHC) collisions as a function of p_T , comparing results from WA98, PHENIX, STAR, CMS, and ALICE experiments. The data are shown alongside theoretical predictions for various parton energy loss scenarios in the quark–gluon plasma, illustrating strong jet quenching effects at RHIC and LHC energies. The figure is taken from Ref. [50].

of high- p_T hadrons, and theoretical model predictions (shown as bands and lines) for different medium parameters and energy loss mechanisms, qualitatively agree with the experimental data. These results underscore the presence of a hot, dense, and strongly interacting medium created in these collisions.

- **Heavy-flavour quark probes:**

Heavy-flavor quarks, particularly charm and bottom quarks, act as essential probes of the QGP formed in high-energy heavy-ion collisions. Among these, the suppression of quarkonium states like J/ψ ($c\bar{c}$; charmonium) and Υ ($b\bar{b}$; bottomonium) is considered one of the clearest signatures of the QGP. The J/ψ meson suppression was originally proposed as an indicator of deconfinement [51]. The principal mechanism causing suppression of these quarkonium states is Debye color screening: the deconfined medium screens the strong force between the heavy quark-antiquark pair, weakening their binding and leading to dissociation of the bound states. Experimental data from SPS, RHIC, and LHC (results from ALICE are shown in Fig. 1.7) consistently show a strong suppression of J/ψ yields in nucleus-nucleus collisions relative to proton-proton collisions, quantified by the nuclear modification factor R_{AA} significantly less than unity.

Bottomonium states exhibit a cleaner suppression pattern owing to their higher mass and less recombination. Their suppression happens sequentially, aligned with their binding energies. The tightly bound ground state $\Upsilon(1S)$ survives higher temperatures, while excited states, $\Upsilon(2S)$ and $\Upsilon(3S)$ dissociate more readily, consistent with theoretical expectations. This sequential melting of $\Upsilon(1S)$, $\Upsilon(2S)$, and $\Upsilon(3S)$ states observed in experiments at RHIC and LHC (results from CMS are shown in Fig. 1.8) provides a precise way to gauge the temperature of the QGP [53].

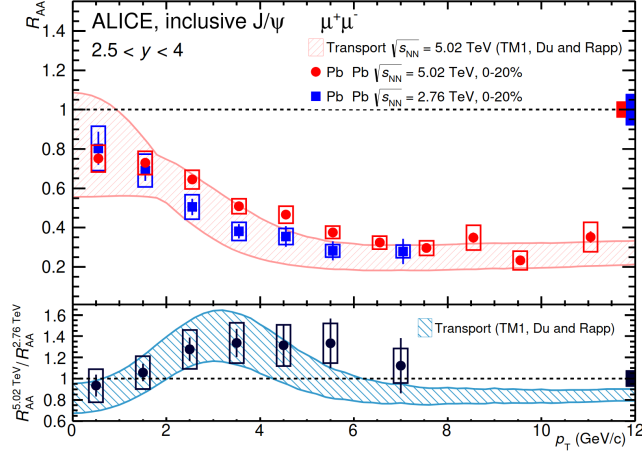


FIGURE 1.7: Transverse momentum dependence of inclusive J/ψ nuclear modification factor R_{AA} in Pb–Pb collisions at $\sqrt{s_{NN}} = 5.02$ TeV and 2.76 TeV, measured by ALICE in the rapidity range $2.5 < y < 4$. Bottom panel shows the ratio of R_{AA} between 5.02 TeV and 2.76 TeV. The shaded band correspond to calculations from a transport model. Error bars and boxes indicate statistical and systematic uncertainties, respectively. The figure is taken from Ref. [52].

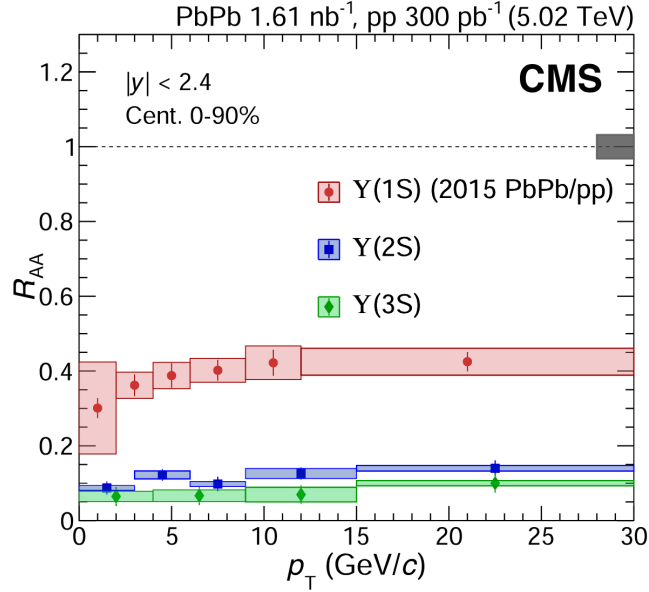


FIGURE 1.8: Transverse momentum dependence of the nuclear modification factor R_{AA} for $\Upsilon(1S)$, $\Upsilon(2S)$, and $\Upsilon(3S)$ mesons measured by the CMS experiment in Pb–Pb collisions at $\sqrt{s_{NN}} = 5.02$ TeV for rapidity $|y| < 2.4$ and 0–90% centrality. The plot demonstrates strong and sequential suppression of the excited bottomonium states relative to the ground state. Statistical and systematic uncertainties are indicated by error bars and boxes, respectively. The figure is taken from Ref. [54].

1.5.2 Soft probes

These probes arise from the low-momentum, thermalized particles that dominate the bulk medium created in heavy-ion collisions. Soft probes provide insight into the collective and macroscopic properties of the QGP, such as its equation of state, transport coefficients, and hydrodynamic evolution. Key observables include strangeness enhancement, anisotropic flow, and particle correlations and fluctuations.

- **Strangeness enhancement:**

Strangeness enhancement, a phenomenon historically proposed as a signature of QGP formation [55, 56], refers to the increased relative production of strange hadrons in high-energy heavy-ion collisions compared to proton–proton interactions at similar energies. In the QGP, the abundant presence of deconfined quarks and gluons facilitates efficient production of strange quark–antiquark pairs through processes like gluon fusion ($gg \rightarrow s\bar{s}$) and quark–antiquark interactions ($u\bar{u} \rightarrow s\bar{s}$, $d\bar{d} \rightarrow s\bar{s}$) [55]. This leads to a rapid achievement of strangeness chemical equilibrium, a state that is much harder to reach in a purely hadronic environment due to higher production thresholds and longer equilibration timescales. Experimentally, strangeness enhancement is quantified by comparing the yield ratios of strange and multi-strange hadrons (such as Λ , Ξ , and Ω) to those of non-strange reference particles like pions, measured in heavy-ion collisions relative to smaller systems such as proton–proton or peripheral heavy-ion interactions. Both RHIC and LHC have observed significant strangeness enhancement, as demonstrated in Fig. 1.9 [59, 60]. The enhancement becomes more pronounced for multi-strange baryons (higher strangeness content) and grows with event multiplicity, which reflects the size and density of the medium created. Notably, recent results have shown that strangeness enhancement, once con-

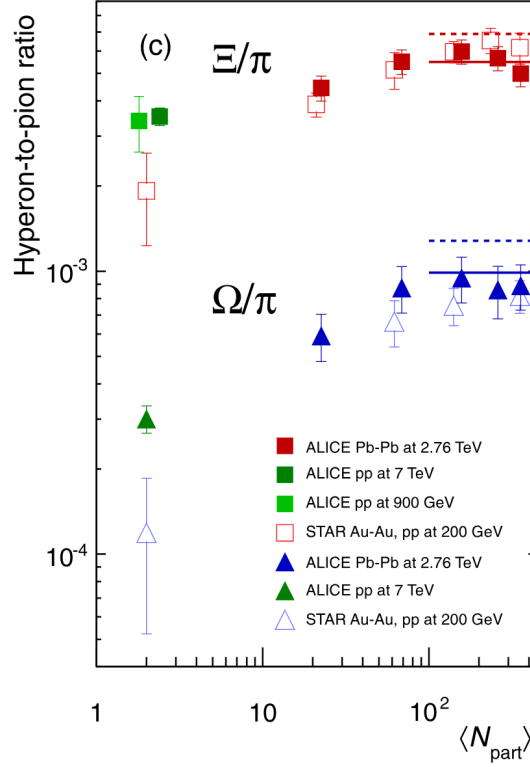


FIGURE 1.9: Hyperon-to-pion ratios (Ξ/π and Ω/π) as a function of the mean number of participating nucleons ($\langle N_{\text{part}} \rangle$) in various collision systems and energies. Results are shown for Pb–Pb collisions at $\sqrt{s_{\text{NN}}} = 2.76$ TeV (ALICE), pp collisions at $\sqrt{s} = 7$ TeV and 900 GeV (ALICE), and Au–Au and pp collisions at $\sqrt{s_{\text{NN}}} = 200$ GeV (STAR). The increasing ratios with system size and event multiplicity clearly illustrate the enhancement of multi-strange baryon production. The solid and dashed lines indicate theoretical predictions from thermal models [57, 58]. Error bars represent statistical and systematic uncertainties. The figure is taken from Ref. [59].

sidered a signature unique to heavy-ion collisions, also emerges in high-multiplicity p–Pb and even pp events, indicating the possible onset of collectivity and partonic effects in these smaller systems as well [61].

- **Anisotropic flow:**

Anisotropic flow is a key observable characterizing collective flow of the hot and dense medium created in relativistic heavy-ion collisions [62–64]. This collective flow refers to the correlated expansion of the medium that causes emission of particles

with characteristic angular and momentum distributions. In non-central heavy-ion collisions, the overlapping region of the two nuclei takes on an elliptical shape in the plane transverse to the beam direction. This spatial anisotropy is conventionally described by the eccentricity ϵ , defined as $\epsilon = \langle y^2 - x^2 \rangle / \langle y^2 + x^2 \rangle$. The coordinates x and y represent the spatial positions of participant nucleons or deposited energy density in the transverse plane, with x along the impact parameter axis and y perpendicular to it. The larger pressure gradients along the short axis cause the QGP to expand more rapidly in that direction. This leads to a larger emission of particles with higher transverse momentum along the reaction plane direction (the plane defined by the beam axis and the impact parameter), manifesting as anisotropic particle flow in momentum space, as illustrated in Fig. 1.10.

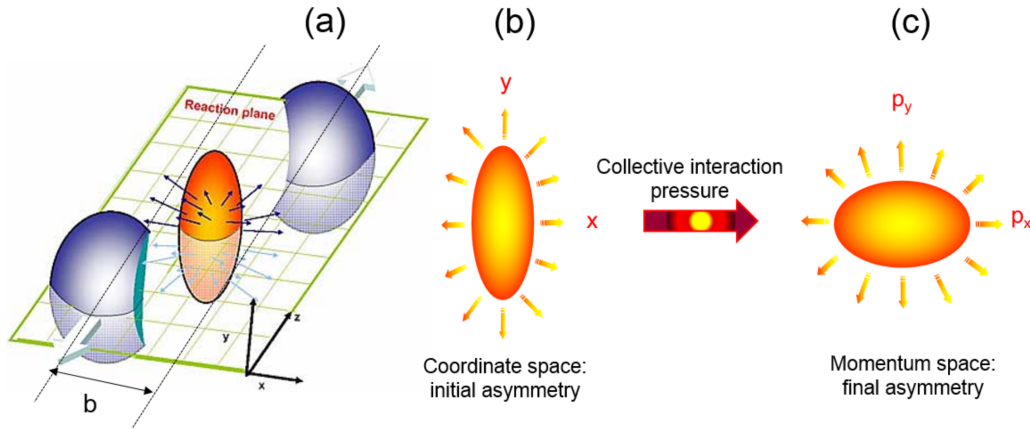


FIGURE 1.10: Illustration of anisotropic flow development in a non-central heavy-ion collision. Panel (a) shows the almond-shaped overlap region in the plane perpendicular to the beam axis. Panel (b) and (c) depicts the initial spatial asymmetry in coordinate space translating into anisotropy in momentum space of emitted particles. The figure is taken from Ref. [65].

To quantify the momentum-space anisotropy, the azimuthal angle φ distribution of emitted particles can be expanded in a Fourier series [66], relative to the event plane

angle, Ψ_n ³:

$$E \frac{d^3N}{dp^3} = \frac{1}{2\pi p_T} \frac{d^2N}{dp_T dy} \left(1 + 2 \sum_{n=1}^{\infty} v_n \cos[n(\varphi - \Psi_n)] \right). \quad (1.13)$$

Here, the Fourier coefficients v_n are known as anisotropic flow coefficients—often referred as n -th harmonic flow. The dominant component of the anisotropic flow, reflecting the initial geometric anisotropy, is the elliptic flow, v_2 . It is defined as

$$v_2 = \langle \cos 2(\varphi - \Psi_2) \rangle, \quad (1.14)$$

averaged over particles and events, where Ψ_2 is the second-order event plane angle.

Experimental measurements from RHIC and LHC have revealed large elliptic flow values along with significant higher-order harmonic coefficients (v_n for $n > 2$) [67–74], providing clear evidence of strong collective expansion and near-perfect fluid behavior of the QGP [45, 75]. This near-perfect fluidity is attributed to the exceptionally low shear viscosity to entropy density ratio (η/s) of the QGP, which approaches the theoretical lower bound of $1/4\pi$ derived from AdS/CFT considerations [76, 77] (see Fig. 1.11). A value of η/s this low implies minimal resistance to flow, enabling the fluid to efficiently translate initial spatial anisotropies into observed momentum anisotropies. Unlike a weakly interacting gas, the QGP behaves as a strongly interacting liquid that thermalizes rapidly and develops collective motion, with the measured anisotropic flows in close agreement with viscous hydrodynamic calculations employing low η/s . An illustrative comparison using ALICE data is shown in Fig. 1.12.

³The event plane angle is an experimental estimate of the azimuthal orientation of a heavy-ion collision's reaction plane. Since the reaction plane cannot be measured directly in experiments, the event plane angle corresponding to the n^{th} harmonic is determined from the azimuthal distribution of emitted particles using the equation:

$$\Psi_n = \frac{1}{n} \tan^{-1} \frac{\langle \sin(n\varphi) \rangle}{\langle \cos(n\varphi) \rangle}.$$

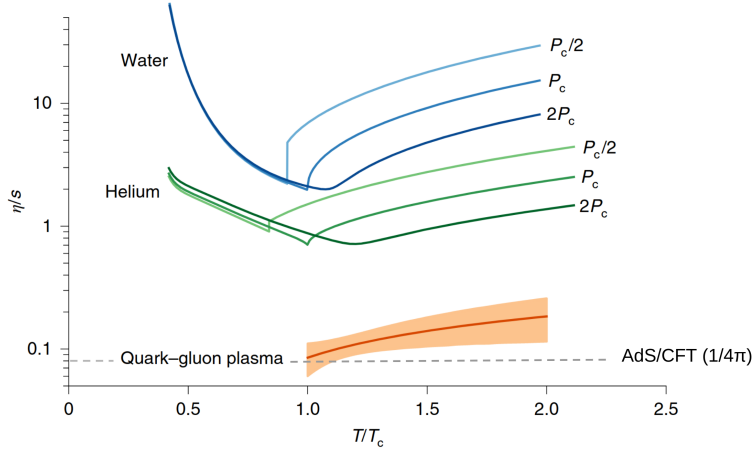


FIGURE 1.11: Shear viscosity to entropy density ratio (η/s) as a function of the temperature normalized to the critical temperature (T/T_c) for conventional substances like water and helium at different pressures, compared with the quark–gluon plasma created in heavy-ion collisions. The dashed line indicates the lower bound ($1/4\pi$) predicted by AdS/CFT calculations. The figure is adapted from Ref. [78].

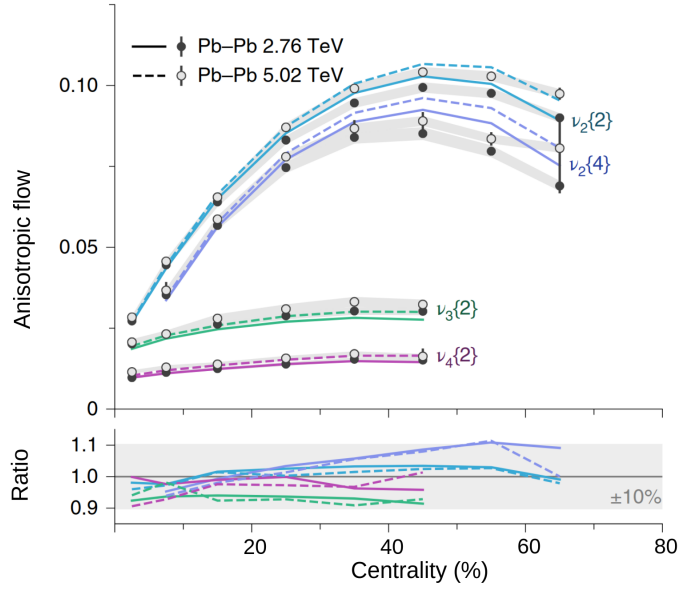


FIGURE 1.12: Centrality dependence of anisotropic flow coefficients $v_2\{2\}$, $v_2\{4\}$, $v_3\{2\}$, and $v_4\{2\}$, measured using multi-particle correlations (where the number in curly braces $\{m\}$ denotes the order of the m -particle correlation) in Pb–Pb collisions at $\sqrt{s_{NN}} = 2.76$ and 5.02 TeV. The experimental data points are compared with corresponding hydrodynamic model predictions indicated by the lines. The lower panel presents the ratio of model predictions to data for both energies, demonstrating agreement within $\pm 10\%$ across centralities. The figure is adapted from Ref. [78].

Recent ALICE high-precision measurements by the ALICE Collaboration for Pb–Pb collisions at $\sqrt{s_{\text{NN}}} = 5.02$ TeV provide detailed $v_2(p_T)$ distributions for multiple identified particle species across a wide range of collision centralities, as shown in Fig. 1.13. The data exhibit a distinct mass ordering at low p_T , consistent with hy-

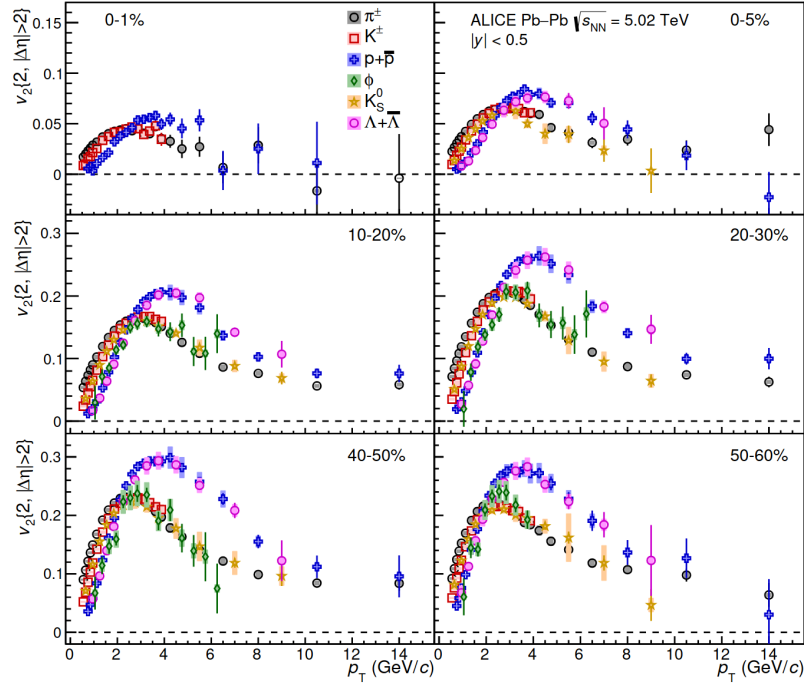


FIGURE 1.13: Transverse momentum dependence of the elliptic flow coefficient, v_2 for identified particle species—pions, kaons, protons, ϕ mesons, K_s^0 , and Λ —measured in Pb–Pb collisions at $\sqrt{s_{\text{NN}}} = 5.02$ TeV with ALICE. Results are displayed for various collision centralities, highlighting the evolution of collective flow strength and particle-type dependence from central to peripheral events. The figure is taken from Ref. [79].

drodynamic flow-driven collective effects [63, 80], while at intermediate p_T a clear baryon-meson splitting (grouping of particles according to the number of quarks they are composed of) emerges. This splitting reflects the quark coalescence mechanism in particle production and signals partonic collectivity prior to hadronization [81]. These comprehensive results place stringent constraints on the QGP’s transport coefficients, particularly the η/s , and strongly validate hydrodynamic models.

- **Particle correlations and fluctuations:**

Particle correlations and fluctuations provide powerful means to probe the phase structure of QCD in heavy-ion collisions [82, 83]. In particular, event-by-event fluctuations of conserved charges such as net-baryon number serve as sensitive indicators of critical phenomena expected near the QCD phase transition and possible critical point. Net-proton fluctuations, which are experimentally accessible proxies for net-baryon fluctuations, are quantified by measuring higher-order cumulants of the event-by-event net-proton distribution. The cumulants (C_n) up to fourth order for the event-by-event distribution of a quantity M are defined as

$$C_1 = \langle M \rangle, \quad (1.15)$$

$$C_2 = \langle (M - \langle M \rangle)^2 \rangle, \quad (1.16)$$

$$C_3 = \langle (M - \langle M \rangle)^3 \rangle, \quad (1.17)$$

$$C_4 = \langle (M - \langle M \rangle)^4 \rangle - 3\langle (M - \langle M \rangle)^2 \rangle^2, \quad (1.18)$$

with angular brackets $\langle \dots \rangle$ representing average over many events. These C_n scale proportionally with the system size, which means they are sensitive to the volume of the system and to event-by-event volume fluctuations. To mitigate these effects, ratios of cumulants are utilized. These ratios not only suppress trivial volume effects but also connect directly to ratios of baryon-number susceptibilities as calculated in LQCD and QCD-based models. A characteristic non-monotonic behavior in these cumulants, especially the fourth-order, as a function of collision energy can signal the system's proximity to a critical point in the QCD phase diagram [84, 85]. The STAR experiment at RHIC has conducted detailed measurements of event-by-event net-proton fluctuations across a wide range of collision energies, as shown in Fig. 1.14.

By examining the energy dependence of the fourth-to-second-order cumulant ratio (C_4/C_2) in central Au+Au collisions, STAR observed a non-monotonic behavior with a statistical significance of 3.1σ relative to Poisson baseline⁴. A more comprehensive overview of results on net-proton fluctuations can be found in Ref. [40].

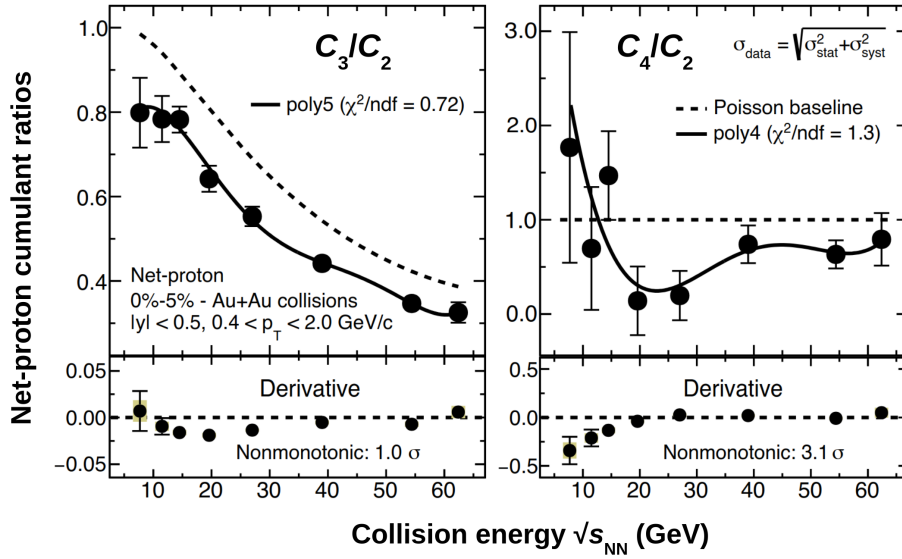


FIGURE 1.14: The ratios of net-proton cumulants C_3/C_2 (left) and C_4/C_2 (right) plotted against the collision energy $\sqrt{s_{NN}}$ in Au+Au collisions at 0–5% centrality, for given kinematic acceptance on y and p_T . Solid lines show polynomial fits (5th order for C_3/C_2 and 4th order for C_4/C_2) to the data points, while dashed lines represent the Poisson baseline for comparison. Below each main plot, the derivative of the fit is shown to highlight the nonmonotonic behavior, with significance levels of 1.0σ for C_3/C_2 and 3.1σ for C_4/C_2 . Error bars combine both statistical and systematic uncertainties. The figure is adapted from Ref. [37].

In addition to fluctuations of conserved charges, event-by-event fluctuations of the mean transverse momentum ($\langle p_T \rangle$) serve as an important observable to characterize the dynamics of the produced medium in heavy-ion collisions [83]. These fluctu-

⁴The Poisson baseline refers to a scenario where fluctuations arise from independent particle production, i.e., event-by-event distribution of proton (N_p) and antiproton ($N_{\bar{p}}$) numbers are Poissonian. As a result, the distribution of the difference of these numbers ($N_p - N_{\bar{p}}$), which is event-by-event net-proton distribution, becomes Skellam, and its cumulants are given by $C_n = \langle N_p \rangle + (-1)^n \langle N_{\bar{p}} \rangle$. Using the average numbers of proton and antiproton numbers, $\langle N_p \rangle$ and $\langle N_{\bar{p}} \rangle$ measured in experiments, this baseline estimates are obtained.

ations arise from event-wise variations in the initial temperature, collective flow, initial-state fluctuations and intrinsic correlations among emitted particles [86–90]. As such, recent studies have shown that $\langle p_T \rangle$ fluctuations can be useful in probing the equation-of-state [91], thermal equilibrium [88], and speed-of-sound [92–95] in the QGP. Experimentally, they are typically quantified using measures such as the two-particle transverse momentum correlator [90, 96] or the dynamical variance of the eventwise $\langle p_T \rangle$ distribution [97], which isolate genuine correlations from purely statistical fluctuations due to finite particle multiplicity. Deviations from statistical expectations indicate the presence of correlated emission patterns driven by initial-state density fluctuations or collective hydrodynamic behavior. For example, a suppression of fluctuations is often associated with strong collective flow and thermalization. Measurements by both STAR and ALICE collaborations have revealed suppressed $\langle p_T \rangle$ fluctuations in most-central collisions [90], as shown in Fig. 1.15 (left panel). Also, the $\langle p_T \rangle$ fluctuations are not expected to show significant energy dependence at LHC energies, which is found consistent with predictions from viscous relativistic hydrodynamic model (see right panel of Fig. 1.15) incorporating realistic initial conditions and transport coefficients. These observations highlight the significance of $\langle p_T \rangle$ fluctuations for studying the properties of the strongly interacting QCD matter created in relativistic heavy-ion collisions.

1.6 Thesis physics motivation

Beyond the established soft probes discussed above, this thesis advances the understanding of the QGP through three complementary analyses. These analyses focus on observables that simultaneously probe the medium’s collective dynamics and its underlying micro-

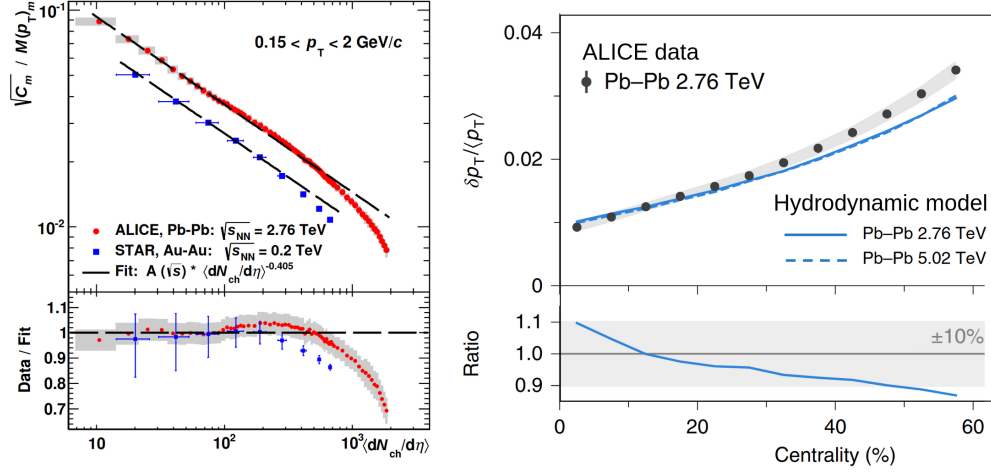


FIGURE 1.15: Left: Relative fluctuations of the event-average p_T , shown as the normalized two-particle correlator for Pb–Pb collisions at $\sqrt{s_{NN}} = 2.76$ TeV (ALICE, red circles) and Au–Au collisions at 0.2 TeV (STAR, blue squares), plotted versus charged-particle multiplicity density $dN_{ch}/d\eta$. The dashed line corresponds to the independent particle production baseline (given by fit with $y \propto x^{-b}$). Right: ALICE data are compared to hydrodynamic model predictions for both 2.76 and 5.02 TeV. Lower panels display data/fit ratios and model/data comparisons. The figures are adapted from Refs. [78] and [90].

scopic degrees of freedom. The selected observable are motivated by their potential to deliver complementary constraints on the transport properties, hydrodynamic response, and thermodynamic characteristics of strongly interacting QCD matter in the high-temperature regime accessed at the LHC.

1.6.1 Higher-order fluctuations of mean transverse momentum

Building upon the second-order analyses discussed in Sec. 1.5.2, this thesis extends the study of event-by-event $\langle p_T \rangle$ fluctuations by measuring higher-order moments, namely skewness and kurtosis. While variance characterizes the width of the $\langle p_T \rangle$ distribution, higher-order moments capture its asymmetry and tail behavior, thereby providing sensitivity to non-Gaussian features arising from dynamical fluctuations. In particular, skewness probes the degree of asymmetry relative to a symmetric Gaussian shape and is expected

to reflect the skewness of the initial energy-density fluctuations in the early stages of the collision [98]. These initial fluctuations propagate through hydrodynamic evolution and imprint on the final-state momentum distributions [87], making skewness a sensitive probe of the medium’s response to initial conditions.

This thesis presents the first comprehensive experimental measurements of skewness and kurtosis of event-by-event $\langle p_T \rangle$ fluctuations in heavy-ion collisions at the LHC. The analysis covers multiple collision systems—including Pb–Pb, Xe–Xe, and pp—enabling a systematic investigation of fluctuation patterns across varying system sizes and initial-state conditions. Comparison of these measurements with state-of-the-art hydrodynamic model calculations allows testing theoretical descriptions of the interplay between initial-state fluctuations and medium response. By accessing higher-order statistical moments, this work aims to enrich our understanding of collective phenomena in the QGP, offering sensitivity to subtle features beyond the reach of conventional variance-based observables. These results have motivated new avenues to probe the complex, emergent behavior of strongly interacting matter created in ultra-relativistic heavy-ion collisions [94, 95].

1.6.2 Radial Flow through novel observable $v_0(p_T)$

In addition to anisotropic flow (discussed in Sec. 1.5.2), the QGP exhibits strong isotropic expansion known as radial flow, driven by substantial pressure gradients acting symmetrically in the transverse plane. This radial expansion shapes the p_T spectra of particles in a mass-dependent manner and serves as a distinct signal of collective behavior. Although typically studied through integrated fits of p_T spectra using blast-wave models, the detailed p_T dependence of radial flow and its role in revealing medium properties—similar to the case of anisotropic flow—remain largely unexplored.

Simultaneous blast-wave fits of p_T spectra yield effective parameters that describe the

overall collective velocity of evolving medium [99, 100], but lack the capacity to resolve detailed momentum-dependent structures and event-by-event fluctuations of radial flow. Consequently, subtle variations and correlations within momentum distributions, induced by radial flow and its fluctuations, have not been systematically studied. This limitation motivates the introduction of a novel p_T -differential observable, $v_0(p_T)$, constructed by analogy with $v_n(p_T)$ [101, 102]. Just as $v_n(p_T)$ captures long-range azimuthal correlations driven by anisotropic flow and its fluctuations, $v_0(p_T)$ captures long-range p_T correlations reflecting radial flow and its fluctuations [101, 102]. The observable also opens avenues for investigating species-dependent features of radial flow, thereby enriching the hydrodynamic characterization of the QGP.

This thesis presents the first measurement of $v_0(p_T)$ for inclusive charged particles and identified particle species in Pb–Pb collisions at the LHC. By systematically analyzing $v_0(p_T)$ across different centralities and comparing with hydrodynamic model calculations, the study aims to provide robust constraints on the transport properties of QGP and deepen understanding of its collective expansion and freeze-out dynamics.

1.6.3 Fluctuations and correlations of conserved charges

The observed sensitivity of higher-order net-proton cumulants to critical dynamics as discussed in Sec. 1.5.2, naturally motivates extending such studies beyond net-baryon fluctuations to a more comprehensive examination of all conserved charges: baryon number, electric charge, and strangeness. These conserved quantum numbers provide fundamental probes into the thermodynamic properties and phase structure of QCD matter. At the LHC, where μ_B approaches zero, measurements of second-order cumulants of net-particle numbers—such as net-pion, net-kaon, and net-proton distributions—provide access to not only fluctuations of individual charge but also cross-correlations like baryon–strangeness,

charge–strangeness, and charge–baryon.

These cross-correlations correspond directly to the mixed susceptibilities calculated in LQCD, providing a rigorous theoretical framework to interpret experimental data [103–107]. Such measurements offer stringent tests of the QGP equation of state and chemical freeze-out conditions, as the behavior of these susceptibilities encodes critical information about underlying QCD thermodynamics—particularly near the crossover region between hadronic and deconfined phases. This comprehensive approach facilitates a deeper understanding of the interplay between microscopic degrees of freedom and macroscopic observables, bridging experimental measurements with first-principles QCD calculations. The investigation of fluctuations and correlations of conserved charges thus forms a central pillar of this thesis, enriching the overall characterization of the strongly interacting QCD medium produced in ultrarelativistic heavy-ion collisions.

1.7 Organization of thesis

Taken together, the three analyses discussed above form a coherent program to investigate the collective dynamics and fluctuation phenomena of QGP at the LHC. They extend the scope of traditional observables by (i) exploring higher-order moments of $\langle p_T \rangle$ fluctuations, (ii) introducing a new measure of radial flow, and (iii) quantifying correlations of conserved charges with direct theoretical relevance to QCD thermodynamics.

The thesis is organized as follows:

- **Chapter 1** introduces the theoretical framework of QCD, QGP, and heavy-ion collisions, together with the motivation for the thesis.
- **Chapter 2 and 3** describe the ALICE detector and data analysis techniques.

- **Chapters 4–6** present the three main results corresponding to the studies outlined in Sec. 1.6.
- **Chapter 7** provides a summary, emphasizing the implications of the results.

Bibliography

- [1] S. L. Glashow. “Partial Symmetries of Weak Interactions”. *Nucl. Phys.* 22 (1961), pp. 579–588.
- [2] Abdus Salam and John Clive Ward. “Electromagnetic and weak interactions”. *Phys. Lett.* 13 (1964), pp. 168–171.
- [3] Steven Weinberg. “A Model of Leptons”. *Phys. Rev. Lett.* 19 (1967), pp. 1264–1266.
- [4] Peter W. Higgs. “Broken symmetries, massless particles and gauge fields”. *Phys. Lett.* 12 (1964), pp. 132–133.
- [5] Murray Gell-Mann. “A Schematic Model of Baryons and Mesons”. *Phys. Lett.* 8 (1964), pp. 214–215.
- [6] Wikipedia contributors. *Standard Model — Wikipedia, The Free Encyclopedia*. URL: https://en.wikipedia.org/wiki/Standard_Model.
- [7] F. Halzen and A. D. Martin. *Quarks and Leptons: An Introductory Course in Modern Particle Physics*. Wiley, 1984.
- [8] David J. Griffiths. *Introduction to Elementary Particles*. Wiley-VCH, 2008.
- [9] P. Paganini. *Fundamentals of Particle Physics: Understanding the Standard Model*. Cambridge University Press, 2024.
- [10] Georges Aad et al. “Observation of a new particle in the search for the Standard Model Higgs boson with the ATLAS detector at the LHC”. *Phys. Lett. B* 716 (2012), pp. 1–29. arXiv: [1207.7214 \[hep-ex\]](#).
- [11] Serguei Chatrchyan et al. “Observation of a New Boson at a Mass of 125 GeV with the CMS Experiment at the LHC”. *Phys. Lett. B* 716 (2012), pp. 30–61. arXiv: [1207.7235 \[hep-ex\]](#).

- [12] Y. Fukuda et al. “Evidence for oscillation of atmospheric neutrinos”. *Phys. Rev. Lett.* 81 (1998), pp. 1562–1567. arXiv: [hep-ex/9807003](#).
- [13] Gianfranco Bertone, Dan Hooper, and Joseph Silk. “Particle dark matter: Evidence, candidates and constraints”. *Phys. Rept.* 405 (2005), pp. 279–390. arXiv: [hep-ph/0404175](#).
- [14] H. David Politzer. “Reliable Perturbative Results for Strong Interactions?” *Phys. Rev. Lett.* 30 (1973). Ed. by J. C. Taylor, pp. 1346–1349.
- [15] David J. Gross and Frank Wilczek. “Ultraviolet Behavior of Nonabelian Gauge Theories”. *Phys. Rev. Lett.* 30 (1973). Ed. by J. C. Taylor, pp. 1343–1346.
- [16] Siegfried Bethke. “Experimental tests of asymptotic freedom”. *Prog. Part. Nucl. Phys.* 58 (2007), pp. 351–386. arXiv: [hep-ex/0606035](#).
- [17] Kenneth G. Wilson. “Confinement of Quarks”. *Phys. Rev. D* 10 (1974). Ed. by J. C. Taylor, pp. 2445–2459.
- [18] John B. Kogut et al. “The Scales of Chiral Symmetry Breaking in Quantum Chromodynamics”. *Phys. Rev. Lett.* 48 (1982), p. 1140.
- [19] Michael Creutz. *Quarks, Gluons and Lattices*. Oxford University Press, 1983.
- [20] Edward V. Shuryak. “Quantum Chromodynamics and the Theory of Superdense Matter”. *Phys. Rept.* 61 (1980), pp. 71–158.
- [21] Edward W. Kolb and Michael S. Turner. *The Early Universe*. Vol. 69. Taylor and Francis, May 2019.
- [22] K. Yagi, T. Hatsuda, and Y. Miake. *Quark-gluon plasma: From big bang to little bang*. Vol. 23. 2005.
- [23] Edward V. Shuryak. “Quark-Gluon Plasma and Hadronic Production of Leptons, Photons and Psions”. *Phys. Lett. B* 78 (1978), p. 150.
- [24] Y. Aoki et al. “The QCD transition temperature: Results with physical masses in the continuum limit”. *Phys. Lett. B* 643 (2006), pp. 46–54. arXiv: [hep-lat/0609068](#).
- [25] A. Bazavov et al. “The chiral and deconfinement aspects of the QCD transition”. *Phys. Rev. D* 85 (2012), p. 054503. arXiv: [1111.1710 \[hep-lat\]](#).
- [26] A. Bazavov et al. “Equation of state in (2+1)-flavor QCD”. *Phys. Rev. D* 90 (2014), p. 094503. arXiv: [1407.6387 \[hep-lat\]](#).

- [27] Szabocs Borsanyi et al. “Full result for the QCD equation of state with 2+1 flavors”. *Phys. Lett. B* 730 (2014), pp. 99–104. arXiv: [1309.5258 \[hep-lat\]](#).
- [28] M. A. Stephanov. “QCD phase diagram: An Overview”. *PoS LAT2006* (2006). Ed. by Tom Blum et al., p. 024. arXiv: [hep-lat/0701002](#).
- [29] Y. Aoki et al. “The Order of the quantum chromodynamics transition predicted by the standard model of particle physics”. *Nature* 443 (2006), pp. 675–678. arXiv: [hep-lat/0611014](#).
- [30] CERN Courier. *STAR hunts QCD critical point*. Accessed: 2025-09-23. 2025. URL: <https://cerncourier.com/star-hunts-qcd-critical-point/>.
- [31] Shinji Ejiri. “Canonical partition function and finite density phase transition in lattice QCD”. *Phys. Rev. D* 78 (2008), p. 074507. arXiv: [0804.3227 \[hep-lat\]](#).
- [32] Juergen Berges, Dirk-Uwe Jungnickel, and Christof Wetterich. “The Chiral phase transition at high baryon density from nonperturbative flow equations”. *Eur. Phys. J. C* 13 (2000), pp. 323–329. arXiv: [hep-ph/9811347](#).
- [33] M. Asakawa and K. Yazaki. “Chiral Restoration at Finite Density and Temperature”. *Nucl. Phys. A* 504 (1989), pp. 668–684.
- [34] M. A. Stephanov. “QCD critical point and event-by-event fluctuations”. *J. Phys. G* 38 (2011). Ed. by Yves Schutz and Urs Achim Wiedemann, p. 124147.
- [35] Krishna Rajagopal and Frank Wilczek. “The Condensed matter physics of QCD”. In: *At the frontier of particle physics. Handbook of QCD. Vol. 1-3*. Ed. by M. Shifman and Boris Ioffe. Nov. 2000, pp. 2061–2151. arXiv: [hep-ph/0011333](#).
- [36] Mark G. Alford. “Color superconductivity in dense quark matter”. In: *TMU - Yale Symposium on Dynamics of Gauge Fields: An External Activity of APCTP*. Mar. 2000, pp. 227–246. arXiv: [hep-ph/0003185](#).
- [37] J. Adam et al. “Nonmonotonic Energy Dependence of Net-Proton Number Fluctuations”. *Phys. Rev. Lett.* 126.9 (2021), p. 092301. arXiv: [2001.02852 \[nucl-ex\]](#).
- [38] L. Adamczyk et al. “Collision Energy Dependence of Moments of Net-Kaon Multiplicity Distributions at RHIC”. *Phys. Lett. B* 785 (2018), pp. 551–560. arXiv: [1709.00773 \[nucl-ex\]](#).

- [39] Xiaofeng Luo and Nu Xu. “Search for the QCD Critical Point with Fluctuations of Conserved Quantities in Relativistic Heavy-Ion Collisions at RHIC : An Overview”. *Nucl. Sci. Tech.* 28.8 (2017), p. 112. arXiv: [1701.02105 \[nucl-ex\]](#).
- [40] A. Pandav, D. Mallick, and B. Mohanty. “Search for the QCD critical point in high energy nuclear collisions”. *Prog. Part. Nucl. Phys.* 125 (2022), p. 103960. arXiv: [2203.07817 \[nucl-ex\]](#).
- [41] Gordon Baym. “Entropy production and the evolution of ultra-relativistic heavy ion collisions”. *Nuclear Physics A* 418 (1984), pp. 525–537. URL: <https://www.sciencedirect.com/science/article/pii/0375947484905736>.
- [42] Gordon Baym. “Ultrarelativistic heavy ion collisions: the first billion seconds”. *Nucl. Phys. A* 956 (2016). Ed. by Y. Akiba et al., pp. 1–10. arXiv: [1701.03972 \[nucl-ex\]](#).
- [43] Shreyasi Acharya et al. “The ALICE experiment: a journey through QCD”. *Eur. Phys. J. C* 84.8 (2024), p. 813. arXiv: [2211.04384 \[nucl-ex\]](#).
- [44] Jean-Yves Ollitrault. “Relativistic hydrodynamics for heavy-ion collisions”. *Eur. J. Phys.* 29 (2008), pp. 275–302. arXiv: [0708.2433 \[nucl-th\]](#).
- [45] Ulrich Heinz and Raimond Snellings. “Collective flow and viscosity in relativistic heavy-ion collisions”. *Ann. Rev. Nucl. Part. Sci.* 63 (2013), pp. 123–151. arXiv: [1301.2826 \[nucl-th\]](#).
- [46] Ramona Vogt. *Ultrarelativistic heavy-ion collisions*. Amsterdam: Elsevier, 2007.
- [47] J. D. Bjorken. “Energy Loss of Energetic Partons in Quark - Gluon Plasma: Possible Extinction of High p(t) Jets in Hadron - Hadron Collisions” (Aug. 1982).
- [48] B. Alver et al. “Importance of correlations and fluctuations on the initial source eccentricity in high-energy nucleus-nucleus collisions”. *Phys. Rev. C* 77 (2008), p. 014906. arXiv: [0711.3724 \[nucl-ex\]](#).
- [49] K. Nakamura et al. “Review of particle physics”. *J. Phys. G* 37 (2010), p. 075021.
- [50] Roman Pasechnik and Michal Šumbera. “Phenomenological Review on Quark–Gluon Plasma: Concepts vs. Observations”. *Universe* 3.1 (2017), p. 7. arXiv: [1611.01533 \[hep-ph\]](#).

- [51] T. Matsui and H. Satz. “ J/ψ Suppression by Quark-Gluon Plasma Formation”. *Phys. Lett. B* 178 (1986), pp. 416–422.
- [52] Jaroslav Adam et al. “ J/ψ suppression at forward rapidity in Pb-Pb collisions at $\sqrt{s_{NN}} = 5.02$ TeV”. *Phys. Lett. B* 766 (2017), pp. 212–224. arXiv: [1606.08197 \[nucl-ex\]](#).
- [53] Serguei Chatrchyan et al. “Observation of Sequential Upsilon Suppression in PbPb Collisions”. *Phys. Rev. Lett.* 109 (2012). [Erratum: *Phys.Rev.Lett.* 120, 199903 (2018)], p. 222301. arXiv: [1208.2826 \[nucl-ex\]](#).
- [54] Armen Tumasyan et al. “Observation of the $\Upsilon(3S)$ meson and sequential suppression of Υ states in PbPb collisions at $\sqrt{s_{NN}} = 5.02$ TeV”. *Phys. Rev. Lett.* 133.2 (2024), p. 022302. arXiv: [2303.17026](#).
- [55] Johann Rafelski and Berndt Muller. “Strangeness Production in the Quark - Gluon Plasma”. *Phys. Rev. Lett.* 48 (1982). [Erratum: *Phys.Rev.Lett.* 56, 2334 (1986)], p. 1066.
- [56] P. Koch, Berndt Muller, and Johann Rafelski. “Strangeness in Relativistic Heavy Ion Collisions”. *Phys. Rept.* 142 (1986), pp. 167–262.
- [57] A. Andronic, P. Braun-Munzinger, and J. Stachel. “Thermal hadron production in relativistic nuclear collisions: The Hadron mass spectrum, the horn, and the QCD phase transition”. *Phys. Lett. B* 673 (2009). [Erratum: *Phys.Lett.B* 678, 516 (2009)], pp. 142–145. arXiv: [0812.1186 \[nucl-th\]](#).
- [58] J. Cleymans et al. “Statistical model predictions for particle ratios at $s(NN)^{1/2} = 5.5$ -TeV”. *Phys. Rev. C* 74 (2006), p. 034903. arXiv: [hep-ph/0604237](#).
- [59] Betty Bezverkhny Abelev et al. “Multi-strange baryon production at mid-rapidity in Pb-Pb collisions at $\sqrt{s_{NN}} = 2.76$ TeV”. *Phys. Lett. B* 728 (2014). [Erratum: *Phys.Lett.B* 734, 409–410 (2014)], pp. 216–227. arXiv: [1307.5543 \[nucl-ex\]](#).
- [60] B. I. Abelev et al. “Enhanced strange baryon production in Au + Au collisions compared to p + p at $s(NN)^{1/2} = 200$ -GeV”. *Phys. Rev. C* 77 (2008), p. 044908. arXiv: [0705.2511 \[nucl-ex\]](#).
- [61] Jaroslav Adam et al. “Enhanced production of multi-strange hadrons in high-multiplicity proton-proton collisions”. *Nature Phys.* 13 (2017), pp. 535–539. arXiv: [1606.07424 \[nucl-ex\]](#).

- [62] Jean-Yves Ollitrault. “Anisotropy as a signature of transverse collective flow”. *Phys. Rev. D* 46 (1992), pp. 229–245.
- [63] D. Teaney, J. Lauret, and Edward V. Shuryak. “Flow at the SPS and RHIC as a quark gluon plasma signature”. *Phys. Rev. Lett.* 86 (2001), pp. 4783–4786. arXiv: [nucl-th/0011058](#).
- [64] Nicolas Borghini and Jean-Yves Ollitrault. “Momentum spectra, anisotropic flow, and ideal fluids”. *Phys. Lett. B* 642 (2006), pp. 227–231. arXiv: [nucl-th/0506045](#).
- [65] R. Nouicer. “New State of Nuclear Matter: Nearly Perfect Fluid of Quarks and Gluons in Heavy Ion Collisions at RHIC Energies”. *Eur. Phys. J. Plus* 131.3 (2016), p. 70. arXiv: [1512.08993 \[nucl-ex\]](#).
- [66] S. Voloshin and Y. Zhang. “Flow study in relativistic nuclear collisions by Fourier expansion of Azimuthal particle distributions”. *Z. Phys. C* 70 (1996), pp. 665–672. arXiv: [hep-ph/9407282](#).
- [67] K. H. Ackermann et al. “Elliptic flow in Au + Au collisions at $\sqrt{s_{NN}} = 130$ GeV”. *Phys. Rev. Lett.* 86 (2001), pp. 402–407. arXiv: [nucl-ex/0009011](#).
- [68] C. Adler et al. “Identified particle elliptic flow in Au + Au collisions at $\sqrt{s_{NN}} = 130$ GeV”. *Phys. Rev. Lett.* 87 (2001), p. 182301. arXiv: [nucl-ex/0107003](#).
- [69] S. S. Adler et al. “Elliptic flow of identified hadrons in Au+Au collisions at $\sqrt{s_{NN}} = 200$ GeV”. *Phys. Rev. Lett.* 91 (2003), p. 182301. arXiv: [nucl-ex/0305013](#).
- [70] K Aamodt et al. “Elliptic flow of charged particles in Pb-Pb collisions at 2.76 TeV”. *Phys. Rev. Lett.* 105 (2010), p. 252302. arXiv: [1011.3914 \[nucl-ex\]](#).
- [71] Betty Bezverkhny Abelev et al. “Elliptic flow of identified hadrons in Pb-Pb collisions at $\sqrt{s_{NN}} = 2.76$ TeV”. *JHEP* 06 (2015), p. 190. arXiv: [1405.4632 \[nucl-ex\]](#).
- [72] Jaroslav Adam et al. “Anisotropic flow of charged particles in Pb-Pb collisions at $\sqrt{s_{NN}} = 5.02$ TeV”. *Phys. Rev. Lett.* 116.13 (2016), p. 132302. arXiv: [1602.01119 \[nucl-ex\]](#).
- [73] A. Adare et al. “Measurement of the higher-order anisotropic flow coefficients for identified hadrons in Au+Au collisions at $\sqrt{s_{NN}} = 200$ GeV”. *Phys. Rev. C* 93.5 (2016), p. 051902. arXiv: [1412.1038 \[nucl-ex\]](#).

- [74] Shreyasi Acharya et al. “Anisotropic flow and flow fluctuations of identified hadrons in Pb–Pb collisions at $\sqrt{s_{\text{NN}}} = 5.02$ TeV”. *JHEP* 05 (2023), p. 243. arXiv: [2206.04587 \[nucl-ex\]](#).
- [75] Edward Shuryak. “Why does the quark gluon plasma at RHIC behave as a nearly ideal fluid?” *Prog. Part. Nucl. Phys.* 53 (2004). Ed. by A. Faessler, pp. 273–303. arXiv: [hep-ph/0312227](#).
- [76] P. Kovtun, Dan T. Son, and Andrei O. Starinets. “Viscosity in strongly interacting quantum field theories from black hole physics”. *Phys. Rev. Lett.* 94 (2005), p. 111601. arXiv: [hep-th/0405231](#).
- [77] Berndt Muller. “From Quark-Gluon Plasma to the Perfect Liquid”. *Acta Phys. Polon. B* 38 (2007). Ed. by Michal Praszalowicz, Marek Kutschera, and Edward Malec, pp. 3705–3730. arXiv: [0710.3366 \[nucl-th\]](#).
- [78] Jonah E. Bernhard, J. Scott Moreland, and Steffen A. Bass. “Bayesian estimation of the specific shear and bulk viscosity of quark–gluon plasma”. *Nature Phys.* 15.11 (2019), pp. 1113–1117.
- [79] S. Acharya et al. “Anisotropic flow of identified particles in Pb-Pb collisions at $\sqrt{s_{\text{NN}}} = 5.02$ TeV”. *JHEP* 09 (2018), p. 006. arXiv: [1805.04390 \[nucl-ex\]](#).
- [80] P. Huovinen et al. “Radial and elliptic flow at RHIC: Further predictions”. *Phys. Lett. B* 503 (2001), pp. 58–64. arXiv: [hep-ph/0101136](#).
- [81] Denes Molnar and Sergei A. Voloshin. “Elliptic flow at large transverse momenta from quark coalescence”. *Phys. Rev. Lett.* 91 (2003), p. 092301. arXiv: [nucl-th/0302014](#).
- [82] Misha A. Stephanov, K. Rajagopal, and Edward V. Shuryak. “Event-by-event fluctuations in heavy ion collisions and the QCD critical point”. *Phys. Rev. D* 60 (1999), p. 114028. arXiv: [hep-ph/9903292](#).
- [83] Henning Heiselberg. “Event-by-event physics in relativistic heavy ion collisions”. *Phys. Rept.* 351 (2001), pp. 161–194. arXiv: [nucl-th/0003046](#).
- [84] R. V. Gavai and Sourendu Gupta. “Lattice QCD predictions for shapes of event distributions along the freezeout curve in heavy-ion collisions”. *Phys. Lett. B* 696 (2011), pp. 459–463. arXiv: [1001.3796 \[hep-lat\]](#).

- [85] B. Stokic, B. Friman, and K. Redlich. “Kurtosis and compressibility near the chiral phase transition”. *Phys. Lett. B* 673 (2009), pp. 192–196. arXiv: [0809.3129 \[hep-ph\]](#).
- [86] Leo Stodolsky. “Temperature fluctuations in multiparticle production”. *Phys. Rev. Lett.* 75 (1995), pp. 1044–1045.
- [87] Piotr Bozek and Wojciech Broniowski. “Transverse-momentum fluctuations in relativistic heavy-ion collisions from event-by-event viscous hydrodynamics”. *Phys. Rev. C* 85 (2012), p. 044910. arXiv: [1203.1810 \[nucl-th\]](#).
- [88] Rupam Samanta et al. “Thermalization at the femtoscale seen in high-energy Pb+Pb collisions”. *Phys. Rev. C* 109.5 (2024), p. L051902. arXiv: [2303.15323 \[nucl-th\]](#).
- [89] Rupam Samanta et al. “Non-Gaussian transverse momentum fluctuations from impact parameter fluctuations”. *Phys. Rev. C* 108.2 (2023), p. 024908. arXiv: [2306.09294 \[nucl-th\]](#).
- [90] Betty Bezverkhny Abelev et al. “Event-by-event mean p_T fluctuations in pp and Pb-Pb collisions at the LHC”. *Eur. Phys. J. C* 74.10 (2014), p. 3077. arXiv: [1407.5530 \[nucl-ex\]](#).
- [91] Jiaxuan Gong, Hendrik Roch, and Chun Shen. “A Gaussian Process Generative Model for QCD Equation of State” (Oct. 2024). arXiv: [2410.22160 \[nucl-th\]](#).
- [92] Fernando G. Gardim, Andre V. Giannini, and Jean-Yves Ollitrault. “Accessing the speed of sound in relativistic ultracentral nucleus-nucleus collisions using the mean transverse momentum”. *Phys. Lett. B* 856 (2024), p. 138937. arXiv: [2403.06052 \[nucl-th\]](#).
- [93] Aram Hayrapetyan et al. “Extracting the speed of sound in quark–gluon plasma with ultrarelativistic lead–lead collisions at the LHC”. *Rept. Prog. Phys.* 87.7 (2024), p. 077801. arXiv: [2401.06896 \[nucl-ex\]](#).
- [94] Georges Aad et al. “Disentangling Sources of Momentum Fluctuations in Xe+Xe and Pb+Pb Collisions with the ATLAS Detector”. *Phys. Rev. Lett.* 133.25 (2024), p. 252301. arXiv: [2407.06413 \[nucl-ex\]](#).

- [95] Ibrahim Jaser Abualrob et al. “Study of $\langle p_T \rangle$ and its higher moments, and extraction of the speed of sound in Pb-Pb collisions with ALICE” (June 2025). arXiv: [2506.10394 \[nucl-ex\]](#).
- [96] J. Adams et al. “Incident energy dependence of pt correlations at RHIC”. *Phys. Rev. C* 72 (2005), p. 044902. arXiv: [nucl-ex/0504031](#).
- [97] K. Adcox et al. “Event-by-event fluctuations in mean p_T and mean e_T in $\sqrt{s_{NN}} = 130$ GeV Au+Au collisions”. *Phys. Rev. C* 66 (2002), p. 024901. arXiv: [nucl-ex/0203015](#).
- [98] Giuliano Giacalone et al. “Skewness of mean transverse momentum fluctuations in heavy-ion collisions”. *Phys. Rev. C* 103.2 (2021), p. 024910. arXiv: [2004.09799 \[nucl-th\]](#).
- [99] L. Adamczyk et al. “Bulk Properties of the Medium Produced in Relativistic Heavy-Ion Collisions from the Beam Energy Scan Program”. *Phys. Rev. C* 96.4 (2017), p. 044904. arXiv: [1701.07065 \[nucl-ex\]](#).
- [100] Shreyasi Acharya et al. “Production of charged pions, kaons, and (anti-)protons in Pb-Pb and inelastic pp collisions at $\sqrt{s_{NN}} = 5.02$ TeV”. *Phys. Rev. C* 101.4 (2020), p. 044907. arXiv: [1910.07678 \[nucl-ex\]](#).
- [101] Björn Schenke, Chun Shen, and Derek Teaney. “Transverse momentum fluctuations and their correlation with elliptic flow in nuclear collision”. *Phys. Rev. C* 102.3 (2020), p. 034905. arXiv: [2004.00690 \[nucl-th\]](#).
- [102] Tribhuban Parida, Rupam Samanta, and Jean-Yves Ollitrault. “Probing collectivity in heavy-ion collisions with fluctuations of the pT spectrum”. *Phys. Lett. B* 857 (2024), p. 138985. arXiv: [2407.17313 \[nucl-th\]](#).
- [103] Sourendu Gupta et al. “Scale for the Phase Diagram of Quantum Chromodynamics”. *Science* 332 (2011), pp. 1525–1528. arXiv: [1105.3934 \[hep-ph\]](#).
- [104] A. Bazavov et al. “Fluctuations and Correlations of net baryon number, electric charge, and strangeness: A comparison of lattice QCD results with the hadron resonance gas model”. *Phys. Rev. D* 86 (2012), p. 034509. arXiv: [1203.0784 \[hep-lat\]](#).

- [105] Heng-Tong Ding, Frithjof Karsch, and Swagato Mukherjee. “Thermodynamics of strong-interaction matter from Lattice QCD”. *Int. J. Mod. Phys. E* 24.10 (2015), p. 1530007. arXiv: [1504.05274 \[hep-lat\]](#).
- [106] H. T. Ding et al. “Chiral Phase Transition Temperature in (2+1)-Flavor QCD”. *Phys. Rev. Lett.* 123.6 (2019), p. 062002. arXiv: [1903.04801 \[hep-lat\]](#).
- [107] Szabolcs Borsanyi et al. “Higher order fluctuations and correlations of conserved charges from lattice QCD”. *JHEP* 10 (2018), p. 205. arXiv: [1805.04445 \[hep-lat\]](#).

A Large Ion Collider Experiment

Contents

2.1 The Large Hadron Collider	48
2.2 ALICE detector	51
2.3 ALICE offline analysis	63

At the world’s highest-energy particle accelerator, the CERN Large Hadron Collider (LHC), ALICE (A Large Ion Collider Experiment) is one of four major detectors at the LHC, dedicated to exploring strongly interacting matter under extreme conditions. The particle beams are accelerated to ultra-relativistic energies on the order of tera-electronvolts (TeV) at the LHC, which facilitates collisions not only of protons and heavy nuclei such as lead but also, in its ongoing Run 3 program, lighter ion species including oxygen and neon. ALICE was conceived to detect signatures of the quark–gluon plasma in heavy-ion collision, while complementary measurements in smaller systems, such as proton-proton (pp) and proton-lead (p–Pb), offer essential baselines for interpretation. The apparatus combines excellent charged-particle tracking with high-precision particle identification,

capabilities that are crucial for the analyses presented in this thesis.

This chapter begins with an overview of the experimental setup, starting from a brief description of the LHC accelerator complex, followed by the layout and main features of the ALICE detector in its Run 2 (2015–2018) configuration. Subsequently, the key ALICE subdetectors involved in this analysis are discussed, with each part focusing on the main features and performance essential for the measurements carried out in this study.

2.1 The Large Hadron Collider

The LHC [1, 2], located approximately 100 meters underground on the border between France and Switzerland near Geneva, is the world's most powerful particle accelerator. It consists of a 27-kilometer circumference circular synchrotron ring in which particle beams are accelerated to velocities near the speed of light and collided at four main interaction points. These points are equipped with large-scale detectors including ALICE, ATLAS, CMS, and LHCb, as shown in Fig. 2.1.

Particles do not start at the LHC ring with full energy (in TeV); instead, they are gradually accelerated through a sequence of smaller accelerators forming the injector chain [3]. This chain prepares and boosts the particle beams to injection energies suitable for the LHC. Moreover, it is important to note that particles in the accelerator are not arranged in a continuous beam but grouped into packets called "bunches". Each bunch contains billions of particles confined within a very short segment of the beam path, typically separated by 25 nanoseconds. This bunching allows collisions to happen in discrete, well-defined intervals at specific points around the ring, which is crucial for detector timing and data collection.

For proton beams, the acceleration begins with protons extracted from hydrogen gas,

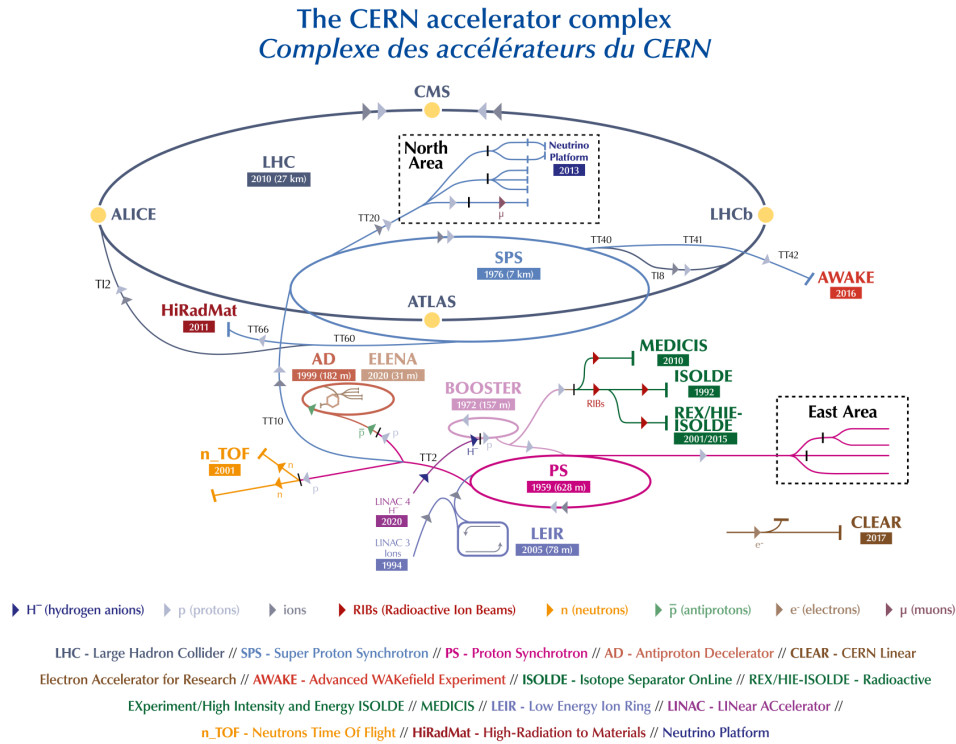


FIGURE 2.1: A schematic overview of the CERN accelerator complex, showing the chain of particle accelerators and transfer lines. The diagram highlights major facilities such as the LHC, SPS, PS, Booster, and LEIR, alongside specialized experiments and beamlines for protons, ions, antiprotons, electrons, muons, and neutrons. Color-coded paths indicate different particle types and the evolution of the complex from initial acceleration to high-energy collision points for experiments like ALICE, ATLAS, CMS, and LHCb, as well as other dedicated facilities with years marking their commencement. The figure is taken from Ref. [4].

which are initially accelerated to around 50 MeV in a linear accelerator called LINAC2. The protons then pass through the Proton Synchrotron Booster (PSB), where they reach energies close to 1.4 GeV. Subsequently, they are transferred to the Proton Synchrotron (PS) reaching approximately 25 GeV, and from there to the Super Proton Synchrotron (SPS), a 7-kilometer ring that accelerates the beams to 450 GeV. Finally, the SPS delivers these high-energy proton bunches into the LHC ring for the last stage of acceleration up to TeV energies. At each stage, acceleration relies on synchronized radio-frequency electric fields

that increase the particles' energy, while magnetic fields guide and focus the beam along the circular accelerator path. For heavy-ion beams, the acceleration sequence is somewhat different. Lead atoms are fully ionized and accelerated initially in LINAC3. The ions then enter the Low Energy Ion Ring (LEIR), followed by the PS and SPS, before injection into the LHC [3]. Injection into the LHC itself is a carefully synchronized multi-step process in which tightly packed bunches of particles are transferred from the SPS to the two counter-rotating beams of the LHC. These beams travel in opposite directions within separate vacuum chambers and intersect exclusively at the four interaction points where the detectors are located.

Building on the overview of the injector chain and beam preparation, it is helpful to understand how these beams lead to observable collisions in the LHC detectors. A key quantity controlling the collision or event rate is the machine luminosity, L , which quantifies the number of collisions, N_{ev} , per unit cross-sectional area per unit time. This relationship can be expressed as:

$$L = \frac{1}{\sigma_{\text{ev}}} \frac{dN_{\text{ev}}}{dt}, \quad (2.1)$$

where σ_{ev} denotes the cross section for the specific event under consideration [1]. Luminosity depends on critical beam parameters such as the number of particles per bunch, the number of bunches per beam, the revolution frequency of the beams, and the transverse beam profile at the interaction point. Maximizing luminosity is essential for obtaining a sufficiently high collision rate to observe rare physical processes. Depending on physics goals and experimental constraints, ATLAS and CMS aimed for a peak luminosity of $L = 10^{34} \text{ cm}^{-2}\text{s}^{-1}$ for proton beams, while ALICE required a peak luminosity of $L = 10^{27} \text{ cm}^{-2}\text{s}^{-1}$ for lead-ion beams. The highest energy achieved for proton beams and lead-ion beams during LHC Run 2 were 6.5 TeV and 2.51 TeV/nucleon, respectively, leading to centre-of-mass energies (\sqrt{s}) of 13 TeV for pp collisions, and 1.04 PeV for Pb–Pb

collisions. In addition, ALICE had also recorded pp collisions at $\sqrt{s} = 5.02$ TeV, p–Pb collisions at $\sqrt{s_{NN}} = 5.02$ and 8.16 TeV, and Xe–Xe collisions at $\sqrt{s_{NN}} = 5.44$ TeV.

The integrated luminosity over the duration of a run can be expressed as

$$L_{\text{int}} = L_o \tau_L \left[1 - \exp \left(\frac{-T_{\text{run}}}{\tau_L} \right) \right], \quad (2.2)$$

where L_0 is the initial peak luminosity, τ_L is the effective luminosity lifetime, and T_{run} is the total length of the luminosity run [1]. The integrated luminosity represents the total collision data accumulated and serves as a crucial indicator of the data volume collected by the experiments. The integrated luminosities recorded for pp collisions at $\sqrt{s} = 5.02$ TeV and Pb–Pb collisions at $\sqrt{s_{NN}} = 5.02$ TeV during the 2015 LHC run are shown in Fig. 2.2. These datasets form the basis for the analyses discussed throughout this thesis.

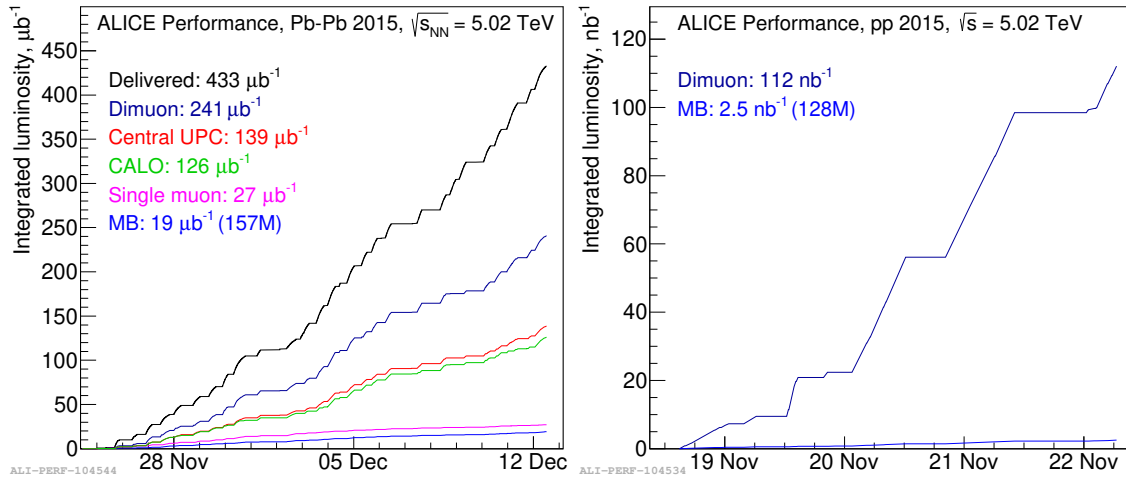


FIGURE 2.2: Total integrated luminosities for different triggers: (left) pp collisions at $\sqrt{s} = 5.02$ TeV, (right) Pb–Pb collisions at $\sqrt{s_{NN}} = 5.02$ TeV, taken in the year 2015. The figures are taken from Refs. [5, 6].

2.2 ALICE detector

The ALICE detector [7, 8] is designed specifically to study the physics of strongly interacting matter and the quark-gluon plasma created in heavy-ion collisions. It is a complex

and versatile apparatus, optimized to cope with the extreme particle multiplicities and high-density environment characteristic of Pb–Pb collisions. With an overall dimension of $16 \times 16 \times 26 \text{ m}^3$ and a weight of approximately 10^4 tonne, it features high detector granularity, a low transverse momentum threshold of $p_T \approx 0.15 \text{ GeV}/c$, and excellent particle identification capabilities up to $20 \text{ GeV}/c$.

The ALICE detector subsystems, as illustrated in Fig. 2.3, are grouped into three main categories: central-barrel detectors, forward detectors, and the MUON spectrometer [7, 8]. The central barrel detectors, housed within a 0.5 T solenoidal magnetic field, are partitioned into 18 equal segments azimuthally and cover a pseudorapidity range of approximately $|\eta| < 0.9$. It includes the primary tracking and particle identification detectors such as the Inner Tracking System (ITS), Time Projection Chamber (TPC), Transition Radiation Detector (TRD), and Time-of-Flight (TOF) system, all of which provide full azimuthal coverage [7, 8]. The TRD primarily identifies electrons by detecting transition radiation photons produced when high-energy electrons traverse materials with varying refractive indices. The other detectors lying within the central barrel are High Momentum Particle Identification Detector (HMPID), Electromagnetic Calorimeter (EMCal), and Photon Spectrometer (PHOS). While PHOS is mainly optimized for precise photon and neutral meson measurements within a limited solid angle, EMCal extends electromagnetic calorimetry coverage in the central barrel, facilitating energy measurements of photons, electrons, and jets with fast triggering capabilities.

The forward detectors extend ALICE’s coverage to small angles relative to the beam axis and include the Forward Multiplicity Detector (FMD), Photon Multiplicity Detector (PMD), V0 detector, T0 detector, and Zero Degree Calorimeter (ZDC). The PMD uses a preshower technique coupled with gas counters to detect photons, while the FMD employs silicon sensors for charged particle counting near $|\eta| \approx 3$ [8]. The Cherenkov-based

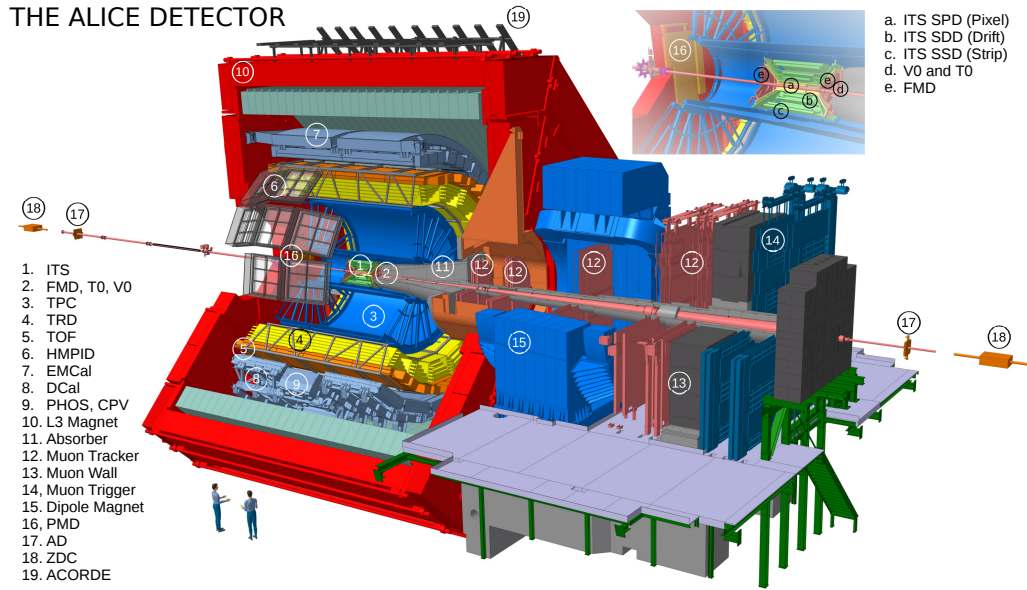


FIGURE 2.3: Schematic illustration of the ALICE detector highlighting its subsystems with numbered labels. The figure is taken from Ref. [9].

T0 detector provides precise timing and longitudinal interaction vertex measurements, essential for event characterization. Complementing these, the V0 detector covers charged particle detection in the asymmetric pseudorapidity regions ($-3.7 < \eta < -1.7$ and $2.8 < \eta < 5.1$), playing a crucial role in event triggering, as well as centrality and event plane determinations. The ZDC, positioned symmetrically around the collision point, also detects spectator nucleons and provides an independent handle on collision centrality.

The ALICE MUON spectrometer consists of five tracking stations, each comprising two cathode pad chambers arranged to provide high-precision spatial measurements of muons. These chambers are installed behind a substantial hadron absorber, which effectively filters out hadrons, allowing predominantly muons to reach the detectors. Located within a 3 Tm dipole magnetic field and covering the range $-4.0 < \eta < 2.5$, the chambers can also track high- p_T muons, mostly coming from beauty and charm decay. To enhance the trigger capabilities, two additional stations equipped with Resistive Plate Chambers (RPCs) are

positioned behind a secondary absorber, that enable triggering on single muons and muon pairs [8].

For spatial reference, ALICE employs a right-handed Cartesian coordinate system with its origin at the LHC interaction point (IP2). The z -axis is aligned along the average beam direction at the interaction point, pointing in the direction of Beam 2, which travels anticlockwise in the LHC. The x -axis is horizontal and points approximately towards the center of the LHC ring, while the y -axis points vertically upwards, perpendicular to both the x and z axes.

Detailed descriptions of the primary sub-detectors employed in the analyses presented in this thesis are provided in the following sections.

2.2.1 Inner Tracking System

The ITS is the innermost component of the ALICE detector, located around the beam pipe in the central barrel [7, 10]. As illustrated in Fig. 2.4, it consists of six concentric layers made from three complementary silicon detector technologies. The two innermost layers are equipped with high-resolution Silicon Pixel Detectors (SPD), followed by two layers of Silicon Drift Detectors (SDD) designed for precise charge collection and position measurements. The outermost two layers incorporate Silicon Strip Detectors (SSD) which aid in extending the tracking volume and improving overall track reconstruction efficiency.

The ITS plays a crucial role in determining primary and secondary vertices with high spatial resolution ($100 \mu m$), enabling the reconstruction of short-lived particles such as charm and strange hadrons. It also improves the momentum and angular resolution of tracks measured by the TPC and provides tracking and particle identification capabilities especially at low transverse momenta. The combined tracking performed by the ITS and TPC achieves a high precision in the plane perpendicular to the beamline, with the position

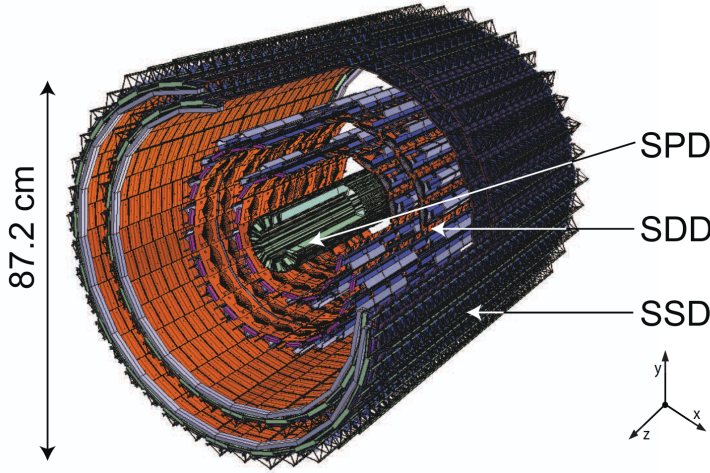


FIGURE 2.4: Schematic representation of the ITS layer arrangement as implemented in the ALICE simulation and reconstruction software. The figure is taken from Ref. [10].

resolution for charged-pion tracks estimated as approximately $[10 + 53/(p_T \sqrt{\sin\theta})] \mu\text{m}$, where p_T is the transverse momentum in GeV/c and θ is the polar angle relative to the beam direction [10]. Furthermore, the ITS achieves a momentum resolution better than 2% for pions with p_T between 0.1 GeV/c and 3 GeV/c , optimized to handle dense track environments with up to 8000 tracks per unit rapidity at mid-rapidity, enabling it to track more than 15,000 particles simultaneously [7].

2.2.2 Time Projection Chamber

The TPC detector, positioned around the ITS, serve as primary tracking detector of ALICE. It is designed as a large hollow cylinder that is oriented along the LHC beam axis and parallel to the detector's solenoidal magnetic field. A schematic representation of this geometry and its key components is shown in Fig. 1 [11]. Its sensitive region extends between an inner radius of about 85 cm and an outer radius of roughly 250 cm, with a longitudinal length of 5 m [11]. At the central plane of the detector, a high-voltage electrode held at 100 kV works in combination with a resistor chain along the cylindrical boundaries to

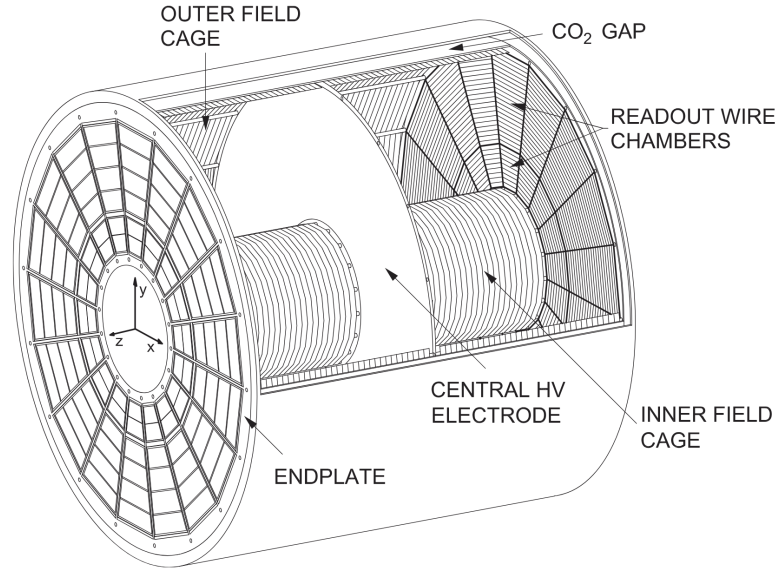


FIGURE 2.5: Schematic representation of the ALICE TPC, showing its key components: the central high-voltage electrode, inner and outer field cages, endplates, readout wire chambers, and the CO₂ insulation gap. The coordinate axes (x, y, z) illustrate the detector's orientation relative to the beam direction. The figure is taken from Ref. [11].

generate a uniform electric field of around 400 V/cm directed along the axis [11]. The chamber is filled with a gas mixture of neon, carbon dioxide, and nitrogen (Ne – CO₂ – N₂) at atmospheric pressure, optimized to provide low diffusion for drifting electrons and stable operation at high rates [11]. When charged particles pass through the medium, they ionize the gas molecules, releasing electrons along their paths. These electrons drift under the influence of the uniform axial electric field toward the readout endplates located at both ends of the detector. The drift velocity is precisely tuned by the choice of gas mixture, ensuring stable and predictable electron transport over distances of more than two meters. At the endplates, the signals are collected in multi-wire proportional chambers (MWPCs) equipped with pad readout. Gas amplification occurs within these chambers, and the induced charges are measured. By recording both the transverse position of the arriving signals in the detector plane and their drift time, referenced to the collision time at the

LHC, the complete three-dimensional trajectories of charged particles can be reconstructed with high accuracy. When these tracks are reconstructed in the presence of the solenoidal magnetic field, the curvature of the trajectories provides a direct measurement of the charged-particle momentum. Because of its high granularity, with 557,568 individual readout channels, the ALICE TPC can finely resolve the spatial and temporal details of particle trajectories even in events with thousands of overlapping tracks [11].

The momentum resolution of the ALICE TPC has been measured using cosmic-ray tracks that cross the detector center, imitating particles from the interaction point. The result, shown in left panel of Fig. 2.6, indicates a resolution better than 6% at $p_T = 10 \text{ GeV}/c$. In addition, the ionization charge measured along the track provides specific energy loss information (dE/dx), which is a key input for particle identification over a broad momentum

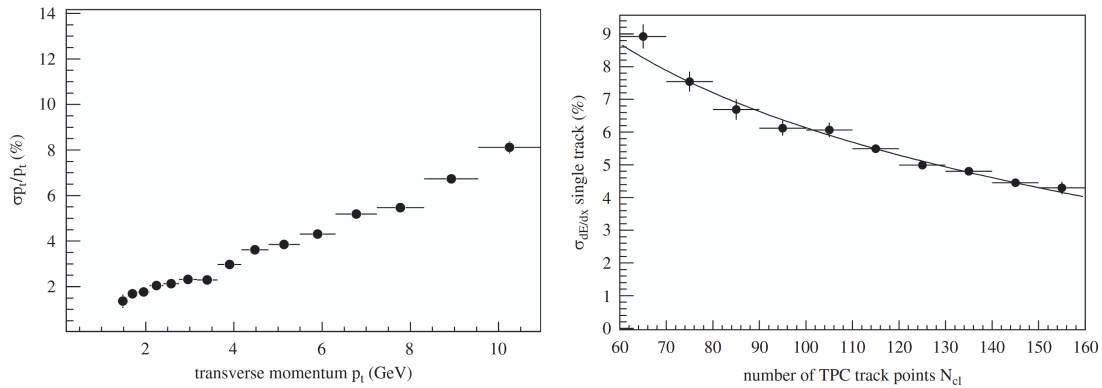


FIGURE 2.6: Left: Specific energy loss resolution, $\sigma_{dE/dx}$ of the ALICE TPC as a function of the number of TPC clusters associated with a single track. Right: Relative transverse momentum resolution of the ALICE TPC as a function of particle transverse momentum. The figures are taken from Ref. [11].

range. The energy resolution, quantified as the relative width of the measured specific energy loss distribution for a single track, depends on the number of TPC clusters (track points) associated with that track. As illustrated in right panel of Fig. 2.6, the dE/dx resolution improves with an increasing number of clusters and reaches values below 5%

for tracks with more than 150 clusters. This high energy resolution allows for reliable separation of different particle species, enhancing the TPC's role in particle identification.

2.2.3 Time-Of-Flight

The TOF detector in ALICE is composed of 1593 glass multi-gap resistive plate chambers (MRPCs). Each MRPC covers a sensitive region of $7.4 \times 120 \text{ cm}^2$, and is subdivided into 96 readout pads, each of size $2.5 \times 3.5 \text{ cm}^2$, leading to a total of 152,928 readout channels. Arranged with cylindrical symmetry, the TOF is positioned around the TRD—which itself encloses the TPC—at an average radial distance of about 3.8 m from the beam axis. In total, the detector spans an active surface of roughly 141 m^2 [12]. The MRPCs are grouped into five modules within each of the 18 azimuthal sectors of the ALICE spaceframe, forming what is referred to as a "TOF supermodule", as illustrated in Fig. 2.7.

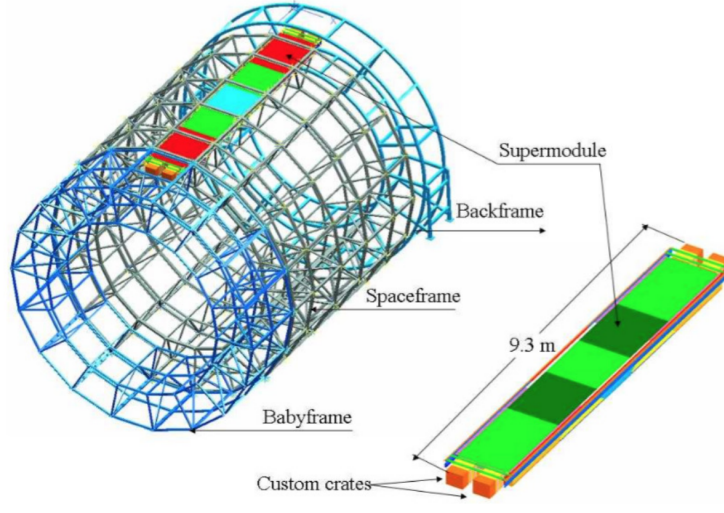
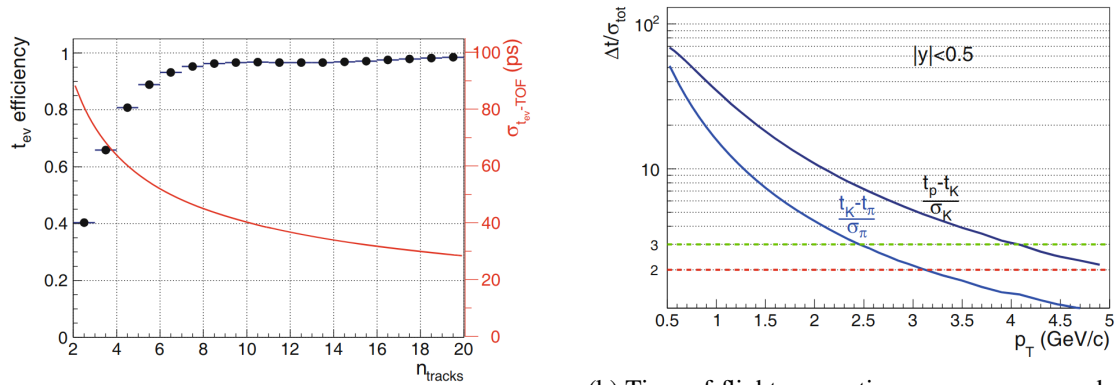


FIGURE 2.7: Schematic representation of the ALICE TOF detector mechanical structure. The left panel illustrates the arrangement of TOF supermodules (highlighted in color) mounted on the cylindrical spaceframe that provides mechanical support, with the “babyframe” and “backframe” also indicated. The right panel shows a detailed representation of a single 9.3 m long supermodule, which houses five MRPC modules and custom electronics crates for readout. The figure is taken from Ref. [12].

Particle identification using the TOF detector relies on measuring the time it takes for a particle to travel from the collision point to the detector and comparing this measured time with the expected time for that particle assuming a specific mass. The measured time-of-flight is calculated by subtracting the event collision time (t_{ev}) from the arrival time recorded by the TOF system (t_{TOF}). The expected propagation time is calculated for each particle species, assuming a given mass, over the known path length from the collision vertex to the TOF system. The timing performance of the TOF system is characterized by its intrinsic resolution, σ_{TOF} , typically around 80 ps (picoseconds), which determines the accuracy of the recorded arrival time. The overall time-of-flight resolution for each particle, σ_{tot} , combines this intrinsic resolution with the resolution of event collision time ($\sigma_{t_{\text{ev}}}$) according to $\sigma_{\text{tot}} = \sqrt{\sigma_{\text{TOF}}^2 + \sigma_{t_{\text{ev}}}^2}$. Although a dedicated T0 detector is deployed for measuring t_{ev} in each event, the TOF system also provides an efficient determination of the event time in high-multiplicity events, as shown in Fig. 2.8a. Both the efficiency



(a) Efficiency (left axis) and time resolution (right axis) of the event collision time measurement shown as a function of reconstructed track multiplicity. The former is represented by black points while the latter is denoted by red curve.

(b) Time-of-flight separation power, expressed in units of total time resolution, for charged hadrons as a function of transverse momentum. The lower and upper curves show the separation between kaons and pions and between protons and kaons, respectively.

FIGURE 2.8: Performance of the ALICE TOF detector. The figures are taken from Ref. [13].

of determining the t_{ev} (left axis) and the corresponding time resolution using the TOF

system, $(\sigma_{t_{\text{ev}}} - \text{TOF})$ are shown as functions of the reconstructed track multiplicity. It can be seen that for events with higher track multiplicity, the efficiency of t_{ev} estimation by TOF approaches unity and the resolution improves substantially, reaching values below 30 ps for more than 10 tracks. Furthermore, Fig. 2.8b demonstrates the TOF detector's capability to distinguish charged particles based on their time-of-flight differences. The system effectively identifies particles in the intermediate momentum range, achieving clear separation between pions, kaons, and protons up to approximately $p_{\text{T}} \approx 5 \text{ GeV}/c$. The horizontal dashed lines indicate the 2σ and 3σ identification thresholds commonly used in particle identification analysis.

2.2.4 V0

The V0 detector system, comprises two arrays, V0A and V0C, positioned asymmetrically around the interaction point at about 340 cm and 90 cm, respectively. These arrays are structured from individual scintillator modules known as counters. In total, there are 32 such counters in each array, arranged in four concentric rings placed around the beam direction. Each ring spans a pseudorapidity range of about half a unit and is segmented azimuthally into eight sectors, with each sector covering 45° as illustrated in Fig. 2.9. The counters themselves are built from plastic scintillator plates into which wavelength-shifting fibres are embedded. When charged particles traverse the scintillator, light is produced and absorbed by the fibres, which convert it to a longer wavelength before guiding it through transparent fibres to photomultiplier tubes, where the signals are read out. Each counter delivers a time resolution better than 1 ns (nanosecond) [15].

The V0 detector arrays measure the amplitude of the signals generated when charged particles pass through the scintillators. This amplitude, which depends on the number and energy deposition of the particles, are used to estimate the charged particle multiplicity in

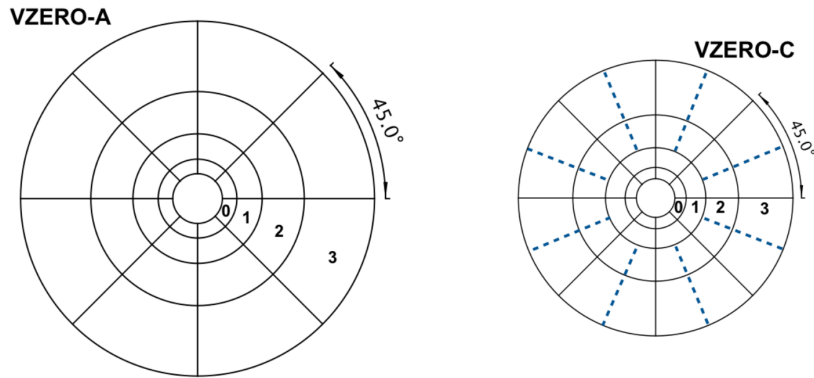


FIGURE 2.9: The schematic layout illustrates the segmentation scheme of the V0 detector arrays in ALICE. The figure is taken from Ref. [14].

the forward and backward pseudorapidity region (close to the beam direction). The measured amplitude distributions enable the determination of collision centrality and facilitate triggering on minimum-bias (MB) or more central collision events. Accurate centrality determination is essential for classifying collision events and interpreting physics results. The centrality determination procedure using V0 amplitude distributions, combined with Glauber model fitting and centrality class definitions, is detailed in Sec. 3.5. Additionally, the V0 system helps reject beam-induced background events, enhancing data quality. It is used for luminosity monitoring and reference in beam scans (Van Der Meer scans [16]) to calibrate the instantaneous luminosity delivered to the experiment [14]. Among all ALICE sub-detectors, the V0 provides the most precise centrality resolution, as highlighted in Fig. 2.10, achieving resolutions around 0.5% for the most central collisions and approximately 2% for peripheral ones. This superior performance surpasses that of other systems such as the TPC, SPD, and ZDC, making V0 the preferred centrality estimator in ALICE. Accordingly, the analysis presented in this thesis uses the V0 as the default centrality estimator.

In summary, the analyses presented in this thesis leverage the complementary capabilities

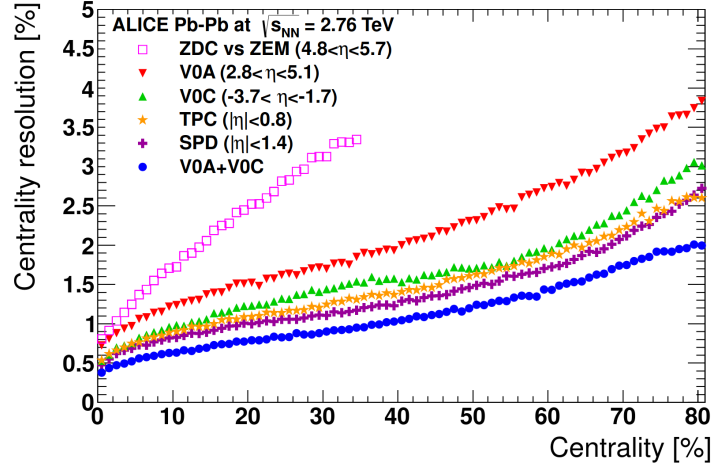


FIGURE 2.10: Centrality resolution as a function of centrality percentile for Pb–Pb collisions at $\sqrt{s_{\text{NN}}} = 2.76$ TeV, comparing performance across different ALICE detectors: ZDC vs ZEM, TPC, SPD, and VZERO. The figure is taken from Ref. [14].

of the ITS, TPC, TOF, and V0 detectors, which are discussed in detail above. The ITS and TPC are used for vertex determination and track reconstruction. Particle identification is performed by using either only TPC dE/dx or combining it with TOF timing information, across the p_T range relevant to the measurements. TPC alone is used for particle identification at low p_T , while both TPC and TOF is used at intermediate p_T to achieve better separation between particle species where the TPC signals begin to overlap. The V0 detector is used for triggering and centrality (for heavy-ion collisions) or multiplicity percentile (for pp collisions) estimation.

2.2.5 Trigger and data acquisition

The trigger system in ALICE is controlled by the Central Trigger Processor (CTP) [7], that is designed to efficiently select physics events of interest from the large number of particle collisions produced by the LHC. It dynamically scales the event selection rates to match the physics goals and the data acquisition system (DAQ) bandwidth limits. The CTP handles diverse running conditions, from heavy-ion collisions with high multiplicity and low rates

to proton-proton collisions with much higher interaction rates. To accommodate the fast detector response requirements, the trigger system operates on three hierarchical levels: Level 0 (L0) delivers a prompt decision within about $1.2 \mu\text{s}$; Level 1 (L1) refines the trigger classification using additional inputs by $6.5 \mu\text{s}$; and Level 2 (L2) applies event pile-up protection and final verification before allowing data readout. The CTP interfaces with detectors via Local Trigger Units (LTUs), which distribute the trigger signals [7]. These LTUs also enable standalone trigger emulation for testing and commissioning purposes. This complex system ensures optimal use of detector resources while maintaining flexibility to operate across varying experimental conditions. For the analyses presented in this thesis, events were selected using the MB trigger. The MB trigger selects inclusive inelastic collisions by requiring signals in both V0A and V0C detector, thereby ensuring an unbiased event sample suitable for general physics analyses. During data acquisition, the selected triggered events are read out from all detectors and passed through the DAQ system, which collects, assembles, and transports data fragments to storage. The DAQ system efficiently handles the high-rate data streams from the detectors by managing event buffering, data flow control, and error handling to ensure reliable and continuous data collection. Subsequently, the High-Level Trigger (HLT) processes the data using real-time reconstruction and calibration algorithms, reducing data volume and improving quality before permanent storage for offline analysis [17]. An in-depth discussion of the architecture and functionalities of CTP and DAQ can be found in Ref. [17].

2.3 ALICE offline analysis

The ALICE offline analysis framework [7] is a comprehensive software system designed for the detector-response simulation, reconstruction, calibration, and physics analysis of

data collected by the ALICE experiment. The framework primarily consists of two main software packages: AliRoot [18] and AliPhysics [19]. AliRoot is the core simulation and reconstruction framework developed within the ROOT data analysis environment and written in C++. It handles the entire chain from event generation, detector simulation (initially based on GEANT3 and later integrating GEANT4), to digitization and reconstruction of raw detector data into physics objects such as tracks and clusters. Built on top of AliRoot, AliPhysics focuses on physics analysis by providing a suite of algorithms and tools for particle identification, event and track selection, extraction of physics observables, and final data analysis tasks required to produce physics results. Both frameworks are tightly integrated with distributed computing resources via the Worldwide LHC Computing Grid [20], enabling efficient processing of the large data volumes generated by the experiment.

2.3.1 Monte Carlo data generation

Monte Carlo (MC) simulations play a crucial role in ALICE analyses by enabling efficiency corrections, detector response studies, and background estimations. For the analyses presented in this thesis, event samples were generated using standard ALICE event generators, including HIJING [21] for heavy-ion collisions and PYTHIA8 [22] for pp collisions. The generated events were processed through the AliRoot framework with detailed detector simulation implemented via GEANT3, which models particle interactions within the ALICE detector geometry. The MC samples produced were used in conjunction with real data to calibrate detector performance and validate analysis procedures. The MC samples produced were used in conjunction with real data to calibrate detector performance and validate analysis procedures. For example, MC closure tests and efficiency estimation performed using MC data are detailed in the subsequent chapters (see Sec. 6.3 in Chapter 4, Sec. 5.4.3 in Chapter 5, and Secs. 6.3.3–6.3.4 in Chapter 6).

Bibliography

- [1] “LHC Machine”. *JINST* 3 (2008). Ed. by Lyndon Evans and Philip Bryant, S08001.
- [2] “LHC Design Report Vol.1: The LHC Main Ring” (June 2004). Ed. by Oliver S. Bruning et al.
- [3] “LHC Design Report. 3. The LHC injector chain” (Dec. 2004). Ed. by M. Benedikt et al.
- [4] Ewa Lopienska. “The CERN accelerator complex, layout in 2022” (2022). General Photo. URL: <https://cds.cern.ch/record/2800984>.
- [5] ALICE Collaboration. *ALICE Figure: Integrated luminosity and trigger statistics*. URL: <https://alice-figure.web.cern.ch/node/8932>.
- [6] ALICE Collaboration. *ALICE Figure: Integrated luminosity and trigger statistics*. URL: <https://alice-figure.web.cern.ch/node/8933>.
- [7] K. Aamodt et al. “The ALICE experiment at the CERN LHC”. *JINST* 3 (2008), S08002.
- [8] Betty Bezverkhny Abelev et al. “Performance of the ALICE Experiment at the CERN LHC”. *Int. J. Mod. Phys. A* 29 (2014), p. 1430044. arXiv: [1402.4476 \[nucl-ex\]](#).
- [9] Arturo Tauro. “ALICE Schematics”. General Photo. 2017. URL: <https://cds.cern.ch/record/2263642>.
- [10] K Aamodt et al. “Alignment of the ALICE Inner Tracking System with cosmic-ray tracks”. *JINST* 5 (2010), P03003. arXiv: [1001.0502 \[physics.ins-det\]](#).
- [11] J. Alme et al. “The ALICE TPC, a large 3-dimensional tracking device with fast readout for ultra-high multiplicity events”. *Nucl. Instrum. Meth. A* 622 (2010), pp. 316–367. arXiv: [1001.1950 \[physics.ins-det\]](#).
- [12] Jaroslav Adam et al. “Determination of the event collision time with the ALICE detector at the LHC”. *Eur. Phys. J. Plus* 132.2 (2017), p. 99. arXiv: [1610.03055 \[physics.ins-det\]](#).
- [13] A. Akindinov et al. “Performance of the ALICE Time-Of-Flight detector at the LHC”. *Eur. Phys. J. Plus* 128 (2013), p. 44.

- [14] E. Abbas et al. “Performance of the ALICE VZERO system”. *JINST* 8 (2013), P10016. arXiv: [1306.3130 \[nucl-ex\]](#).
- [15] P Cortese et al. “ALICE: Physics performance report, volume I”. *J. Phys. G* 30 (2004). Ed. by F Carminati et al., pp. 1517–1763.
- [16] Vinod Chohan. “Simon van der Meer and his legacy to CERN and particle accelerators” (Dec. 2012). arXiv: [1212.4320 \[physics.hist-ph\]](#).
- [17] Christian Wolfgang Fabjan et al. *ALICE trigger data-acquisition high-level trigger and control system*. Technical design report. ALICE. Geneva: CERN, 2004. URL: <https://cds.cern.ch/record/684651>.
- [18] ALICE Collaboration. *AliRoot: ALICE Software Framework*. <https://github.com/alisw/AliRoot>.
- [19] ALICE Collaboration. *AliPhysics: ALICE Analysis Framework*. <https://github.com/alisw/AliPhysics>. 2016.
- [20] Jamie Shiers. “The Worldwide LHC Computing Grid (worldwide LCG)”. *Computer Physics Communications* 177 (July 2007), pp. 219–223.
- [21] Xin-Nian Wang and Miklos Gyulassy. “HIJING: A Monte Carlo model for multiple jet production in p p, p A and A A collisions”. *Phys. Rev. D* 44 (1991), pp. 3501–3516.
- [22] Torbjörn Sjöstrand et al. “An introduction to PYTHIA 8.2”. *Comput. Phys. Commun.* 191 (2015), pp. 159–177. arXiv: [1410.3012 \[hep-ph\]](#).

Experimental data and analysis methodology

Contents

3.1	Datasets	68
3.2	Event selection	68
3.3	Track selection	69
3.4	Particle identification	70
3.5	Centrality determination	73
3.6	Statistical uncertainty estimation	75
3.7	Systematic uncertainty estimation	76

This chapter outlines the experimental data and the analysis methodology that form the common foundation of all measurements presented in the subsequent chapters of this thesis, helping to avoid repetition later. The analyses of higher-order mean transverse momentum fluctuations (Chapter 4), radial flow using the observable $v_0(p_T)$ (Chapter 5) and correlations among conserved charges using net-particle numbers (Chapter 6) are

carried out using the same dataset recorded with the ALICE detector at the LHC. The procedures for event and track selection, centrality determination, and particle identification are described here in detail, along with the general approaches for estimating statistical and systematic uncertainties. Analysis-specific corrections and uncertainty evaluations, which depend on the observable under consideration, are discussed separately in their respective chapters.

3.1 Datasets

In this thesis, data from three types of collisions recorded by the ALICE detector during the Run2 of the LHC are analyzed. The heavy-ion collision datasets examined consist of lead–lead (Pb–Pb) collisions and xenon–xenon (Xe–Xe) collisions, with centre-of-mass energies per nucleon pair ($\sqrt{s_{NN}}$) of 5.02 TeV and 5.44 TeV, respectively. Chapter 4 also includes data from proton–proton (pp) collisions at a centre-of-mass energy (\sqrt{s}) of 5.02 TeV. The Pb–Pb and pp datasets were acquired in 2015, while the Xe–Xe dataset was collected in 2017. All three datasets are utilized in the analysis described in Chapter 4, whereas Chapters 5 and 6 focus exclusively on the Pb–Pb dataset. After applying the standard event (collision) selection criteria (discussed in the next section 3.2), the approximate number of events used for the analyses presented in this thesis from the three datasets are: 80 million for Pb–Pb, 1.2 million for Xe–Xe, and 95 million for pp.

3.2 Event selection

A rigorous event selection is essential to ensure that the analyzed dataset corresponds to genuine collision events while effectively suppressing background and poorly reconstructed events. The selection procedure consists of multiple stages aimed at maximizing data

quality and physics relevance. The initial criterion requires fulfilling the minimum-bias (MB) trigger condition, which ensures that the recorded events correspond to hadronic interactions. For an event to satisfy the MB trigger condition, it is necessary that at least one signal is detected in each of the V0A and V0C scintillator arrays [1, 2], which are situated on opposite sides of the collision vertex, aligned with the direction of the beam.

Following trigger selection, events must contain a well-reconstructed primary vertex. To guarantee uniform detector acceptance and reliable track reconstruction, events are selected only if their primary vertex lies within 10 cm on either side of the nominal interaction point along the beam trajectory. Events outside this fiducial volume are excluded from further analysis. Furthermore, a reconstructed vertex is accepted as real only if it has one or more associated tracks, ensuring the collision is genuine.

An additional quality assurance step applied for the Pb–Pb collisions data involves the rejection of pile-up events, where multiple collisions occur within a single bunch crossing, leading to the reconstruction of several primary vertices. Such events can distort multiplicity measurements and bias correlation observables, making their removal essential for obtaining reliable physics results. They are identified and removed using algorithms based on correlations of recorded signals between two detectors. This selection criterion typically excludes approximately 14% of the triggered events, enhancing the purity of the analyzed dataset. Collectively, these requirements select good-quality events suitable for analysis while reducing background contamination.

3.3 Track selection

In all analyses presented in this thesis, the selection of tracks follows the standard prescriptions of the ALICE Collaboration, optimized to suppress background contributions

while retaining tracks relevant for physics measurements. Only those charged-particles are considered, whose tracks are reconstructed in the central barrel of ALICE within the pseudorapidity window, $|\eta| < 0.8$. In this η window, the detector exhibits uniform azimuthal acceptance, ensuring consistent sensitivity to particle trajectories across all angular orientations. The lower bound on transverse-momentum is set at $p_T > 0.2$ GeV/ c to ensure reliable track reconstruction, while the upper bound depends on the specific analysis and are stated in the corresponding chapters. Each track must register at least 70 out of a total possible 159 space points in the Time Projection Chamber (TPC) [1, 3], as well as a minimum of one hit in the two innermost layers of the Inner Tracking System (ITS) [1]. These conditions provide adequate leverage for track fitting and ensure a precise determination of the distance of closest approach (DCA) to the primary vertex. Limits on both the transverse and longitudinal DCA components (which are DCA_{xy} and DCA_z respectively) are applied to reduce interference from particles originating from secondary decays or material effects. Finally, the quality of the track reconstruction fit is ensured by imposing an upper limit on the reduced chi-squared value (χ^2) per degree of freedom, set to 4 (tighter criteria of 2.5 for Pb–Pb collisions) in the TPC, and 36 in the ITS. Overall, these requirements are intended to retain well-reconstructed tracks suitable for the analyses in this work.

3.4 Particle identification

Particle identification (PID) in ALICE is achieved primarily using the TPC and the Time-Of-Flight (TOF) [4] detector. The TPC determines how much energy charged particles lose while traversing within its gas-filled region. These specific energy loss (dE/dx) measurements are then compared against theoretical predictions from a parameterized Bethe-Bloch function [5]. On the other hand, the TOF measures the time that particles

take to travel from the collision point to the detector surface, allowing the velocity β to be calculated and combined with momentum to test mass hypotheses. At low momenta, the TPC alone provides sufficient separation, while at higher momenta, the TOF complements the TPC to extend PID capabilities, as shown in Fig. 3.1.

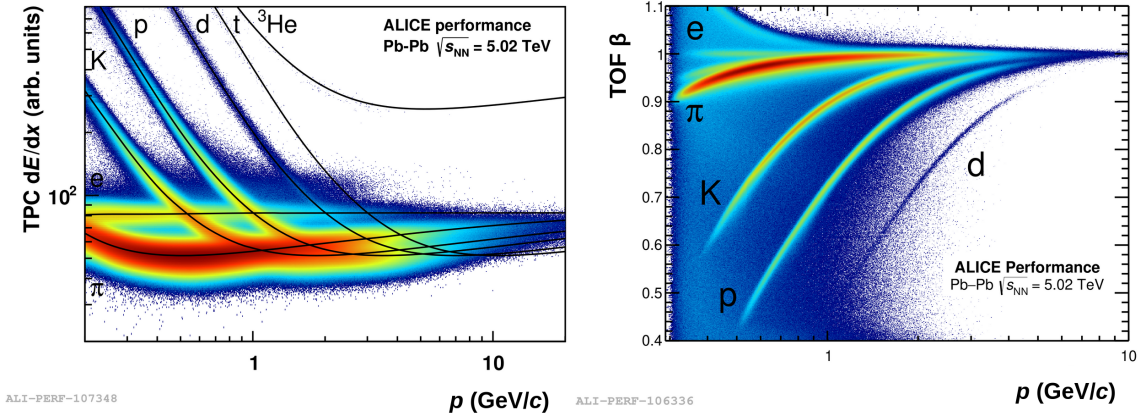


FIGURE 3.1: Particle identification performance in ALICE for Pb–Pb collisions at $\sqrt{s_{NN}} = 5.02$ TeV. (Left) TPC specific energy loss (dE/dx) versus momentum over charge (p/z), showing clear separation of particle species (π , K, p, d, t, ^3He). (Right) TOF measured velocity (β) versus momentum, with visible bands for electrons, pions, kaons, protons, and deuterons. These distributions demonstrate the capability of the ALICE detectors to discriminate between different charged hadrons over a broad momentum range. The figures are taken from Refs. [6, 7].

For the analysis presented in Chapter 6, the identification of pions (π^+ , π^-), kaons (K^+ , K^-), and protons (p , \bar{p}) is carried out by applying selection criteria based on responses from both the TPC and TOF detectors. The TPC response is quantified by the variable $n\sigma_i^{\text{TPC}}$, that represents the normalized difference between the measured value of dE/dx and its predicted value assuming the particle's identity is species i . In the TPC, tracks with p_T less than 0.5 GeV/c are designated as pions if they satisfy $|n\sigma_{\text{pion}}^{\text{TPC}}| < 2$. Similarly, tracks are identified as kaons (or protons) if they satisfy $|n\sigma_{\text{kaon}}^{\text{TPC}}| < 2$ (or $|n\sigma_{\text{proton}}^{\text{TPC}}| < 2$) for $p_T < 0.5$ GeV/c (or $p_T < 0.6$ GeV/c). For particles with higher p_T ($p_T > 0.5$ GeV/c for π^\pm and K^\pm , and $p_T > 0.6$ GeV/c for $p(\bar{p})$), identification leverages information from both the

TPC and TOF detectors. In this p_T range, tracks are classified as i if the combined selection criterion $|n\sigma_i^{\text{TPC+TOF}}| < 2$ is met, where $n\sigma_i^{\text{TPC+TOF}}$ defined as $\sqrt{(n\sigma_i^{\text{TPC}})^2 + (n\sigma_i^{\text{TOF}})^2}$. The $n\sigma_i^{\text{TOF}}$ term represents the normalized difference between the measured and expected flight time of a particle species i , similar to that of TPC. These selection criteria together ensure that the p_T -integrated purity of the selected samples of pions, kaons, and protons remains above 98% within the p_T acceptance range used in the analysis (upper limit is less than 2.0 GeV/c).

In Chapter 5, the analysis requires extending the PID to higher p_T values, up to about $p_T \sim 6$ GeV/c. At this momenta, the separation power of both detectors diminishes because the dE/dx and TOF responses for different species converge, resulting in overlapping signals that limit the effectiveness of straightforward cut-based selections. To address this, a Bayesian approach [8] is employed. This method combines responses from both detectors with species-dependent priors to calculate the probability that a track belongs to a given particle type, reflecting the expected relative abundance of each particle type in the given p_T interval [9]. By interpreting the detector response probabilistically, the Bayesian method improves discrimination in regions of response overlap and reduces the risk of misidentification. Tracks are retained if their Bayesian probability exceeds a minimum threshold (0.95 for pions, 0.9 for kaons and protons), and if they satisfy $|n\sigma_i^{\text{TPC}}| < 3$ and $|n\sigma_i^{\text{TOF}}| < 3$. This approach ensures high purity of selected samples and has been previously applied in ALICE measurements of anisotropic flow of pions, kaons, and protons upto high p_T [10]. The p_T -differential purity thus achieved is higher than 98% (97%) for pions (protons) in the range $0.2 < p_T < 6.0$ GeV/c ($0.4 < p_T < 6.0$ GeV/c), while for kaons, the purity remains higher than 95% in $0.2 < p_T < 4.0$ GeV/c, and is nearly 90% in $4.0 < p_T < 6.0$ GeV/c.

In summary, both PID methods aim to maintain reasonably high identification purity

for pions, kaons, and protons across the momentum range used in the respective analyses.

3.5 Centrality determination

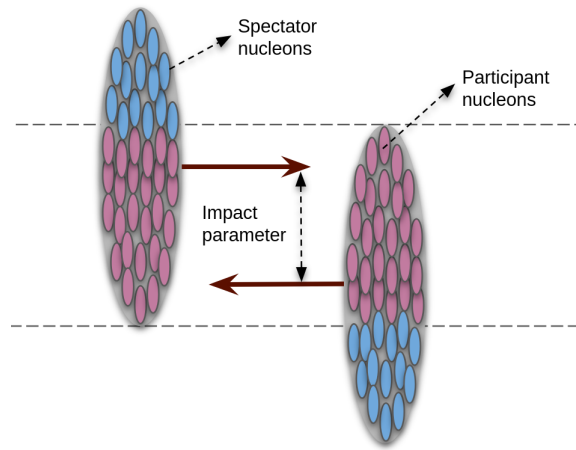


FIGURE 3.2: Diagram illustrating the geometry of a relativistic heavy-ion collision with nonzero impact parameter. Lorentz contraction flattens the nuclei along their direction of motion (as indicated by arrows), making them appear disk-like. Nucleons within the overlapping region are classified as participants; those outside (beyond dashed lines) are spectators. The impact parameter quantifies the distance between the centers of the colliding nuclei in the transverse plane.

In heavy-ion collisions, centrality of a given event serves as an indicator of how much the two nuclei overlap, thereby reflecting the size of the interaction region. It is closely related to the impact parameter b , which defines the separation between the centers of the colliding nuclei along the transverse axis. Although the impact parameter b cannot be measured directly, centrality is inferred from observables sensitive to collision geometry, notably charged-particle multiplicity or energy deposited in forward detectors. Figure 3.2 schematically represents the collision geometry: for head-on collisions ($b = 0$), nuclei fully overlap and all nucleons participate; for non-zero b , only nucleons in the overlap region take part (participants), while those outside remain spectators.

The ALICE experiment employs several detectors for centrality determination, with the V0 scintillator arrays (V0A and V0C) serving as the primary ones. These detectors measure the total signal amplitude for each collision, which correlates with the number of charged particles produced. To connect the measured V0 amplitude distribution with collision geometry, we use a Monte Carlo Glauber model, which simulates nucleon positions inside nuclei and estimates the number of participating nucleons for each collision event. This is combined with a negative binomial distribution (NBD) particle production model, allowing a fit to the experimental V0 amplitude spectrum [11]. Centrality intervals are then defined as percentile bins in this distribution: e.g., the 0–5% interval corresponds to the most central events (highest multiplicities), while the 70–80% interval characterizes more peripheral collisions. Figure 3.3 shows the V0 amplitude distribution for MB triggered Pb–Pb collisions at $\sqrt{s_{\text{NN}}} = 5.02$ TeV, with a vertex selection within ± 10 cm, overlaid with the combined fit with Glauber and NBD (referred as NBD-Glauber). The resulting NBD-Glauber fit reproduces the measured distribution within a few percent across the full multiplicity range, adding quantitative confidence to the centrality determination procedure. Once the centrality intervals are defined, average geometrical quantities such as the number of participant nucleons (N_{part}) and binary nucleon-nucleon collisions (N_{coll}) are assigned. This establishes a direct link between the defined centralities and the initial collision geometry, enabling meaningful interpretation of collision dynamics within each centrality bin. Overall, this centrality determination procedure provides a practical mapping between measured multiplicity and the underlying collision geometry.

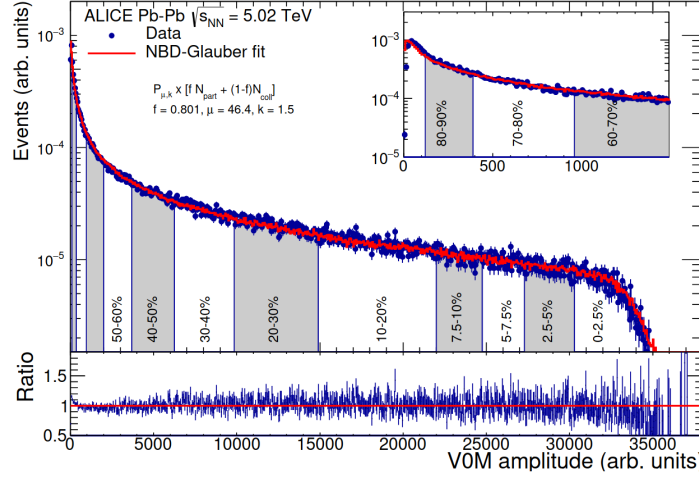


FIGURE 3.3: The V0 scintillators' amplitude distribution for Pb–Pb collisions at $\sqrt{s_{NN}} = 5.02$ TeV. The line represents the NBD-Glauber fit to the data, while the inset provides a closer view of the most peripheral collisions. In the bottom panel, the ratio of experimental data to fit is shown. The figure is taken from Ref. [12].

3.6 Statistical uncertainty estimation

The statistical uncertainties for the measurements presented in this thesis are estimated using the bootstrap resampling method [13], an established and versatile statistical technique to quantify uncertainties even in scenarios where analytic error propagation is challenging. Bootstrap involves generating multiple new datasets, known as bootstrap samples, by randomly sampling with replacement from the original dataset. Starting with the original dataset containing n_{tot} events, B number of bootstrap samples are created, each having the same size n_{tot} . Since the sampling is done with replacement, individual events can appear multiple times in a given bootstrap sample or not at all. An illustration of this sampling method is provided in Fig. 3.4.

For each bootstrap sample, the observable of interest, denoted X , is recalculated, resulting in a distribution of B bootstrap estimates. The statistical uncertainty on X (σ_X) is then obtained from the variance of this bootstrap distribution, as given in Eq. 3.1, thereby

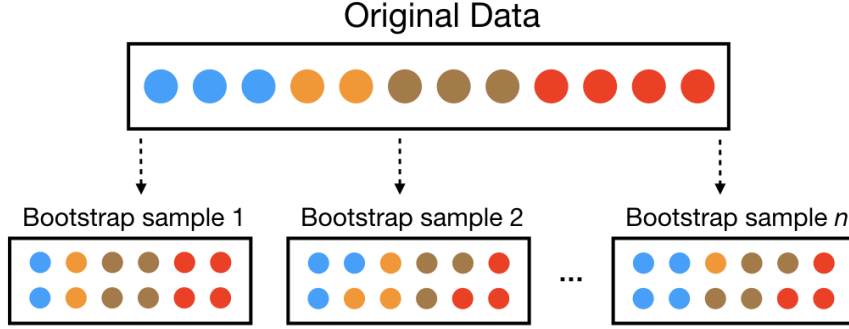


FIGURE 3.4: Illustration of bootstrap sampling: multiple new datasets (bootstrap samples) are generated by randomly sampling with replacement from the original dataset. Each bootstrap sample may contain repeated or omitted data points, enabling robust statistical inference about the original population. The figure is taken from Ref. [14].

providing a data-driven estimate of uncertainty that does not require strong parametric assumptions.

$$\sigma_X = \sqrt{\text{Var}(X)} = \sqrt{\frac{B}{B-1} \left[\frac{1}{B} \sum_{b=1}^B X_b^2 - \left(\frac{1}{B} \sum_{b=1}^B X_b \right)^2 \right]} \quad (3.1)$$

Each analysis has employed $B = 100$ bootstrap samples, a choice that balances computational demands with estimator stability. Numerical studies have shown that the variance estimates obtained using $B = 100$ samples are robust: increasing the number of bootstrap samples further changes the estimated variance by less than 2%. This demonstrates that the chosen sample size is sufficient to ensure stable uncertainty estimation. The bootstrap method thus serves as a reliable approach for estimating statistical uncertainties in the analyses presented later in the thesis.

3.7 Systematic uncertainty estimation

Systematic uncertainties form an essential part of the total uncertainty in experimental measurements, originating from potential biases, limitations, or imperfections in the detector, data acquisition, and analysis procedures. Unlike statistical uncertainties, which arise from

random fluctuations and decrease with larger datasets, systematic effects do not diminish with increasing statistics and can introduce consistent shifts in the measured observables.

In this thesis, the systematic uncertainties associated with the measured quantities are estimated by varying (either tightening or loosening about their default value) event selection, track selection, and PID selection criteria. For event selection, these uncertainties primarily stem from variations in the allowed range of primary vertex position along the beam axis, and from modifications to the pileup rejection criteria when applicable. Additionally, uncertainties arising from fluctuations and finite precision in centrality class determination are also considered. Track selection uncertainties encompass changes to the DCA cut values, both DCA_{xy} and DCA_z , variations in the number of reconstructed space points in the TPC, and modification to the nominal χ^2 values that determine the quality of the track fit. In analyses where efficiency corrections are not applied, the minimal differences observed in the comparison between observable calculated with generated (truth) and reconstructed (with detector effects) in Monte Carlo studies are incorporated directly into the systematic uncertainties. Conversely, for analyses involving efficiency corrections, each systematic variation is propagated by recalculating the efficiency and correcting the observable accordingly before estimating the systematic uncertainty. This procedure ensures consistent treatment of efficiency effects across all variations, maintaining a rigorous evaluation of systematic uncertainties.

The systematic uncertainty for any given source influencing an observable (y) is evaluated using Eq. 3.2,

$$(\Delta y)_{\text{source}} = \sqrt{\frac{1}{N} \sum_{i=1}^N (y_{\text{default}} - y_i)^2} \quad (3.2)$$

where N denotes the total number of applied variations for that source, y_{default} is the value of the observable obtained with the default selection criteria, and y_i is the value obtained

under the i^{th} variation. The systematic uncertainties originating from separate sources are considered independent, and thus, the overall systematic uncertainty is calculated by combining them in quadrature:

$$(\Delta y)_{\text{total}} = \sqrt{\sum_{j=1}^n (\Delta y)_j^2} \quad (3.3)$$

where j indexes the different sources of uncertainty.

We also acknowledge that some sources—for example, track DCA and TPC space point variations—may exhibit correlations. While these correlations are not explicitly accounted for in the current evaluation, the assumption of independence is a common approximation that simplifies the uncertainty estimation. Potential correlations might cause the total systematic uncertainty to be slightly under- or over-estimated; however, their effect is expected to be smaller than the quoted systematic uncertainties. This approach is widely adopted in experimental high-energy physics and provides a robust framework for uncertainty quantification. Detailed discussions of the systematic uncertainty contributions, specific to each analysis, are provided in the respective chapters (see Table. 4.1 or Sec. 5.4.4 and 6.3.5 in Chapter 4, 5, and 6, respectively).

In summary, this procedure provides a consistent framework to estimate and combine the main sources of systematic uncertainty affecting the measurements discussed in this thesis.

Bibliography

- [1] K. Aamodt et al. “The ALICE experiment at the CERN LHC”. *JINST* 3 (2008), S08002.
- [2] E. Abbas et al. “Performance of the ALICE VZERO system”. *JINST* 8 (2013), P10016. arXiv: [1306.3130 \[nucl-ex\]](https://arxiv.org/abs/1306.3130).

- [3] G Dellacasa et al. “ALICE technical design report of the Time Projection Chamber”. *CERN-LHCC-2000-001* (Jan. 2000). URL: <https://cds.cern.ch/record/451098>.
- [4] G. Dellacasa et al. “ALICE technical design report of the Time-Of-Flight system (TOF)”. *CERN-LHCC-2000-012* (Feb. 2000). URL: <https://cds.cern.ch/record/545834>.
- [5] Betty Bezverkhny Abelev et al. “Performance of the ALICE Experiment at the CERN LHC”. *Int. J. Mod. Phys. A* 29 (2014), p. 1430044. arXiv: [1402.4476 \[nucl-ex\]](#).
- [6] ALICE Collaboration. *ALICE Figure: TPC performance figures*. URL: <https://alice-figure.web.cern.ch/node/9219>.
- [7] ALICE Collaboration. *ALICE Figure: TOF performance figures*. URL: <https://alice-figure.web.cern.ch/node/9150>.
- [8] Phil Gregory. *Bayesian Logical Data Analysis for the Physical Sciences*. Cambridge University Press, 2005.
- [9] Jaroslav Adam et al. “Particle identification in ALICE: a Bayesian approach”. *Eur. Phys. J. Plus* 131.5 (2016), p. 168. arXiv: [1602.01392 \[physics.data-an\]](#).
- [10] S. Acharya et al. “Anisotropic flow of identified particles in Pb-Pb collisions at $\sqrt{s_{NN}} = 5.02$ TeV”. *JHEP* 09 (2018), p. 006. arXiv: [1805.04390 \[nucl-ex\]](#).
- [11] Betty Abelev et al. “Centrality determination of Pb-Pb collisions at $\sqrt{s_{NN}} = 2.76$ TeV with ALICE”. *Phys. Rev. C* 88.4 (2013), p. 044909. arXiv: [1301.4361 \[nucl-ex\]](#).
- [12] “Centrality determination in heavy ion collisions”. ALICE-PUBLIC-2018-011 (2018). URL: <https://cds.cern.ch/record/2636623>.
- [13] Rudolf J. Beran and Gilles R Ducharme. *Asympotic theory for bootstrap methods in statistics*. Canadá: Les Publications CRM, 1991.
- [14] Hamza Naviwala. *Understanding Bootstrap Sampling: A Guide for Data Enthusiasts*. URL: <https://datasciencedojo.com/blog/bootstrap-sampling/>.

Higher-order fluctuations of mean transverse momentum

Contents

4.1	Introduction	82
4.2	Observable	84
4.3	Analysis details	87
4.4	Results and discussions	94
4.5	Summary	101
A.1	Simplification of multi-particle p_T correlators	105

Mean transverse momentum fluctuations quantify the event-by-event variation of average transverse momentum ($\langle p_T \rangle$) in heavy-ion collisions, and are sensitive to the initial-state geometry, energy density, and collective expansion dynamics of the system. The higher-order fluctuations, characterized by cumulants of increasing order, such as the skewness, and kurtosis, help isolate non-Gaussian features and probe correlations beyond simple statistical expectations. In this chapter, we present the first measurement of skewness and kurtosis of

$\langle p_T \rangle$ fluctuations across different collision systems: Pb–Pb collisions at $\sqrt{s_{NN}} = 5.02$ TeV, Xe–Xe collisions at $\sqrt{s_{NN}} = 5.44$ TeV, and pp collisions at $\sqrt{s} = 5.02$ TeV. The chapter begins with the motivation and theoretical framework, followed by the description of the analysis methodology. Results are then presented and discussed in relation to relevant theoretical expectations.

4.1 Introduction

Understanding the intricate dynamics of relativistic heavy-ion collisions requires observables that encapsulate the complex interplay between initial-state conditions and the evolution of the created medium. Fluctuations of the event-wise $\langle p_T \rangle$ emerge as an essential tool to probe these dynamics beyond inclusive measurements. Relativistic hydrodynamic simulations have revealed that event-wise $\langle p_T \rangle$ is closely linked to the initial size and energy density of the fireball: an anticorrelation exists between the fireball’s initial transverse size and the $\langle p_T \rangle$ generated while a positive correlation is observed with the initial energy density (see Fig. 4.1) [1, 2]. These relationships imply that variations in $\langle p_T \rangle$ reflect fluctuations in the initial state geometry and energy of the system, which are evolved by the subsequent hydrodynamic response of the system. While the second-order fluctuation measures provide insights into the strength of these variations, higher-order cumulants beyond second order carry information on the shape and tails of the underlying $\langle p_T \rangle$ distributions. These higher moments may enhance the sensitivity to subtle dynamical effects arising from the fluctuating initial density profile, such as hot spots¹ or spatial irregularities.

Hydrodynamic studies in Ref. [3] have offered initial insights into the behavior of the

¹In heavy-ion collisions, ‘hot spots’ refer to localized regions of elevated energy density or temperature within the initial energy profile, caused by fluctuations in nucleon positions and their interactions in the colliding nuclei.

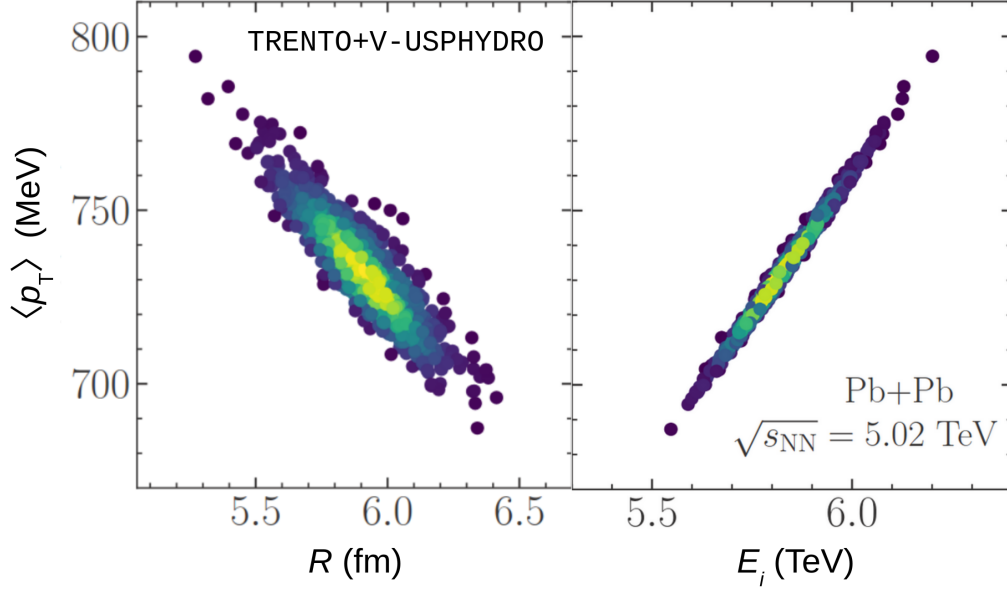


FIGURE 4.1: Correlation between the event-by-event mean transverse momentum $\langle p_T \rangle$ and initial-state properties in Pb+Pb collisions at $\sqrt{s_{NN}} = 5.02$ TeV: (left) anticorrelation with the initial transverse size R of the fireball, and (right) positive correlation with the initial energy E_i , as obtained from T_RENTo+V-USPHYDRO (referred as TRENTO+V-USPHYDRO in figure) simulations. The figure is adapted from Ref. [2].

skewness of event-by-event $\langle p_T \rangle$ fluctuations. These calculations reveal that the observed skewness in $\langle p_T \rangle$ arises predominantly from the asymmetry in initial energy density fluctuations, established at the very beginning of the hydrodynamic evolution rather than at the final freeze-out stage. By employing initial conditions generated by the T_RENTo model [4] and evolving the system through viscous hydrodynamic simulation with v-USPHYDRO [5], a significant positive skewness in the $\langle p_T \rangle$ distribution is predicted as shown in Fig. 4.2. This skewness magnitude goes beyond what would be expected from simple independent particle emission, indicating correlated collective behavior during the system's expansion. These theoretical insights motivate the detailed exploration of higher-order cumulants of $\langle p_T \rangle$ fluctuations as sensitive probes of the fluctuating initial conditions and the dynamical evolution of the QGP.

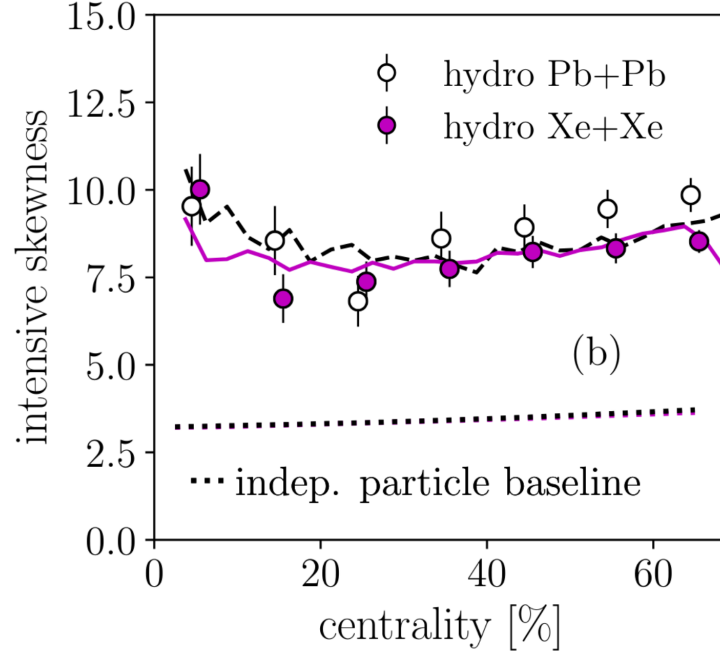


FIGURE 4.2: Centrality dependence of the intensive skewness of event-by-event mean transverse momentum distributions for hydrodynamic models in Pb+Pb (open circles) and Xe+Xe (filled circles) collisions at $\sqrt{s_{NN}} = 5.02$ TeV and 5.44 TeV, respectively, compared to the independent particle emission baseline (dotted line). Error bars represent statistical uncertainties. The figure is taken from Ref. [3].

4.2 Observable

The event-wise $\langle p_T \rangle$ of charged particles is defined as

$$\langle p_T \rangle = \frac{\sum_{i=1}^{N_{ch}} p_{T,i}}{N_{ch}}, \quad (4.1)$$

where $p_{T,i}$ denotes the transverse momentum of the i th particle, and N_{ch} is the total number of charged particles detected in the event. The average of $\langle p_T \rangle$ over all events in the sample is denoted as $\langle \langle p_T \rangle \rangle$, and given by

$$\langle \langle p_T \rangle \rangle = \frac{1}{n_{events}} \sum_{j=1}^{n_{events}} \langle p_T \rangle_j, \quad (4.2)$$

where j indexes the events and n_{events} is the total number of events in the sample.

A common method of analyzing fluctuations of event-by-event $\langle p_T \rangle$ is to calculate the cumulants of its distribution, but this approach combines both random statistical fluctuations and the genuine dynamical fluctuations we want to study. To better isolate the true dynamical correlations, this analysis uses multiparticle p_T correlators [6], which yield zero values for completely random, uncorrelated particle samples. The two-particle p_T correlator, $\langle \Delta p_{T,i} \Delta p_{T,j} \rangle$, and the three-particle correlator, $\langle \Delta p_{T,i} \Delta p_{T,j} \Delta p_{T,k} \rangle$, are expressed algebraically as

$$\begin{aligned} & \langle \Delta p_{T,i} \Delta p_{T,j} \rangle \\ &= \left\langle \frac{\sum_{i,j,i \neq j}^{N_{\text{ch}}} (p_{T,i} - \langle \langle p_T \rangle \rangle) (p_{T,j} - \langle \langle p_T \rangle \rangle)}{N_{\text{ch}}(N_{\text{ch}} - 1)} \right\rangle_{\text{ev}} = \left\langle \frac{Q_1^2 - Q_2}{N_{\text{ch}}(N_{\text{ch}} - 1)} \right\rangle_{\text{ev}} - \left\langle \frac{Q_1}{N_{\text{ch}}} \right\rangle_{\text{ev}}^2, \quad (4.3) \end{aligned}$$

$$\begin{aligned} & \langle \Delta p_{T,i} \Delta p_{T,j} \Delta p_{T,k} \rangle \\ &= \left\langle \frac{\sum_{i,j,k,i \neq j \neq k}^{N_{\text{ch}}} (p_{T,i} - \langle \langle p_T \rangle \rangle) (p_{T,j} - \langle \langle p_T \rangle \rangle) (p_{T,k} - \langle \langle p_T \rangle \rangle)}{N_{\text{ch}}(N_{\text{ch}} - 1)(N_{\text{ch}} - 2)} \right\rangle_{\text{ev}} \\ &= \left\langle \frac{Q_1^3 - 3Q_2Q_1 + 2Q_3}{N_{\text{ch}}(N_{\text{ch}} - 1)(N_{\text{ch}} - 2)} \right\rangle_{\text{ev}} - 3 \left\langle \frac{Q_1^2 - Q_2}{N_{\text{ch}}(N_{\text{ch}} - 1)} \right\rangle_{\text{ev}} \left\langle \frac{Q_1}{N_{\text{ch}}} \right\rangle_{\text{ev}} + 2 \left\langle \frac{Q_1}{N_{\text{ch}}} \right\rangle_{\text{ev}}^3, \quad (4.4) \end{aligned}$$

in terms of moments, $Q_n = \sum_{i=1}^{N_{\text{ch}}} p_{T,i}^n$ with $n = 1, 2, 3, \dots$, where the notation $\langle \dots \rangle_{\text{ev}}$ indicates that the quantity is averaged across all events. These expressions in Eqs. 4.3 and 4.4 efficiently avoid self-correlations by constraining the indices in the summations. Because Q_n values can be computed with a single iteration over particles in each event, this approach reduces computational complexity compared to direct nested summations, which would otherwise become exceedingly demanding for events with the large particle multiplicities. Extending this, the four-particle correlator, $\langle \Delta p_{T,i} \Delta p_{T,j} \Delta p_{T,k} \Delta p_{T,l} \rangle$, is similarly derived

as follows:

$$\begin{aligned}
 & \langle \Delta p_{T,i} \Delta p_{T,j} \Delta p_{T,k} \Delta p_{T,l} \rangle \\
 &= \left\langle \frac{\sum_{i,j,k,l, i \neq j \neq k \neq l}^{N_{\text{ch}}} (p_{T,i} - \langle \langle p_T \rangle \rangle) (p_{T,j} - \langle \langle p_T \rangle \rangle) (p_{T,k} - \langle \langle p_T \rangle \rangle) (p_{T,l} - \langle \langle p_T \rangle \rangle)}{N_{\text{ch}}(N_{\text{ch}} - 1)(N_{\text{ch}} - 2)(N_{\text{ch}} - 3)} \right\rangle_{\text{ev}} \\
 &= \left\langle \frac{Q_1^4 - 6Q_1^2 Q_2 + 8Q_1 Q_3 - 6Q_1^2 Q_2 + 3Q_2^2}{N_{\text{ch}}(N_{\text{ch}} - 1)(N_{\text{ch}} - 2)(N_{\text{ch}} - 3)} \right\rangle_{\text{ev}} - 4 \left\langle \frac{Q_1^3 - 3Q_2 Q_1 + 2Q_3}{N_{\text{ch}}(N_{\text{ch}} - 1)(N_{\text{ch}} - 2)} \right\rangle_{\text{ev}} \left\langle \frac{Q_1}{N_{\text{ch}}} \right\rangle_{\text{ev}} \\
 &+ 6 \left\langle \frac{Q_1^2 - Q_2}{N_{\text{ch}}(N_{\text{ch}} - 1)} \right\rangle_{\text{ev}} \left\langle \frac{Q_1}{N_{\text{ch}}} \right\rangle_{\text{ev}}^2 - 3 \left\langle \frac{Q_1}{N_{\text{ch}}} \right\rangle_{\text{ev}}^4. \tag{4.5}
 \end{aligned}$$

The derivation of these three Eqs. 4.3, 4.4, and 4.5 can be found in Appendix A.1.

To characterize the asymmetry of the distribution of event-wise $\langle p_T \rangle$, two different skewness measures are used: the standardized skewness, $\gamma_{\langle p_T \rangle}$, and the intensive skewness, $\Gamma_{\langle p_T \rangle}$. While $\gamma_{\langle p_T \rangle}$ reflects both intrinsic fluctuations and system-size effects, including participant number dependence, $\Gamma_{\langle p_T \rangle}$ is constructed to be independent of system size, isolating intrinsic dynamical fluctuations [3]. Both of these are defined using multi-particle transverse momentum correlators involving two- and three-particle combinations [3]. The standardized skewness is expressed as

$$\gamma_{\langle p_T \rangle} = \frac{\langle \Delta p_{T,i} \Delta p_{T,j} \Delta p_{T,k} \rangle}{\langle \Delta p_{T,i} \Delta p_{T,j} \rangle^{3/2}}, \tag{4.6}$$

while the intensive skewness takes the form

$$\Gamma_{\langle p_T \rangle} = \frac{\langle \Delta p_{T,i} \Delta p_{T,j} \Delta p_{T,k} \rangle \langle \langle p_T \rangle \rangle}{\langle \Delta p_{T,i} \Delta p_{T,j} \rangle^2}. \tag{4.7}$$

The kurtosis, $\kappa_{\langle p_T \rangle}$, quantifying the peakedness of the $\langle p_T \rangle$ distribution, is defined using the four-particle correlator as

$$\kappa_{\langle p_T \rangle} = \frac{\langle \Delta p_{T,i} \Delta p_{T,j} \Delta p_{T,k} \Delta p_{T,l} \rangle}{\langle \Delta p_{T,i} \Delta p_{T,j} \rangle^2}. \tag{4.8}$$

These quantities describe the detailed structure of the transverse momentum fluctuations using statistically robust, correlation-sensitive methods.

4.3 Analysis details

This section outlines the methodology and key steps for analyzing event-by-event fluctuations of the $\langle p_T \rangle$ distributions of charged particles across different collision systems and centrality/multiplicity classes. It includes a detailed discussion of the Monte Carlo (MC) closure tests for the observables and the associated systematic uncertainties. The analysis uses the kinematic acceptance range $0.2 < p_T < 3.0$ GeV/ c and $|\eta| < 0.8$, consistent with previous ALICE measurements of second-order $\langle p_T \rangle$ fluctuations [7].

The first step is to verify that the observed $\langle p_T \rangle$ fluctuations are not caused by variations in N_{ch} within a centrality class, since $\langle p_T \rangle$ is calculated event-by-event using Eq. 4.1. For each centrality interval, the minimum track count $N_{\text{ch}}^{\text{min}}$ is determined, and this number of tracks is randomly selected per event to construct a reference $\langle p_T \rangle$ distribution free from multiplicity fluctuation. The left panel of Fig. 4.3 compares the original distribution with the fixed- N_{ch} distribution for the most central Pb–Pb collisions (0–5% centrality). Gaussian fits to both reveal positive skewness (a longer tail to the right) in each case. Similar skewness is observed in semicentral and peripheral events (see the other panels of Fig. 4.3), confirming that the skewness arises from genuine physics rather than trivial multiplicity fluctuations. As such, extracting higher-order moments of $\langle p_T \rangle$ fluctuations promises insight into genuine dynamical correlations.

Building on this, we assess the robustness of the skewness and kurtosis observables against detector effects via MC closure tests. Simulated events are generated using HIJING [9] for Pb–Pb and Xe–Xe, and PYTHIA8 [10, 11] for pp collisions, with particle transport modeled by GEANT3 [12] to reproduce ALICE detector conditions during data taking. Comparisons between generated (truth-level) and reconstructed (detector-level) observables, without efficiency corrections, show excellent agreement within uncertainties

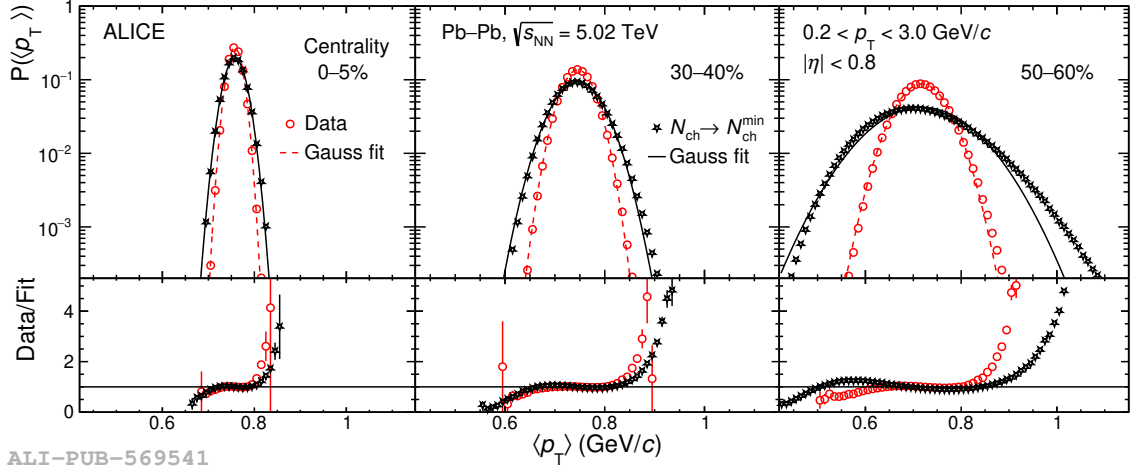


FIGURE 4.3: The probability distributions of $\langle p_T \rangle$, measured for different centrality intervals in Pb–Pb collisions at $\sqrt{s_{NN}} = 5.02$ TeV. True distributions (red open circles) are compared to reference distributions (black stars) along with their corresponding Gaussian fits (dashed red lines for data, solid black lines for reference distributions (see text for details) for each centrality interval. The lower panels show the ratio between the measured distribution and the corresponding fit. The figure is taken from Ref. [8].

(Figs. 4.4–4.6). Closure levels for standardized skewness, intensive skewness, and kurtosis exceed 96–99% across all systems. Residual differences are included as systematic uncertainties (Table 4.1).

In Pb–Pb collisions, observables are measured across 18 equal-width centrality intervals from 0% to 90%, while Xe–Xe collisions are divided into four broader intervals (0–20%, 20–40%, 40–60%, 60–80%) due to limited statistics. For pp, events are classified into ten multiplicity intervals (0–1%, 1–5%, ..., 70–100%), with multiplicity definition given in Ref. [13]. The $\langle p_T \rangle$ correlators are first calculated in unit-width multiplicity bins within each centrality class and then combined using the centrality bin width correction (CBWC) method [14] to remove artificial fluctuations from finite bin widths.

Systematic uncertainties are evaluated separately for each collision system by varying event and track selection criteria. Event selection variations include changing the accepted range of the collision vertex along the beam axis and modifying pileup removal conditions.

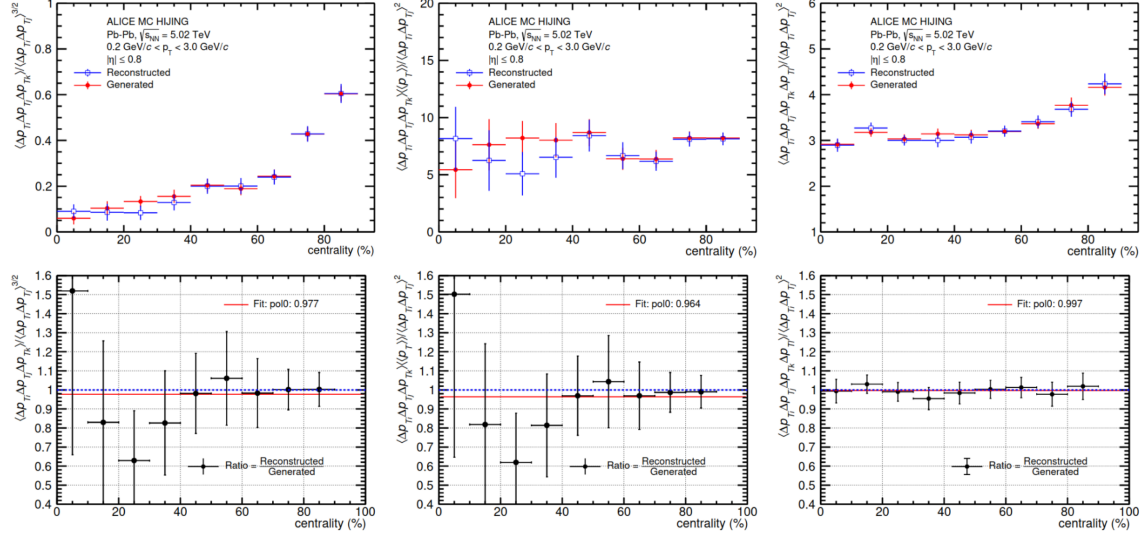


FIGURE 4.4: Comparison between reconstructed and generated (truth) results for standardized skewness (left), intensive skewness (middle), and kurtosis (right) of $\langle p_T \rangle$ fluctuations in Pb-Pb collisions at $\sqrt{s_{NN}} = 5.02$ TeV using the HIJING event generator. The top row presents the measured quantities as a function of centrality, while the bottom row displays the ratio of reconstructed to generated quantities, which is fitted with a zeroth-order polynomial (red solid line). The blue dashed line at unity is shown for reference that would represent 100% closure, and the obtained closure values are also denoted. The vertical bars represent only statistical uncertainties.

Track selection checks vary thresholds on the transverse and longitudinal distances of closest approach (DCA_{xy} , DCA_z), the number of space points reconstructed in the TPC, and track fit quality. Each individual source contributes a percentage range that depends on collision system and event centrality or multiplicity. All sources of uncertainty are treated as independent, and the overall systematic uncertainty is calculated by adding all contributions in quadrature. The MC closure uncertainty, derived from the comparison of generated and reconstructed simulated events, is also included in these totals. Table 4.1 presents the total contributions to the systematic uncertainty for the standardized skewness, intensive skewness, and kurtosis in Pb-Pb, Xe-Xe, and pp collisions.

Comparison of measurements across different collision systems is better achieved using

TABLE 4.1: Summary of the main sources and ranges of systematic uncertainties associated with the standardized skewness $\gamma_{\langle p_T \rangle}$, intensive skewness $\Gamma_{\langle p_T \rangle}$, and kurtosis $\kappa_{\langle p_T \rangle}$, measured in Pb–Pb, Xe–Xe, and pp collisions at different collision energies. The uncertainties are evaluated by varying experimental conditions and analysis selections independently. Ranges are given where uncertainties depend on centrality or multiplicity.

Observables	Sources of systematic uncertainty	Pb–Pb	Xe–Xe	pp
$\gamma_{\langle p_T \rangle}$	Vertex z -position	0.7–2.7%	1.5–9.1%	0.3–0.8%
	Pileup	0.5–6.4%	–	–
	MC closure	2.3%	2.6%	2.7%
	$n_{\text{TPCcrossedrows}}$	0.6–3.8%	2.6–6.8%	0.9–1.9%
	$\chi^2_{\text{TPC}}/n_{\text{TPCclusters}}$	0.5–2.6%	3.4–6.5%	0.1–0.4%
	$\chi^2_{\text{ITS}}/n_{\text{ITSclusters}}$	0.5–2.2%	3.6–11.3%	< 0.1%
	DCA _{xy}	0.6–4.5%	2.5–7.3%	0.5–1.1%
	DCA _z	0.4–1.8%	2.8–5.9%	< 0.1%
	Total	2.9–8.7%	9.1–17.2%	2.9–3.6%
$\Gamma_{\langle p_T \rangle}$	Vertex z -position	0.6–2.7%	1.7–9.1%	0.3–0.8%
	Pileup	0.5–6.3%	–	–
	MC closure	3.6%	2.3%	0.4%
	$n_{\text{TPCcrossedrows}}$	0.8–3.8%	3.0–7.0%	0.3–1.7%
	$\chi^2_{\text{TPC}}/n_{\text{TPCclusters}}$	0.4–2.7%	3.6–6.9%	0.1–0.3%
	$\chi^2_{\text{ITS}}/n_{\text{ITSclusters}}$	0.4–2.2%	3.7–11.4%	< 0.1%
	DCA _{xy}	0.7–4.7%	0.4–4.2%	0.3–1%
	DCA _z	0.4–1.9%	2.7–6.0%	< 0.1%
	Total	4–9%	9.5–17.6%	0.8–2.1%
$\kappa_{\langle p_T \rangle}$	Vertex z -position	0.1–3.6%	0.9–4.5%	0.1–1.4%
	Pileup	0.2–4.5%	–	–
	MC closure	0.3%	1.3%	0.9%
	$n_{\text{TPCcrossedrows}}$	0.1–1.3%	3.0–7.0%	0.3–1.7%
	$\chi^2_{\text{TPC}}/n_{\text{TPCclusters}}$	0.1–1.8%	0.9–4.6%	0.1–1.1%
	$\chi^2_{\text{ITS}}/n_{\text{ITSclusters}}$	0.1–0.9%	1.2–3.9%	< 0.1%
	DCA _{xy}	0.1–2.3%	0.3–0.9%	0.5–3.3%
	DCA _z	0.1–2.9%	0.7–1.9%	< 0.1%
	Total	0.5–7.3%	2.7–11.7% %	1.8–4.7%

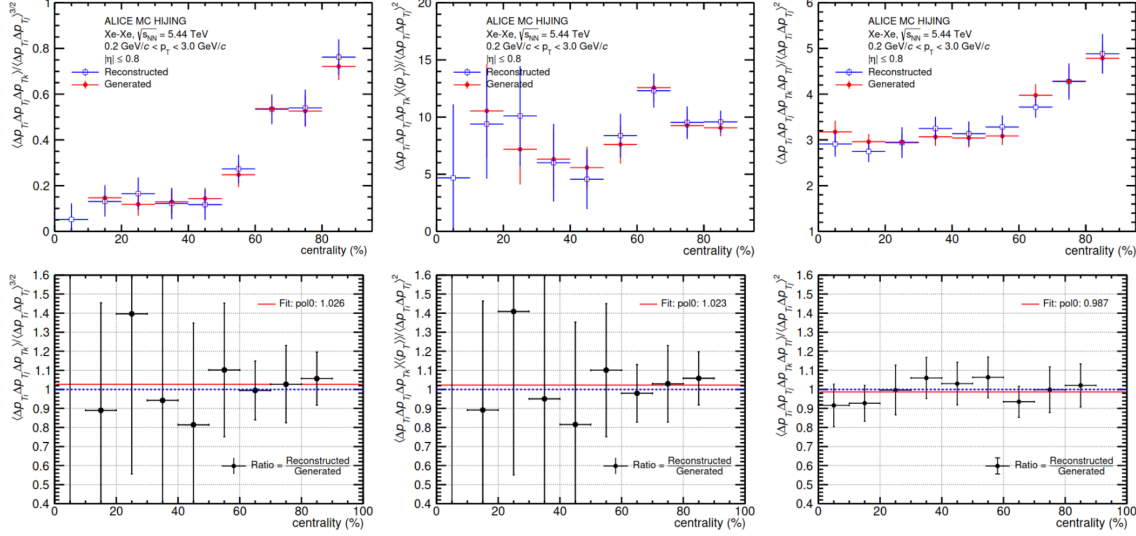


FIGURE 4.5: Comparison between reconstructed and generated (truth) results for standardized skewness (left), intensive skewness (middle), and kurtosis (right) of $\langle p_T \rangle$ fluctuations in Xe–Xe collisions at $\sqrt{s_{NN}} = 5.44$ TeV using the HIJING event generator. The top row presents the measured quantities as a function of centrality, while the bottom row displays the ratio of reconstructed to generated quantities, which is fitted with a zeroth-order polynomial (red solid line). The blue dashed line at unity is shown for reference that would represent 100% closure, and the obtained closure values are also denoted. The vertical bars represent only statistical uncertainties.

the midrapidity charged-particle multiplicity density, $\langle dN_{ch}/d\eta \rangle_{|\eta| < 0.5}$, rather than centrality classes. This choice is motivated by the fact that centrality intervals such as 0–10% do not correspond to equivalent collision geometries in systems like Pb–Pb and Xe–Xe. Therefore, for this analysis, $\langle dN_{ch}/d\eta \rangle_{|\eta| < 0.5}$ values are determined for the specific centrality intervals in which the measurements are performed.

For Pb–Pb and Xe–Xe collisions, the $\langle dN_{ch}/d\eta \rangle_{|\eta| < 0.5}$ values corresponding to given centrality classes (0–2.5%, 2.5–5%, 5–7.5%, 7.5–10%, 10–20%, 20–30%, ...) are taken from Refs. [15, 16]. The mean number of accepted charged particles, $\langle N_{acc} \rangle$, within the kinematic acceptance of this analysis, are also determined for these centrality intervals. The correlation between these $\langle dN_{ch}/d\eta \rangle_{|\eta| < 0.5}$ values and corresponding $\langle N_{acc} \rangle$ are fitted

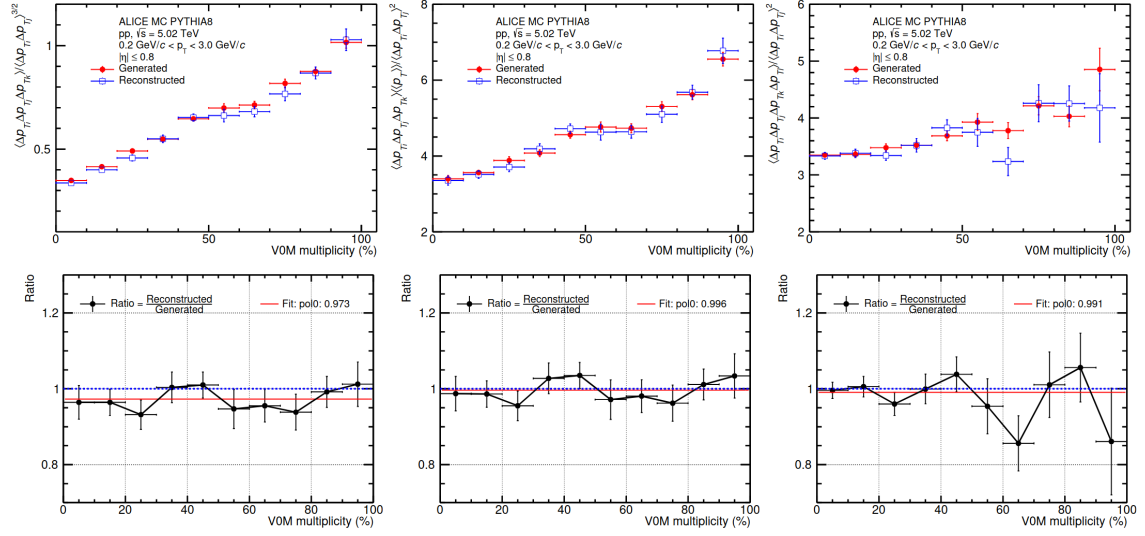


FIGURE 4.6: Comparison between reconstructed and generated (truth) results for standardized skewness (left), intensive skewness (middle), and kurtosis (right) of $\langle p_T \rangle$ fluctuations in pp collisions at $\sqrt{s} = 5.02$ TeV using the PYTHIA event generator. The top row presents the measured quantities as a function of VOM multiplicity percentile, while the bottom row displays the ratio of reconstructed to generated quantities, which is fitted with a zeroth-order polynomial (red solid line). The blue dashed line at unity is shown for reference that would represent 100% closure, and the obtained closure values are also denoted. The vertical bars represent only statistical uncertainties.

with a first-order polynomial (see Figs. 4.7 and 4.8). The resulting fit parameters are then used to convert $\langle N_{\text{acc}} \rangle$ from the centrality classes used in this analysis to $\langle dN_{\text{ch}}/d\eta \rangle_{|\eta| < 0.5}$, following the procedure employed in previous ALICE studies [7].

The uncertainties for thus obtained $\langle dN_{\text{ch}}/d\eta \rangle_{|\eta| < 0.5}$ values are estimated by calculating the upper and lower bounds, i.e., $\langle dN_{\text{ch}}/d\eta \rangle_{|\eta| < 0.5} \pm \sigma$ (represented by the dashed lines in figure), where σ denotes the total uncertainty. Each bound was fitted independently using a first-order polynomial, identical to the procedure for the central values. The final uncertainty was obtained by averaging the deviations between the central fit and the upper/lower fits.

For pp collisions, the values of $\langle dN_{\text{ch}}/d\eta \rangle_{|\eta| < 0.5}$ for different VOM multiplicity classes are taken directly from Ref. [13], as the observables of this analysis are evaluated in the

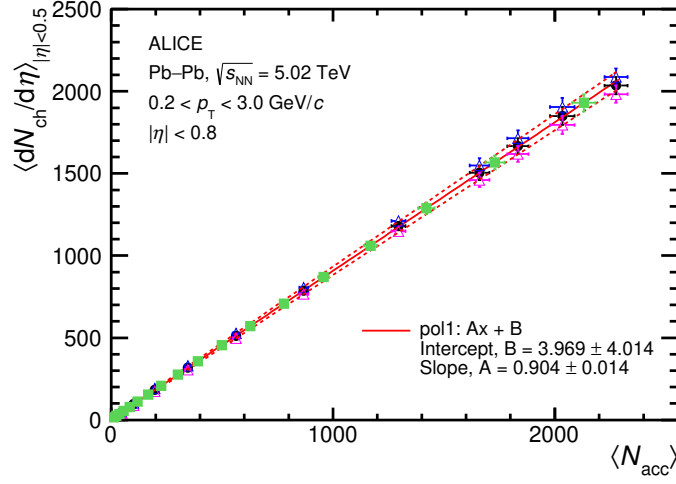


FIGURE 4.7: Correlation between the mean accepted charged-particle multiplicity $\langle N_{acc} \rangle$ for the kinematic region $0.2 < p_T < 3.0$ GeV/c and $|\eta| < 0.8$ and the midrapidity charged-particle density $\langle dN_{ch}/d\eta \rangle_{|\eta| < 0.5}$ for Pb-Pb collisions at $\sqrt{s_{NN}} = 5.02$ TeV. Central values and the values shifted up and down by their uncertainty are fitted with a first-order polynomial to enable conversion between centrality intervals and multiplicity density for system comparisons.

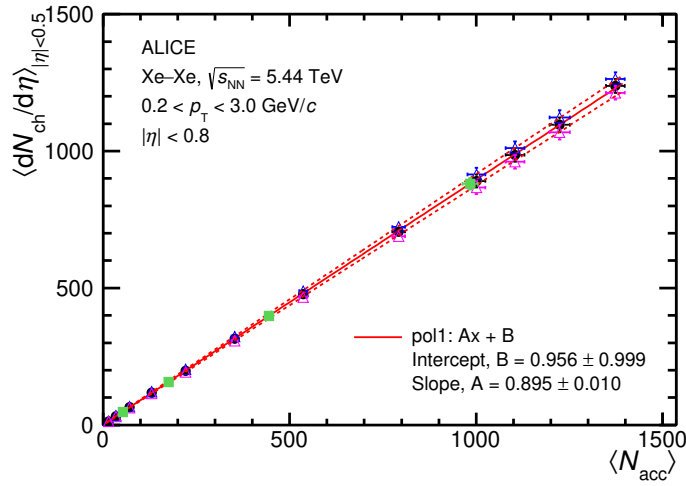


FIGURE 4.8: Correlation between the mean accepted charged-particle multiplicity $\langle N_{acc} \rangle$ for the kinematic region $0.2 < p_T < 3.0$ GeV/c and $|\eta| < 0.8$ and the midrapidity charged-particle density $\langle dN_{ch}/d\eta \rangle_{|\eta| < 0.5}$ for Xe-Xe collisions at $\sqrt{s_{NN}} = 5.44$ TeV. Central values and the values shifted up and down by their uncertainty are fitted with a first-order polynomial to enable conversion between centrality intervals and multiplicity density for system comparisons.

same multiplicity intervals. The values are also provided in Table 4.2.

TABLE 4.2: The values of $\langle dN_{\text{ch}}/d\eta \rangle_{|\eta|<0.5}$ for different multiplicity classes in pp, $\sqrt{s} = 5.02$ TeV taken from [13].

VOM percentile (%)	$\langle dN_{\text{ch}}/d\eta \rangle_{ \eta <0.5}$
0 - 1	$18.5 \pm 0.17 \pm 0.16$
1 - 5	$14.51 \pm 0.14 \pm 0.12$
5 - 10	$11.93 \pm 0.11 \pm 0.10$
10 - 15	$10.30 \pm 0.10 \pm 0.09$
15 - 20	$9.12 \pm 0.09 \pm 0.08$
20 - 30	$7.76 \pm 0.08 \pm 0.07$
30 - 40	$6.34 \pm 0.06 \pm 0.06$
40 - 50	$5.22 \pm 0.05 \pm 0.05$
50 - 70	$3.94 \pm 0.04 \pm 0.04$
70 - 100	$2.42 \pm 0.02 \pm 0.03$

4.4 Results and discussions

4.4.1 Standardized skewness

The behavior of the standardized skewness, $\gamma_{\langle p_T \rangle}$ (defined in Eq. 4.6) in Pb–Pb and Xe–Xe collisions at $\sqrt{s_{\text{NN}}} = 5.02$ TeV and 5.44 TeV, respectively, is plotted against the system size indicated by the cube root of the average charged-particle multiplicity density, $\langle dN_{\text{ch}}/d\eta \rangle_{|\eta|<0.5}^{1/3}$ in Fig. 4.9. The latter quantity serves as an effective measure of system size, as it correlates linearly with femtoscopic radii representing the fireball size at kinetic freeze-out [17]. The uncertainty in $\langle dN_{\text{ch}}/d\eta \rangle_{|\eta|<0.5}^{1/3}$ is determined by propagating the associated uncertainty in $\langle dN_{\text{ch}}/d\eta \rangle_{|\eta|<0.5}$. An overall decreasing trend in $\gamma_{\langle p_T \rangle}$ is observed as $\langle dN_{\text{ch}}/d\eta \rangle_{|\eta|<0.5}^{1/3}$ increases for both collision systems. This trend is consistent with fluctuations in a dilution scenario caused by superposition of partially independent

particle-emitting sources [7, 18]. If the fluctuations in $\langle p_T \rangle$ were purely statistical and driven by finite particle counts (N), then $\gamma_{\langle p_T \rangle}$ would approximately scale as $1/N$. A modest increase of $\gamma_{\langle p_T \rangle}$ in the most central Pb–Pb collisions ($\langle dN_{\text{ch}}/d\eta \rangle_{|\eta|<0.5}^{1/3} > 11$) is also observed within uncertainties, potentially linked to a reduction in the two-particle momentum correlations $\langle \Delta p_{T,i} \Delta p_{T,j} \rangle$. This was previously observed in Ref. [7].

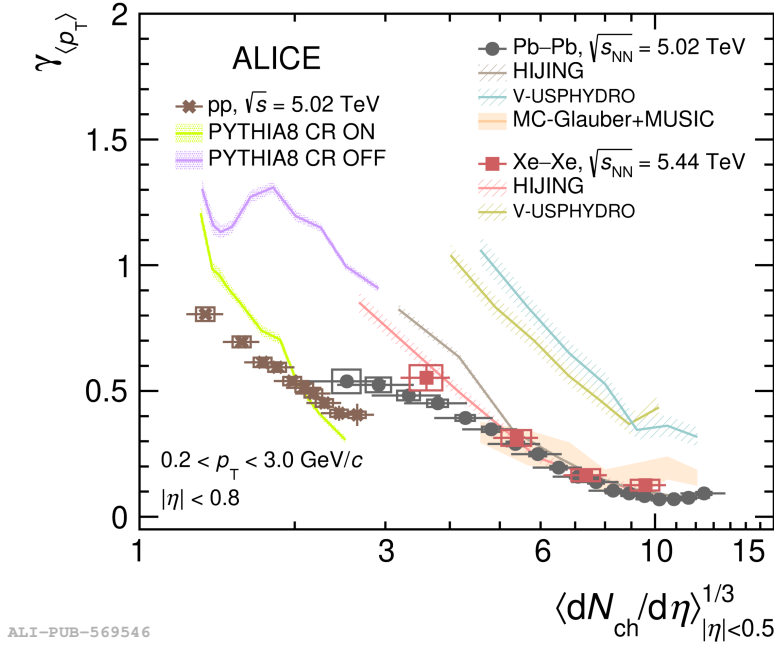


FIGURE 4.9: Standardized skewness $\gamma_{\langle p_T \rangle}$ of the event-averaged transverse momentum distribution is shown as a function of the cubic root of midrapidity charged-particle density, $\langle dN_{\text{ch}}/d\eta \rangle_{|\eta|<0.5}^{1/3}$ in Pb–Pb collisions at $\sqrt{s_{\text{NN}}} = 5.02$ TeV, Xe–Xe collisions at $\sqrt{s_{\text{NN}}} = 5.44$ TeV and pp collisions at $\sqrt{s} = 5.02$ TeV. Colored bands represent predictions from event generators (PYTHIA8, HIJING) and hydrodynamic simulations (V-USPHYDRO, and MC-Glauber+MUSIC). Statistical and systematic uncertainties are represented by vertical bars and shaded boxes, respectively. The figure is taken from Ref. [8].

The results are compared with hydrodynamic calculations based on the v-USPHYDRO model, which employs T_RENTo initial conditions and a specific shear viscosity of $\eta/s = 0.047$ [3]. The model qualitatively captures the decreasing trend of $\gamma_{\langle p_T \rangle}$ with system size, although it slightly overestimates the magnitude across most multiplicity ranges. Moreover,

while the simulation predicts higher values of $\gamma_{\langle p_T \rangle}$ for Pb–Pb than Xe–Xe collisions at similar multiplicities, the experimental data show no such distinct system dependence.

Model comparisons are also made using HIJING [9], a Monte Carlo event generator that treats heavy-ion collisions as a superposition of independent nucleon–nucleon interactions, incorporating various phenomena like multiple minijet production with initial and final state radiation or nuclear effects such as parton shadowing and jet quenching. The version used here, HIJING/ $B\bar{B}$ v2.0 [19], reproduces the observed trend in the semiperipheral to semicentral regions but shows a stronger dependence on system size compared to the data.

Further theoretical comparison is performed with the MC-Glauber + MUSIC framework, which uses a MC Glauber approach [20] for modeling the initial geometry, followed by relativistic hydrodynamic evolution through MUSIC [21] with $\eta/s = 0.1$. Both HIJING and MC-Glauber + MUSIC rely on Glauber-based initial conditions, though they differ in the treatment of the subsequent medium evolution. Interestingly, for Pb–Pb collisions, the predicted $\gamma_{\langle p_T \rangle}$ values from both models are nearly identical in the semicentral and semiperipheral regions, implying a limited sensitivity of this observable to later-stage collective dynamics and a stronger dependence on the initial-state geometry.

The Pb–Pb and Xe–Xe measurements are also compared to results from pp collisions at $\sqrt{s} = 5.02$ TeV. In the pp system, $\gamma_{\langle p_T \rangle}$ decreases more steeply with $\langle dN_{\text{ch}}/d\eta \rangle_{|\eta| < 0.5}^{1/3}$ and remains systematically smaller than in Pb–Pb collisions across the overlapping multiplicity interval. These measurements are confronted with PYTHIA8 simulations [11], which incorporate perturbative QCD processes and have successfully reproduced diverse pp observables at LHC energies [22–24]. The color reconnection (CR) mechanism [25], a feature available in PYTHIA8 that allows color strings from different parton interactions to recombine, is known to generate flow-like correlations in small systems. When CR is switched off (PYTHIA8 CR OFF), the model fails to describe the observed $\gamma_{\langle p_T \rangle}$ trend

both in magnitude and shape. However, enabling CR (PYTHIA8 CR ON) improves the agreement, qualitatively reproducing the multiplicity dependence though with a steeper slope than seen in experimental data.

Thus, the standardized skewness primarily reflects fluctuations driven by the initial collision geometry and the number of particle-emitting sources, showing reduced magnitude with increasing system size.

4.4.2 Intensive skewness

Figure 4.10 displays the intensive skewness (see Eq. 4.7) as a function of $\langle dN_{\text{ch}}/d\eta \rangle_{|\eta|<0.5}^{1/3}$, for Pb–Pb collisions at $\sqrt{s_{\text{NN}}} = 5.02$ TeV and Xe–Xe collisions at $\sqrt{s_{\text{NN}}} = 5.44$ TeV. The dashed colored lines represent the independent baselines, $\Gamma_{\text{independent}}$, calculated separately for each system using the formula [3]:

$$\Gamma_{\text{independent}} = \frac{\langle (p_T - \langle p_T \rangle)^3 \rangle \langle p_T \rangle}{\langle (p_T - \langle p_T \rangle)^2 \rangle^2}, \quad (4.9)$$

where $\langle p_T \rangle$ is the average transverse momentum across all events within a given centrality class. To determine $\Gamma_{\text{independent}}$, the p_T spectra for each centrality bin are used. The second and third central moments of the p_T distribution, $\langle (p_T - \langle p_T \rangle)^2 \rangle$ and $\langle (p_T - \langle p_T \rangle)^3 \rangle$, are calculated from these spectra, and their ratio gives the baseline value for each centrality. For Pb–Pb and Xe–Xe collisions, the spectra come from Refs. [26] and [27], respectively. The centrality classes are translated into $\langle dN_{\text{ch}}/d\eta \rangle_{|\eta|<0.5}$ and its cubic root for plotting.

The results show that the intensive skewness remains positive and above the independent baseline across all system sizes in both collision systems. This matches qualitatively with hydrodynamic model predictions from v-USPHYDRO, though the model does not exactly reproduce the measured values. The HIJING model describes the decreasing trend of $\Gamma_{\langle p_T \rangle}$ in the semiperipheral to semicentral region (roughly $3.8 \leq \langle dN_{\text{ch}}/d\eta \rangle_{|\eta|<0.5}^{1/3} \leq 8.9$) but fails

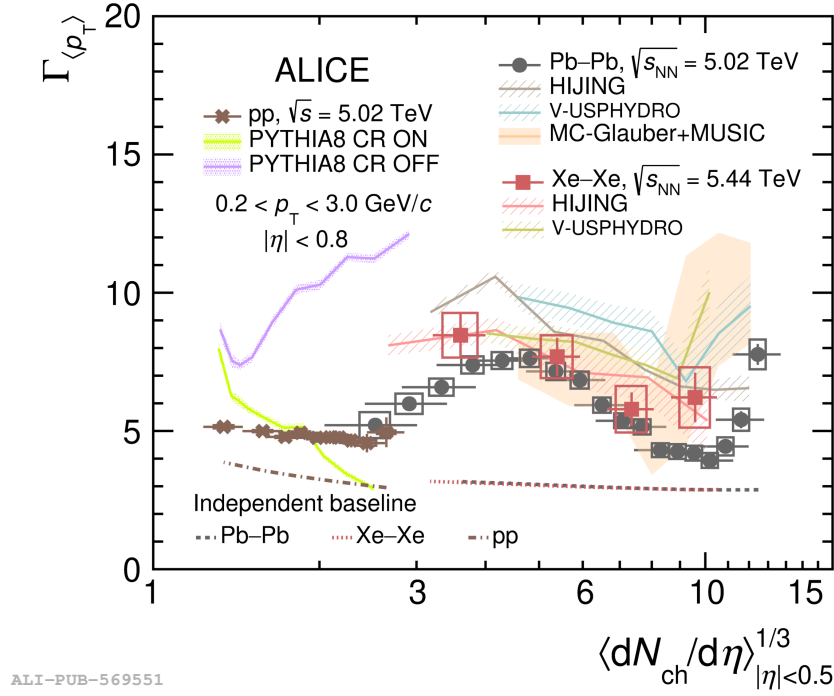


FIGURE 4.10: Intensive skewness $\Gamma_{\langle p_T \rangle}$ of the event-averaged transverse momentum distribution is shown as a function of the cubic root of midrapidity charged-particle density, $\langle dN_{ch}/d\eta \rangle_{|\eta|<0.5}^{1/3}$ in Pb–Pb collisions at $\sqrt{s_{NN}} = 5.02$ TeV, Xe–Xe collisions at $\sqrt{s_{NN}} = 5.44$ TeV and pp collisions at $\sqrt{s} = 5.02$ TeV. Colored bands represent predictions from event generators (PYTHIA8, HIJING) and hydrodynamic simulations (V-USPHYDRO, and MC-Glauber+MUSIC). Statistical and systematic uncertainties are represented by vertical bars and shaded boxes, respectively. Independent baseline calculations for each system are also displayed (dotted lines) for reference. The figure is taken from Ref. [8].

to explain the increase seen from semicentral to central collisions ($9.0 \leq \langle dN_{ch}/d\eta \rangle_{|\eta|<0.5}^{1/3} \leq 12.4$). The rise of both $\gamma_{\langle p_T \rangle}$ and $\Gamma_{\langle p_T \rangle}$ for system sizes above 11 in Pb–Pb collisions may indicate the onset of thermalization [28, 29]. In a nearly thermalized regime, as the medium becomes denser, stronger pressure gradients develop, generating enhanced collective radial flow. This flow shifts the p_T distribution of emitted particles more towards higher p_T , producing a larger $\langle p_T \rangle$. At fixed multiplicity, higher density also corresponds to a smaller geometric overlap and reduced impact-parameter fluctuations, which may contribute to the

observed skewness increase in the most central events [28, 29]. The MC-Glauber+MUSIC hydrodynamic calculations show a similar pattern to the data for $\Gamma_{\langle p_T \rangle}$ in Pb–Pb collisions and fit the data better than the v-USPHYDRO model. Both hydrodynamic models with different initial conditions capture the rise in most central collisions, highlighting the need for further theoretical study to fully explain this effect.

Measurements from pp collisions at $\sqrt{s} = 5.02$ TeV are also presented with their baselines, calculated using p_T spectra from Ref. [30]. Here also, positive intensive skewness above baseline is observed, but the non-monotonic behavior seen in heavy-ion collisions is greatly reduced. Instead, $\Gamma_{\langle p_T \rangle}$ gently decreases as multiplicity grows. In PYTHIA8 simulations, turning off CR causes $\Gamma_{\langle p_T \rangle}$ to increase with multiplicity, contrary to data. Enabling CR improves the description but still does not fully reproduce the measured trend.

In summary, the intensive skewness reveals the combined effects of initial geometry and collective dynamics, with its increase in central collisions indicating emerging thermalization.

4.4.3 Kurtosis

Figure 4.11 shows the kurtosis calculated using Eq. 4.8 as a function of $\langle dN_{\text{ch}}/d\eta \rangle_{|\eta| < 0.5}^{1/3}$, for Pb–Pb collisions at $\sqrt{s_{\text{NN}}} = 5.02$ TeV and Xe–Xe collisions at $\sqrt{s_{\text{NN}}} = 5.44$ TeV. The dotted line marks the Gaussian kurtosis value, which provides a reference for completely independent particle emission. In both Pb–Pb and Xe–Xe systems, the kurtosis decreases as the system size grows and approaches the Gaussian reference near the most central Pb–Pb collisions. When comparing to HIJING model predictions, the model replicates the general downward trend but predicts a steeper decline in kurtosis than observed. This steeper drop is due to HIJING’s inherent system size effect following an approximate $1/N$

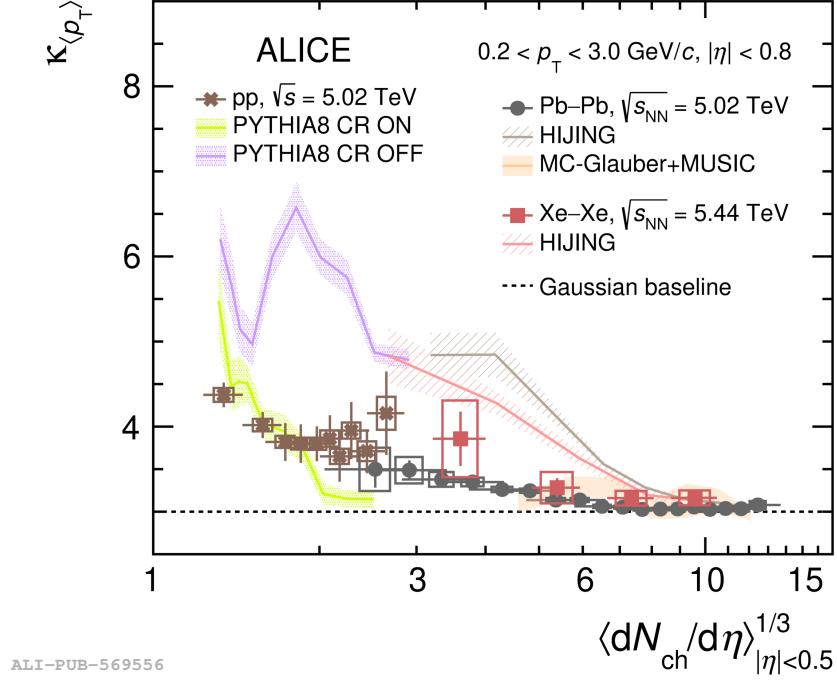


FIGURE 4.11: Kurtosis $\kappa_{\langle p_T \rangle}$ of the event-averaged transverse momentum distribution is shown as a function of the cubic root of midrapidity charged-particle density, $\langle dN_{ch}/d\eta \rangle_{|\eta|<0.5}^{1/3}$ in Pb–Pb collisions at $\sqrt{s_{NN}} = 5.02$ TeV, Xe–Xe collisions at $\sqrt{s_{NN}} = 5.44$ TeV and pp collisions at $\sqrt{s} = 5.02$ TeV. Colored bands represent predictions from event generators (PYTHIA8, HIJING) and hydrodynamic simulation (MC-Glauber+MUSIC). The dashed curve marks the Gaussian expectation for reference. Vertical lines depict statistical uncertainties, with boxes illustrating the systematic error range for each data point. The figure is taken from Ref. [8].

scaling. Over the full multiplicity range, HIJING consistently overestimates the kurtosis compared to the data.

The MC-Glauber+MUSIC hydrodynamic calculations align well with the data from central to semiperipheral collisions, specifically within the $\langle dN_{ch}/d\eta \rangle_{|\eta|<0.5}^{1/3}$ range of 5.4 to 12.4. Additionally, Fig. 4.11 includes measurements from pp collisions at $\sqrt{s} = 5.02$ TeV. Here, kurtosis decreases with multiplicity but remains above the Gaussian baseline even at the highest multiplicity values. PYTHIA8 simulations that incorporate the CR mechanism

reproduce the observed behavior, whereas the version with CR disabled fails to describe the measured kurtosis altogether.

Overall, the kurtosis shows how four-particle correlations weaken with increasing system size, approaching Gaussian behavior in large collisions, and this trend is well described by hydrodynamic models.

4.5 Summary

This work presents the first measurements of higher-order fluctuations of $\langle p_T \rangle$, including skewness and kurtosis, for charged particles produced in Pb–Pb, Xe–Xe, and pp collisions at LHC energies. Two types of skewness, standardized and intensive, have been analyzed using three- and two-particle p_T correlations as a function of the system size, represented by $\langle dN_{\text{ch}}/d\eta \rangle_{|\eta|<0.5}^{1/3}$. The standardized skewness decreases with increasing system size across all collision systems studied. Positive intensive skewness, exceeding the independent particle baseline and consistent with hydrodynamic model expectations from Ref. [3], is observed in both Pb–Pb and Xe–Xe data. This positive trend in intensive skewness is also confirmed in pp collisions at a similar energy.

HIJING model simulations, which do not include hydrodynamic evolution, reproduce the qualitative pattern of intensive skewness within the range $3.8 \leq \langle dN_{\text{ch}}/d\eta \rangle_{|\eta|<0.5}^{1/3} \leq 8.9$ but fail to account for the sharp increase seen in central collisions. This marked rise is captured by hydrodynamic calculations in both v-USPHYDRO and MC-Glauber+MUSIC frameworks. The MC-Glauber+MUSIC model matches the measured values of both standardized and intensive skewness well in the range $4.8 \leq \langle dN_{\text{ch}}/d\eta \rangle_{|\eta|<0.5}^{1/3} \leq 12.4$, while v-USPHYDRO tends to overpredict these measures. The differences between these hydrodynamic models highlight the sensitivity of skewness measurements to details of

the initial collision geometry. Moreover, standardized skewness results from HIJING and MC-Glauber+MUSIC are notably similar, indicating that this observable may primarily respond to initial-state features rather than the details of the system evolution. In pp collisions, PYTHIA8 simulations with color reconnection enabled qualitatively reproduce the experimental results.

Kurtosis, calculated using two- and four-particle p_T correlators, decreases as the system size increases. This trend is qualitatively supported by HIJING calculations in Pb–Pb and Xe–Xe collisions, although the model does not quantitatively match the measurements. Hydrodynamic predictions from MC-Glauber+MUSIC successfully reproduce the centrality-dependent kurtosis in the range $4.8 \leq \langle dN_{ch}/d\eta \rangle_{|\eta|<0.5}^{1/3} \leq 12.4$, with values approaching those expected for a Gaussian distribution. The experimental data converging toward the Gaussian baseline in the most central Pb–Pb collisions, together with agreement from hydrodynamic models, suggests the formation of a locally thermalized medium in these events.

Bibliography

- [1] Piotr Bozek and Wojciech Broniowski. “Transverse-momentum fluctuations in relativistic heavy-ion collisions from event-by-event viscous hydrodynamics”. *Phys. Rev. C* 85 (2012), p. 044910. arXiv: [1203.1810 \[nucl-th\]](#).
- [2] Giuliano Giacalone et al. “Correlation between mean transverse momentum and anisotropic flow in heavy-ion collisions”. *Phys. Rev. C* 103.2 (2021), p. 024909. arXiv: [2004.01765 \[nucl-th\]](#).
- [3] Giuliano Giacalone et al. “Skewness of mean transverse momentum fluctuations in heavy-ion collisions”. *Phys. Rev. C* 103.2 (2021), p. 024910. arXiv: [2004.09799 \[nucl-th\]](#).

- [4] J. Scott Moreland, Jonah E. Bernhard, and Steffen A. Bass. “Alternative ansatz to wounded nucleon and binary collision scaling in high-energy nuclear collisions”. *Phys. Rev. C* 92.1 (2015), p. 011901. arXiv: [1412.4708 \[nucl-th\]](#).
- [5] Jacquelyn Noronha-Hostler et al. “Bulk Viscosity Effects in Event-by-Event Relativistic Hydrodynamics”. *Phys. Rev. C* 88.4 (2013), p. 044916. arXiv: [1305.1981 \[nucl-th\]](#).
- [6] Sergei A. Voloshin. “Mean $p(t)$ fluctuations from two particle and four particle correlations” (June 2002). arXiv: [nucl-th/0206052](#).
- [7] Betty Bezverkhny Abelev et al. “Event-by-event mean p_T fluctuations in pp and Pb-Pb collisions at the LHC”. *Eur. Phys. J. C* 74.10 (2014), p. 3077. arXiv: [1407.5530 \[nucl-ex\]](#).
- [8] Shreyasi Acharya et al. “Skewness and kurtosis of mean transverse momentum fluctuations at the LHC energies”. *Phys. Lett. B* 850 (2024), p. 138541. arXiv: [2308.16217 \[nucl-ex\]](#).
- [9] Xin-Nian Wang and Miklos Gyulassy. “HIJING: A Monte Carlo model for multiple jet production in p p, p A and A A collisions”. *Phys. Rev. D* 44 (1991), pp. 3501–3516.
- [10] Torbjorn Sjöstrand, Stephen Mrenna, and Peter Z. Skands. “PYTHIA 6.4 Physics and Manual”. *JHEP* 05 (2006), p. 026. arXiv: [hep-ph/0603175](#).
- [11] Torbjörn Sjöstrand et al. “An introduction to PYTHIA 8.2”. *Comput. Phys. Commun.* 191 (2015), pp. 159–177. arXiv: [1410.3012 \[hep-ph\]](#).
- [12] René Brun et al. “GEANT Detector Description and Simulation Tool”. *CERN-W5013* (Oct. 1994).
- [13] Shreyasi Acharya et al. “Pseudorapidity distributions of charged particles as a function of mid- and forward rapidity multiplicities in pp collisions at $\sqrt{s} = 5.02, 7$ and 13 TeV”. *Eur. Phys. J. C* 81.7 (2021), p. 630. arXiv: [2009.09434 \[nucl-ex\]](#).
- [14] Xiaofeng Luo et al. “Volume fluctuation and auto-correlation effects in the moment analysis of net-proton multiplicity distributions in heavy-ion collisions”. *J. Phys. G* 40 (2013), p. 105104. arXiv: [1302.2332 \[nucl-ex\]](#).

- [15] Jaroslav Adam et al. “Centrality dependence of the charged-particle multiplicity density at midrapidity in Pb-Pb collisions at $\sqrt{s_{NN}} = 5.02$ TeV”. *Phys. Rev. Lett.* 116.22 (2016), p. 222302. arXiv: [1512.06104 \[nucl-ex\]](#).
- [16] Shreyasi Acharya et al. “Centrality and pseudorapidity dependence of the charged-particle multiplicity density in Xe–Xe collisions at $\sqrt{s_{NN}} = 5.44$ TeV”. *Phys. Lett. B* 790 (2019), pp. 35–48. arXiv: [1805.04432 \[nucl-ex\]](#).
- [17] K. Aamodt et al. “Two-pion Bose-Einstein correlations in central Pb-Pb collisions at $\sqrt{s_{NN}} = 2.76$ TeV”. *Phys. Lett. B* 696 (2011), pp. 328–337. arXiv: [1012.4035 \[nucl-ex\]](#).
- [18] J. Adams et al. “Incident energy dependence of pt correlations at RHIC”. *Phys. Rev. C* 72 (2005), p. 044902. arXiv: [nucl-ex/0504031](#).
- [19] V. Topor Pop et al. “Baryon junction loops and the baryon-meson anomaly at high energies”. *Phys. Rev. C* 70 (2004), p. 064906. arXiv: [nucl-th/0407095](#).
- [20] B. Alver et al. “The PHOBOS Glauber Monte Carlo” (May 2008). arXiv: [0805.4411 \[nucl-ex\]](#).
- [21] Bjoern Schenke, Sangyong Jeon, and Charles Gale. “(3+1)D hydrodynamic simulation of relativistic heavy-ion collisions”. *Phys. Rev. C* 82 (2010), p. 014903. arXiv: [1004.1408 \[hep-ph\]](#).
- [22] Jaroslav Adam et al. “Charged-particle multiplicities in proton–proton collisions at $\sqrt{s} = 0.9$ to 8 TeV”. *Eur. Phys. J. C* 77.1 (2017), p. 33. arXiv: [1509.07541 \[nucl-ex\]](#).
- [23] S. Acharya et al. “Charged-particle multiplicity distributions over a wide pseudorapidity range in proton-proton collisions at $\sqrt{s} = 0.9, 7$, and 8 TeV”. *Eur. Phys. J. C* 77.12 (2017), p. 852. arXiv: [1708.01435 \[hep-ex\]](#).
- [24] Betty Abelev et al. “Multiplicity dependence of the average transverse momentum in pp, p-Pb, and Pb-Pb collisions at the LHC”. *Phys. Lett. B* 727 (2013), pp. 371–380. arXiv: [1307.1094 \[nucl-ex\]](#).
- [25] Torbjorn Sjostrand and Maria van Zijl. “A Multiple Interaction Model for the Event Structure in Hadron Collisions”. *Phys. Rev. D* 36 (1987), p. 2019.

- [26] S. Acharya et al. “Transverse momentum spectra and nuclear modification factors of charged particles in pp, p-Pb and Pb-Pb collisions at the LHC”. *JHEP* 11 (2018), p. 013. arXiv: [1802.09145 \[nucl-ex\]](#).
- [27] Shreyasi Acharya et al. “Transverse momentum spectra and nuclear modification factors of charged particles in Xe-Xe collisions at $\sqrt{s_{NN}} = 5.44$ TeV”. *Phys. Lett. B* 788 (2019), pp. 166–179. arXiv: [1805.04399 \[nucl-ex\]](#).
- [28] Rupam Samanta et al. “Thermalization at the femtoscale seen in high-energy Pb+Pb collisions”. *Phys. Rev. C* 109.5 (2024), p. L051902. arXiv: [2303.15323 \[nucl-th\]](#).
- [29] Rupam Samanta et al. “Non-Gaussian transverse momentum fluctuations from impact parameter fluctuations”. *Phys. Rev. C* 108.2 (2023), p. 024908. arXiv: [2306.09294 \[nucl-th\]](#).
- [30] Shreyasi Acharya et al. “Charged-particle production as a function of multiplicity and transverse sphericity in pp collisions at $\sqrt{s} = 5.02$ and 13 TeV”. *Eur. Phys. J. C* 79.10 (2019), p. 857. arXiv: [1905.07208 \[nucl-ex\]](#).

A.1 Simplification of multi-particle p_T correlators

This section presents the derivation of multi-particle p_T correlators in terms of Q_n moments, as shown in Eqs. 4.3, 4.4, and 4.5. For simplicity, $p_{T,i}$ is represented as p_i in the following equations.

A.1.1 2-particle p_T correlator, $\langle \Delta p_i \Delta p_j \rangle$

From the definition of two-particle p_T correlator, we have

$$\langle \Delta p_i \Delta p_j \rangle = \left\langle \frac{\sum_{i,j,i \neq j}^{N_{ch}} (p_i - \langle \langle p_T \rangle \rangle) (p_j - \langle \langle p_T \rangle \rangle)}{N_{ch}(N_{ch} - 1)} \right\rangle_{ev} \quad (4.10)$$

Simplifying the numerator of $\langle \Delta p_i \Delta p_j \rangle$, we have

$$\begin{aligned} \sum_{i,j,i \neq j}^{N_{\text{ch}}} (p_i - \langle \langle p_T \rangle \rangle) (p_j - \langle \langle p_T \rangle \rangle) &= \sum_{i,j,i \neq j}^{N_{\text{ch}}} p_i p_j - \langle \langle p_T \rangle \rangle \sum_{i,j,i \neq j}^{N_{\text{ch}}} (p_i + p_j) + \langle \langle p_T \rangle \rangle^2 \sum_{i,j,i \neq j}^{N_{\text{ch}}} 1 \\ &= \sum_{i,j,i \neq j}^{N_{\text{ch}}} p_i p_j - 2 \langle \langle p_T \rangle \rangle \sum_{i,j,i \neq j}^{N_{\text{ch}}} p_i + \langle \langle p_T \rangle \rangle^2 \sum_{i,j,i \neq j}^{N_{\text{ch}}} 1 \end{aligned} \quad (4.11)$$

The first term of Eq. 4.11 is

$$\begin{aligned} \sum_{i,j,i \neq j}^{N_{\text{ch}}} p_i p_j &= \sum_i^{N_{\text{ch}}} \sum_j^{N_{\text{ch}}} p_i p_j - \sum_i^{N_{\text{ch}}} p_i^2 \\ &= \sum_i^{N_{\text{ch}}} p_i \sum_j^{N_{\text{ch}}} p_j - \sum_i^{N_{\text{ch}}} p_i^2 \\ &= \left(\sum_i^{N_{\text{ch}}} p_i \right)^2 - \sum_i^{N_{\text{ch}}} p_i^2 \\ &= Q_1^2 - Q_2 \end{aligned} \quad (4.12)$$

and the second term of Eq. 4.11 is

$$\begin{aligned} \sum_{i,j,i \neq j}^{N_{\text{ch}}} p_i &= \sum_i^{N_{\text{ch}}} \sum_j^{N_{\text{ch}}} p_i - \sum_i^{N_{\text{ch}}} p_i \\ &= \sum_i^{N_{\text{ch}}} p_i \sum_j^{N_{\text{ch}}} 1 - \sum_i^{N_{\text{ch}}} p_i \\ &= N_{\text{ch}} \sum_i^{N_{\text{ch}}} p_i - \sum_i^{N_{\text{ch}}} p_i \\ &= (N_{\text{ch}} - 1) \sum_i^{N_{\text{ch}}} p_i \\ &= (N_{\text{ch}} - 1) Q_1 \end{aligned} \quad (4.13)$$

Using Eq. 4.11, Eq. 4.12 and Eq. 4.13 we have

$$\begin{aligned}
& \frac{\sum_{i,j,i \neq j}^{N_{\text{ch}}} (p_i - \langle \langle p_T \rangle \rangle)(p_j - \langle \langle p_T \rangle \rangle)}{N_{\text{ch}}(N_{\text{ch}} - 1)} \\
&= \frac{\sum_{i,j,i \neq j}^{N_{\text{ch}}} p_i p_j - 2\langle \langle p_T \rangle \rangle \sum_{i,j,i \neq j}^{N_{\text{ch}}} p_i + \langle \langle p_T \rangle \rangle^2 \sum_{i,j,i \neq j}^{N_{\text{ch}}} 1}{N_{\text{ch}}(N_{\text{ch}} - 1)} \\
&= \frac{(Q_1^2 - Q_2) - 2\langle \langle p_T \rangle \rangle (N_{\text{ch}} - 1)Q_1 + \langle \langle p_T \rangle \rangle^2 N_{\text{ch}}(N_{\text{ch}} - 1)}{N_{\text{ch}}(N_{\text{ch}} - 1)} \\
&= \frac{Q_1^2 - Q_2}{N_{\text{ch}}(N_{\text{ch}} - 1)} - 2\langle \langle p_T \rangle \rangle \frac{Q_1}{N_{\text{ch}}} + \langle \langle p_T \rangle \rangle^2
\end{aligned} \tag{4.14}$$

Hence,

$$\begin{aligned}
\langle \Delta p_i \Delta p_j \rangle &= \left\langle \frac{\sum_{i,j,i \neq j}^{N_{\text{ch}}} (p_i - \langle \langle p_T \rangle \rangle)(p_j - \langle \langle p_T \rangle \rangle)}{N_{\text{ch}}(N_{\text{ch}} - 1)} \right\rangle_{\text{ev}} \\
&= \left\langle \frac{Q_1^2 - Q_2}{N_{\text{ch}}(N_{\text{ch}} - 1)} \right\rangle_{\text{ev}} - 2\langle \langle p_T \rangle \rangle \left\langle \frac{Q_1}{N_{\text{ch}}} \right\rangle_{\text{ev}} + \langle \langle p_T \rangle \rangle^2 \\
&= \left\langle \frac{Q_1^2 - Q_2}{N_{\text{ch}}(N_{\text{ch}} - 1)} \right\rangle_{\text{ev}} - \left\langle \frac{Q_1}{N_{\text{ch}}} \right\rangle_{\text{ev}}^2
\end{aligned} \tag{4.15}$$

A.1.2 3-particle p_T correlator, $\langle \Delta p_i \Delta p_j \Delta p_k \rangle$

From the definition of three-particle p_T correlator, we have

$$\langle \Delta p_i \Delta p_j \Delta p_k \rangle = \left\langle \frac{\sum_{i,j,k,i \neq j \neq k}^{N_{\text{ch}}} (p_i - \langle \langle p_T \rangle \rangle)(p_j - \langle \langle p_T \rangle \rangle)(p_k - \langle \langle p_T \rangle \rangle)}{N_{\text{ch}}(N_{\text{ch}} - 1)(N_{\text{ch}} - 2)} \right\rangle_{\text{ev}} \tag{4.16}$$

The numerator of $\langle \Delta p_i \Delta p_j \Delta p_k \rangle$ is equal to

$$\begin{aligned}
 & \sum_{\substack{i,j,k \\ i \neq j \neq k}}^{N_{\text{ch}}} (p_i - \langle p_T \rangle)(p_j - \langle p_T \rangle)(p_k - \langle p_T \rangle) \\
 &= \sum_{\substack{i,j,k \\ i \neq j \neq k}}^{N_{\text{ch}}} p_i p_j p_k + \langle p_T \rangle^2 \sum_{\substack{i,j,k \\ i \neq j \neq k}}^{N_{\text{ch}}} (p_i + p_j + p_k) - \langle p_T \rangle \sum_{\substack{i,j,k \\ i \neq j \neq k}}^{N_{\text{ch}}} (p_i p_j + p_j p_k + p_i p_k) \\
 &\quad - \langle p_T \rangle^3 \sum_{\substack{i,j,k \\ i \neq j \neq k}}^{N_{\text{ch}}} 1 \\
 &= \sum_{\substack{i,j,k \\ i \neq j \neq k}}^{N_{\text{ch}}} p_i p_j p_k + 3 \langle p_T \rangle^2 \sum_{\substack{i,j,k \\ i \neq j \neq k}}^{N_{\text{ch}}} p_i - 3 \langle p_T \rangle \sum_{\substack{i,j,k \\ i \neq j \neq k}}^{N_{\text{ch}}} p_i p_j - \langle p_T \rangle^3 \sum_{\substack{i,j,k \\ i \neq j \neq k}}^{N_{\text{ch}}} 1 \\
 &= \sum_{\substack{i,j,k \\ i \neq j \neq k}}^{N_{\text{ch}}} p_i p_j p_k + 3(N_{\text{ch}} - 1)(N_{\text{ch}} - 2) \langle p_T \rangle^2 \sum_i^{N_{\text{ch}}} p_i - 3(N_{\text{ch}} - 2) \langle p_T \rangle \sum_{\substack{i,j \\ i \neq j}}^{N_{\text{ch}}} p_i p_j \\
 &\quad - N_{\text{ch}}(N_{\text{ch}} - 1)(N_{\text{ch}} - 2) \langle p_T \rangle^3
 \end{aligned} \tag{4.17}$$

The first term of Eq. 4.17 can be expanded as

$$\begin{aligned}
 \sum_{\substack{i,j,k \\ i \neq j \neq k}}^{N_{\text{ch}}} p_i p_j p_k &= \sum_{\substack{i \\ i \neq j, i \neq k}}^{N_{\text{ch}}} p_i \sum_{\substack{j,k \\ j \neq k}}^{N_{\text{ch}}} p_j p_k \\
 &= \sum_{i, i \neq j}^{N_{\text{ch}}} p_i \left[\left(\sum_j^{N_{\text{ch}}} p_j \right)^2 - \sum_j^{N_{\text{ch}}} p_j^2 \right] \\
 &= \sum_{i, i \neq j}^{N_{\text{ch}}} p_i \left(\sum_j^{N_{\text{ch}}} p_j \right)^2 - \sum_{i, j, i \neq j}^{N_{\text{ch}}} p_i p_j^2
 \end{aligned} \tag{4.18}$$

Again, the first term of Eq. 4.18 is

$$\sum_{i, i \neq j}^{N_{\text{ch}}} p_i \left(\sum_j^{N_{\text{ch}}} p_j \right)^2 = \left[\sum_i^{N_{\text{ch}}} p_i \left(\sum_j^{N_{\text{ch}}} p_j \right)^2 - \sum_i^{N_{\text{ch}}} p_i^3 - 2 \sum_{i, j, i \neq j}^{N_{\text{ch}}} p_i p_j^2 \right] \tag{4.19}$$

Therefore, Eq. 4.18 reduces to

$$\begin{aligned}
\sum_{\substack{i,j,k \\ i \neq j \neq k}}^{N_{\text{ch}}} p_i p_j p_k &= \left[\sum_i^{N_{\text{ch}}} p_i \left(\sum_j^{N_{\text{ch}}} p_j \right)^2 - \sum_i^{N_{\text{ch}}} p_i^3 - 2 \sum_{i,j,i \neq j}^{N_{\text{ch}}} p_i p_j^2 \right] - \sum_{i,j,i \neq j}^{N_{\text{ch}}} p_i p_j^2 \\
&= \left(\sum_j^{N_{\text{ch}}} p_j \right)^3 - \sum_i^{N_{\text{ch}}} p_i^3 - 3 \left(\sum_{i,j}^{N_{\text{ch}}} p_i p_j^2 - \sum_i^{N_{\text{ch}}} p_i^3 \right) \\
&= \left(\sum_j^{N_{\text{ch}}} p_j \right)^3 + 2 \sum_i^{N_{\text{ch}}} p_i^3 - 3 \sum_i^{N_{\text{ch}}} p_i \sum_j^{N_{\text{ch}}} p_j^2 \\
&= Q_1^3 + 2Q_3 - 3Q_1 Q_2
\end{aligned} \tag{4.20}$$

Using Eq. 4.17, Eq. 4.20 and Eq. 4.12 in Eq. 4.16, finally we have

$$\begin{aligned}
&\langle \Delta p_i \Delta p_j \Delta p_k \rangle \\
&= \left\langle \frac{\sum_{i,j,k,i \neq j \neq k}^{N_{\text{ch}}} (p_i - \langle \langle p_T \rangle \rangle)(p_j - \langle \langle p_T \rangle \rangle)(p_k - \langle \langle p_T \rangle \rangle)}{N_{\text{ch}}(N_{\text{ch}} - 1)(N_{\text{ch}} - 2)} \right\rangle_{\text{ev}} \\
&= \left\langle \frac{Q_1^3 + 2Q_3 - 3Q_1 Q_2}{N_{\text{ch}} - 1)(N_{\text{ch}} - 2)} \right\rangle_{\text{ev}} + 3 \langle \langle p_T \rangle \rangle^2 \left\langle \frac{Q_1}{N_{\text{ch}}} \right\rangle_{\text{ev}} - 3 \langle \langle p_T \rangle \rangle \left\langle \frac{Q_1^2 - Q_2}{N_{\text{ch}}(N_{\text{ch}} - 1)} \right\rangle_{\text{ev}} - \langle \langle p_T \rangle \rangle^3 \\
&= \left\langle \frac{Q_1^3 + 2Q_3 - 3Q_1 Q_2}{N_{\text{ch}} - 1)(N_{\text{ch}} - 2)} \right\rangle_{\text{ev}} + 2 \left\langle \frac{Q_1}{N_{\text{ch}}} \right\rangle_{\text{ev}}^3 - 3 \left\langle \frac{Q_1}{N_{\text{ch}}} \right\rangle_{\text{ev}} \left\langle \frac{Q_1^2 - Q_2}{N_{\text{ch}}(N_{\text{ch}} - 1)} \right\rangle_{\text{ev}}
\end{aligned} \tag{4.21}$$

A.1.3 4-particle p_T correlator, $\langle \Delta p_i \Delta p_j \Delta p_k \Delta p_l \rangle$

From the definition of four-particle p_T correlator, we have

$$\begin{aligned}
&\langle \Delta p_i \Delta p_j \Delta p_k \Delta p_l \rangle \\
&= \left\langle \frac{\sum_{i,j,k,l,i \neq j \neq k \neq l}^{N_{\text{ch}}} (p_i - \langle \langle p_T \rangle \rangle)(p_j - \langle \langle p_T \rangle \rangle)(p_k - \langle \langle p_T \rangle \rangle)(p_l - \langle \langle p_T \rangle \rangle)}{N_{\text{ch}}(N_{\text{ch}} - 1)(N_{\text{ch}} - 2)(N_{\text{ch}} - 3)} \right\rangle_{\text{ev}}
\end{aligned}$$

The numerator of $\langle \Delta p_i \Delta p_j \Delta p_k \Delta p_l \rangle$ can be expanded as

$$\begin{aligned}
 & \sum_{\substack{i,j,k,l \\ i \neq j \neq k \neq l}}^{N_{\text{ch}}} (p_i - \langle \langle p_T \rangle \rangle) (p_j - \langle \langle p_T \rangle \rangle) (p_k - \langle \langle p_T \rangle \rangle) (p_l - \langle \langle p_T \rangle \rangle) \\
 &= \sum_{\substack{i,j,k,l \\ i \neq j \neq k \neq l}}^{N_{\text{ch}}} p_i p_j p_k p_l - \langle \langle p_T \rangle \rangle \sum_{\substack{i,j,k,l \\ i \neq j \neq k \neq l}}^{N_{\text{ch}}} (p_i p_j p_k + p_i p_j p_l + p_i p_k p_l + p_j p_k p_l) \\
 & \quad + \langle \langle p_T \rangle \rangle^2 \sum_{\substack{i,j,k,l \\ i \neq j \neq k \neq l}}^{N_{\text{ch}}} (p_i p_j + p_i p_k + p_i p_l + p_j p_k + p_j p_l + p_k p_l) \\
 & \quad - \langle \langle p_T \rangle \rangle^3 \sum_{\substack{i,j,k,l \\ i \neq j \neq k \neq l}}^{N_{\text{ch}}} (p_i + p_j + p_k + p_l) + \langle \langle p_T \rangle \rangle^4 \sum_{\substack{i,j,k,l \\ i \neq j \neq k \neq l}}^{N_{\text{ch}}} 1
 \end{aligned} \tag{4.22}$$

Therefore,

$$\begin{aligned}
 & \sum_{\substack{i,j,k,l \\ i \neq j \neq k \neq l}}^{N_{\text{ch}}} (p_i - \langle \langle p_T \rangle \rangle) (p_j - \langle \langle p_T \rangle \rangle) (p_k - \langle \langle p_T \rangle \rangle) (p_l - \langle \langle p_T \rangle \rangle) \\
 &= \sum_{\substack{i,j,k,l \\ i \neq j \neq k \neq l}}^{N_{\text{ch}}} p_i p_j p_k p_l - 4 \langle \langle p_T \rangle \rangle \sum_{\substack{i,j,k,l \\ i \neq j \neq k \neq l}}^{N_{\text{ch}}} p_i p_j p_k + 6 \langle \langle p_T \rangle \rangle^2 \sum_{\substack{i,j,k,l \\ i \neq j \neq k \neq l}}^{N_{\text{ch}}} p_i p_j \\
 & \quad - 4 \langle \langle p_T \rangle \rangle^3 \sum_{\substack{i,j,k,l \\ i \neq j \neq k \neq l}}^{N_{\text{ch}}} p_i + \langle \langle p_T \rangle \rangle^4 \sum_{\substack{i,j,k,l \\ i \neq j \neq k \neq l}}^{N_{\text{ch}}} 1 \\
 &= \sum_{\substack{i,j,k,l \\ i \neq j \neq k \neq l}}^{N_{\text{ch}}} p_i p_j p_k p_l - 4 \langle \langle p_T \rangle \rangle (N_{\text{ch}} - 3) \sum_{\substack{i,j,k \\ i \neq j \neq k}}^{N_{\text{ch}}} p_i p_j p_k + 6 \langle \langle p_T \rangle \rangle^2 (N_{\text{ch}} - 3) (N_{\text{ch}} - 2) \sum_{\substack{i,j \\ i \neq j}}^{N_{\text{ch}}} p_i p_j \\
 & \quad - 4 (N_{\text{ch}} - 3) (N_{\text{ch}} - 2) (N_{\text{ch}} - 1) \langle \langle p_T \rangle \rangle^3 \sum_i^{N_{\text{ch}}} p_i + \langle \langle p_T \rangle \rangle^4 (N_{\text{ch}} - 3) (N_{\text{ch}} - 2) (N_{\text{ch}} - 1) N_{\text{ch}}
 \end{aligned} \tag{4.23}$$

The first term of Eq. 4.23 can be simplified as

$$\begin{aligned}
 \sum_{\substack{i,j,k,l \\ i \neq j \neq k \neq l}}^{N_{\text{ch}}} p_i p_j p_k p_l &= \sum_i^{N_{\text{ch}}} p_i \sum_{\substack{j,k \\ j \neq k \neq l}}^{N_{\text{ch}}} p_j p_k p_l \\
 &= \sum_{\substack{i \\ i \neq j, i \neq k}}^{N_{\text{ch}}} p_i \left[\left(\sum_j^{N_{\text{ch}}} p_j \right)^3 + 2 \sum_j^{N_{\text{ch}}} p_j^3 - 3 \sum_{j,k}^{N_{\text{ch}}} p_j p_k^2 \right] \\
 &= \sum_{\substack{i \\ i \neq j}}^{N_{\text{ch}}} p_i \left(\sum_j^{N_{\text{ch}}} p_j \right)^3 + 2 \sum_{\substack{i,j \\ i \neq j}}^{N_{\text{ch}}} p_i p_j^3 - 3 \sum_{\substack{i,j,k \\ i \neq j, i \neq k}}^{N_{\text{ch}}} p_i p_j p_k^2
 \end{aligned} \tag{4.24}$$

Again, the first term of Eq. 4.24 simplifies to

$$\begin{aligned}
 \sum_{\substack{i \\ i \neq j}}^{N_{\text{ch}}} p_i \left(\sum_j^{N_{\text{ch}}} p_j \right)^3 &= \sum_i^{N_{\text{ch}}} p_i \left(\sum_j^{N_{\text{ch}}} p_j \right)^3 - \sum_i^{N_{\text{ch}}} p_i^4 - 3 \sum_{\substack{i,j \\ i \neq j}}^{N_{\text{ch}}} p_i^3 p_j - 3 \sum_{\substack{i,j \\ i \neq j}}^{N_{\text{ch}}} p_i^2 p_j^2 - 3 \sum_{\substack{i,j,k \\ i \neq j \neq k}}^{N_{\text{ch}}} p_i^2 p_j p_k \\
 &= \left(\sum_i^{N_{\text{ch}}} p_i \right)^4 - \sum_i^{N_{\text{ch}}} p_i^4 - 3 \left(\sum_{i,j}^{N_{\text{ch}}} p_i^3 p_j - \sum_i^{N_{\text{ch}}} p_i^4 \right) - 3 \left(\sum_{i,j}^{N_{\text{ch}}} p_i^2 p_j^2 - \sum_i^{N_{\text{ch}}} p_i^4 \right) - 3 \sum_{\substack{i \\ i \neq j \neq k}}^{N_{\text{ch}}} p_i^2 p_j p_k
 \end{aligned} \tag{4.25}$$

The last term of Eq. 4.25 reduces to

$$\begin{aligned}
 \sum_{\substack{i \\ i \neq j \neq k}}^{N_{\text{ch}}} p_i^2 p_j p_k &= \sum_{\substack{i \\ i \neq j, i \neq k}}^{N_{\text{ch}}} p_i^2 \left(\sum_{\substack{j,k \\ j \neq k}}^{N_{\text{ch}}} p_j p_k \right) = \sum_{\substack{i \\ i \neq j, i \neq k}}^{N_{\text{ch}}} p_i^2 \left(\sum_{j,k}^{N_{\text{ch}}} p_j p_k - \sum_j^{N_{\text{ch}}} p_j^2 \right) \\
 &= \sum_{\substack{i \\ i \neq j}}^{N_{\text{ch}}} p_i^2 \left(\sum_j^{N_{\text{ch}}} p_j \right)^2 - \sum_{\substack{i \\ i \neq j}}^{N_{\text{ch}}} p_i^2 p_j^2
 \end{aligned} \tag{4.26}$$

where,

$$\begin{aligned}
 \sum_{i,i \neq j}^{N_{\text{ch}}} p_i^2 \left(\sum_j^{N_{\text{ch}}} p_j \right)^2 &= \sum_i^{N_{\text{ch}}} p_i^2 \left(\sum_j^{N_{\text{ch}}} p_j \right)^2 - \sum_i^{N_{\text{ch}}} p_i^4 - 2 \sum_{i,j,i \neq j}^{N_{\text{ch}}} p_i p_j^3 \\
 &= \sum_i^{N_{\text{ch}}} p_i^2 \left(\sum_j^{N_{\text{ch}}} p_j \right)^2 - \sum_i^{N_{\text{ch}}} p_i^4 - 2 \left(\sum_{i,j}^{N_{\text{ch}}} p_i p_j^3 - \sum_i^{N_{\text{ch}}} p_i^4 \right) \\
 &= \sum_i^{N_{\text{ch}}} p_i^2 \left(\sum_j^{N_{\text{ch}}} p_j \right)^2 + \sum_i^{N_{\text{ch}}} p_i^4 - 2 \sum_{i,j}^{N_{\text{ch}}} p_i p_j^3
 \end{aligned} \tag{4.27}$$

Therefore,

$$\begin{aligned}
 \sum_{i,i \neq j \neq k}^{N_{\text{ch}}} p_i^2 p_j p_k &= \left[\sum_i^{N_{\text{ch}}} p_i^2 \left(\sum_j^{N_{\text{ch}}} p_j \right)^2 + \sum_i^{N_{\text{ch}}} p_i^4 - 2 \sum_{i,j}^{N_{\text{ch}}} p_i p_j^3 \right] - \left(\sum_{i,j}^{N_{\text{ch}}} p_i^2 p_j^2 - \sum_i^{N_{\text{ch}}} p_i^4 \right) \\
 &= \sum_i^{N_{\text{ch}}} p_i^2 \left(\sum_j^{N_{\text{ch}}} p_j \right)^2 + 2 \sum_i^{N_{\text{ch}}} p_i^4 - 2 \sum_{i,j}^{N_{\text{ch}}} p_i p_j^3 - \sum_{i,j}^{N_{\text{ch}}} p_i^2 p_j^2
 \end{aligned} \tag{4.28}$$

So, the first term of Eq. 4.24 finally becomes

$$\begin{aligned}
 \sum_{i,i \neq j}^{N_{\text{ch}}} p_i \left(\sum_j^{N_{\text{ch}}} p_j \right)^3 &= \left(\sum_i^{N_{\text{ch}}} p_i \right)^4 - \sum_i^{N_{\text{ch}}} p_i^4 - 3 \left(\sum_{i,j}^{N_{\text{ch}}} p_i^3 p_j - \sum_i^{N_{\text{ch}}} p_i^4 \right) - 3 \left(\sum_{i,j}^{N_{\text{ch}}} p_i^2 p_j^2 - \sum_i^{N_{\text{ch}}} p_i^4 \right) \\
 &\quad - 3 \left[\sum_i^{N_{\text{ch}}} p_i^2 \left(\sum_j^{N_{\text{ch}}} p_j \right)^2 + 2 \sum_i^{N_{\text{ch}}} p_i^4 - 2 \sum_{i,j}^{N_{\text{ch}}} p_i p_j^3 - \sum_{i,j}^{N_{\text{ch}}} p_i^2 p_j^2 \right] \\
 &= \left(\sum_i^{N_{\text{ch}}} p_i \right)^4 - \sum_i^{N_{\text{ch}}} p_i^4 + 3 \sum_{i,j}^{N_{\text{ch}}} p_i^3 p_j - 3 \sum_i^{N_{\text{ch}}} p_i^2 \left(\sum_j^{N_{\text{ch}}} p_j \right)^2 \\
 &= Q_1^4 - Q_4 + 3Q_3Q_1 - 3Q_1^2Q_2
 \end{aligned} \tag{4.29}$$

Furthermore, the second term of Eq. 4.24 is equal to

$$\sum_{i,j,i \neq j}^{N_{\text{ch}}} p_i p_j^3 = \sum_{i,j}^{N_{\text{ch}}} p_i p_j^3 - \sum_i^{N_{\text{ch}}} p_i^4 = \sum_i^{N_{\text{ch}}} p_i \sum_j^{N_{\text{ch}}} p_j^3 - \sum_i^{N_{\text{ch}}} p_i^4 = Q_1Q_3 - Q_4 \tag{4.30}$$

and, the last term of Eq. 4.24 is equal to

$$\begin{aligned}
 \sum_{\substack{i,j,k \\ i \neq j, i \neq k}}^{N_{\text{ch}}} p_i p_j p_k^2 &= \sum_{i,j,k}^{N_{\text{ch}}} p_i p_j p_k^2 - \sum_{i,j}^{N_{\text{ch}}} p_i^3 p_j - \sum_{i,j}^{N_{\text{ch}}} p_i^2 p_j^2 + \sum_i^{N_{\text{ch}}} p_i^4 \\
 &= \left(\sum_i^{N_{\text{ch}}} p_i \right)^2 \sum_j^{N_{\text{ch}}} p_j^2 - \sum_i^{N_{\text{ch}}} p_i \sum_j^{N_{\text{ch}}} p_j^3 - \left(\sum_i^{N_{\text{ch}}} p_i^2 \right)^2 + \sum_i^{N_{\text{ch}}} p_i^4 \\
 &= Q_1^2 Q_2 - Q_1 Q_3 - Q_2^2 + Q_4
 \end{aligned} \tag{4.31}$$

Eq. 4.24 henceforth reduces to

$$\begin{aligned}
 \sum_{\substack{i,j,k,l \\ i \neq j \neq k \neq l}}^{N_{\text{ch}}} p_i p_j p_k p_l &= (Q_1^4 - Q_4 + 3Q_3 Q_1 - 3Q_1^2 Q_2) + 2(Q_1 Q_3 - Q_4) - 3(Q_1^2 Q_2 - Q_1 Q_3 - Q_2^2 + Q_4) \\
 &= Q_1^4 - 6Q_4 + 8Q_1 Q_3 - 6Q_1^2 Q_2 + 3Q_2^2
 \end{aligned} \tag{4.32}$$

Using Eq. 4.32, Eq. 4.20 and Eq. 4.12 in Eq. 4.23, the numerator of the 4-particle p_T in Eq. 4.22 reduces to

$$\begin{aligned}
 \sum_{\substack{i,j,k,l \\ i \neq j \neq k \neq l}}^{N_{\text{ch}}} (p_i - \langle \langle p_T \rangle \rangle) (p_j - \langle \langle p_T \rangle \rangle) (p_k - \langle \langle p_T \rangle \rangle) (p_l - \langle \langle p_T \rangle \rangle) &= (Q_1^4 - 6Q_4 + 8Q_1 Q_3 - 6Q_1^2 Q_2 + 3Q_2^2) - 4\langle \langle p_T \rangle \rangle (N_{\text{ch}} - 3)(Q_1^3 - 2Q_3 - 3Q_1 Q_2) \\
 &\quad + 6\langle \langle p_T \rangle \rangle^2 (N_{\text{ch}} - 3)(N_{\text{ch}} - 2)(Q_1^2 - Q_2) - 4(N_{\text{ch}} - 3)(N_{\text{ch}} - 2)(N_{\text{ch}} - 1)\langle \langle p_T \rangle \rangle^3 Q_1 \\
 &\quad + \langle \langle p_T \rangle \rangle^4 (N_{\text{ch}} - 3)(N_{\text{ch}} - 2)(N_{\text{ch}} - 1)N_{\text{ch}}
 \end{aligned} \tag{4.33}$$

Therefore, Eq. 4.22 finally leads to

$$\begin{aligned}
 & \langle \Delta p_i \Delta p_j \Delta p_k \Delta p_l \rangle \\
 &= \left\langle \frac{\sum_{i,j,k,l, i \neq j \neq k \neq l}^{N_{\text{ch}}} (p_i - \langle \langle p_T \rangle \rangle) (p_j - \langle \langle p_T \rangle \rangle) (p_k - \langle \langle p_T \rangle \rangle) (p_l - \langle \langle p_T \rangle \rangle)}{N_{\text{ch}}(N_{\text{ch}} - 1)(N_{\text{ch}} - 2)(N_{\text{ch}} - 3)} \right\rangle_{\text{ev}} \\
 &= \left\langle \frac{Q_1^4 - 6Q_1Q_2 + 8Q_1Q_3 - 6Q_1^2Q_2 + 3Q_2^2}{N_{\text{ch}}(N_{\text{ch}} - 1)(N_{\text{ch}} - 2)(N_{\text{ch}} - 3)} \right\rangle_{\text{ev}} - 4\langle \langle p_T \rangle \rangle \left\langle \frac{Q_1^3 - 3Q_2Q_1 + 2Q_3}{N_{\text{ch}}(N_{\text{ch}} - 1)(N_{\text{ch}} - 2)} \right\rangle_{\text{ev}} \\
 &\quad + 6\langle \langle p_T \rangle \rangle^2 \left\langle \frac{Q_1^2 - Q_2}{N_{\text{ch}}(N_{\text{ch}} - 1)} \right\rangle_{\text{ev}} - 4\langle \langle p_T \rangle \rangle^3 \left\langle \frac{Q_1}{N_{\text{ch}}} \right\rangle_{\text{ev}} + \langle \langle p_T \rangle \rangle^4 \\
 &= \left\langle \frac{Q_1^4 - 6Q_1Q_2 + 8Q_1Q_3 - 6Q_1^2Q_2 + 3Q_2^2}{N_{\text{ch}}(N_{\text{ch}} - 1)(N_{\text{ch}} - 2)(N_{\text{ch}} - 3)} \right\rangle_{\text{ev}} - 4 \left\langle \frac{Q_1^3 - 3Q_2Q_1 + 2Q_3}{N_{\text{ch}}(N_{\text{ch}} - 1)(N_{\text{ch}} - 2)} \right\rangle_{\text{ev}} \left\langle \frac{Q_1}{N_{\text{ch}}} \right\rangle_{\text{ev}} \\
 &\quad + 6 \left\langle \frac{Q_1^2 - Q_2}{N_{\text{ch}}(N_{\text{ch}} - 1)} \right\rangle_{\text{ev}} \left\langle \frac{Q_1}{N_{\text{ch}}} \right\rangle_{\text{ev}}^2 - 3 \left\langle \frac{Q_1}{N_{\text{ch}}} \right\rangle_{\text{ev}}^4
 \end{aligned} \tag{4.34}$$

Radial flow using $v_0(p_T)$

Contents

5.1	Introduction and motivation	116
5.2	Observable and methodology	118
5.3	Hydrodynamic predictions	119
5.4	Analysis details	122
5.5	Results and discussions	127
5.6	Summary	155

The study of collective motion within the hot and dense medium created in relativistic heavy-ion collisions offers key insights into the properties of the quark–gluon plasma (QGP). Among various collective phenomena, radial flow refers to the isotropic outward expansion of the medium, which strongly influences the transverse momentum (p_T) spectra of the emitted particles. In this chapter, radial flow is investigated through the observable $v_0(p_T)$, and we present the first measurement of $v_0(p_T)$ for inclusive charged particles, pions, kaons, and protons across different centralities in Pb–Pb collisions at $\sqrt{s_{NN}} = 5.02$ TeV. These measurements provide a new means to study radial flow in a p_T -differential way,

and to probe its dependence on particle mass and collision centrality. The chapter begins with the motivation and definition of the observable, then details the analysis methodology, followed by results and their comparison across particle species and centralities. Finally, the implications of these findings are discussed in the context of hydrodynamic descriptions of heavy-ion collisions.

5.1 Introduction and motivation

Radial flow emerges as a fundamental feature of the collective expansion of the QGP, driven by the system's overall pressure buildup early in the collision evolution. It manifests as a common outward push imparted to all particles. When the system cools to the point of kinetic freeze-out, particles decouple from the medium and their momentum distributions retain the combined imprints of thermal motion and collective expansion. A commonly used framework to describe this stage is the Boltzmann-Gibbs blast-wave model [1], which provides a simplified, hydrodynamics-inspired picture. In this model, the p_T spectra of the emitted particles are governed by two key parameters: the average transverse expansion velocity ($\langle\beta_T\rangle$), which encodes the strength of the collective flow, and the kinetic freeze-out temperature (T_{kin}), which characterizes the thermal conditions of the medium at decoupling. The interplay of these two parameters determines the shape of final p_T spectra of particles. Figure 5.1 demonstrates the impact of these effects on the p_T distributions for pions, kaons, and protons, obtained using the blast-wave model. The dashed blue lines correspond to a scenario without radial flow ($\langle\beta_T\rangle = 0$), leading to steep, thermal-like spectra that fall off rapidly at higher p_T . In contrast, the solid orange lines ($\langle\beta_T\rangle = 0.5$) represent strong radial flow, resulting in noticeably flatter p_T distributions. The effect is especially pronounced for heavier particles, such as protons, which acquire a larger momentum boost from the

collective flow, compared to lighter ones.

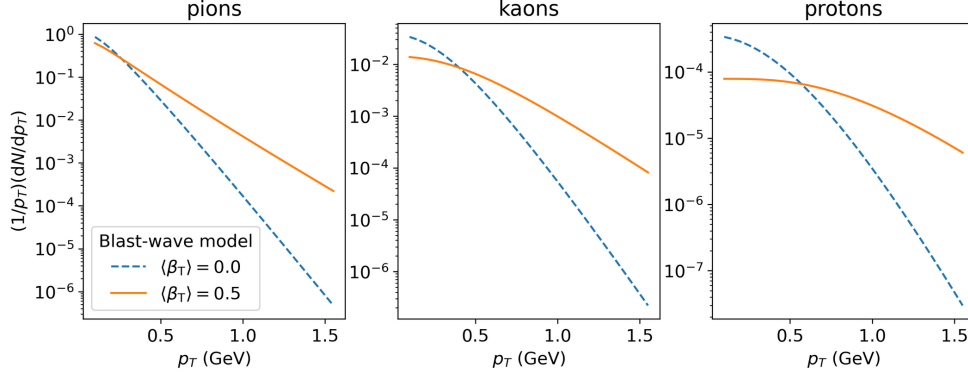


FIGURE 5.1: Blast-wave model predictions for the transverse momentum (p_T) spectra of pions, kaons, and protons, shown for two scenarios: without radial flow ($\langle\beta_T\rangle = 0$, dashed blue line) and with significant radial flow ($\langle\beta_T\rangle = 0.5$, solid orange line).

Traditional methods for characterizing radial flow in experimental data rely on the simultaneous fitting of measured p_T spectra for different hadron species using the blast-wave model [2, 3]. This procedure yields a single, p_T -integrated value of the average transverse expansion velocity ($\langle\beta_T\rangle$) for each centrality class. However, because $\langle\beta_T\rangle$ encapsulates only the overall strength of the radial flow, it does not directly capture p_T -differential phenomena such as the mass ordering of the flow harmonics, $v_n(p_T)$, at low p_T , nor the baryon-meson splitting observed at intermediate p_T . Also, inclusive p_T spectrum analyses do not generally suppress short-range pseudorapidity (η) correlations, which often arise from processes like resonance decays and near-side jets. Such correlations are termed nonflow, as they do not originate from genuine hydrodynamic collective behavior. To address these limitations, the $v_0(p_T)$ observable was developed [4], that emerged as a powerful tool for probing radial flow in a more differential manner. By measuring correlations between event-wise mean p_T and particle yields in individual p_T bins, and suppressing nonflow via η gap, $v_0(p_T)$ enables direct investigation of radial flow features across particle species and collision centralities, that are inaccessible with traditional

methods using p_T spectra.

5.2 Observable and methodology

Following the definition provided in Ref. [4], the observable $v_0(p_T)$ is expressed as

$$v_0(p_T) = \frac{\langle \delta f(p_T) \delta[p_T] \rangle}{\langle f(p_T) \rangle \sigma_{[p_T]}}, \quad (5.1)$$

where angle brackets $\langle \dots \rangle$ denote an average over events and square brackets $[\dots]$ denote an average over particles within a single event. The quantity $f(p_T) = \frac{n(p_T)}{\int_{p_T} n(p_T)}$ represents the fraction of particles in each p_T bin relative to the total number of particles in that event¹, $\delta f(p_T) = f(p_T) - \langle f(p_T) \rangle$ represents the deviation of $f(p_T)$ in that p_T bin from its ensemble average, $[p_T]$ is the event-wise mean p_T , and $\delta[p_T] = [p_T] - \langle [p_T] \rangle$ denotes the deviation of mean p_T of a single event from its ensemble average. The quantity $\sigma_{[p_T]}$ is the standard deviation of the event-wise mean p_T given by

$$\sigma_{[p_T]} = \sqrt{\langle [p_T]^2 \rangle - \langle [p_T] \rangle^2}. \quad (5.2)$$

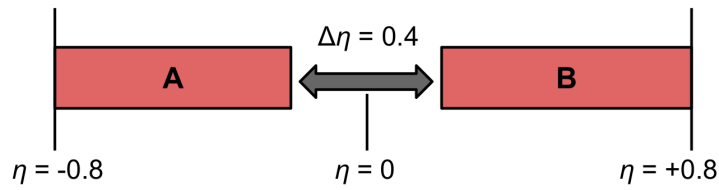


FIGURE 5.2: Schematic illustration of the sub-event method with a pseudorapidity gap ($\Delta\eta = 0.4$). Regions A ($-0.8 < \eta < -0.2$) and B ($0.2 < \eta < 0.8$) are separated to suppress nonflow effects from short-range correlations in the measurement.

To suppress nonflow contributions and better isolate collective effects, the sub-event method is employed in the measurement of $v_0(p_T)$. In this approach, the event is divided

¹Here, $n(p_T)$ is the number of particles in a single event falling into a given p_T bin, and $\int_{p_T} n(p_T)$ denotes the total multiplicity of that event.

into two pseudorapidity regions (sub-events, illustrated in Fig. 5.2), ensuring a sufficient separation in η to reduce short-range correlations, and correlates $f(p_T)$ and mean p_T in distinct η regions using the relation [5] given below

$$v_0(p_T) = \frac{\langle f_A(p_T)[p_T]_B \rangle - \langle f_A(p_T) \rangle \langle [p_T]_B \rangle}{\langle f_A(p_T) \rangle \sigma'_{[p_T]}}, \quad (5.3)$$

where

$$\sigma'_{[p_T]} = \sqrt{\langle [p_T]_A [p_T]_B \rangle - \langle [p_T]_A \rangle \langle [p_T]_B \rangle}. \quad (5.4)$$

In Eq. 5.5, constituent terms are evaluated for all charged particles, and hence the resulting value of $v_0(p_T)$ corresponds to that of inclusive charged particles (often referred as h^\pm). To extend this measurement to identified particle species, the fraction $f_A(p_T)$ should be replaced by $f_{A,s}(p_T)$, where the subscript s denotes the selected species (such as pions, kaons, or protons). The corresponding expression for $v_0(p_T)$ for identified particles becomes

$$v_0(p_T) = \frac{\langle f_{A,s}(p_T)[p_T]_B \rangle - \langle f_{A,s}(p_T) \rangle \langle [p_T]_B \rangle}{\langle f_{A,s}(p_T) \rangle \sigma'_{[p_T]}}, \quad (5.5)$$

where $[p_T]$ and $\sigma'_{[p_T]}$ continue to be computed for the inclusive charged-particles [4].

5.3 Hydrodynamic predictions

Hydrodynamic simulations reveal several distinctive features of $v_0(p_T)$:

(a) The sign of $v_0(p_T)$ varies with transverse momentum—it is negative at low p_T and positive at higher p_T [4, 5]. This behavior stems from the relationship between event-by-event mean- p_T fluctuations and the shape of the particle spectra, as illustrated in Fig. 5.3. Events with an above-average mean p_T (represented by green dashed line) show an enhanced proportion of high- p_T particles and a reduced fraction of low- p_T ones, while the reverse occurs for events with a below-average mean p_T (represented by blue dashed

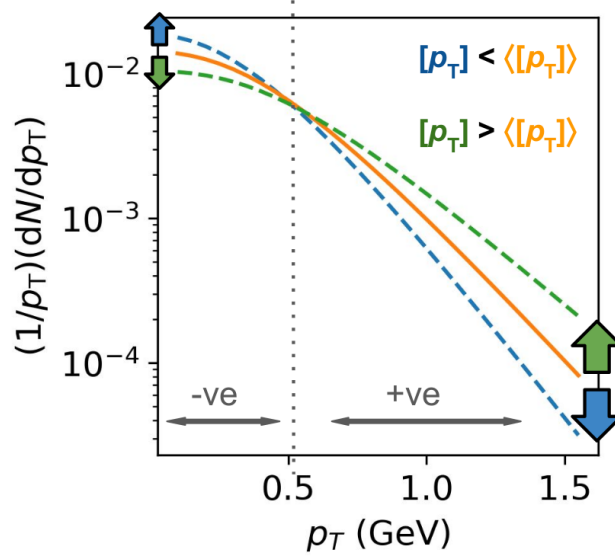


FIGURE 5.3: Illustration of how fluctuations in event-wise mean transverse momentum $[p_T]$ influence the shape of the p_T spectrum. Events with $[p_T] < \langle [p_T] \rangle$ (blue dashed line) and $[p_T] > \langle [p_T] \rangle$ (green dashed line) show opposite changes in particle yields at low and high p_T , resulting in negative and positive correlations in $v_0(p_T)$ respectively.

line). In the former case, $\delta[p_T]$ is positive, and $\delta f(p_T)$ is negative at low p_T but positive at high p_T , resulting in correspondingly negative and positive correlations between these quantities. Conversely, for the latter case with below-average mean p_T , $\delta[p_T]$ is negative, and $\delta f(p_T)$ is positive at low p_T and negative at high p_T , again producing negative and positive correlations but with reversed signs.

This sign-change behavior of $v_0(p_T)$ is also captured in a basic model [4] using exponential p_T spectra of the form $dN/dp_T = (2p_T N) \frac{\exp(-2p_T/[p_T])}{[p_T]^2}$ with fluctuating parameters, N and $[p_T]$. In this model, the analytic result (given in Eq. 5.6) directly illustrates the sign change driven by mean p_T fluctuations ($\sigma_{[p_T]}$).

$$v_0(p_T) \approx 2 \frac{\sigma_{[p_T]}}{\langle [p_T] \rangle} \left(\frac{p_T}{\langle [p_T] \rangle} - 1 \right) \quad (5.6)$$

(b) For identified hadron species, $v_0(p_T)$ exhibits a distinct species-dependent pattern, with a clear mass ordering [4, 5] as shown in Fig. 5.4.

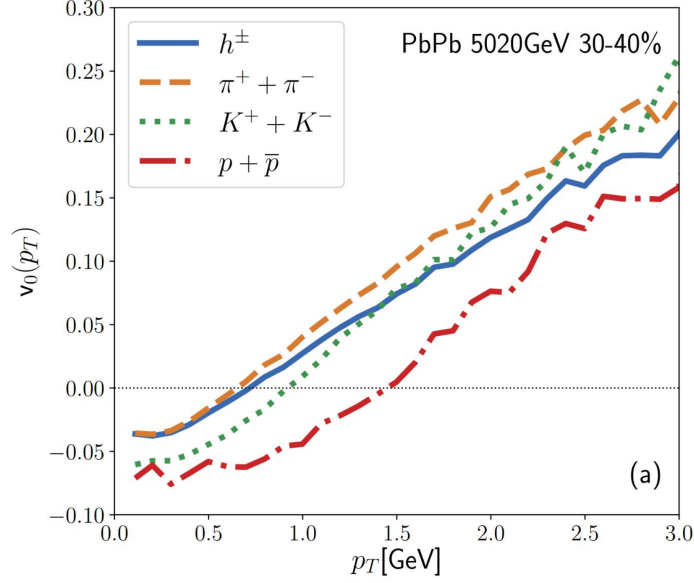


FIGURE 5.4: Transverse momentum dependence of $v_0(p_T)$ for inclusive charged particles (h^\pm), pions ($\pi^+ + \pi^-$), kaons ($K^+ + K^-$), and protons ($p + \bar{p}$) in Pb–Pb collisions at $\sqrt{s_{NN}} = 5.02$ TeV for the 30–40% centrality interval. The figure is taken from Ref. [4].

This behavior can be described by the approximate relation,

$$v_0(p_T) \approx \frac{\sigma_{[p_T]}}{\langle [p_T] \rangle} (p_T - m_T v), \quad (5.7)$$

where v denotes the velocity of the hydrodynamically expanding fluid, and $m_T = \sqrt{p_T^2 + m_0^2}$ is the transverse mass of particle[5]. This equation shows how the particle momentum and mass combine with the fluid velocity to shape $v_0(p_T)$. The mass ordering of $v_0(p_T)$ is similar to that observed for $v_2(p_T)$ and higher-order anisotropic flow harmonics [6–11], underscoring that $v_0(p_T)$ effectively captures hydrodynamic effects in the evolving QGP medium [5, 12–15].

(c) The magnitude of $v_0(p_T)$ exhibits a dependence on event centrality, scaling inversely with the square root of the charged particle density, $(\sqrt{dN_{ch}/d\eta})$ [4]. When normalized by $v_0 = \sigma_{[p_T]}/\langle [p_T] \rangle$, which itself shows a similar inverse scaling, the ratio $v_0(p_T)/v_0$ remains nearly invariant across different system sizes at fixed collision energy [5]. This

universal scaling behavior reduces sensitivity to the absolute magnitude of event-by-event fluctuations, analogous to the scaling observed in normalized anisotropic flow coefficients $v_n(p_T)/v_n$ [16].

(d) In addition, $v_0(p_T)$ provides sensitivity to the bulk properties of the medium, particularly the bulk viscosity and the equation of state of QCD matter [5, 17]. Since it reflects the radial expansion dynamics of the system, its response to bulk viscosity effects is more pronounced, while the influence of shear viscosity is negligible [5]. This makes $v_0(p_T)$ a complementary observable to anisotropic flow coefficients, offering an additional handle to constrain the thermodynamic and transport properties of the QGP.

5.4 Analysis details

This section outlines the key aspects of the analysis procedure used to extract $v_0(p_T)$ from experimental data. We start by assessing the purity of the selected particle samples. Next, we investigate how varying the pseudorapidity gap influences the measured observable. Because $v_0(p_T)$ is insensitive to tracking and particle-identification (PID) inefficiencies, no efficiency corrections are necessary. To verify the robustness of the observable, we perform Monte Carlo (MC) closure tests. Finally, we detail the various sources of systematic uncertainty and quantify their impact on the measurements.

5.4.1 Purity of selected particles

Accurate identification of particle species is essential for reliable measurement of $v_0(p_T)$. A key quantity in this context is the purity, which measures the fraction of correctly identified particles within a selected sample; higher purity values indicate reduced contamination from misidentified species. The purity is calculated as a function of p_T , and is defined

as the ratio of the number of correctly identified particles to the total number of particles selected by the PID procedure. Figure 5.5 presents the p_T -dependent purity for pions (top left), kaons (top right), and protons (bottom) in Pb–Pb collisions at $\sqrt{s_{NN}} = 5.02$ TeV, within the kinematic acceptance used in the analysis. The results indicate excellent PID performance: the purity exceeds 98% in $0.2 < p_T < 6.0$ GeV/ c , and 97% for protons in $0.4 < p_T < 6.0$ GeV/ c . For kaons, the purity remains above 95% up to $p_T = 4.0$ GeV/ c , and is close to 90% in the range $4.0 < p_T < 6.0$ GeV/ c .

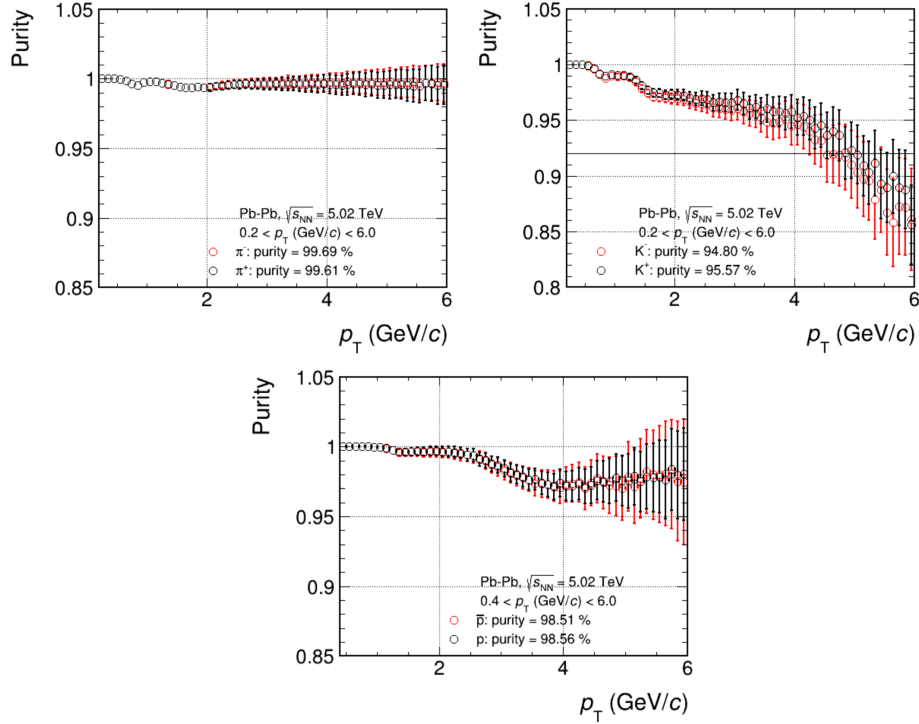


FIGURE 5.5: Purity as a function of transverse momentum (p_T) for identified pions (top left), kaons (top right), and protons (bottom) in Pb–Pb collisions at $\sqrt{s_{NN}} = 5.02$ TeV. Results are shown separately for particles and antiparticles, selected within the acceptance $|\eta| < 0.8$ and $0.2 < p_T < 6.0$ GeV/ c . The values, greater than 0.9 for kaons and close to 1 for pions, and protons, indicate high sample purity for all particle species across the measured p_T intervals. Average purity values for each species are also noted in the panels.

5.4.2 Effect of pseudorapidity-gap variation

A careful treatment of short-range correlations (nonflow effects) is important in order to reliably separate them from the long-range collective contributions to $v_0(p_T)$. Such correlations, originating from processes like resonance decays, near-side jets, and other few-particle interactions, are typically confined within limited pseudorapidity (η) intervals. To explore their possible impact, the dependence of $v_0(p_T)$ on the pseudorapidity gap ($\Delta\eta$) has been studied for different collision centralities. Figure 5.6 shows $v_0(p_T)$ for inclusive charged particles as a function of p_T with varying η -gap sizes ($\Delta\eta$ ranging from 0 to 1 in steps of 0.2) across three centrality intervals. For $p_T < 3$ GeV/c, the variation with

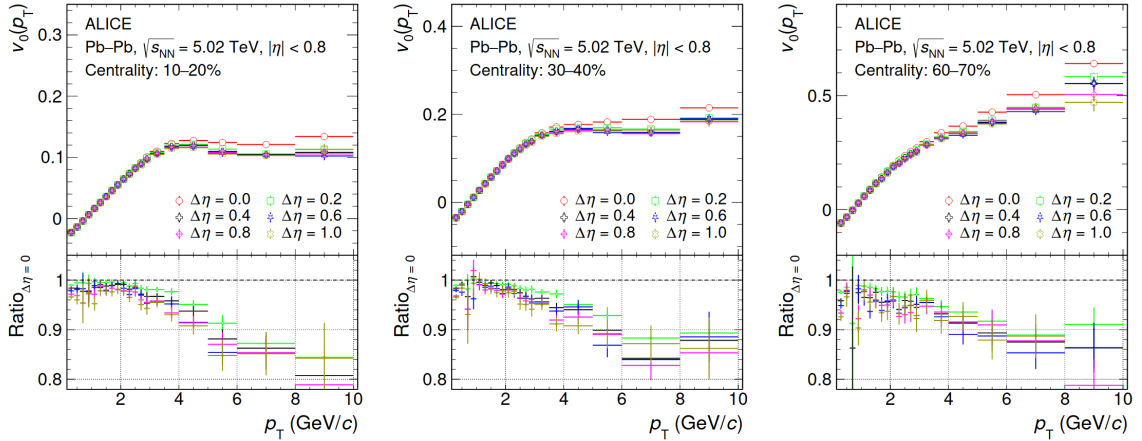


FIGURE 5.6: Dependence of $v_0(p_T)$ on the pseudorapidity gap ($\Delta\eta$) for inclusive charged particles in Pb–Pb collisions at $\sqrt{s_{\text{NN}}} = 5.02$ TeV, shown for three centrality intervals: 10–20%, 30–40%, and 60–70%. Top panels display $v_0(p_T)$ for various $\Delta\eta$ values, while bottom panels present the ratio with respect to zero gap ($\Delta\eta = 0$), illustrating the suppression of nonflow effects with the inclusion of η -gap, across different centralities. The figure is taken from Ref. [18].

respect to $\Delta\eta = 0$ is relatively small, within about 2% in central and semicentral collisions, and up to 8% in peripheral events. At higher p_T , differences of up to 15% are observed between results with and without an η -gap in the peripheral collisions. Beyond $\Delta\eta = 0.2$, the results become largely independent of gap size, motivating the choice of $\Delta\eta = 0.4$ as

the default analysis setting. Variations with $\Delta\eta$ equals to 0.5 and 0.6 are used to estimate related systematic uncertainties.

5.4.3 Monte Carlo closure of $v_0(p_T)$

To verify that the observable $v_0(p_T)$ is not influenced by detector effects such as tracking and PID efficiencies, a MC closure test was carried out. Events were generated using the HIJING model [19, 20], and particle transport through the ALICE detector was simulated with GEANT3 [21]. The simulated detector signals were then processed and reconstructed using the same methods applied to the real experimental data. Figure 5.7 compares $v_0(p_T)$ obtained from the original generated events with that from the reconstructed events for inclusive charged particles across three centrality classes. The close agreement within uncertainties shows that detector inefficiencies do not introduce significant bias in measuring $v_0(p_T)$. Although statistical fluctuations are noticeable, the strong correlation between the generated and reconstructed results supports the robustness of this closure test.

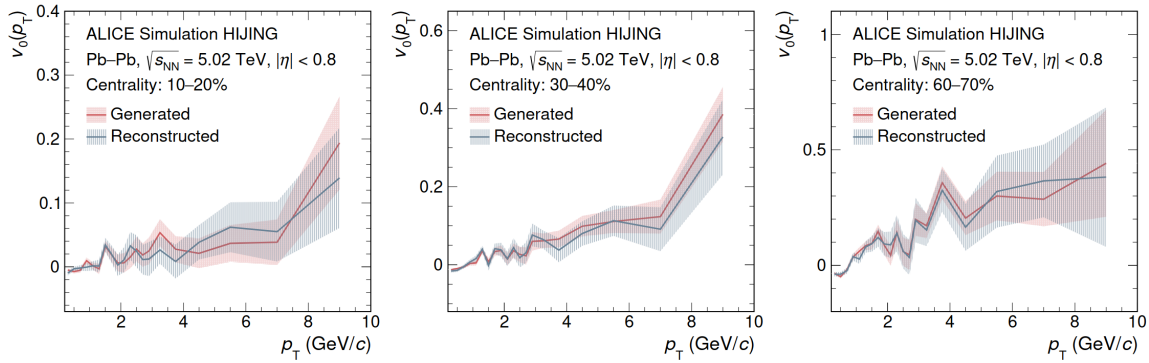


FIGURE 5.7: Comparison of $v_0(p_T)$ obtained from generated events and corresponding reconstructed ones for inclusive charged particles in Pb–Pb collisions at $\sqrt{s_{NN}} = 5.02$ TeV, simulated with HIJING and ALICE detector modeling. Results are shown for three centrality intervals (10–20%, 30–40%, and 60–70%). The close agreement between generated and reconstructed values across all centrality classes demonstrates that detector effects do not significantly bias the measurement of $v_0(p_T)$. The figure is taken from Ref. [18].

5.4.4 Systematic uncertainty

The evaluation of systematic uncertainties in $v_0(p_T)$ follows the standard ALICE methodology for flow and fluctuation measurements. Systematic sources are quantified by varying event selection, track selection, and particle identification (PID) criteria, as detailed in Chapter 3. For each centrality interval and particle species, the uncertainties are computed as a function of p_T . Key sources include adjustments to vertex position cuts, pileup rejection, centrality determination, track quality criteria, and pseudorapidity-gap size. To address uncertainties in centrality estimation, centrality classes are redefined based on the charged-particle multiplicity distribution measured at midrapidity [22]. PID uncertainties are estimated by varying the identification probability thresholds. Individual contributions are considered statistically independent and combined in quadrature to obtain the total systematic uncertainty for each p_T bin. A decomposition into correlated and uncorrelated components is not performed, as this level of detail is not required for the present analysis and is consistent with procedures used in previous flow measurements.

While every effort has been made to ensure a careful and comprehensive evaluation of systematic effects, it is acknowledged that such estimates may still be subject to residual or unaccounted sources of uncertainty. The methodology adopted here aims to be as rigorous and transparent as possible, consistent with ALICE standards, and may be further refined as future analyses benefit from improved detector understanding, upgraded calibration techniques, and higher-statistics data sets.

The resulting systematic uncertainties (absolute values) for inclusive charged hadrons, pions, kaons, and protons are shown in Figs. 5.8–5.11 as a function of p_T for centrality classes 10–20%, 30–40%, and 60–70%. For all particle species, the total uncertainty slightly increases with p_T and tends to be larger in more peripheral collisions. While

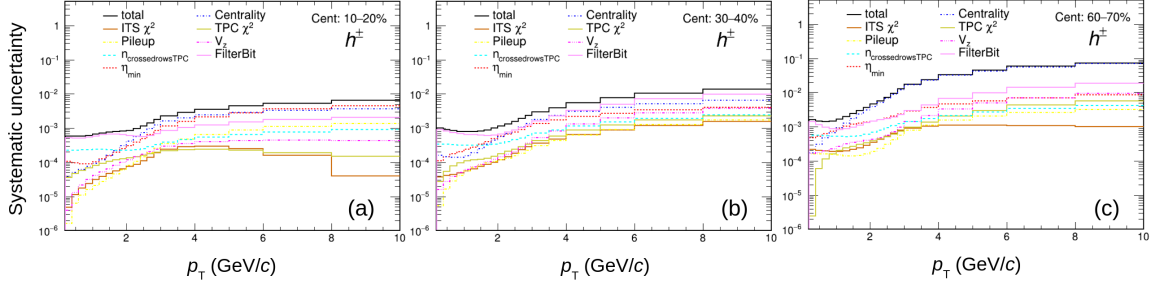


FIGURE 5.8: Systematic uncertainties (absolute value) in the measurement of $v_0(p_T)$ for inclusive charged particles as a function of p_T in three centrality classes (10–20%, 30–40%, and 60–70%). The contributions from individual sources, including centrality estimation, pileup rejection, tracking quality cuts (fit of TPC χ^2 , ITS χ^2 , filter bit selection that controls DCA, TPC crossed rows), primary vertex position (V_z), minimum pseudorapidity-gap (η_{\min}), and the total combined uncertainty, are shown separately.

uncertainties from centrality determination and variation of track DCA dominate for inclusive charged hadrons, PID-related contributions become significant for identified particles, particularly pions. The centrality-related uncertainties are largest in the 60–70% interval, primarily due to the reduced particle multiplicity, which leads to poorer centrality resolution and consequently larger event classification fluctuations. Overall, the systematic uncertainties remain sufficiently small to ensure robustness of the physics conclusions drawn from the data. For instance, in the 30–40% centrality interval, the p_T -averaged total systematic uncertainties are approximately 3.8% for inclusive charged particles, 17.7% for pions, 13.9% for kaons, and 16.2% for protons.

5.5 Results and discussions

5.5.1 $v_0(p_T)$ measurements

Figure 5.12 shows the centrality dependence of $v_0(p_T)$ for inclusive charged particles in three representative centrality intervals: 10–20% (central), 30–40% (semicentral), and 60–70% (peripheral). Across all centralities, $v_0(p_T)$ is found to be negative for p_T below

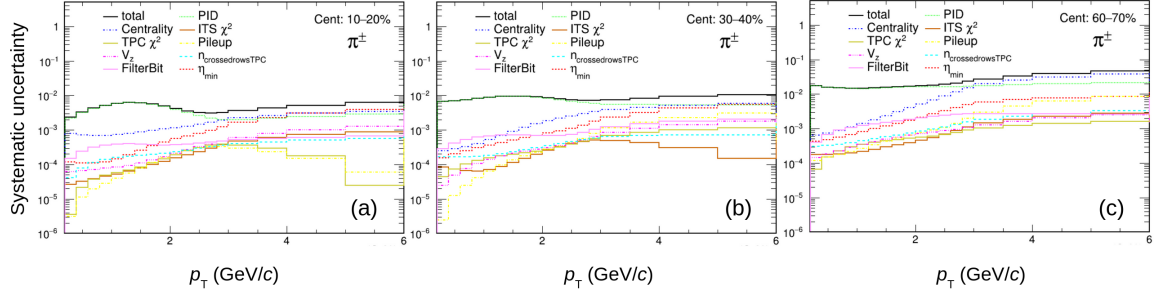


FIGURE 5.9: Systematic uncertainties (absolute value) in the measurement of $v_0(p_T)$ for pions as a function of p_T in three centrality classes (10–20%, 30–40%, and 60–70%). The contributions from individual sources, including centrality estimation, pileup rejection, tracking quality cuts (fit of TPC χ^2 , ITS χ^2 , filter bit selection that controls DCA, TPC crossed rows), primary vertex position (V_z), particle identification (PID), minimum pseudorapidity-gap (η_{min}), and the total combined uncertainty, are shown separately.

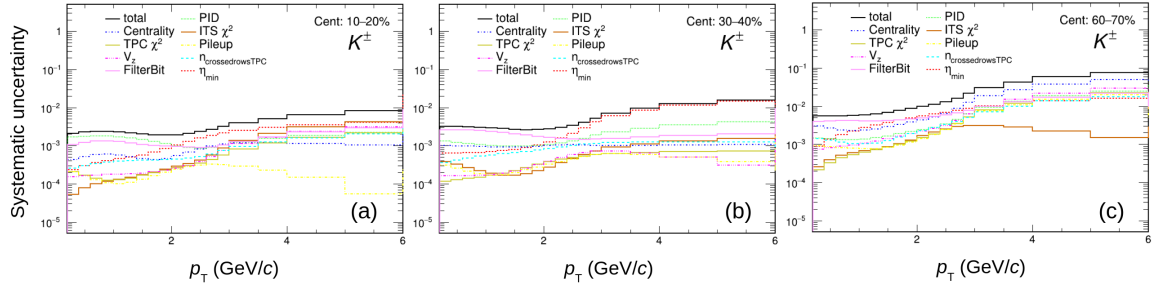


FIGURE 5.10: Systematic uncertainties (absolute value) in the measurement of $v_0(p_T)$ for kaons as a function of p_T in three centrality classes (10–20%, 30–40%, and 60–70%). The contributions from individual sources, including centrality estimation, pileup rejection, tracking quality cuts (fit of TPC χ^2 , ITS χ^2 , filter bit selection that controls DCA, TPC crossed rows), primary vertex position (V_z), particle identification (PID), minimum pseudorapidity-gap (η_{min}), and the total combined uncertainty, are shown separately.

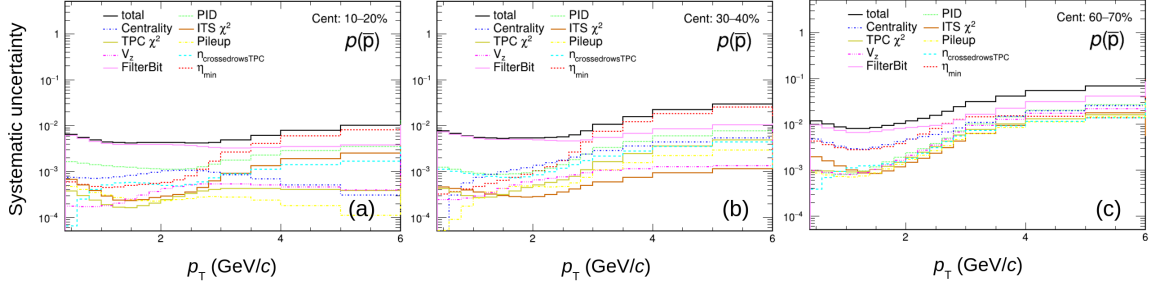


FIGURE 5.11: Systematic uncertainties (absolute value) in the measurement of $v_0(p_T)$ for protons as a function of p_T in three centrality classes (10–20%, 30–40%, and 60–70%). The contributions from individual sources, including centrality estimation, pileup rejection, tracking quality cuts (fit of TPC χ^2), ITS χ^2 , filter bit selection that controls DCA, TPC crossed rows), primary vertex position (V_z), particle identification (PID), minimum pseudorapidity-gap (η_{\min}), and the total combined uncertainty, are shown separately.

0.8 GeV/c, reflecting an anti-correlation between event-by-event fluctuations in mean p_T and p_T spectra of particles, as discussed in Sec. 5.3. As p_T increases up to 4.0 GeV/c, $v_0(p_T)$ rises approximately linearly, with the slope becoming steeper from central to more peripheral collisions. This behavior is consistent with the theoretical predictions [4], and can be attributed to the growing magnitude of mean- p_T fluctuations when moving from more central to peripheral collisions (see Eq. 5.6). Beyond $p_T = 4.0$ GeV/c, the linear rise in $v_0(p_T)$ weakens, particularly in central and semicentral collisions, whereas peripheral collisions exhibit a more gradual change.

To interpret these trends, comparisons are made with results from the hydrodynamic framework of IP-Glasma+MUSIC+UrQMD, which reliably reproduces several ALICE experimental measurements, including multiplicity, mean p_T , and flow coefficients [23] as shown in Appendix. This state-of-the-art framework models the full evolution of the collision system, starting from fluctuating initial conditions provided by IP-Glasma [24], which encodes gluon saturation effects and early-time energy density fluctuations, through the viscous hydrodynamic expansion simulated by MUSIC [25], and finally the hadronic rescat-

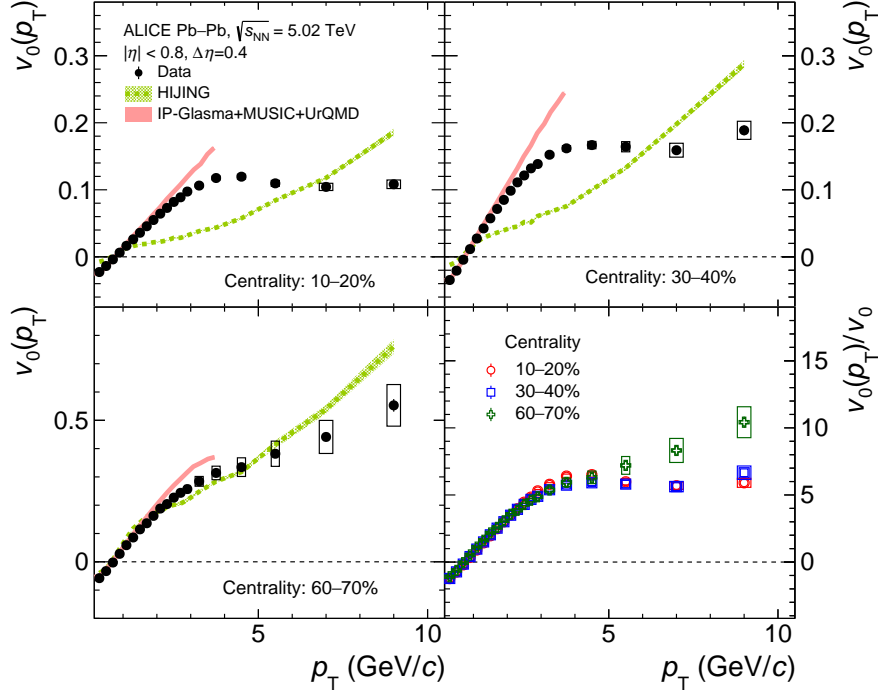


FIGURE 5.12: Transverse momentum dependence of $v_0(p_T)$ for inclusive charged particles in Pb–Pb collisions at $\sqrt{s_{NN}} = 5.02$ TeV. The measurements for three centrality intervals 10–20% (top-left), 30–40% (top-right), and 60–70% (bottom-left) are compared to expectations from HIJING [19] and IP-Glasma+MUSIC+UrQMD [23] models. The bottom right panel presents the normalized ratio $v_0(p_T)/v_0$ as a function of p_T for the three centrality intervals. Statistical uncertainties are shown as bars and systematic uncertainties as boxes. The figure is taken from Ref. [18].

tering and freeze-out phase handled by UrQMD [26, 27]. The inclusion of temperature-dependent transport coefficients, such as the specific shear and bulk viscosities, allows the model to realistically capture the dynamic response of the medium, while the equation of state based on lattice QCD calculations [28] ensures a faithful representation of the phase transition from quark-gluon plasma to hadronic matter. Across all centralities, the model accurately reproduces the data at low p_T ($p_T < 2.0$ GeV/c), where collective flow governs particle emission patterns. In this regime, the observed momentum correlations arise naturally from the hydrodynamic expansion of the system, that convert initial spatial energy

density fluctuations into collective outward motion. However, at higher p_T , deviations between model predictions and experimental data arise, indicating that hydrodynamics alone may not fully capture all relevant physics in this region. Effects such as jet-medium interactions and other non-collective processes are likely to play an increasingly important role [29, 30].

In addition to hydrodynamic calculations, comparisons are made with the HIJING model [19, 20] to provide a baseline for non-collective particle production. HIJING accounts for processes such as mini-jet production, resonance decays, and nuclear shadowing but does not include collective flow dynamics. It qualitatively reproduces high- p_T particle yields originating from initial hard scatterings, but underestimates the particle yields and average transverse momentum at low p_T due to the absence of flow. As a result, HIJING completely fails to describe the behavior of $v_0(p_T)$ in central and semicentral collisions, particularly at low p_T where the collective expansion of the medium is a dominant effect. In contrast, for peripheral collisions characterized by smaller system size and lower energy density, HIJING successfully captures the general trends and magnitude of the data up to high p_T , indicating a stronger influence of hard scatterings and jet production in these conditions.

The scaled observable $v_0(p_T)/v_0$ is shown as a function of p_T for the three centrality intervals in the bottom right panel of Fig. 5.12. In central and semicentral collisions, the data points converge onto a single curve, demonstrating that the normalization by v_0 effectively cancels the centrality-dependent variation of $v_0(p_T)$. This trend also agrees with the theoretical expectations discussed in Sec. 5.3. However, for peripheral collisions, slight deviations from this scaling become apparent at $p_T > 5$ GeV/c, signaling a growing impact of processes beyond collective flow, such as back-to-back jet production and mini-jet fragmentation. The qualitatively similar trends observed between the data and HIJING

model predictions in this regime further support the interpretation that non-collective effects contribute significantly to the observed deviations.

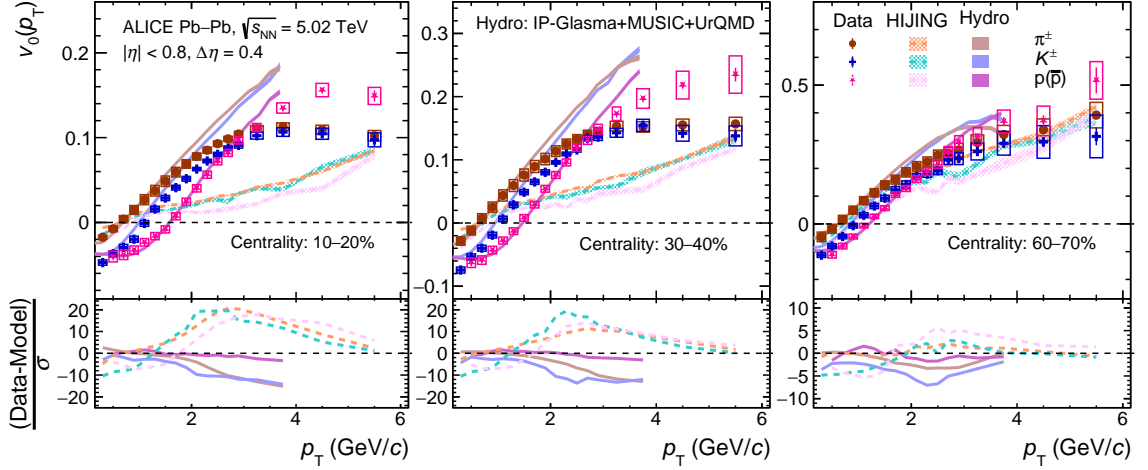


FIGURE 5.13: Transverse momentum dependence of $v_0(p_T)$ for pions (π^\pm), kaons (K^\pm), and protons ($p(\bar{p})$) in Pb–Pb collisions at $\sqrt{s_{NN}} = 5.02$ TeV. Measurements for three centrality intervals, 10–20% (left), 30–40% (middle), and 60–70% (right), are compared with HIJING [19] and IP-Glasma+MUSIC+UrQMD [23] models. Statistical uncertainties are shown as bars and systematic uncertainties as boxes. The lower panels present the normalized difference between data and models, $(\text{Data}-\text{Model})/\sigma$. The figure is taken from Ref. [18].

Figure 5.13 presents the variation of $v_0(p_T)$ with p_T up to 6 GeV/c for pions, kaons, and protons across three centrality classes. The overall p_T dependence of individual hadron species closely follows that seen for inclusive charged hadrons. At low p_T (below 3 GeV/c), a clear mass ordering is observed with heavier particles exhibiting smaller values of $v_0(p_T)$, i.e., $v_0(p_T)^{\text{pions}} > v_0(p_T)^{\text{kaons}} > v_0(p_T)^{\text{protons}}$. This behavior is consistent with the predictions from hydrodynamic calculations, reflecting the collective hydrodynamic expansion of the medium [5, 14, 15]. Above $p_T = 3$ GeV/c, protons exhibit a larger $v_0(p_T)$ than pions and kaons, which themselves are consistent within uncertainties. This behavior is analogous to the baryon-meson splitting observed for anisotropic flow coefficients at RHIC and LHC [7–

11]. and suggests quark recombination as the dominant particle production mechanism at intermediate p_T . The splitting is strongest in central (10–20%) and negligible in peripheral (60–70%) collisions, which may reflect system-size effects—with larger, denser systems favoring recombination and smaller ones being dominated by fragmentation [31].

The measurements for the three hadron species are also compared with hydrodynamic model predictions. The IP-Glasma+MUSIC+UrQMD model successfully reproduces the observed mass-dependence of $v_0(p_T)$ across all centralities, with protons described accurately up to about 3 GeV/c. Kaons and pions data are described up to approximately 2 GeV/c and 1.5 GeV/c, respectively, beyond which deviations become increasingly significant. In contrast, the HIJING model fails to capture essential features of the data: it neither reproduces the characteristic mass ordering due to collective flow nor the baryon-meson separation at higher p_T . For peripheral collisions, HIJING qualitatively matches the pion trend but overestimates for kaons and protons, especially at low p_T .

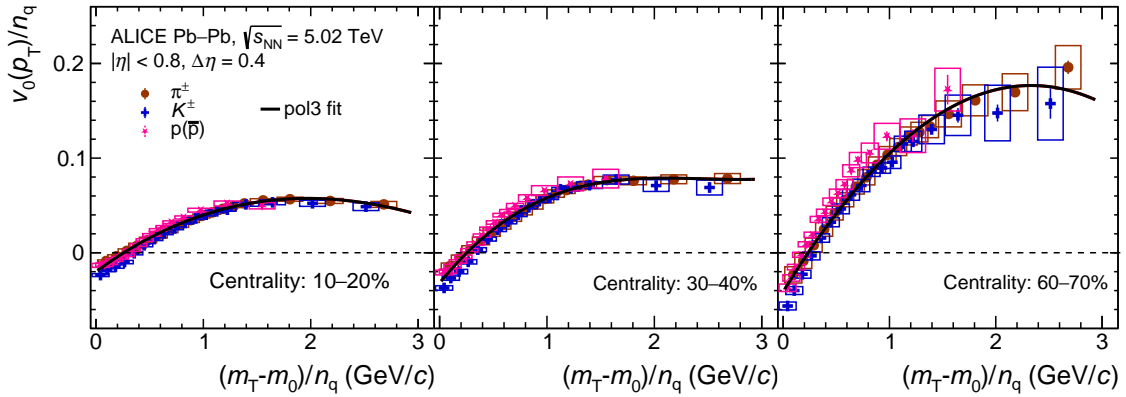


FIGURE 5.14: The $v_0(p_T)$ values for pions (π^\pm), kaons (K^\pm), and protons ($p(\bar{p})$) are scaled by the number of constituent quarks (n_q), and displayed as a function of transverse kinetic energy per constituent quark, $(m_T - m_0)/n_q$, measured in Pb–Pb collisions at $\sqrt{s_{NN}} = 5.02$ TeV. The results are presented for three centrality intervals: 10–20% (left), 30–40% (middle), and 60–70% (right). The solid curve shows a smooth cubic fit to the pion data, providing a clear representation of the overall trend. The figure is taken from Ref. [18].

When $v_0(p_T)$ is scaled by the number of constituent quarks (n_q) and plotted against the transverse kinetic energy per quark, $(m_T - m_0)/n_q$, the results from all particle species approximately converge onto a single curve, as shown in Fig. 5.14, demonstrating the quark number scaling (NCQ scaling) behavior. This scaling is a signature of partonic collectivity—indicating that the quarks were flowing collectively before hadronization and subsequently combine (recombine) into hadrons, preserving this flow pattern.

5.5.2 Sensitivity to transport and thermodynamic properties

In this section, we illustrate the sensitivity of $v_0(p_T)$ to transport coefficients of QGP medium, QCD equation of state (EOS), and initial conditions of heavy-ion collisions, using the measurements for the representative centrality interval, 10–20%. The data shown in the Figs. 5.15, 5.16, and 5.19, correspond to the same measurements presented in the top-left panel of Fig. 5.12, but zoomed in on the low- p_T region.

A comparison of $v_0(p_T)$ for charged hadrons (h^\pm) against hydrodynamic model predictions under three different scenarios: (a) both shear viscosity (η/s) and bulk viscosity (ζ/s) vary with temperature, (b) temperature-dependent η/s with $\zeta/s = 0$, and (c) constant $\eta/s = 0.6$ with $\zeta/s = 0$, is shown in Fig. 5.15. Scenario (a) uses the identical model setup as in Figs. 5.12 and 5.13. The temperature dependence of η/s and ζ/s over the 150–400 MeV range is detailed in Refs. [23, 32, 33]. Notably, scenarios (b) and (c), both with $\zeta/s = 0$, yield similar $v_0(p_T)$ predictions despite differing treatments of η/s (one is a temperature dependent function and other is constant). In contrast, scenario (a), which includes temperature-dependent bulk viscosity ζ/s , shows a distinct deviation. This highlights that $v_0(p_T)$ is predominantly sensitive to ζ/s , unlike other observables such as v_n coefficients and p_T -spectra, which respond to both shear and bulk viscosities. The underlying reason behind the sensitivity of $v_0(p_T)$ to ζ/s is that ζ/s controls the system's

resistance to isotropic expansion, affecting the development of radial flow. Hydrodynamic calculations incorporating temperature-dependent ζ/s provide a better description of the data at low p_T , while the behavior at higher p_T (above 1.2 GeV/c) suggests the need for further theoretical improvements.

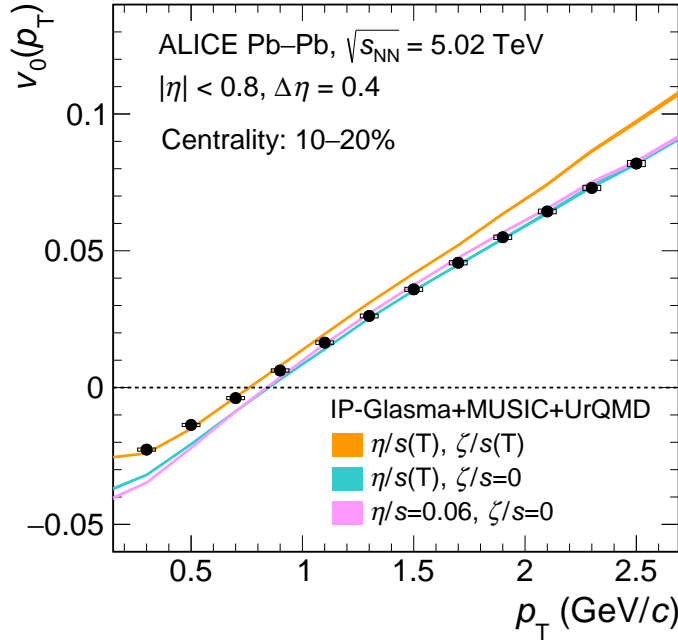


FIGURE 5.15: Transverse momentum dependence of $v_0(p_T)$ of inclusive charged particles in 10–20% central Pb–Pb collisions at $\sqrt{s_{NN}} = 5.02$ TeV, compared to IP-Glasma+MUSIC+UrQMD [23] calculations for variations in transport coefficients, η/s and ζ/s . Statistical (systematic) uncertainties are represented by vertical bars (boxes). The statistical uncertainties are also smaller than the marker size and thus not visible. The figure is taken from Ref. [18].

Figure 5.16 presents a comparison between the same experimental measurements and hydrodynamic model predictions employing three different equation of state (EOS) parametrizations: EOS1, EOS2, and the lattice QCD (LQCD)-based EOS [28] (represented by the orange curve in the left panel). EOS1 and EOS2 are constructed for QCD matter at zero net-baryon density using a Gaussian Process Regression model constrained

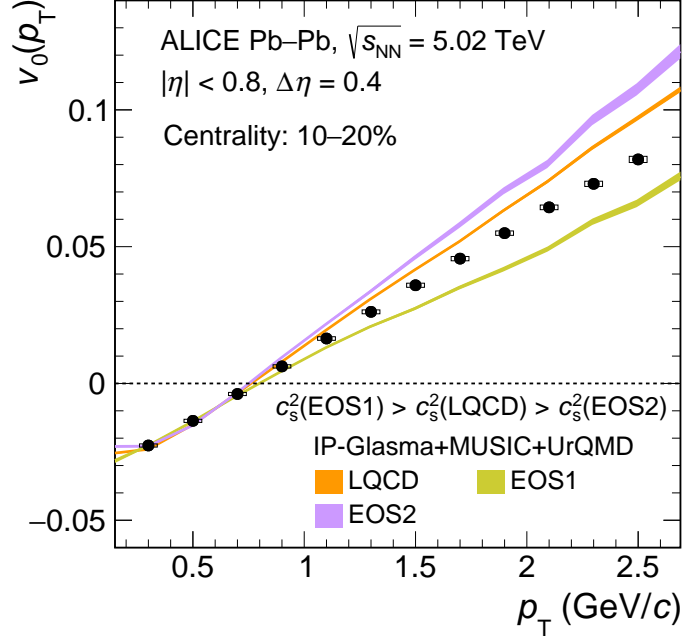


FIGURE 5.16: Transverse momentum dependence of $v_0(p_T)$ of inclusive charged particles in 10–20% central Pb–Pb collisions at $\sqrt{s_{\text{NN}}} = 5.02$ TeV, compared to IP-Glasma+MUSIC+UrQMD [23] calculations for different equations of state (EOS). Statistical (systematic) uncertainties are represented by vertical bars (boxes). The statistical uncertainties are also smaller than the marker size and thus not visible. The figure is taken from Ref. [18].

by LQCD calculations [17]. These EOS also incorporate transport coefficients (η/s and ζ/s) that comply with causality requirements in relativistic viscous hydrodynamics. Within the temperature range of 150–250 MeV, EOS1 exhibits a notably higher squared speed of sound, c_s^2 , compared to EOS2, with the LQCD-based EOS positioned between the two, as shown in the right panel of Fig. 5.17. A larger c_s^2 leads to a faster and more uniform expansion, which enhances the radial flow but suppresses its fluctuations, consequently reducing the slope of $v_0(p_T)$ [17]. The dependence of the slope term of $v_0(p_T)$ scaled with $\sqrt{N_{\text{ch}}}$, for the different EOS is shown in Fig. 5.18. Accordingly, the ordering of the slopes is the inverse of that of c_s^2 , with $\text{slope}_{\text{EOS2}} > \text{slope}_{\text{LQCD}} > \text{slope}_{\text{EOS1}}$. For $p_T < 1$ GeV/c,

$v_0(p_T)$ remains largely insensitive to changes in the EOS, and model predictions agree well with the data. However, above 1 GeV/c, EOS2 tends to overestimate the measurements, whereas EOS1 underestimates them, underscoring the sensitivity of $v_0(p_T)$ to the choice of EOS. Overall, the LQCD-based EOS provides a better description of the experimental data compared to the other two EOS. In summary, this study reveals that $v_0(p_T)$ above 1 GeV/c is sensitive to the QCD equation of state; the LQCD-based EOS best describes data.

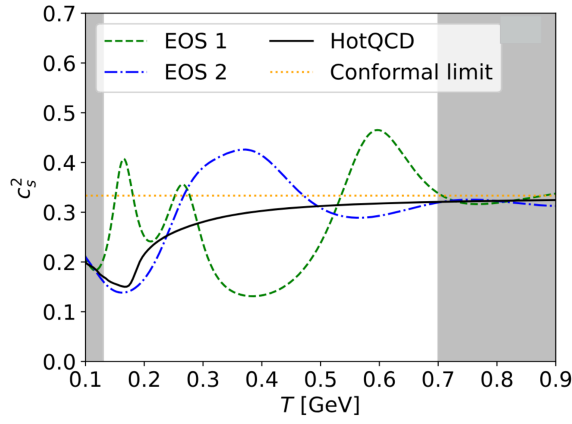


FIGURE 5.17: Squared speed of sound (c_s^2) as a function of temperature (T) for three QCD equations of state: EOS1 (green dashed line), EOS2 (blue dash-dotted line), and the lattice QCD-based HotQCD EOS (solid black line). The conformal limit ($c_s^2 = 1/3$) is indicated by the dotted orange line. This figure is taken from Ref. [17].

Figure 5.19 demonstrates the sensitivity of $v_0(p_T)$ to the initial energy density profile by comparing hydrodynamic simulations conducted with and without subnucleonic fluctuations in the initial conditions (IC). The IP-Glasma IC model incorporates fluctuations across multiple length scales, originating from both nuclear geometry and the subnucleonic parton distributions [23]. These spatial modifications in the IC affect the initial pressure gradients, thereby affecting the evolution of radial flow and its associated fluctuations. Simulations performed without subnucleonic fluctuations produce a noticeably steeper

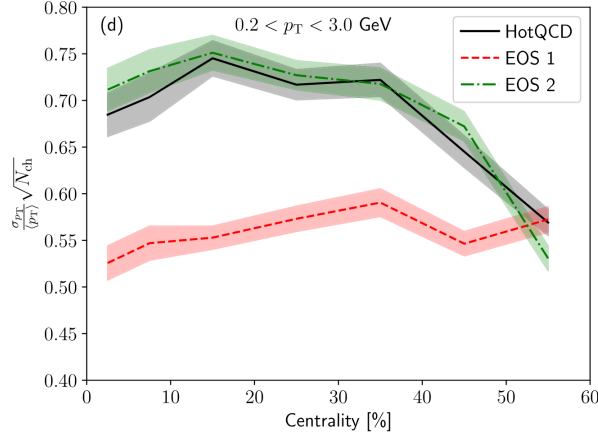


FIGURE 5.18: Centrality dependence of the slope term of $v_0(p_T)$ scaled with $\sqrt{N_{\text{ch}}}$ for $0.2 < p_T < 3.0$ GeV/c, comparing predictions from EOS1 (red dashed line), EOS2 (green dash-dotted line), and the lattice QCD-based HotQCD EOS (solid black line). Shaded bands indicate model uncertainties. This figure is taken from Ref. [17].

$v_0(p_T)$ slope, consistent with results obtained using the alternative initial-state TRENTo model [34] as reported in Ref. [5]. In contrast, including subnucleonic fluctuations in the IP-Glasma framework leads to a significantly improved agreement with experimental data, underscoring the importance of initial-state spatial structures in shaping the observed radial flow dynamics.

5.5.3 Blast-wave modelling of $v_0(p_T)$

To get more insights from the $v_0(p_T)$ measurements and connect them with the conventional observable of average transverse expansion velocity, $\langle\beta_T\rangle$, the Boltzmann-Gibbs Blast-Wave (BGBW) model [1] is employed, as introduced in Sec. 5.1. This model characterizes the momentum distributions at freeze-out for particles originating from a thermalized and collectively expanding medium, using two principal parameters: $\langle\beta_T\rangle$ and T_{kin} . Henceforth,

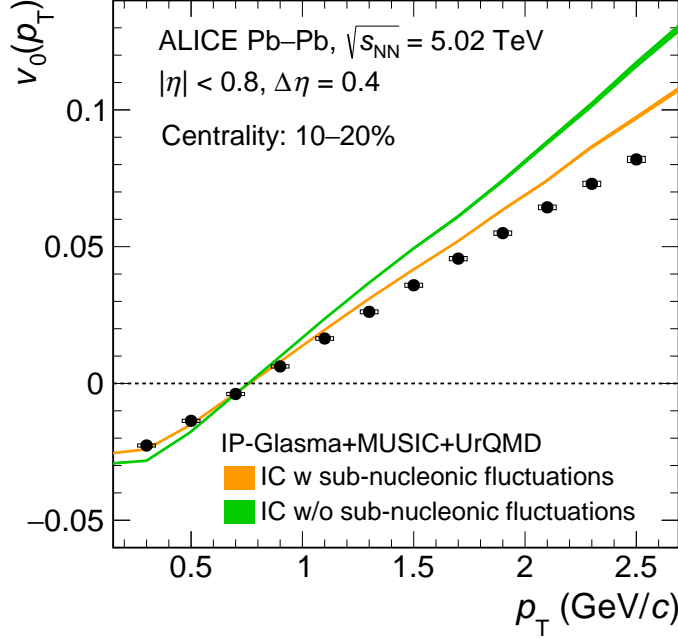


FIGURE 5.19: Transverse momentum dependence of $v_0(p_T)$ of inclusive charged particles in 10–20% central Pb–Pb collisions at $\sqrt{s_{\text{NN}}} = 5.02$ TeV, compared to IP-Glasma+MUSIC+UrQMD [23] calculations for initial conditions (IC) with (w) and without (w/o) sub-nucleonic fluctuations (right). Statistical (systematic) uncertainties are represented by vertical bars (boxes). The statistical uncertainties are also smaller than the marker size and thus not visible. The figure is taken from Ref. [18].

within this framework, the p_T spectra of emitted particles are determined by:

$$E \frac{d^3N}{dp^3} \propto \int_0^R m_T I_0 \left(\frac{p_T \sinh(\rho)}{T_{\text{kin}}} \right) K_1 \left(\frac{m_T \cosh(\rho)}{T_{\text{kin}}} \right) r \, dr, \quad (5.8)$$

where the transverse mass is $m_T = \sqrt{p_T^2 + m_0^2}$, I_0 and K_1 denote modified Bessel functions, and r stands for the radial coordinate in the transverse plane [3]. This equation forms the basis for our event-by-event BGBW simulations that generate p_T spectra used to estimate $v_0(p_T)$. The profile of collective radial expansion, ρ , is captured through the following parametrization [3]:

$$\rho = \tanh^{-1} \beta_T(r) = \tanh^{-1} \left[\left(\frac{r}{R} \right)^n \beta_s \right], \quad (5.9)$$

with R as the fireball radius, $\beta_T(r)$ as the local radial flow velocity, β_s being the maximum transverse velocity at the surface, and n is known as the exponent, defining the velocity profile shape. The average transverse expansion velocity $\langle\beta_T\rangle$ is then linked to the surface velocity β_s according to:

$$\langle\beta_T\rangle = \frac{\int_0^R \beta_T(r) r \, dr}{\int_0^R r \, dr} \implies \beta_s = \langle\beta_T\rangle \left(\frac{n+2}{2} \right). \quad (5.10)$$

This equation allows one to determine the corresponding β_s for a given $\langle\beta_T\rangle$. It is important to note here that in the absence of any event-by-event dynamical fluctuations, $v_0(p_T)$ is essentially zero, indicating that non-zero values are driven by variations in the underlying freeze-out conditions. To realistically account for these event-by-event fluctuations in the BGBW model, both T_{kin} and β_s are treated as random variables following Gaussian distributions across events. Four distinct scenarios are investigated, each allowing for independent variation of the mean or the event-by-event fluctuation width of these parameters:

- (1) variation of the mean value of β_s while keeping its width and T_{kin} fixed,
- (2) variation of the fluctuation width of β_s while keeping its mean value and T_{kin} fixed,
- (3) variation of the mean value of T_{kin} while keeping its width and β_s constant, and
- (4) variation of the fluctuation width of T_{kin} while its mean value and β_s are held fixed.

For each of these scenarios, event-by-event parameters are sampled and $v_0(p_T)$ for pions, kaons, and protons are estimated. These configurations allow us to systematically study the sensitivity of $v_0(p_T)$ to underlying collective dynamics and thermal fluctuations. In the following sections, we discuss these results in detail.

Figure 5.20 shows the effect of varying the mean value of β_s , on the evolution of $v_0(p_T)$ for pions (left), kaons (middle), and protons (right). Four values of β_s , ranging from 0.697 to 0.927, are considered at fixed $T_{\text{kin}} = 0.094$ GeV and β_s fluctuation width $\sigma(\beta_s) = 0.006$. It is observed for all particle species that $v_0(p_T)$ shifts from negative values

at low p_T to positive values beyond a certain threshold momentum, $p_{T,\text{sep}}$, consistent with earlier observations from both data and hydrodynamic calculations. As β_s increases, $p_{T,\text{sep}}$ also moves to higher values, thereby bringing the onset of positive $v_0(p_T)$ at larger $p_{T,\text{sep}}$ values. This shift is strongest for protons, followed by kaons and then pions, reflecting the mass dependence of radial flow: stronger radial flow enhances the separation in the $v_0(p_T)$ evolution among different hadron species. The left panel illustrates the pion

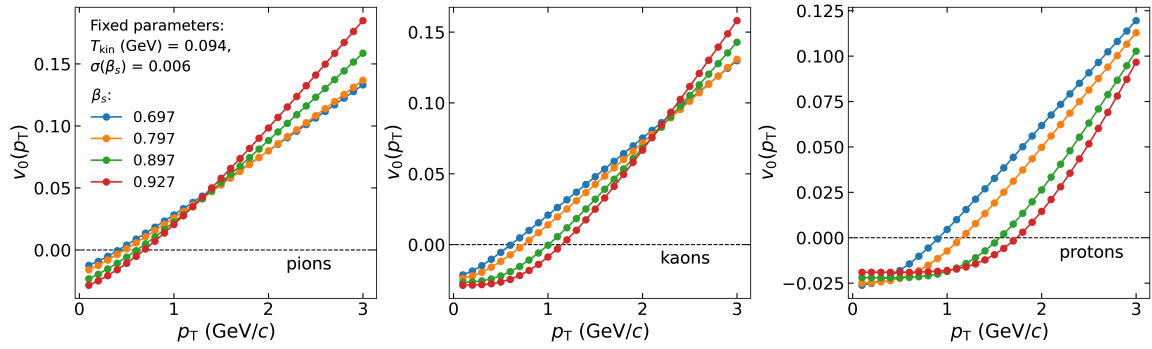


FIGURE 5.20: Transverse momentum dependence of $v_0(p_T)$ for pions (left), kaons (middle), and protons (right), obtained from the blast-wave model incorporating Gaussian fluctuations in the transverse expansion velocity at the surface. The kinetic freeze-out temperature (T_{kin}) and the fluctuation width of the surface velocity $\sigma(\beta_s)$ are fixed at 0.094 GeV and 0.006, respectively, while the mean surface velocity β_s is varied in the range [0.697, 0.927]. The figure is taken from Ref. [35].

results, where $v_0(p_T)$ exhibits an almost linear increase across all β_s values. For p_T below 1.5 GeV/c, higher β_s values correspond to a decrease in $v_0(p_T)$, while above $p_T = 1.5$ GeV/c, increasing β_s enhances $v_0(p_T)$. The middle panel shows kaon results, which display a more pronounced nonlinear dependence on p_T with increasing β_s , compared to that of pions. For $p_T < 2.5$ GeV/c, an increase in β_s leads to a decrease in $v_0(p_T)$, exhibiting a trend qualitatively similar to that observed for pions but with a more pronounced non-linearity. The p_T value at which $v_0(p_T)$ reverses its behavior and starts to rise with β_s is shifted to higher momenta compared to pions. After this transition point, $v_0(p_T)$ grows more rapidly with p_T as β_s increases, though the overall change in magnitude remains

relatively small. The right panel shows the results for protons, which demonstrates the most significant nonlinear response to variations in β_s among the three particle species examined. When β_s value is quite small, $v_0(p_T)$ increases almost linearly with p_T . However, with the increase in β_s , the evolution of $v_0(p_T)$ becomes progressively more nonlinear, even exceeding the nonlinear effects observed for kaons. In the low- p_T region ($p_T < 0.5$ GeV/c), changes in β_s value have little impact, but at higher p_T ($p_T > 1$ GeV/c), larger β_s values prominently suppress $v_0(p_T)$. A similar behavior is also observed for both pions and kaons.

Figure 5.21 presents $v_0(p_T)$ for variation in the β_s fluctuation width, $\sigma(\beta_s)$. The results are again shown separately for pions (left), kaons (middle), and protons (right). While the T_{kin} and the mean value of β_s are fixed, $\sigma(\beta_s)$ is systematically increased from 0.003 to 0.015. The results demonstrate a clear and significant influence of $\sigma(\beta_s)$ on $v_0(p_T)$ across all three particle species. As the magnitude of fluctuations in β_s grows, there is

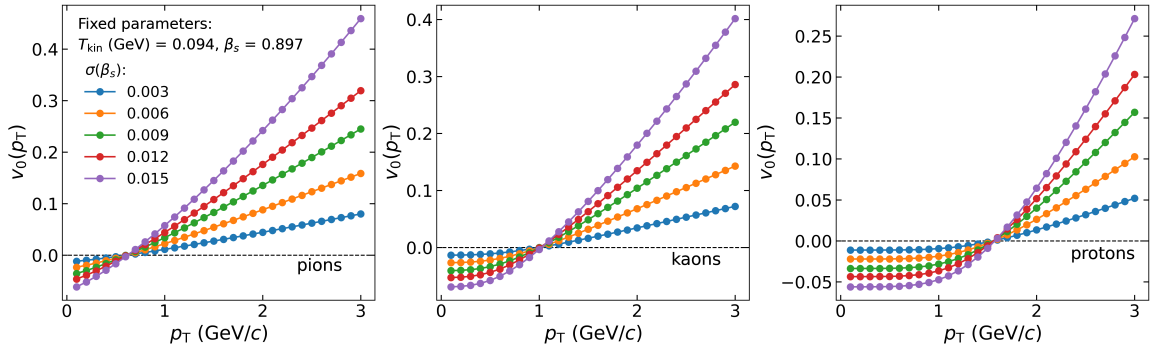


FIGURE 5.21: Transverse momentum dependence of $v_0(p_T)$ for pions (left), kaons (middle), and protons (right), obtained from the blast-wave model incorporating Gaussian fluctuations in the transverse expansion velocity at the surface. $v_0(p_T)$ of pions (left), kaons (middle), and protons (right) in blast-wave model for Gaussian-fluctuations of transverse expansion velocity at the surface. The kinetic freeze-out temperature (T_{kin}) and mean value of fluctuations β_s are kept fixed at 0.094 GeV and 0.897, respectively, while the width $\sigma(\beta_s)$ is varied in the range [0.003, 0.015] [35].

an overall enhancement in the absolute values of $v_0(p_T)$ both below and above the $p_{T,\text{sep}}$. This enhancement is more pronounced for p_T above $p_{T,\text{sep}}$, and the effect intensifies with

increasing p_T . Notably, the position of $p_{T,\text{sep}}$, which marks the transition from negative to positive values of $v_0(p_T)$, remains unchanged regardless of the fluctuation width.

Figure 5.22 demonstrates the impact of fluctuations in the T_{kin} on the magnitude of $v_0(p_T)$. Here, β_s is held constant at 0.897 and the fluctuation width of T_{kin} is also set as 0.003 GeV, while the mean value of T_{kin} is systematically varied. The response of pions (left), kaons (middle), and protons (right) is explored over a T_{kin} range from 0.064 GeV to 0.114 GeV. For p_T below $p_{T,\text{sep}}$, $v_0(p_T)$ remains largely insensitive to changes in T_{kin} , across all three particle species. However, for p_T above $p_{T,\text{sep}}$, an increasing T_{kin} causes a marked reduction in $v_0(p_T)$, with the effect becoming more significant at higher p_T . This behavior indicates that higher kinetic temperatures, which correspond to enhanced thermal motion, tend to smooth out fluctuations in the p_T spectra, thereby diminishing the magnitude of $v_0(p_T)$. Additionally, the characteristic mass-dependent hierarchy and separation in $v_0(p_T)$

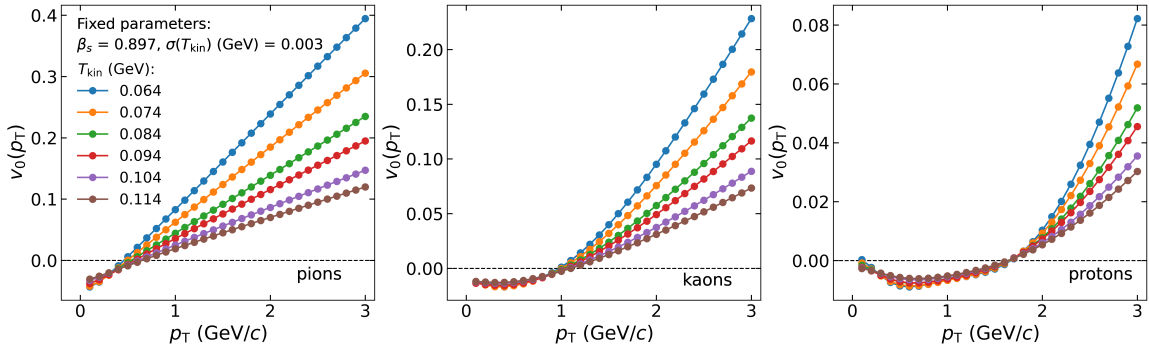


FIGURE 5.22: Transverse momentum dependence of $v_0(p_T)$ for pions (left), kaons (middle), and protons (right), obtained from the blast-wave model incorporating Gaussian fluctuations in the transverse expansion velocity at the surface. $v_0(p_T)$ of pions (left), kaons (middle), and protons (right) in blast-wave model for Gaussian-fluctuations of kinetic freeze-out temperature. The transverse expansion velocity at the surface (β_s) and width of fluctuations $\sigma(T_{\text{kin}})$ are kept fixed at 0.897 and 0.003 GeV, respectively, while the mean value T_{kin} is varied in the range [0.064, 0.114] GeV [35].

among the particle species remain mostly unchanged against variations in T_{kin} . This is in contrast with the more pronounced sensitivity to fluctuations in β_s (variation in the mean

value of β_s), which exert a stronger influence on these mass-dependent features.

Figure 5.23 presents the variation of $v_0(p_T)$ with p_T for pions (left), kaons (middle), and protons (right), focusing on the influence of T_{kin} fluctuation width, $\sigma(T_{\text{kin}})$. Here, $\sigma(T_{\text{kin}})$ is varied between 0.003 GeV and 0.01 GeV, while β_s is fixed at 0.897 and the mean value of T_{kin} is set to 0.094 GeV. The findings demonstrate a pronounced sensitivity of $v_0(p_T)$ to changes in $\sigma(T_{\text{kin}})$ for all three particle species, exhibiting trends similar to those previously observed with $\sigma(\beta_s)$ in Fig. 5.21. Increasing the fluctuation width leads to an overall amplification in the magnitude of $v_0(p_T)$ both below and above $p_{T,\text{sep}}$. This enhancement is especially significant at higher p_T values.

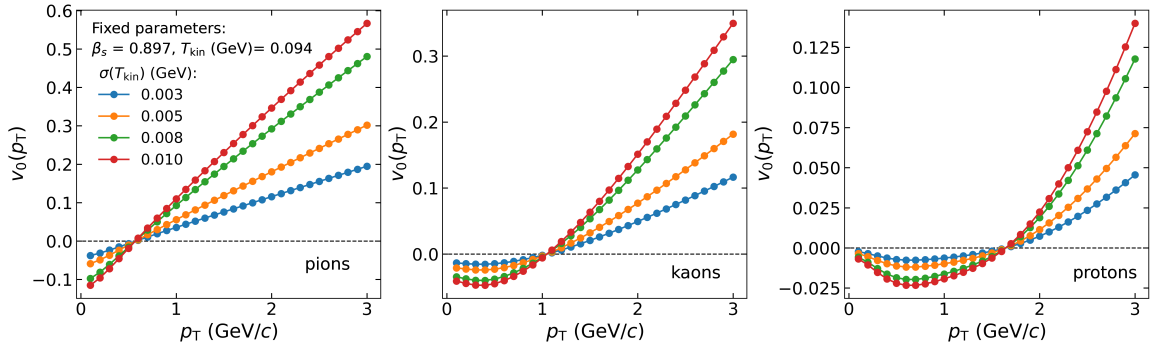


FIGURE 5.23: Transverse momentum dependence of $v_0(p_T)$ for pions (left), kaons (middle), and protons (right) obtained from the blast-wave model incorporating Gaussian fluctuations in the transverse expansion velocity at the surface. $v_0(p_T)$ of pions (left), kaons (middle), and protons (right) in blast-wave model for Gaussian-fluctuations of kinetic freeze-out temperature. The transverse expansion velocity at the surface (β_s) and mean value of fluctuations T_{kin} are kept fixed at 0.897 and 0.094 GeV, respectively, while the width $\sigma(T_{\text{kin}})$ is varied in the range [0.003, 0.010] GeV [35].

Table 5.1 highlights how collective expansion and thermal motion influence the structure of $v_0(p_T)$ within the BGBW model through variations of β_s , T_{kin} , and their fluctuations. While the blast-wave framework does not account for initial-state geometry or the full dynamical evolution of the collision, it effectively captures the key physics behind mass ordering observed in $v_0(p_T)$ and also its overall behavior. The results illustrate that radial

flow and its event-by-event fluctuations, together with changes in the freeze-out temperature, play a central role in shaping the p_T -differential trends of $v_0(p_T)$ across particle species. In summary, this blast-wave modelling demonstrates that event-by-event fluctuations in β_s and T_{kin} govern the observed species dependence of $v_0(p_T)$.

TABLE 5.1: Summary of the key findings from the blast-wave model investigation of $v_0(p_T)$ by the variation of mean values for transverse expansion velocity (β_s), kinetic freeze-out temperature (T_{kin}), and their fluctuations ($\sigma(\beta_s)$ and $\sigma(T_{\text{kin}})$).

Parameter increased	Observed trends
β_s (mean)	Increases the difference in $v_0(p_T)$ between particle species (pronounced mass ordering). $v_0(p_T)$ increases at high p_T but decreases at low p_T . The separation momentum $p_{T,\text{sep}}$ shifts to higher values, with the effect more pronounced for heavier particles.
$\sigma(\beta_s)$	Enhances $v_0(p_T)$ across the whole p_T range. No change is observed in the position of $p_{T,\text{sep}}$.
T_{kin} (mean)	No change in the difference in $v_0(p_T)$ between particle species. $v_0(p_T)$ decreases above $p_{T,\text{sep}}$, while no change is seen below $p_{T,\text{sep}}$. The $p_{T,\text{sep}}$ increases more for lighter particles: maximal for pions and negligible for protons.
$\sigma(T_{\text{kin}})$	Increases $v_0(p_T)$, particularly at high p_T . No change is observed in the position of $p_{T,\text{sep}}$.

5.5.4 Extraction of blast-wave model parameters

The parameters of the blast-wave model, discussed in Sec. 5.5.3, were determined by comparing the model predictions of $v_0(p_T)$ for pions, kaons, and protons with the corresponding experimental data in three centrality classes (10–20%, 30–40%, and 60–70%). The extraction of these parameters was performed using a Bayesian inference framework, which provides a probabilistic means to infer model parameters by combining prior knowledge with observed data.

In Bayesian inference, the goal is to estimate the posterior probability distribution of the parameters, given by Bayes' theorem:

$$P(\theta|\text{data}) \propto \mathcal{L}(\text{data}|\theta)P(\theta), \quad (5.11)$$

where $P(\theta)$ is the prior distribution and $\mathcal{L}(\text{data}|\theta)$ is the likelihood function that quantifies the agreement between model predictions and experimental measurements. Assuming Gaussian-distributed experimental uncertainties, the log-likelihood function used in this analysis is given by

$$\log \mathcal{L}(\text{data}|\theta) = -\frac{1}{2} \sum_{\text{particles}} \sum_i \left(\frac{v_0^{\text{model}}(p_{T,i}; \theta) - v_0^{\text{data}}(p_{T,i})}{\sigma_i} \right)^2 \quad (5.12)$$

where $\theta = \{\beta_s, T_{\text{kin}}, \sigma(\beta_s), \sigma(T_{\text{kin}}), n\}$ denotes the parameter vector, $v_0^{\text{model}}(p_{T,i}; \theta)$ is the blast-wave model prediction for the i -th p_T bin, $v_0^{\text{data}}(p_{T,i})$ is the corresponding experimental measurement, and σ_i is the experimental uncertainty in the i -th bin. Here, the outer summation runs over the three particle species (pions, kaons, and protons), and the inner summation runs over the p_T bins i . Maximizing this log-likelihood (equivalent to minimizing chi-squared, $\chi^2 = -2\log \mathcal{L}$) yields the most probable parameter estimates.

To efficiently sample the posterior distributions and quantify uncertainties, Markov Chain Monte Carlo (MCMC) techniques were employed. This approach enables a detailed exploration of the multidimensional parameter space and provides insight into parameter correlations and credible intervals. The resulting posterior distributions for all fitted parameters are presented in Figs. 5.24, 5.25, and 5.26.

Uniform, non-informative priors were defined within physically motivated ranges based on kinetic freeze-out conditions established in previous heavy-ion studies at LHC energies. The prior limits for $\sigma(T_{\text{kin}})$ and $\sigma(\beta_s)$ varied with centrality—0–0.02 GeV for 10–20%, 0–0.05 GeV for 30–40%, and 0–0.06 GeV for 60–70%—while the complete prior ranges

used across all centralities are summarized in Table 5.2. Sensitivity tests involving a moderate $\pm 10 - 20\%$ expansion of these ranges confirmed that the posterior estimates remained stable, indicating that the data predominantly constrained the parameters.

A common set of parameters was fitted simultaneously to the $v_0(p_T)$ distributions of all three particle species within each centrality class. The fitting was performed over the same p_T intervals used for p_T -spectra fitting [3]: 0.2–1 GeV/ c for pions, 0.2–1.4 GeV/ c for kaons, and 0.4–2.6 GeV/ c for protons.

TABLE 5.2: Uniform prior ranges used for the blast-wave model parameters in the Bayesian analysis of $v_0(p_T)$ for pions, kaons, and protons [35].

Model parameter	Prior ranges
n	[0.0, 2.0]
β_s	[0.50, 0.92]
T_{kin} (GeV)	[0.02, 0.30]
$\sigma(\beta_s)$	[0.0, 0.06]
$\sigma(T_{\text{kin}})$ (GeV)	[0.0, 0.06]

In the 10–20% centrality interval, the Bayesian parameter estimation provides the following median values with 68% credible intervals: $\beta_s = 0.8929^{+0.0048}_{-0.0051}$, $T_{\text{kin}} = 0.0863^{+0.0056}_{-0.0050}$ GeV, $\sigma(\beta_s) = 0.0056^{+0.0005}_{-0.0004}$, and $\sigma(T_{\text{kin}}) = 0.0002^{+0.0002}_{-0.0001}$ GeV. These extracted values of β_s and T_{kin} agree with kinetic freeze-out parameters measured using p_T spectra by ALICE [3]. Using these estimates, the blast-wave model predictions for $v_0(p_T)$ were generated and compared with experimental data, as shown in Fig. 5.27. The lower panel of the figure presents the residuals, calculated as $(\text{data} - \text{model})/\sigma_{\text{data}}$, where σ_{data} denotes the total experimental uncertainty. Residual values close to zero indicate agreement, while fluctuations within about 2σ point to compatibility between the model and the data. This comparison shows that the extracted blast-wave parameters provide a good description of the measurements, with protons exhibiting the best agreement, followed by kaons and then pions.

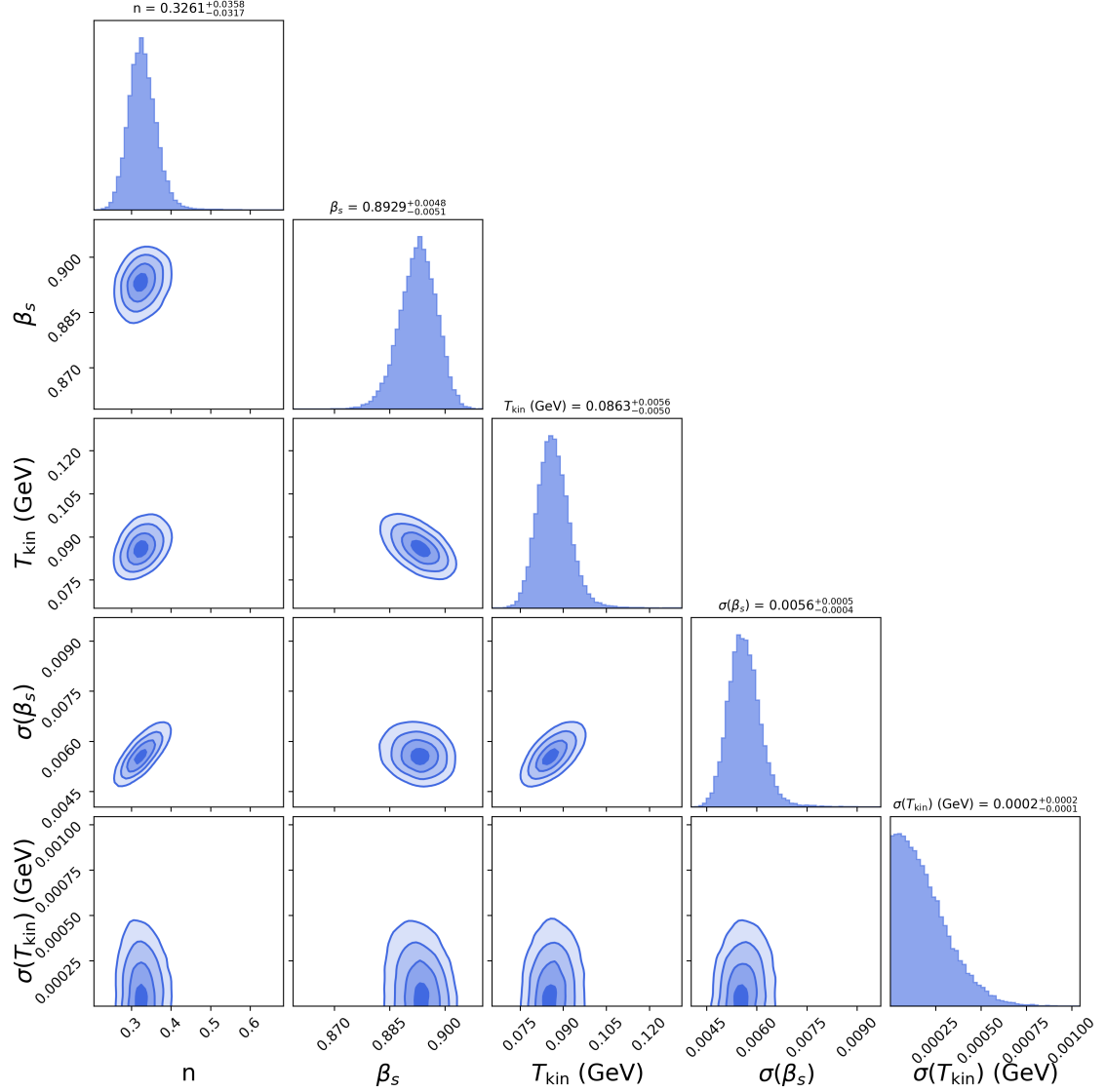


FIGURE 5.24: The posterior distributions and parameter correlations for n , β_s , T_{kin} , $\sigma(\beta_s)$, and $\sigma(T_{\text{kin}})$ using $v_0(p_T)$ measurements of pions, kaons, and protons for centrality classes 10–20%. The diagonal panels display the marginalized probability distributions of individual parameters, while the off-diagonal panels show the 2D joint distributions with contour levels indicating confidence regions. The plot suggests correlations between some parameters, highlighting the uncertainties in their estimations. The figure is taken from Ref. [35].

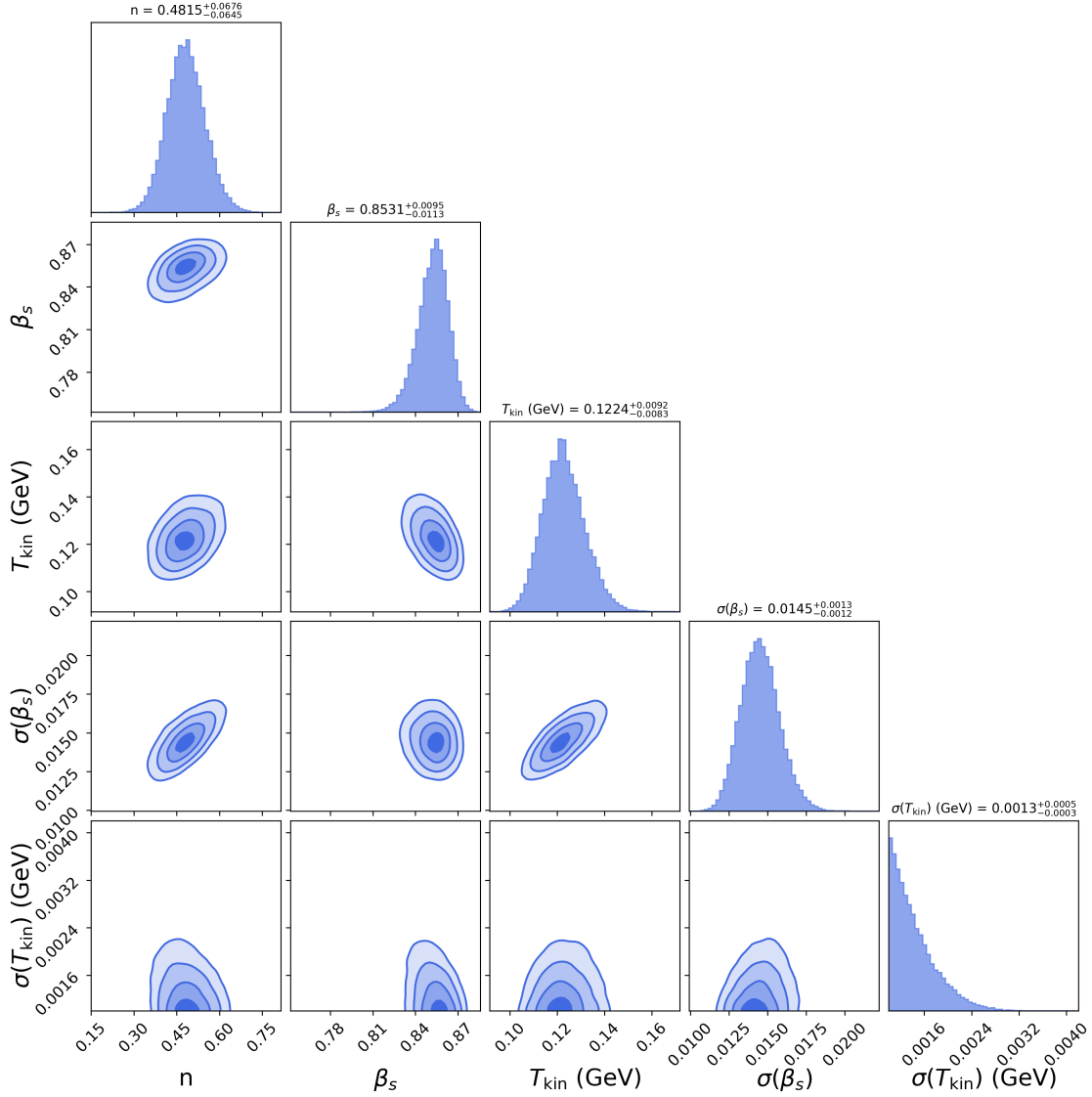


FIGURE 5.25: The posterior distributions and parameter correlations for n , β_s , T_{kin} , $\sigma(\beta_s)$, and $\sigma(T_{\text{kin}})$ using $v_0(p_T)$ measurements of pions, kaons, and protons for centrality classes 30–40%. The diagonal panels display the marginalized probability distributions of individual parameters, while the off-diagonal panels show the 2D joint distributions with contour levels indicating confidence regions. The plot suggests correlations between some parameters, highlighting the uncertainties in their estimations [35].

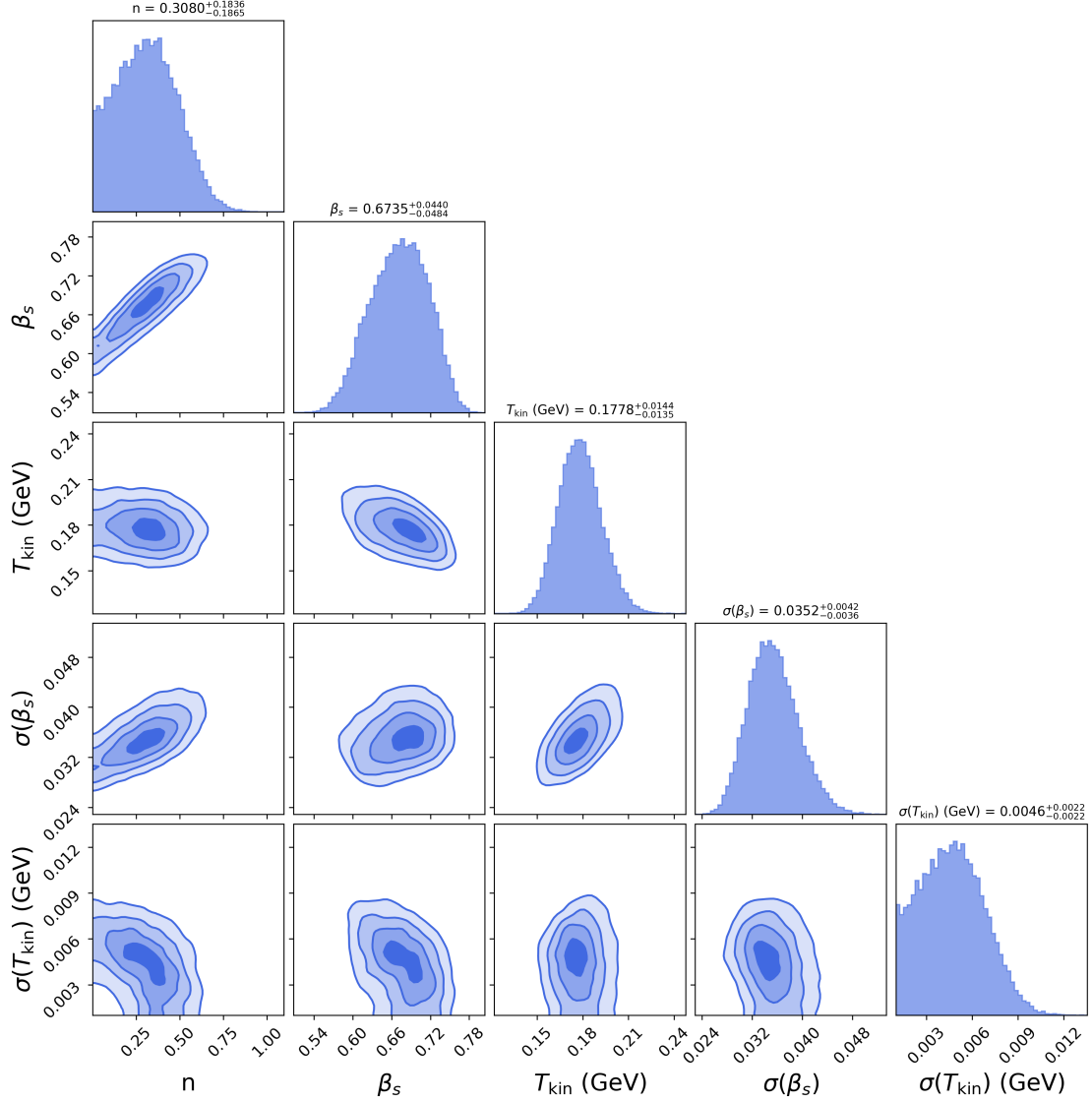


FIGURE 5.26: The posterior distributions and parameter correlations for n , β_s , T_{kin} , $\sigma(\beta_s)$, and $\sigma(T_{\text{kin}})$ using $v_0(p_T)$ measurements of pions, kaons, and protons for centrality classes 60–70%. The diagonal panels display the marginalized probability distributions of individual parameters, while the off-diagonal panels show the 2D joint distributions with contour levels indicating confidence regions. The plot suggests correlations between some parameters, highlighting the uncertainties in their estimations [35].

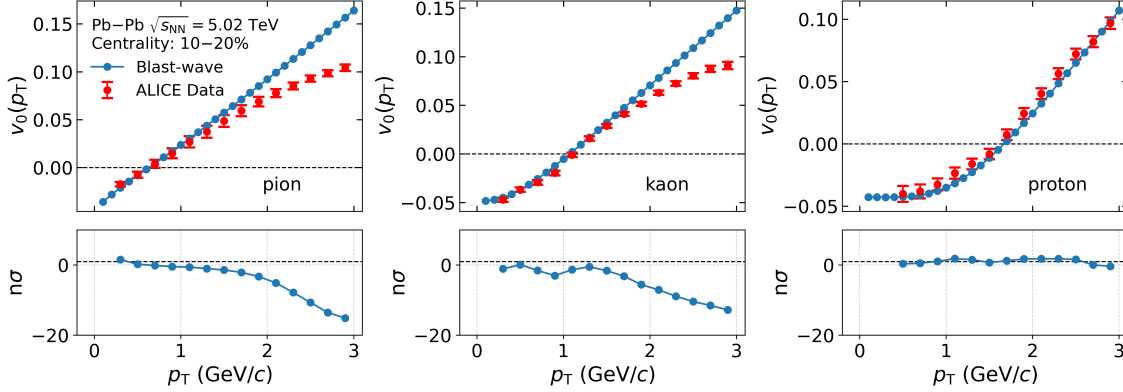


FIGURE 5.27: Transverse momentum dependence of $v_0(p_T)$ of pions (left), kaons (middle), and protons (right) in Pb–Pb collisions at $\sqrt{s_{NN}} = 5.02$ TeV for centrality interval 10–20%. The measurements of ALICE (red marker) are compared to blast-wave predictions obtained with the best-fit parameters. The bottom panels show the residual, $n\sigma = (\text{data} - \text{model})/\text{error}_{\text{data}}$. The figure is taken from Ref. [35].

The extracted parameter values together with their uncertainties for all three centrality classes are summarized in Table 5.3. Model-to-data comparisons for the 30–40% and 60–70% intervals are displayed in Figs. 5.28 and 5.29. A pronounced centrality dependence of β_s is evident from the extracted values. In central collisions (10–20%), β_s reaches ~ 0.893 , consistent with strong collective expansion. Moving towards more peripheral events, this value decreases gradually to ~ 0.853 for 30–40% and further to ~ 0.674 for 60–70%, indicating the expected reduction in radial flow strength as system size decreases. Thus, Bayesian inference of the blast-wave parameters yields physically meaningful ranges that not only reproduce the data but also provide quantitative constraints on freeze-out conditions in heavy-ion collisions.

An increasing trend is observed for T_{kin} from central to peripheral collisions, rising from about 0.086 GeV in the 10–20% centrality interval to approximately 0.122 GeV in the 30–40% and 0.178 GeV in the 60–70% centrality interval. This behavior aligns with the expectation that particles freeze out earlier at higher temperatures in peripheral collisions

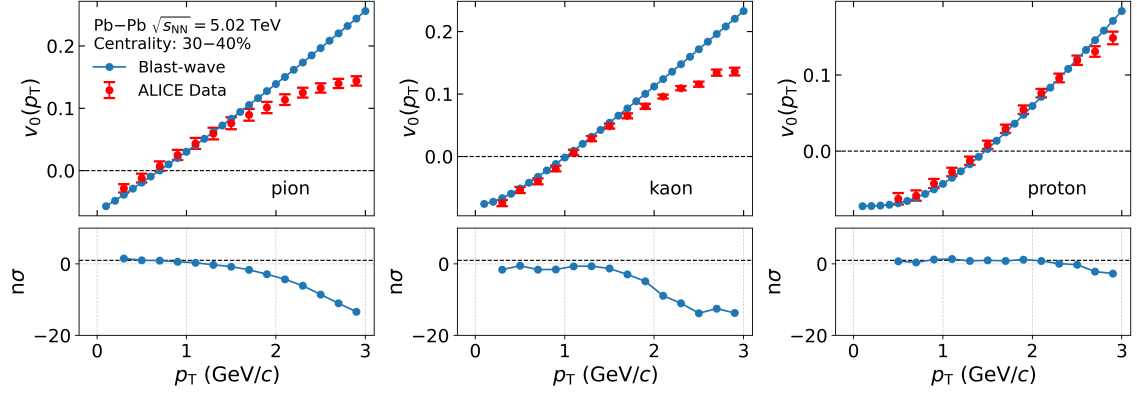


FIGURE 5.28: Transverse momentum dependence of $v_0(p_T)$ of pions (left), kaons (middle), and protons (right) in Pb–Pb collisions at $\sqrt{s_{NN}} = 5.02$ TeV for centrality interval 30–40%. The measurements of ALICE (red marker) are compared to blast-wave predictions obtained with the best-fit parameters. The bottom panels show the residual, $n\sigma = (\text{data} - \text{model})/\text{error}_{\text{data}}$ [35].

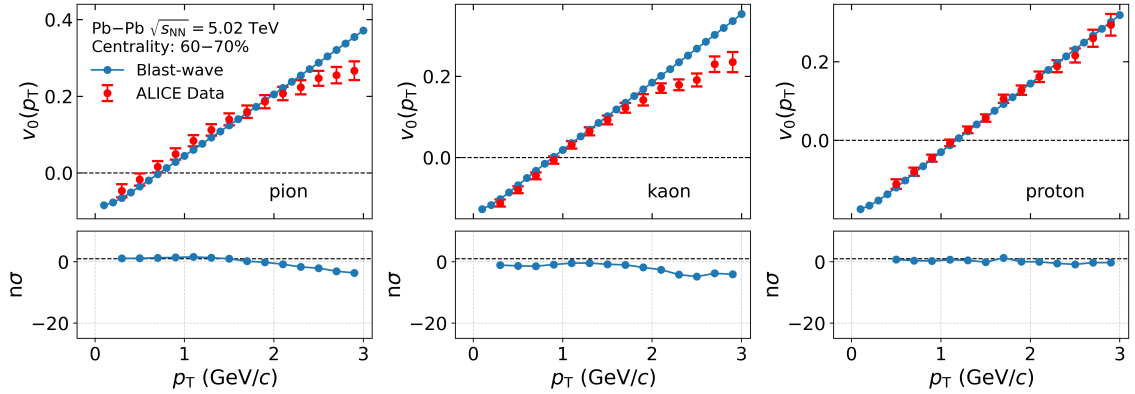


FIGURE 5.29: Transverse momentum dependence of $v_0(p_T)$ of pions (left), kaons (middle), and protons (right) in Pb–Pb collisions at $\sqrt{s_{NN}} = 5.02$ TeV for centrality interval 60–70%. The measurements of ALICE (red marker) are compared to blast-wave predictions obtained with the best-fit parameters. The bottom panels show the residual, $n\sigma = (\text{data} - \text{model})/\text{error}_{\text{data}}$ [35].

TABLE 5.3: Extracted blast-wave parameters and their event-by-event fluctuation width for different centrality intervals [35].

Centrality	n	β_s	T_{kin} (GeV)	$\sigma(\beta_s)$	$\sigma(T_{\text{kin}})$ (GeV)
10–20%	$0.3261^{+0.0358}_{-0.0317}$	$0.8929^{+0.0048}_{-0.0051}$	$0.0863^{+0.0056}_{-0.0050}$	$0.0056^{+0.0005}_{-0.0004}$	$0.0002^{+0.0002}_{-0.0001}$
30–40%	$0.4815^{+0.0676}_{-0.0645}$	$0.8531^{+0.0095}_{-0.0113}$	$0.1224^{+0.0092}_{-0.0083}$	$0.0145^{+0.0013}_{-0.0012}$	$0.0013^{+0.0005}_{-0.0003}$
60–70%	$0.3080^{+0.1836}_{-0.1865}$	$0.6735^{+0.0440}_{-0.0484}$	$0.1778^{+0.0144}_{-0.0135}$	$0.0352^{+0.0042}_{-0.0036}$	$0.0046^{+0.0022}_{-0.0022}$

as a consequence of shorter lifetime and reduced system size. In contrast, the system undergoes longer expansion and cooling before freeze-out occurs in central collisions. In peripheral collisions, blast-wave fits may return anomalously large T_{kin} values, in some cases even surpassing the QCD crossover temperature of 0.155–0.160 GeV[36]. This tendency largely reflects the challenges encountered when using the blast-wave formalism in systems that are relatively small or exhibit low particle density, conditions under which local thermal equilibrium may not be well established. The underlying model assumes a smoothly expanding source and a thermally defined freeze-out surface; however, such simplifications become problematic in situations where initial-state fluctuations or non-equilibrium effects play a substantial role. Consequently, the fit may compensate by assigning large values to T_{kin} in order to achieve good agreement with the data.

The fluctuation widths, $\sigma(\beta_s)$, and $\sigma(T_{\text{kin}})$, exhibit a clear increasing trend from central to peripheral collisions. The extracted value of $\sigma(\beta_s)$ is about 0.006 in the 10–20% centrality interval, that rises to about 0.014 and 0.035 at 30–40% and 60–70% centrality interval, respectively. This behavior indicates that the event-by-event variability in the collective flow strength becomes more pronounced as the system size decreases. Likewise, $\sigma(T_{\text{kin}})$ increases from roughly 0.0002 GeV to 0.0013 GeV and further to 0.0046 GeV across the same centrality intervals. This reflects enhanced thermal fluctuations at kinetic freeze-out for peripheral collisions, which can be attributed to the reduced size and shorter

lifetime of the system in these collisions.

Figure 5.30 presents a comparison between the β_s and T_{kin} parameters extracted in this work using $v_0(p_T)$ measurements and the corresponding values obtained from blast-wave fits to p_T spectra reported in Ref. [3]. In Ref. [3], $\langle\beta_T\rangle$ values are reported across different centralities and we have calculated corresponding β_s values using Eq. 5.10. It is important to note that uncertainties associated with the parameters extracted from p_T spectra fits were determined through conventional fitting techniques, such as chi-square minimization or likelihood-based methods, whereas the uncertainties here are derived via a Bayesian inference approach. In the left panel, the β_s values are compared from both approaches, and they agree well for the 10–20% and 30–40% centrality intervals. However, a deviation of approximately 2.6σ is observed in the 60–70% centrality interval. On the other hand, the right panel shows clear differences in the T_{kin} obtained by two methods. The temperatures from the $v_0(p_T)$ analysis are generally higher than those from the p_T spectra fits. For the 10–20% centrality range, the two results are quite close, differing by only about 1.2σ . However, for more peripheral collisions (30–40% and 60–70%), the deviations grow more pronounced, reaching 2.2σ and 3.2σ , respectively.

The discrepancy can be attributed to the different sensitivities of the two observables to resonance decays. The p_T spectra receive significant contributions from short-lived resonances, especially at low p_T , which broaden and soften the distributions and lower the apparent freeze-out temperature in blast-wave fits. In contrast, $v_0(p_T)$ is measured with an η gap, which suppresses correlation that are short-range in η . Therefore, the impact of resonance decay products on $v_0(p_T)$ is minimal, leading to a higher extracted temperature.

Furthermore, in peripheral collisions, the blast-wave model’s fundamental assumptions—such as a uniform freeze-out surface and smooth collective flow—may break down due to increased local fluctuations and reduced particle densities. Under these conditions, the

p_T spectra are likely influenced by emissions occurring later from resonance-rich regions, while the observable $v_0(p_T)$ mainly captures particles emitted earlier from the system's more thermalized regions. This can lead to differences in the T_{kin} values obtained from each measurement, with the parameter derived from $v_0(p_T)$ likely representing the conditions of the system's thermalized core more accurately. Altogether, this results underscore that the freeze-out characteristics derived from $v_0(p_T)$ and p_T spectra represent complementary aspects, each reflecting distinct but related facets of the freeze-out dynamics and the overall evolution of the system.

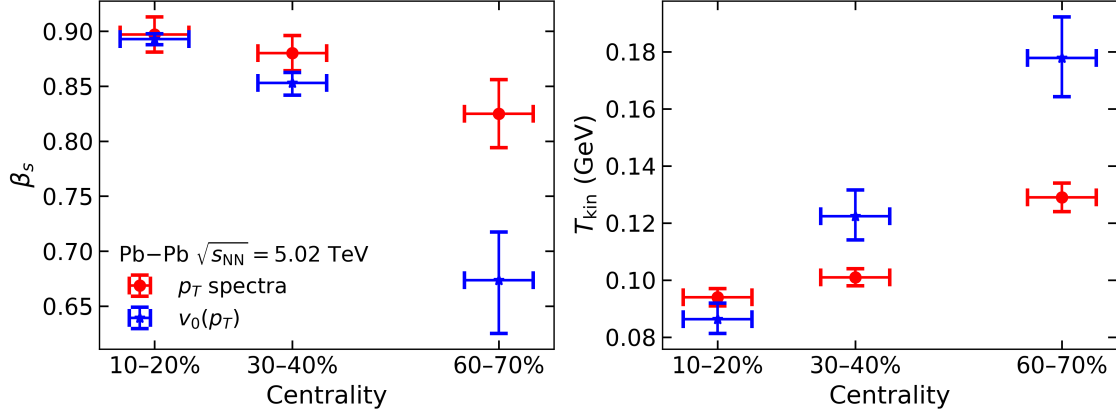


FIGURE 5.30: Comparison of the extracted surface radial flow velocity (β_s , left) and kinetic freeze-out temperature (T_{kin} , right) as a function of centrality. The results from this analysis, obtained via blast-wave model fits to $v_0(p_T)$ measurements, are shown together with values previously determined from blast-wave fits to p_T spectra reported in Ref. [3]. Vertical bars indicate the uncertainties estimated from fit for each point. The figure is taken from Ref. [35].

5.6 Summary

This work presents the first measurement of $v_0(p_T)$, a novel observable sensitive to radial flow in heavy-ion collisions, extracted using a pseudorapidity-gap method that suppresses nonflow effects and isolates long-range transverse momentum correlations. The mea-

measurements exhibit a characteristic mass ordering at low p_T consistent with hydrodynamic collective expansion, while at higher p_T , protons exhibit larger values than pions and kaons. This baryon–meson separation supports quark recombination as the dominant hadronization mechanism in this p_T region. The measurements also show approximate NCQ scaling, that reflects the partonic origin of the correlations captured by the observable. Comparisons with the IP-Glasma+MUSIC+UrQMD hydrodynamic model show good agreement at low p_T , while deviations at higher p_T and in peripheral collisions highlight the role of non-collective processes. Sensitivity studies indicate that $v_0(p_T)$ is influenced by the bulk-viscosity ζ/s and the equation of state, both of which alter the isotropic expansion of the medium, while remaining largely insensitive to the shear viscosity η/s . Additionally, the observable responds to the system’s initial and its event-by-event fluctuations, which influence the pressure gradients driving the collective expansion.

The transverse momentum dependence of $v_0(p_T)$ was further explored using a blast-wave model incorporating Gaussian event-by-event fluctuations in both the transverse expansion velocity and the kinetic freeze-out temperature. This model successfully reproduces the key qualitative features observed in the data, such as the development of mass ordering with increasing radial flow and the species-specific transition of $v_0(p_T)$ from negative to positive values. Within this approach, we systematically studied how the mean values of β_s , T_{kin} , and their fluctuation width ($\sigma(\beta_s)$ and $\sigma(T_{\text{kin}})$) shape the p_T dependence of the observable. At lower mean values of β_s , $v_0(p_T)$ exhibits minimal dependence on particle mass; however, as β_s increases, a distinct mass ordering emerges, indicative of stronger radial flow effects. The $v_0(p_T)$ values transition from negative at low p_T to positive above a species-dependent separation momentum $p_{T,\text{sep}}$, which shifts to higher p_T value with increasing β_s . Additionally, an increase in the mean T_{kin} lowers the magnitude of $v_0(p_T)$, whereas fluctuations in β_s and T_{kin} enhance it.

Building on this, Bayesian parameter estimation was applied to fit the blast-wave model to the experimental data across the three centrality intervals: 10–20%, 30–40%, and 60–70%. The extracted parameters show a clear trend of decreasing β_s alongside increasing T_{kin} from central to peripheral collisions, reflecting a reduction in collective flow and earlier freeze-out in smaller systems. Correspondingly, the fluctuation widths $\sigma(\beta_s)$ and $\sigma(T_{\text{kin}})$ grow from central to peripheral collisions, indicating enhanced event-by-event variation. Model predictions derived from the best-fit parameters accurately reproduce the experimental data at low p_T , with the closest agreement observed for protons across an extended p_T range (up to 3 GeV/c), followed by kaons and pions. The results effectively demonstrate how the interplay between radial flow, thermal motion, and their event-by-event fluctuations governs the behavior of $v_0(p_T)$ across centrality intervals. Altogether, these findings establish $v_0(p_T)$ as a robust probe of the medium's thermodynamic and transport properties as well as of the dynamics of hadronization.

Key findings from this study are as follows:

- Experimental results are consistent with the hydrodynamic picture of the QGP, supporting collective expansion and quark recombination processes.
- $v_0(p_T)$ is mainly sensitive to bulk viscosity and the QCD equation of state.
- The blast-wave model incorporating event-by-event fluctuations in β_s and T_{kin} successfully reproduces the mass ordering and p_T dependence observed in data.

Bibliography

- [1] Ekkard Schnedermann, Josef Sollfrank, and Ulrich W. Heinz. “Thermal phenomenology of hadrons from 200-A/GeV S+S collisions”. *Phys. Rev. C* 48 (1993), pp. 2462–2475. arXiv: [nucl-th/9307020](#).
- [2] L. Adamczyk et al. “Bulk Properties of the Medium Produced in Relativistic Heavy-Ion Collisions from the Beam Energy Scan Program”. *Phys. Rev. C* 96.4 (2017), p. 044904. arXiv: [1701.07065 \[nucl-ex\]](#).
- [3] Shreyasi Acharya et al. “Production of charged pions, kaons, and (anti-)protons in Pb-Pb and inelastic pp collisions at $\sqrt{s_{NN}} = 5.02$ TeV”. *Phys. Rev. C* 101.4 (2020), p. 044907. arXiv: [1910.07678 \[nucl-ex\]](#).
- [4] Björn Schenke, Chun Shen, and Derek Teaney. “Transverse momentum fluctuations and their correlation with elliptic flow in nuclear collision”. *Phys. Rev. C* 102.3 (2020), p. 034905. arXiv: [2004.00690 \[nucl-th\]](#).
- [5] Tribhuban Parida, Rupam Samanta, and Jean-Yves Ollitrault. “Probing collectivity in heavy-ion collisions with fluctuations of the p_T spectrum”. *Phys. Lett. B* 857 (2024), p. 138985. arXiv: [2407.17313 \[nucl-th\]](#).
- [6] C. Adler et al. “Identified particle elliptic flow in Au + Au collisions at $\sqrt{s_{NN}} = 130$ GeV”. *Phys. Rev. Lett.* 87 (2001), p. 182301. arXiv: [nucl-ex/0107003](#).
- [7] S. S. Adler et al. “Elliptic flow of identified hadrons in Au+Au collisions at $\sqrt{s_{NN}} = 200$ GeV”. *Phys. Rev. Lett.* 91 (2003), p. 182301. arXiv: [nucl-ex/0305013](#).
- [8] Betty Bezverkhny Abelev et al. “Elliptic flow of identified hadrons in Pb-Pb collisions at $\sqrt{s_{NN}} = 2.76$ TeV”. *JHEP* 06 (2015), p. 190. arXiv: [1405.4632 \[nucl-ex\]](#).
- [9] Shreyasi Acharya et al. “Anisotropic flow and flow fluctuations of identified hadrons in Pb–Pb collisions at $\sqrt{s_{NN}} = 5.02$ TeV”. *JHEP* 05 (2023), p. 243. arXiv: [2206.04587 \[nucl-ex\]](#).
- [10] A. Adare et al. “Measurement of the higher-order anisotropic flow coefficients for identified hadrons in Au+Au collisions at $\sqrt{s_{NN}} = 200$ GeV”. *Phys. Rev. C* 93.5 (2016), p. 051902. arXiv: [1412.1038 \[nucl-ex\]](#).

- [11] Jaroslav Adam et al. “Higher harmonic flow coefficients of identified hadrons in Pb-Pb collisions at $\sqrt{s_{\text{NN}}} = 2.76$ TeV”. *JHEP* 09 (2016), p. 164. arXiv: [1606.06057 \[nucl-ex\]](#).
- [12] P. Huovinen et al. “Radial and elliptic flow at RHIC: Further predictions”. *Phys. Lett. B* 503 (2001), pp. 58–64. arXiv: [hep-ph/0101136](#).
- [13] D. Teaney, J. Lauret, and Edward V. Shuryak. “Flow at the SPS and RHIC as a quark gluon plasma signature”. *Phys. Rev. Lett.* 86 (2001), pp. 4783–4786. arXiv: [nucl-th/0011058](#).
- [14] Jean-Yves Ollitrault. “Relativistic hydrodynamics for heavy-ion collisions”. *Eur. J. Phys.* 29 (2008), pp. 275–302. arXiv: [0708.2433 \[nucl-th\]](#).
- [15] Nicolas Borghini and Jean-Yves Ollitrault. “Momentum spectra, anisotropic flow, and ideal fluids”. *Phys. Lett. B* 642 (2006), pp. 227–231. arXiv: [nucl-th/0506045](#).
- [16] Morad Aaboud et al. “Measurement of the azimuthal anisotropy of charged particles produced in $\sqrt{s_{\text{NN}}} = 5.02$ TeV Pb+Pb collisions with the ATLAS detector”. *Eur. Phys. J. C* 78.12 (2018), p. 997. arXiv: [1808.03951 \[nucl-ex\]](#).
- [17] Jiaxuan Gong, Hendrik Roch, and Chun Shen. “A Gaussian Process Generative Model for QCD Equation of State” (Oct. 2024). arXiv: [2410.22160 \[nucl-th\]](#).
- [18] Shreyasi Acharya et al. “Long-range transverse momentum correlations and radial flow in Pb–Pb collisions at the LHC” (Apr. 2025). arXiv: [2504.04796 \[nucl-ex\]](#).
- [19] Xin-Nian Wang and Miklos Gyulassy. “HIJING: A Monte Carlo model for multiple jet production in p p, p A and A A collisions”. *Phys. Rev. D* 44 (1991), pp. 3501–3516.
- [20] V. Topor Pop et al. “Baryon junction loops and the baryon-meson anomaly at high energies”. *Phys. Rev. C* 70 (2004), p. 064906. arXiv: [nucl-th/0407095](#).
- [21] René Brun et al. “GEANT Detector Description and Simulation Tool”. *CERN-W5013* (Oct. 1994).
- [22] “Centrality determination in heavy ion collisions”. *ALICE-PUBLIC-2018-011* (Aug. 2018).

- [23] Heikki Mäntysaari et al. “Probing nuclear structure of heavy ions at energies available at the CERN Large Hadron Collider”. *Phys. Rev. C* 110.5 (2024), p. 054913. arXiv: [2409.19064 \[nucl-th\]](#).
- [24] Bjoern Schenke, Prithwish Tribedy, and Raju Venugopalan. “Fluctuating Glasma initial conditions and flow in heavy ion collisions”. *Phys. Rev. Lett.* 108 (2012), p. 252301. arXiv: [1202.6646 \[nucl-th\]](#).
- [25] Bjoern Schenke, Sangyong Jeon, and Charles Gale. “(3+1)D hydrodynamic simulation of relativistic heavy-ion collisions”. *Phys. Rev. C* 82 (2010), p. 014903. arXiv: [1004.1408 \[hep-ph\]](#).
- [26] S. A. Bass et al. “Microscopic models for ultrarelativistic heavy ion collisions”. *Prog. Part. Nucl. Phys.* 41 (1998), pp. 255–369. arXiv: [nucl-th/9803035](#).
- [27] M. Bleicher et al. “Relativistic hadron hadron collisions in the ultrarelativistic quantum molecular dynamics model”. *J. Phys. G* 25 (1999), pp. 1859–1896. arXiv: [hep-ph/9909407](#).
- [28] A. Bazavov et al. “Equation of state in (2+1)-flavor QCD”. *Phys. Rev. D* 90 (2014), p. 094503. arXiv: [1407.6387 \[hep-lat\]](#).
- [29] Peter F. Kolb and Ulrich W. Heinz. “Hydrodynamic description of ultrarelativistic heavy ion collisions” (May 2003). Ed. by Rudolph C. Hwa and Xin-Nian Wang, pp. 634–714. arXiv: [nucl-th/0305084](#).
- [30] Jacquelyn Noronha-Hostler et al. “Event-by-event hydrodynamics + jet energy loss: A solution to the $R_{AA} \otimes v_2$ puzzle”. *Phys. Rev. Lett.* 116.25 (2016), p. 252301. arXiv: [1602.03788 \[nucl-th\]](#).
- [31] R. J. Fries et al. “Hadron production in heavy ion collisions: Fragmentation and recombination from a dense parton phase”. *Phys. Rev. C* 68 (2003), p. 044902. arXiv: [nucl-th/0306027](#).
- [32] Jonah E. Bernhard et al. “Applying Bayesian parameter estimation to relativistic heavy-ion collisions: simultaneous characterization of the initial state and quark-gluon plasma medium”. *Phys. Rev. C* 94.2 (2016), p. 024907. arXiv: [1605.03954 \[nucl-th\]](#).

- [33] Jonah E. Bernhard, J. Scott Moreland, and Steffen A. Bass. “Bayesian estimation of the specific shear and bulk viscosity of quark–gluon plasma”. *Nature Phys.* 15.11 (2019), pp. 1113–1117.
- [34] J. Scott Moreland, Jonah E. Bernhard, and Steffen A. Bass. “Alternative ansatz to wounded nucleon and binary collision scaling in high-energy nuclear collisions”. *Phys. Rev. C* 92.1 (2015), p. 011901. arXiv: [1412.4708 \[nucl-th\]](#).
- [35] Swati Saha, Ranbir Singh, and Bedangadas Mohanty. “pT-differential radial flow in a blast-wave model”. *Phys. Rev. C* 112.2 (2025), p. 024902. arXiv: [2505.19697 \[nucl-ex\]](#).
- [36] A. Bazavov et al. “The chiral and deconfinement aspects of the QCD transition”. *Phys. Rev. D* 85 (2012), p. 054503. arXiv: [1111.1710 \[hep-lat\]](#).

Measurement of correlations among conserved charges

Contents

6.1	Introduction	164
6.2	Observable	170
6.3	Analysis details	171
6.4	Results and discussions	186
6.5	Summary	202
6.6	Outlook	203

Baryon number, electric charge, and strangeness are fundamental quantities preserved in strong interactions due to underlying QCD symmetries. Studying the interplay of these quantum numbers in heavy-ion collisions offers a powerful means to probe the properties of strongly interacting matter. In particular, fluctuations and correlations of net-conserved charges such as the net-electric charge (Q), the net-baryon (B), and the net-strangeness (S) numbers provide key insights into the QCD phase structure [1–5]. These quantities are

defined event-by-event as the difference between the number of particles and antiparticles carrying the respective quantum numbers. Practically, net-protons, net-kaons, and net-charged particles are used as proxies for net-baryon, net-strangeness, and net-electric charge, with their fluctuations reflecting the underlying dynamics.

In this chapter, we present a detailed study of correlations of these conserved charges in Pb–Pb collisions at $\sqrt{s_{\text{NN}}} = 5.02$ TeV. The discussion begins with the theoretical motivation and methodology, followed by results and discussions. The measurements are confronted with theoretical expectations to quantify the effects of resonance decays, global conservation laws, and medium-induced modifications, thereby advancing our understanding of QCD matter at LHC energies.

6.1 Introduction

6.1.1 Theoretical motivation

In lattice QCD, fluctuations and correlations of conserved charges are expressed through generalized susceptibilities, which are derivatives of the reduced pressure (P/T^4) with respect to the chemical potentials associated with baryon, strangeness, and electric charge (μ_B , μ_S , and μ_Q) as given by,

$$\chi_{B,Q,S}^{lmn} = \left[\frac{\partial^{(l+m+n)} (P/T^4)}{\partial^l (\mu_B/T) \partial^m (\mu_Q/T) \partial^n (\mu_S/T)} \right]_{(\mu_B, \mu_Q, \mu_S)=0} \quad (6.1)$$

where (l, m, n) represents the order of susceptibility and T is the temperature. These susceptibilities are sensitive to the effective degrees of freedom in the medium: in the hadronic phase, they reflect the integer-valued conserved charges carried by hadrons, while in the deconfined phase they reveal the fractional charges carried by quarks. Henceforth, the study of correlations among conserved charges in experiments is strongly motivated by their

direct connection to fundamental QCD thermodynamic susceptibilities. Mathematically, this relationship is expressed as

$$\chi_{B,Q,S}^{lmn} = \frac{1}{VT^3} \kappa_{B,Q,S}^{lmn} \quad (6.2)$$

with V being the volume of the system under consideration. In this work, we have focused specifically on the second-order susceptibilities, which are directly related to the variances and covariances among the conserved charge distributions. If we expand Eq. 6.2, it can then be written as

$$\begin{pmatrix} \chi_B^2 & \chi_{B,Q}^{11} & \chi_{B,S}^{11} \\ \chi_{Q,B}^{11} & \chi_Q^2 & \chi_{Q,S}^{11} \\ \chi_{S,B}^{11} & \chi_{S,Q}^{11} & \chi_S^2 \end{pmatrix} = \frac{1}{VT^3} \begin{pmatrix} \kappa_B^2 & \kappa_{B,Q}^{11} & \kappa_{B,S}^{11} \\ \kappa_{Q,B}^{11} & \kappa_Q^2 & \kappa_{Q,S}^{11} \\ \kappa_{S,B}^{11} & \kappa_{S,Q}^{11} & \kappa_S^2 \end{pmatrix}. \quad (6.3)$$

In Eq. 6.3, the diagonal terms $(\kappa_B^2, \kappa_Q^2, \kappa_S^2)$ correspond to variances of net-baryon, net-charge, and net-strangeness distributions, respectively. These variances quantify the magnitude of event-by-event fluctuations in each conserved charge. The off-diagonal terms $(\kappa_{B,Q}^{11}, \kappa_{B,S}^{11}, \kappa_{Q,B}^{11}, \kappa_{Q,S}^{11}, \kappa_{S,B}^{11}, \kappa_{S,Q}^{11})$ represent the covariances between different pairs of conserved charges, capturing their mutual correlations. Due to the inherent symmetry of covariance matrices, these off-diagonal terms satisfy $\kappa_{Q,B}^{11} = \kappa_{B,Q}^{11}$, $\kappa_{B,S}^{11} = \kappa_{S,B}^{11}$, and $\kappa_{Q,S}^{11} = \kappa_{S,Q}^{11}$. Consequently, only three independent covariance terms exist.

Building on this, it is customary to consider ratios of these susceptibilities or cumulants, as such ratios eliminate the explicit dependence on V and T . This cancellation is particularly valuable since V and T are often not directly accessible in experiments. Ratios therefore provide dimensionless, volume- and temperature-independent observables that enable a more direct comparison between experimental measurements and theoretical predictions of QCD thermodynamic susceptibilities. The following conserved charge correlations are

primarily studied using these ratios:

$$C_{Q,B} = \frac{\chi_{Q,B}^{11}}{\chi_B^2} = \frac{\kappa_{Q,B}^{11}}{\kappa_B^2}, \quad (6.4)$$

$$C_{Q,S} = \frac{\chi_{Q,S}^{11}}{\chi_S^2} = \frac{\kappa_{Q,S}^{11}}{\kappa_S^2}, \quad (6.5)$$

$$C_{B,S} = \frac{\chi_{B,S}^{11}}{\chi_S^2} = \frac{\kappa_{B,S}^{11}}{\kappa_S^2}. \quad (6.6)$$

6.1.2 Experimental proxies for conserved charges

Since it is experimentally challenging to measure all baryons and strange particles on an event-by-event basis, approximate proxies are employed in the analysis. In particular, the net-proton number, defined as the difference between the number of protons and antiprotons, $\Delta p = N_p - N_{\bar{p}}$, is commonly used as a proxy for the net-baryon number, while the net-kaon number, $\Delta K = N_{K^+} - N_{K^-}$ serves as an effective proxy for net-strangeness. The net-electric charge is then constructed as the sum of the net-pion, net-kaon, and net-proton numbers, $\Delta Q = \Delta \pi + \Delta K + \Delta p$, with $\Delta \pi = N_{\pi^+} - N_{\pi^-}$.

Studies based on the Hadron Resonance Gas (HRG) model have examined the role of different hadron species in shaping both diagonal and off-diagonal susceptibilities of conserved charges [6]. Results from these studies have shown that correlations such as baryon–electric charge (BQ) and electric charge–strangeness (QS) are mainly driven by the contributions of protons and kaons, which along with pions constitute the bulk of charged particles produced in heavy-ion collisions. On the other hand, the baryon–strangeness (BS) correlation is strongly affected by strange baryons, including hyperons and multi-strange states, whose detection on an event-by-event basis is limited by reconstruction efficiencies.

6.1.3 Review of previous studies

The importance of off-diagonal cumulants in probing correlations between conserved charges was first emphasized in Ref. [7] through studies of BS correlations. In particular, the so-called ‘‘Koch ratio’’,

$$C_{B,S} = -\frac{3\chi_{B,S}^{11}}{\chi_S^2}, \quad (6.7)$$

was introduced as a sensitive probe of the degrees of freedom carrying baryon number and strangeness. A value consistent with hadronic expectations reflects strangeness bound in baryons, while deviations may indicate the onset of deconfinement where strangeness is carried by quarks. Lattice QCD calculations have since then provided rigorous and quantitative evaluations of conserved charge correlations across the QCD phase transition region [2]. At temperatures below ~ 150 MeV, the results are consistent with HRG model expectations. For temperatures above, the results obtained with LQCD relative to the corresponding HRG model results are given in Table. 6.1.

TABLE 6.1: Ratios of QCD thermodynamic susceptibilities (second-order) to corresponding HRG model results for different temperatures. The table is taken from Ref. [2].

Temperature	155 MeV	160 MeV	165 MeV	170 MeV
$\chi_B^2 / (\chi_B^2)_{\text{HRG}}$	1.049(79)	1.020(80)	0.972(72)	0.898(60)
$\chi_Q^2 / (\chi_Q^2)_{\text{HRG}}$	0.924(36)	0.895(41)	0.861(44)	0.818(41)
$\chi_S^2 / (\chi_S^2)_{\text{HRG}}$	1.240(116)	1.235(111)	1.212(106)	1.171(96)
$\chi_{B,S}^2 / (\chi_{B,S}^{11})_{\text{HRG}}$	1.353(159)	1.384(135)	1.356(116)	1.280(96)
$\chi_{B,Q}^2 / (\chi_{B,Q}^{11})_{\text{HRG}}$	0.804(86)	0.717(67)	0.633(51)	0.544(42)
$\chi_{Q,S}^2 / (\chi_{Q,S}^{11})_{\text{HRG}}$	1.139(74)	1.144(68)	1.150(67)	1.144(64)

The STAR collaboration has systematically studied these conserved charged correlations using net-protons, net-kaons, and net-pion numbers in Au+Au collisions at RHIC over the energy range $\sqrt{s_{\text{NN}}} = 7.7\text{--}200$ GeV [8]. This analysis introduced the following

ratios:

$$C_{p,K} = \frac{\kappa_{p,K}^{11}}{\kappa_K^2}, \quad C_{Q,K} = \frac{\kappa_{Q,K}^{11}}{\kappa_K^2}, \quad C_{Q,p} = \frac{\kappa_{Q,p}^{11}}{\kappa_p^2}, \quad (6.8)$$

as a proxy of BS, QS, and QB correlations as shown in Fig. 6.1. Since the off-diagonal

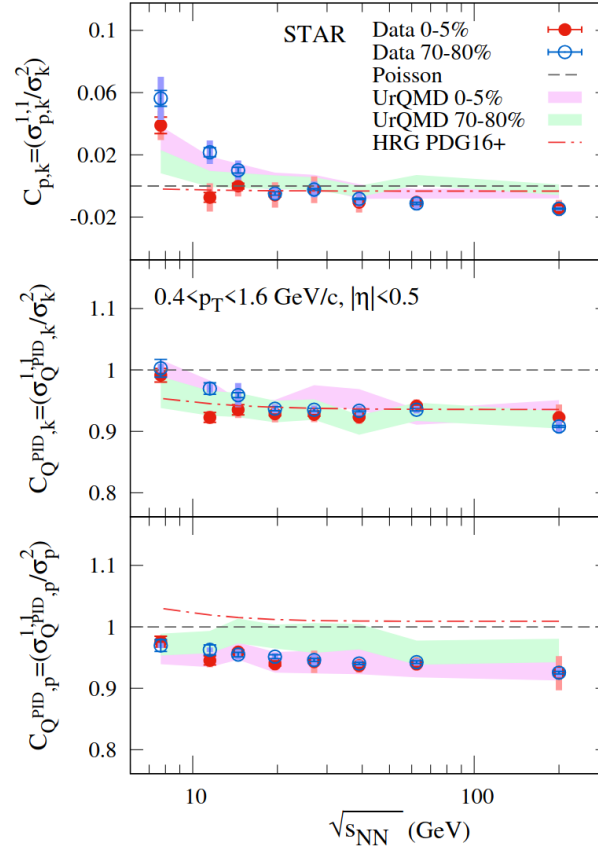


FIGURE 6.1: The correlations, $C_{p,K}$ (top), $C_{Q,K}$ (middle), and $C_{Q,p}$ (bottom) as a function of centre-of-mass energy per nucleon pair, $\sqrt{s_{NN}}$ for Au+Au collisions. The markers correspond to data points from the STAR experiment while the colored bands are from UrQMD model calculations. The results from the HRG model are shown as red dot-dashed curves, while the Poisson expectation is indicated by black dashed lines. Statistical uncertainties are represented by bars, and systematic uncertainties are illustrated using shaded boxes. This figure is taken from Ref. [8].

cumulants associated with net-electric charge, $\kappa_{Q,K}^{11}$ and $\kappa_{Q,p}^{11}$ contain contributions from the

diagonal cumulants of net-kaons and net-protons, these ratios can be expanded as

$$C_{Q,K} = \frac{\kappa_{p,K}^{11}}{\kappa_K^2} + \frac{\kappa_{\pi,K}^{11}}{\kappa_K^2} + 1, \quad (6.9)$$

$$C_{Q,p} = \frac{\kappa_{p,K}^{11}}{\kappa_p^2} + \frac{\kappa_{\pi,p}^{11}}{\kappa_p^2} + 1, \quad (6.10)$$

illustrating how correlations among different hadron species contribute to the measured observables.

6.1.4 Non-critical effects influencing cumulant measurements

The cumulants of net-particle numbers carrying conserved charges are not only sensitive to QCD thermodynamics but are also influenced by several additional effects. These effects can complicate the isolation of genuine signals of the QCD phase transition in heavy-ion collisions. For instance, correlations arise from global and local conservation of baryon number, electric charge, and strangeness, which impose constraints on particle production both for the entire system and within smaller regions of the fireball [9, 10]. Event-by-event fluctuations in the system size, commonly referred to as volume fluctuations, further modify the observed cumulants by changing particle multiplicities [11, 12]. Resonance decays, in which unstable hadrons transform into stable particles, can alter final-state correlations and potentially obscure genuine fluctuation signals [13, 14]. Additional contributions stem from initial-state fluctuations [15], caused by random variations in the positions of nucleons within the colliding nuclei, and from thermal blurring [16], which spreads out momentum distributions due to thermal motion of emitted particles. A careful separation and qualitative understanding of these non-critical contributions is therefore essential for interpreting conserved charge cumulants and for drawing reliable conclusions about the QCD phase structure.

6.2 Observable

In this section, we define the cumulants of net-particle distributions for pions, kaons, protons, and net-electric charge explicitly. The second-order diagonal cumulants of each net-particle distributions are expressed as:

$$\kappa_{\pi}^2 = \langle (\Delta\pi)^2 \rangle - \langle (\Delta\pi) \rangle^2, \quad (6.11)$$

$$\kappa_K^2 = \langle (\Delta K)^2 \rangle - \langle (\Delta K) \rangle^2, \quad (6.12)$$

$$\kappa_p^2 = \langle (\Delta p)^2 \rangle - \langle (\Delta p) \rangle^2, \quad (6.13)$$

$$\kappa_Q^2 = \langle (\Delta Q)^2 \rangle - \langle (\Delta Q) \rangle^2, \quad (6.14)$$

while the off-diagonal cumulants are given by

$$\kappa_{\pi,K}^{11} = \langle (\Delta\pi\Delta K) \rangle - \langle (\Delta\pi) \rangle \langle (\Delta K) \rangle, \quad (6.15)$$

$$\kappa_{\pi,p}^{11} = \langle (\Delta\pi\Delta p) \rangle - \langle (\Delta\pi) \rangle \langle (\Delta p) \rangle, \quad (6.16)$$

$$\kappa_{p,K}^{11} = \langle (\Delta p\Delta K) \rangle - \langle (\Delta p) \rangle \langle (\Delta K) \rangle, \quad (6.17)$$

$$\kappa_{Q,K}^{11} = \langle (\Delta Q\Delta K) \rangle - \langle (\Delta Q) \rangle \langle (\Delta K) \rangle, \quad (6.18)$$

$$\kappa_{Q,p}^{11} = \langle (\Delta Q\Delta p) \rangle - \langle (\Delta Q) \rangle \langle (\Delta p) \rangle. \quad (6.19)$$

The angular brackets $\langle \dots \rangle$ in the above equations indicate an average calculated over the full set of collision events under study. Therefore, the net-particle numbers $\Delta\pi$, ΔK , Δp , and ΔQ are measured on an event-by-event basis and form the foundation for calculating the cumulants.

6.3 Analysis details

This section outlines the main steps followed to analyze the correlations of net-pions, net-kaons, net-protons, and net-electric charge using experimental data. The analysis begins with a detailed evaluation of particle sample purity to ensure accurate identification of the relevant species. Subsequently, the centrality bin width correction is applied that reduces the impact of volume fluctuations that can bias the correlation results. We then assess the effects of detector inefficiencies on net-particle multiplicities and implement efficiency corrections for the cumulants accordingly. The robustness of these corrections is also verified using Monte Carlo (MC) closure tests. Finally, all significant sources of systematic uncertainties are identified and their contributions to the total uncertainty of the correlation measurements are quantified.

6.3.1 Purity of identified samples

The purity of pions, kaons, and protons was evaluated as a function of p_T , as shown in Fig. 6.2. The results cover up to a maximum p_T of 2 GeV/c, which is the upper limit on p_T of particles used for the analysis. Within the p_T range relevant for this study, the integrated purities for pions, kaons, and protons are found to be approximately 99.8%, 98.5%, and 99.8% respectively. These high purity values indicate minimal contamination from misidentified particles, thereby significantly enhancing the reliability of the measured cumulants and correlation observables.

6.3.2 Centrality bin-width correction

Centrality bin width correction (CBWC) is a crucial procedure used to mitigate the effect of volume fluctuations that arise due to the finite size of centrality bins in heavy-ion collision

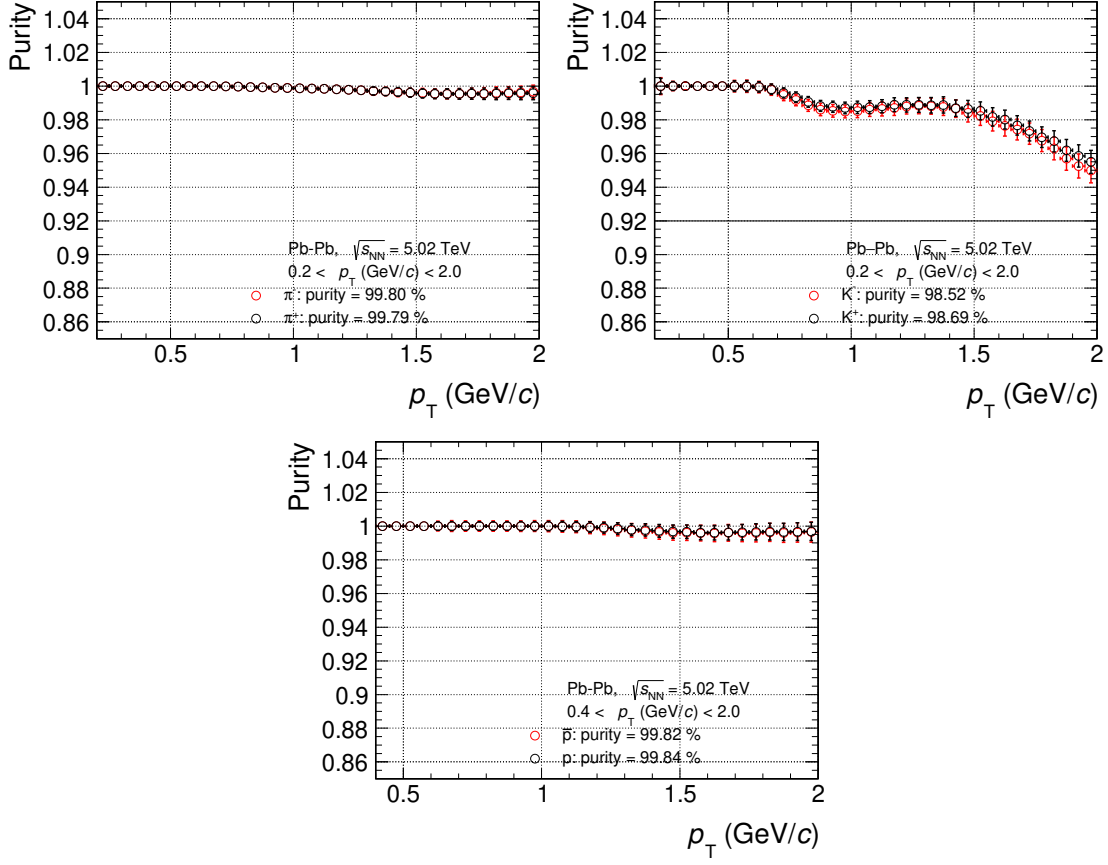


FIGURE 6.2: The p_T dependence of purities of pions (top-left), kaons (top-right), and protons (bottom) up to 2 GeV/c in Pb–Pb collisions at $\sqrt{s_{NN}} = 5.02$ TeV. The black markers represent particle (π^+ , K^+ , and p) while red markers represent anti-particle (π^- , K^- , and \bar{p}), and the integrated purity values for the respective particle are given in the legend.

analyses. Within a wide centrality interval, the number of participating nucleons—and therefore the system volume—can vary, potentially biasing the measurement of fluctuations and correlations of conserved charges. To address this, CBWC subdivides each centrality bin into finer sub-bins, calculates the cumulants within these smaller bins, and then combines the results. The cumulant for the full centrality bin is obtained as a weighted sum of the sub-bin cumulants using the relation:

$$\kappa_n = \frac{\sum_a \kappa_{n,a} N_a}{\sum_a N_a}, \quad (6.20)$$

where $\kappa_{n,a}$ is the n^{th} order cumulant calculated in the a^{th} sub-bin, and N_a is the corresponding number of events.

In this analysis, cumulants were first evaluated in narrow 1% centrality sub-bins and then combined using CBWC to obtain results for broader 5% centrality intervals. Figure 6.3 illustrates the comparison of cumulants obtained for different final bin sizes: 2%, 4%, 5% and 10%, all incorporating CBWC down to 1% sub-bins. The results for different centrality bin size lie on top of each other and no deviation is obtained. This implies that CBWC effectively eliminated volume fluctuation for the case shown. Furthermore, Fig. 6.4 presents a comparison between results with and without CBWC. The consistency observed in both cases suggests that, for the observables considered in this analysis, the impact of volume fluctuations is negligible.

6.3.3 Detector efficiencies and correction of cumulants

Detector efficiencies are an important consideration in heavy-ion collision experiments, as even small inefficiencies can distort the measured net-particle distributions and bias the cumulants extracted from them. Figure 6.5 illustrates this effect by showing two-dimensional event-by-event correlations between generated and reconstructed net-particle multiplicities for pions, kaons, and protons in Pb–Pb collisions at $\sqrt{s_{\text{NN}}} = 5.02$ TeV. The generated net-particle multiplicities correspond to HIJING-simulated events [17], while the reconstructed values are obtained from the same events after being propagated through the ALICE detector simulation with GEANT3 [18] and processed using the same reconstruction procedures as applied to real data. The spread around the diagonal line reflects the impact of detector inefficiencies and reconstruction effects, which become more pronounced for kaons and protons compared to pions due to their lower production rates and different interaction cross section. To account for these effects, efficiency corrections

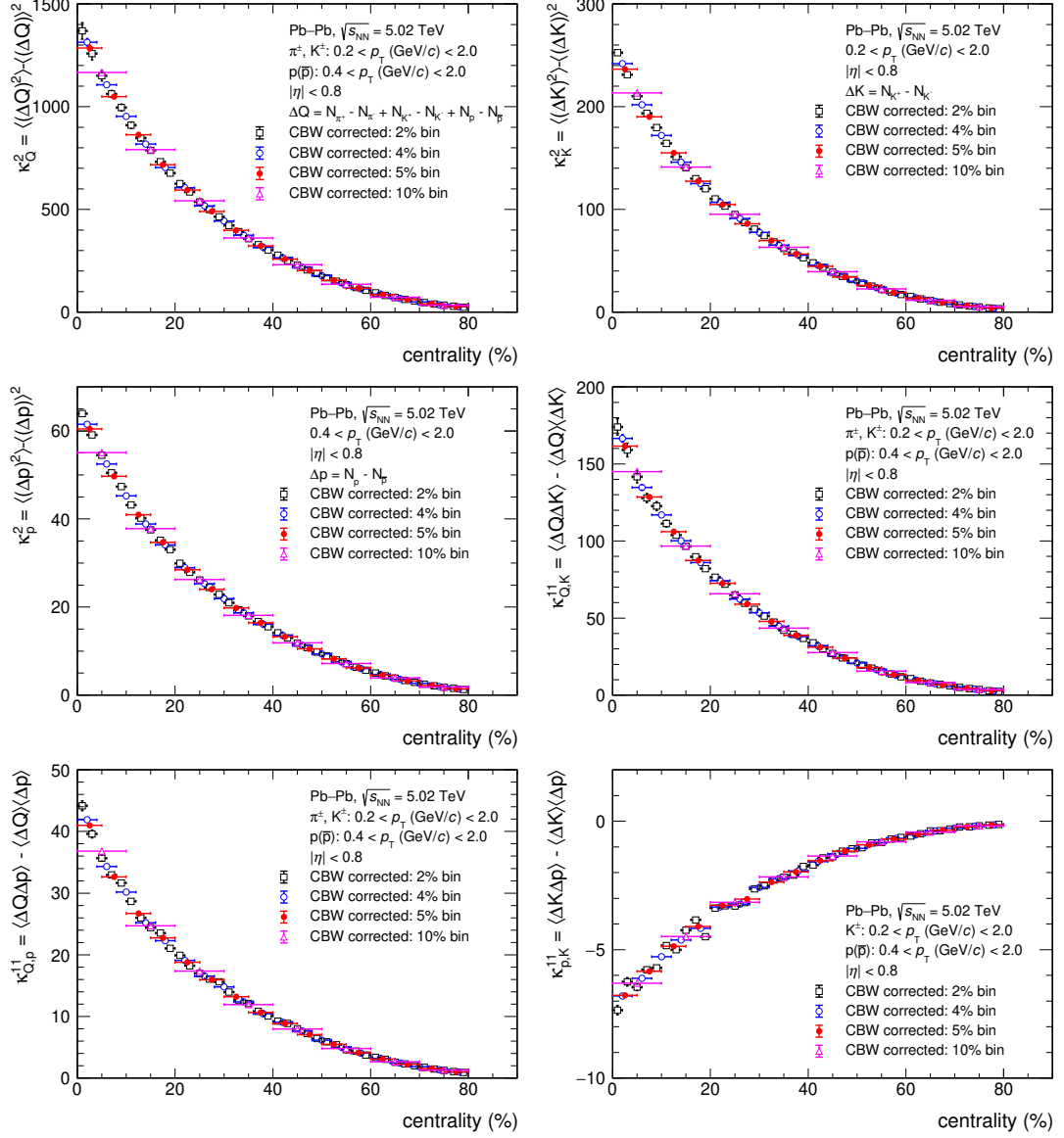


FIGURE 6.3: The centrality dependence of second-order cumulants of net-charge, net-kaon and net-proton in Pb-Pb collisions at $\sqrt{s_{NN}} = 5.02$ TeV. The different colored markers represent different centrality bin width.

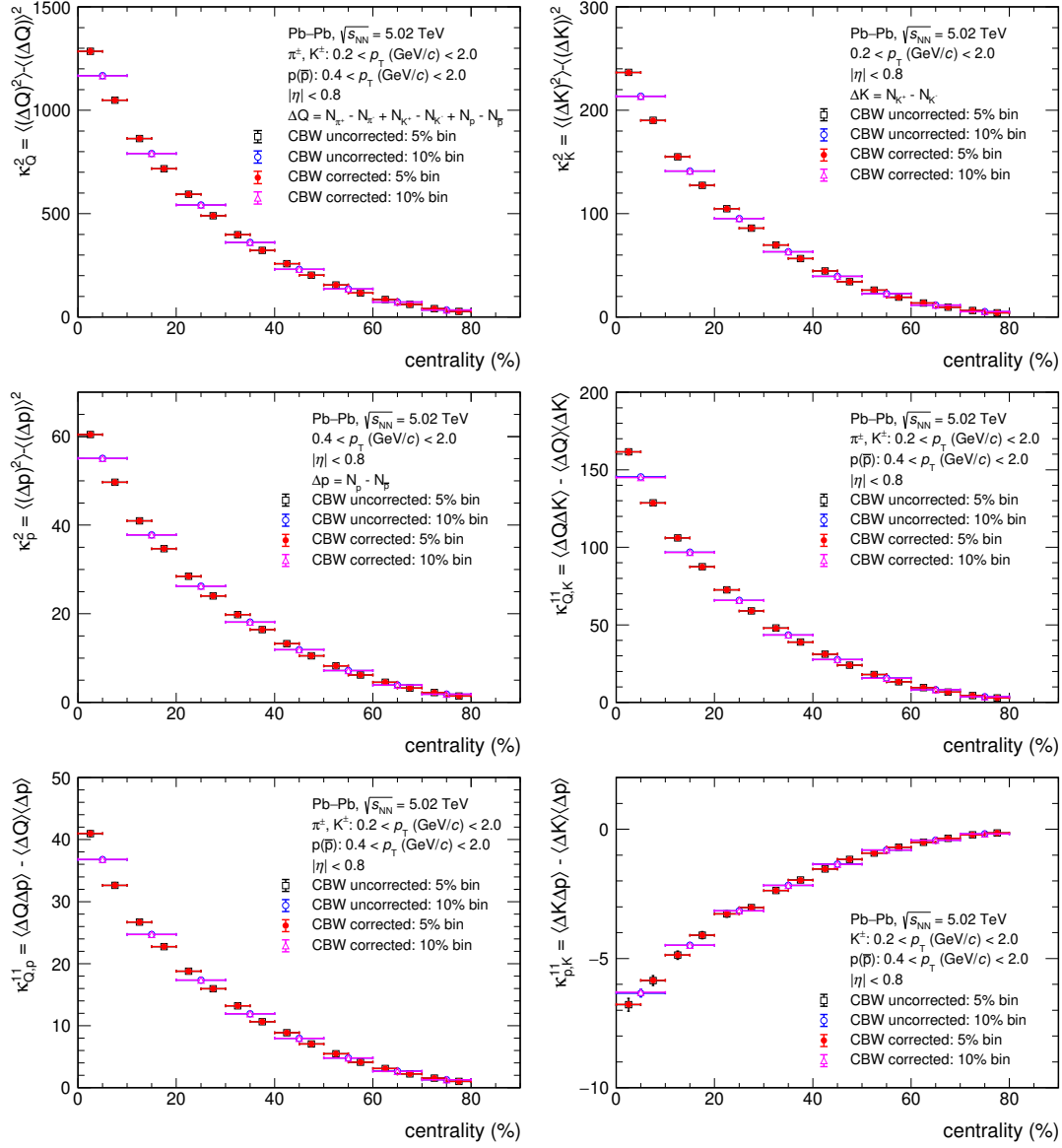


FIGURE 6.4: Comparison of centrality bin width (CBW) corrected and uncorrected results of second-order cumulants of net-charge, net-kaon and net-proton as a function of centrality in Pb-Pb collisions at $\sqrt{s_{NN}} = 5.02$ TeV.

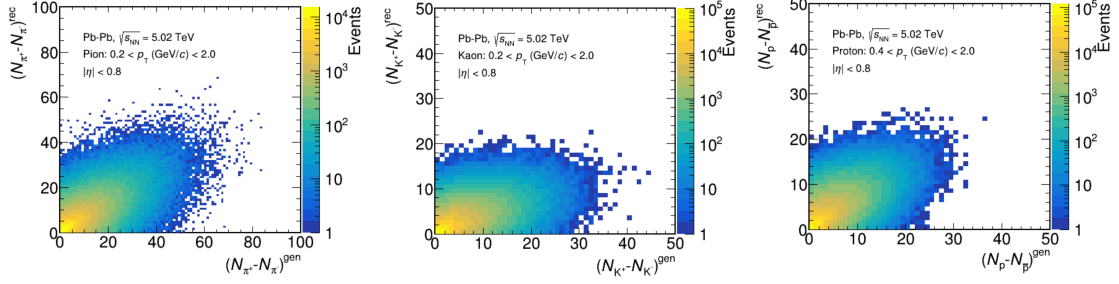


FIGURE 6.5: Two-dimensional event-by-event distributions correlating generated and reconstructed net-particle numbers in Pb–Pb collisions at $\sqrt{s_{NN}} = 5.02$ TeV, obtained using the HIJING event generator. From left to right, the panels correspond to net-pion, net-kaon, and net-proton multiplicities.

are applied using well-established techniques based on binomial response of the detector. In this approach, the measured multiplicity distribution is related to the true underlying distribution through a binomial probability characterized by the detector efficiency, ϵ . The efficiency corrected cumulants of net-particle numbers are then obtained from the measured particle numbers and efficiencies using analytical relations as provided in Refs. [19, 20]. The correction procedure is implemented in two stages: first, detection efficiencies for particles and antiparticles of each species are extracted independently as functions of p_T in each centrality class. In the second stage, the diagonal and off-diagonal cumulants calculated from reconstructed tracks are corrected on a track-by-track basis using the efficiencies together with the analytical expressions.

The efficiencies are calculated as the ratio of the number of reconstructed and identified particles ($N_{\text{rec,PID}}$) to that actually produced (N_{gen}) within the chosen kinematic acceptance, defined as:

$$\epsilon(p_T) = \frac{N_{\text{rec,PID}}(p_T)}{N_{\text{gen}}(p_T)}. \quad (6.21)$$

Figures 6.6, 6.7, and 6.8 show the p_T -dependent efficiencies for pions, kaons, and protons, obtained separately for particles and antiparticles in different centrality intervals. The efficiencies vary significantly with p_T and show a mild centrality dependence: for example,

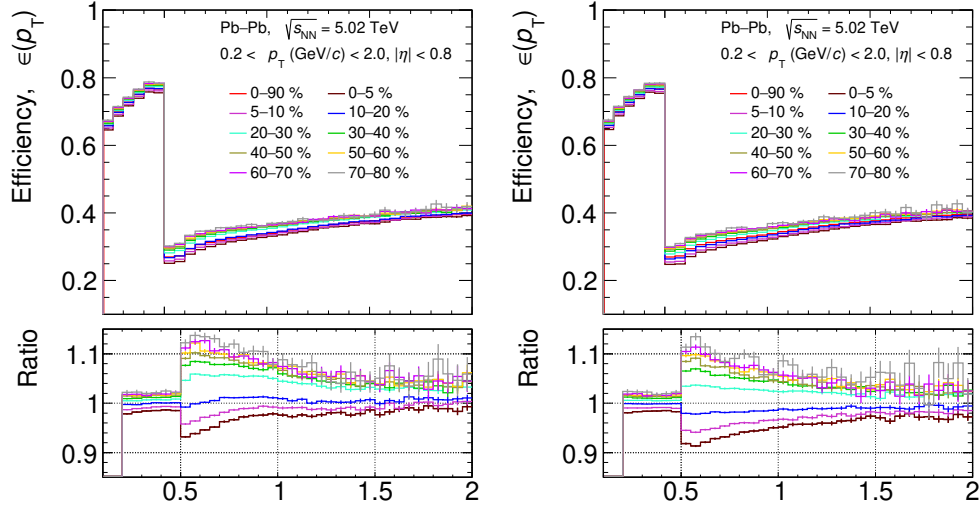


FIGURE 6.6: The p_T dependence of efficiency for pions, π^+ (left) and π^- (right), across different centrality intervals in Pb-Pb collisions at $\sqrt{s_{NN}} = 5.02$ TeV. The bottom panel shows the ratio of efficiencies in a given centrality interval relative to those in the 0-90% interval.

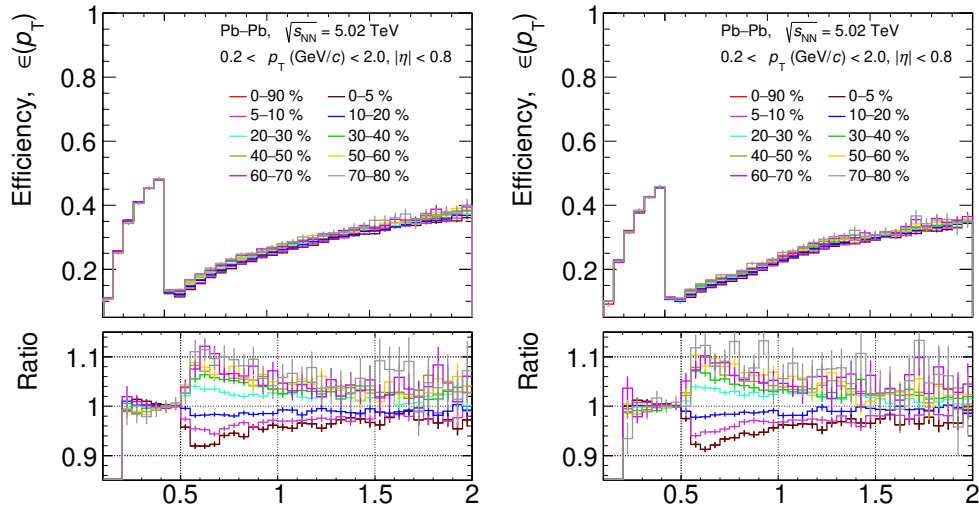


FIGURE 6.7: The p_T dependence of efficiency for pions, K^+ (left) and K^- (right), across different centrality intervals in Pb-Pb collisions at $\sqrt{s_{NN}} = 5.02$ TeV. The bottom panel shows the ratio of efficiencies in a given centrality interval relative to those in the 0-90% interval.

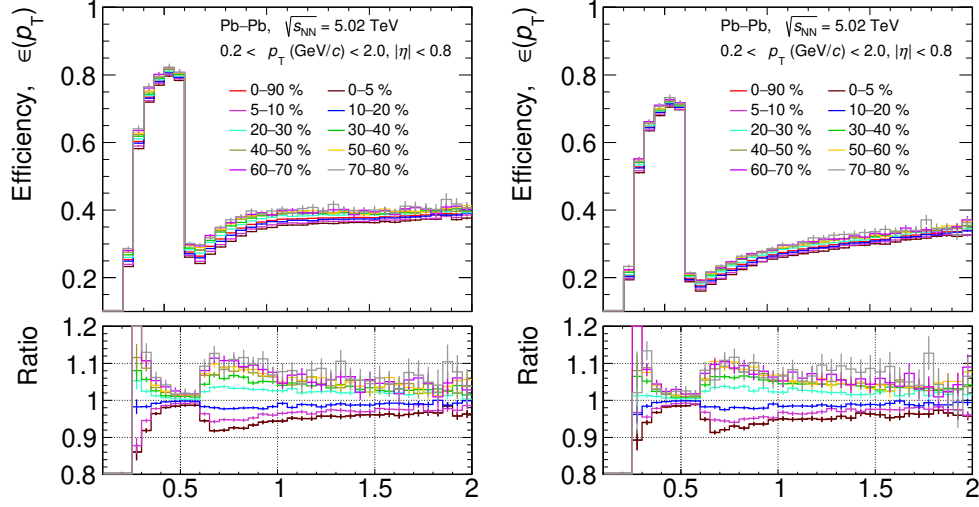


FIGURE 6.8: The p_T dependence of efficiency for pions, p (left) and \bar{p} (right), across different centrality intervals in Pb–Pb collisions at $\sqrt{s_{NN}} = 5.02$ TeV. The bottom panel shows the ratio of efficiencies in a given centrality interval relative to those in the 0–90% interval.

at $p_T \approx 0.5$ GeV/ c , the selection efficiencies reach about 78% for pions, 50% for kaons, and 80% for protons; while at $p_T \approx 1.0$ GeV/ c , they decrease to roughly 38%, 30%, and 40%, respectively. This trend reflects the combined effects of detector acceptance, track reconstruction efficiency, and particle identification performance across phase space. The bottom panels showing the ratio of efficiencies in different centrality intervals to the 0–90% centrality bin further demonstrates that the efficiencies vary by no more than about 10% across centrality intervals.

The corrected net-particle numbers for pions, kaons, and protons are calculated using the following relations:

$$q_{1,1}(\pi) = \sum_{i=0}^{N_{\pi^+}} \frac{1}{\epsilon_i(\pi^+)} - \sum_{j=0}^{N_{\pi^-}} \frac{1}{\epsilon_j(\pi^-)}, \quad (6.22)$$

$$q_{1,1}(K) = \sum_{i=0}^{N_{K^+}} \frac{1}{\epsilon_i(K^+)} - \sum_{j=0}^{N_{K^-}} \frac{1}{\epsilon_j(K^-)}. \quad (6.23)$$

and

$$q_{1,1}(p) = \sum_{i=0}^{N_p} \frac{1}{\epsilon_i(p)} - \sum_{j=0}^{N_{\bar{p}}} \frac{1}{\epsilon_j(\bar{p})}, \quad (6.24)$$

where the indices i and j label individual detected particles and antiparticles within the event. Each term $1/\epsilon_i$ corresponds to the inverse efficiency associated with the p_T and centrality of the detected particle i . This inverse efficiency weighting compensates for detector reconstruction and PID inefficiencies on a track-by-track basis. The total efficiency-corrected net-electric charge is then given by the sum over all relevant species:

$$q_{1,1}(Q) = q_{1,1}(\pi) + q_{1,1}(K) + q_{1,1}(p). \quad (6.25)$$

The efficiency corrected second-order diagonal cumulant for each net-particle number is calculated as

$$\kappa_\alpha^2 = \langle q_{1,1}(\alpha)^2 \rangle - \langle q_{1,1}(\alpha) \rangle^2 + \langle q_{2,1}(\alpha) \rangle - \langle q_{2,2}(\alpha) \rangle, \quad (6.26)$$

where α refers to any of the particle species—pions (π), kaons (K), or protons (p)—and the averages are taken over all events. The quantities $q_{2,1}(\alpha)$ and $q_{2,2}(\alpha)$ are defined by

$$q_{2,1}(\alpha) = \sum_{i=0}^{N_{\alpha^+}} \frac{1}{\epsilon_i(\alpha^+)} + \sum_{j=0}^{N_{\alpha^-}} \frac{1}{\epsilon_j(\alpha^-)} \text{ and } q_{2,2}(\alpha) = \sum_{i=0}^{N_{\alpha^+}} \frac{1}{\epsilon_i^2(\alpha^+)} + \sum_{j=0}^{N_{\alpha^-}} \frac{1}{\epsilon_j^2(\alpha^-)}, \quad (6.27)$$

where α^+ and α^- denote the particle and antiparticle of species α , respectively. For net-electric charge, the second-order diagonal cumulant, (κ_Q^2) is also obtained using Eq. 6.26 and the definitions for $q_{m,n}(Q)$:

$$q_{m,n}(Q) = q_{m,n}(\pi) + q_{m,n}(K) + q_{m,n}(p). \quad (6.28)$$

This definition is analogous to the relation for $q_{1,1}(Q)$ as in Eq. 6.25. The efficiency-corrected second-order off-diagonal cumulants for any pair of particle species ($\kappa_{\pi,p}^{11}$, $\kappa_{\pi,K}^{11}$, $\kappa_{p,K}^{11}$) are obtained using the relation

$$\kappa_{\alpha,\beta}^{11} = \langle q_{1,1}(\alpha)q_{1,1}(\beta) \rangle - \langle q_{1,1}(\alpha) \rangle \langle q_{1,1}(\beta) \rangle, \quad (6.29)$$

where α and β indicate any of the two from the considered species, π , K, or p. For net-electric charge, the off-diagonal cumulants ($\kappa_{Q,p}^{11}$ and $\kappa_{Q,K}^{11}$) are calculated as

$$\kappa_{Q,\alpha}^{11} = \langle q_{1,1}(Q)q_{1,1}(\alpha) \rangle - \langle q_{1,1}(Q) \rangle \langle q_{1,1}(\alpha) \rangle + \langle q_{2,1}(\alpha) \rangle - \langle q_{2,2}(\alpha) \rangle, \quad (6.30)$$

where α refers to either K or p.

In summary, the efficiency correction framework described here enables robust measurement of event-by-event net-particle multiplicity fluctuations in heavy-ion collisions. By systematically accounting for detector reconstruction and PID effects through analytic corrections applied at the track level, this methodology recovers the true net-particle cumulants, enabling reliable physics conclusions from the measured data.

6.3.4 Monte Carlo closure test for efficiency correction procedure

The efficiency correction methodology described in previous section is further tested and validated through a Monte Carlo (MC) closure test. For this test, we again use the simulated events generated by the HIJING event generator which are propagated through a detailed detector simulation and reconstruction framework using GEANT3, replicating the actual detector response and reconstruction performance. The net-particle cumulants are then independently calculated from both the generated (true) particle distributions and the reconstructed (detector-level) tracks corrected by the efficiency procedure (discussed in previous section).

Figure 6.9 presents the comparison of the second-order cumulants for net-pions, net-kaons, net-protons, and net-electric charge as a function of centrality. The generated cumulants (true values) are plotted alongside the reconstructed cumulants corrected for detector inefficiencies. The results demonstrate that the efficiency corrections successfully recover the true cumulants across the full centrality range within statistical uncertainties.

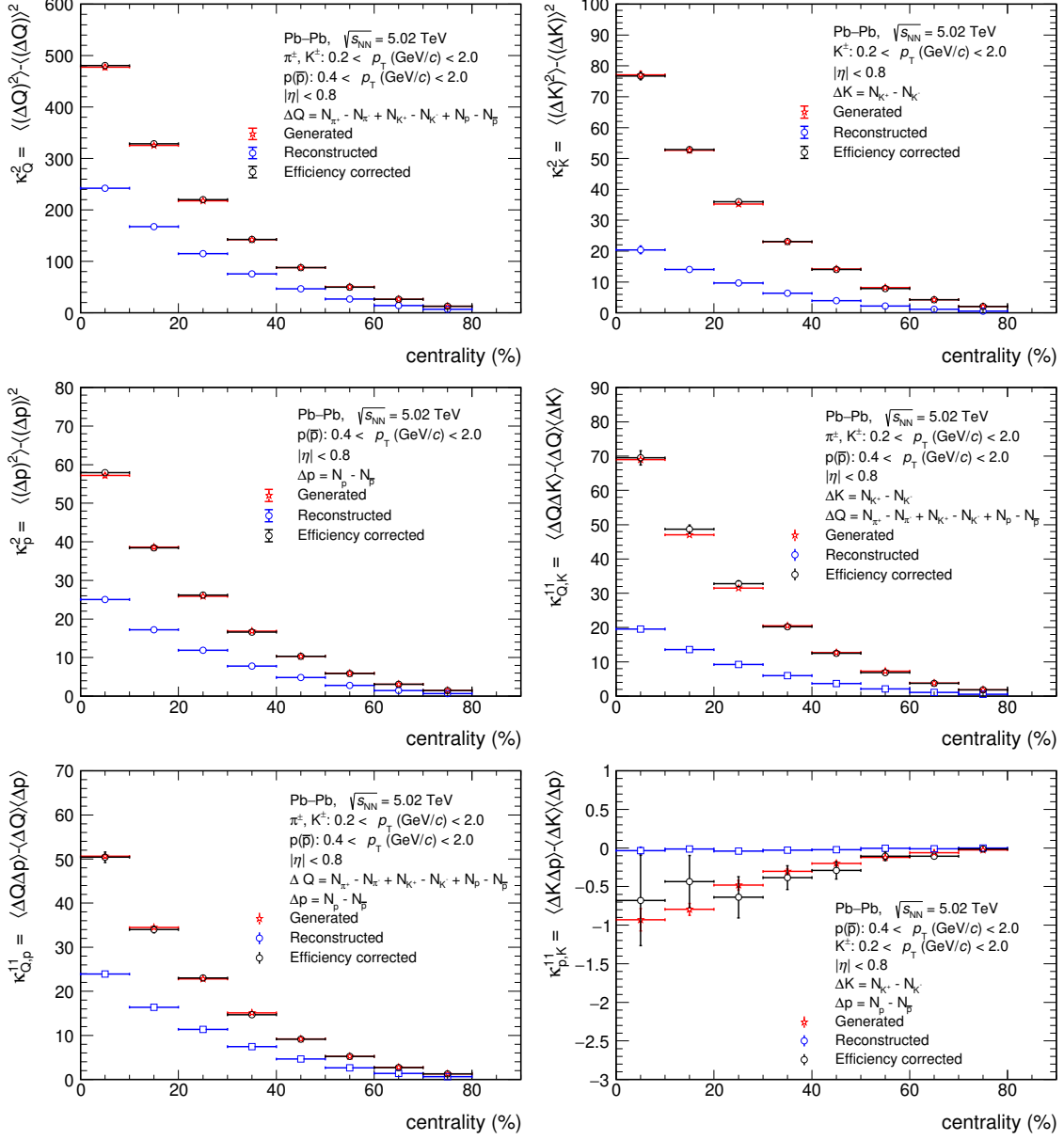


FIGURE 6.9: Results of the Monte Carlo closure test for efficiency correction procedures in Pb-Pb collisions at $\sqrt{s_{NN}} = 5.02$ TeV. Shown are the second-order diagonal and off-diagonal cumulants for net-charge, net-kaon, and net-proton distributions as a function of collision centrality. The generated cumulants (red markers) are compared to reconstructed values before (blue markers) and after (black markers) efficiency correction. The efficiency-corrected cumulants closely match the generated results, demonstrating the validity of the correction method within statistical uncertainties.

6.3.5 Systematic uncertainties

The systematic uncertainties on measured cumulants are also estimated following the general procedure discussed in Chapter 3. The cumulants and all subsequent ratios are evaluated by independently varying each of the key selection criteria. In this section, we mainly discuss the systematic uncertainty sources and their contributions.

Event selection effects are evaluated by adjusting constraints on the vertex position and the treatment of potential pileup, consistently yielding uncertainties below 2% throughout all centrality intervals. For estimating uncertainty related to centrality determination, classes are redefined using the midrapidity charged-particle multiplicity distribution [21], which introduces up to 7% uncertainty in peripheral and less than 4% in central collisions. Track selection influences are examined by systematically altering the allowed ranges for the distance of closest (DCA) approach, the minimum number of TPC space points required, and the fit quality in both the TPC and ITS systems. Increasing the threshold for TPC space points has negligible impact, while adjusting DCA constraints results in 1–3% variation. Changes to the track-fit chi-square per point introduce uncertainties below 2% for the TPC and under 4% for the ITS across all collision centralities. Particle identification uncertainties are evaluated by modifying selection criteria on $n\sigma_i^{\text{TPC}}$ and $n\sigma_i^{\text{TPC+TOF}}$ between 2σ and 2.5σ , leading to uncertainties of 3–6% depending on centrality.

Contribution from all the individual sources as well as the total system uncertainty for the three main observables, $C_{p,K}$, $C_{Q,K}$, and $C_{Q,p}$ are summarized in Table. 6.2.

6.3.6 Brief review of theoretical models used for comparison

In order to interpret the experimental measurements, it is essential to confront them with theoretical expectations. This section gives a concise description of the models used for

TABLE 6.2: Systematic uncertainty contributions to $C_{p,K}$, $C_{Q,K}$, and $C_{Q,p}$ in Pb–Pb collisions at $\sqrt{s_{NN}} = 5.02$ TeV. For each source, the range indicates the lowest and highest uncertainty values observed over all centrality intervals [22].

Sources of systematic uncertainty	$C_{p,K}$ (in %)	$C_{Q,K}$ (in %)	$C_{Q,p}$ (in %)
Vertex z -position	0.9–1.4	<0.5	<0.2
Centrality estimator	1.3–6.9	0.1–0.8	0.3–1.3
Pileup rejection	0.1–1.4	<0.3	<0.2
Space points in TPC	0.6–3.8	<0.5	<0.2
χ^2 per space point in TPC	0.7–1.2	<0.4	<0.2
χ^2 per space point in ITS	0.3–2.8	<0.4	<0.2
DCA _{xy} & DCA _z	1.6–3.9	0.4–1.2	0.3–1.0
PID	1.8–5.6	0.4–1.4	0.6–1.6
Total	5.5–8.8	0.8–2.1	1.1–1.8

comparison in this study. The cumulants are calculated in these models as a function of centrality. To investigate the physical mechanisms driving the observed correlations, the measurements are compared to predictions from three distinct theoretical frameworks: HIJING [17], EPOS LHC [23], and Thermal-FIST (denoted as TheFIST in figures) [24]. Each of these approaches provides a distinct description of collision dynamics and hadronization, and resonance decays are included in all cases. Resonance decay implementation in each of these model are also briefly discussed.

HIJING and EPOS model

The HIJING/ $B\bar{B}$ v2.0 model [25] considers nucleus–nucleus interactions as a superposition of binary nucleon–nucleon collisions. It incorporates several perturbative QCD effects such as mini-jet production, baryon junction transport, shadowing of parton distributions, and jet quenching. However, it does not include mechanisms related to thermal equilibrium or collective flow, and thus provides a non-thermal baseline for comparison.

The EPOS LHC model [23], on the other hand, embeds collective features by dividing parton ladders into two components: a dense central core and a more dilute corona. This allows it to mimic bulk medium effects in high-density regions while still treating peripheral regions differently. EPOS LHC is a tuned version of the EPOS 1.99 framework [26], but unlike the original version, it does not perform a full 3D hydrodynamic simulation followed by a hadronic cascade. Instead, it uses some parametrizations that retain an effective treatment of collectivity while simplifying the underlying dynamics.

Thermal-FIST model

Thermal-FIST represents a HRG model that employs thermal–statistical methods to describe hadronization. In this framework, hadron yields at chemical freeze-out are derived from the system’s partition function. The model depends on three key parameters: the chemical freeze-out temperature (T_{chem}), the fireball volume per unit rapidity (dV/dy), and the strangeness saturation factor (γ_s) [27, 28]. These parameters are constrained using ALICE measurements of hadron yields for different centralities [29–32], while p_T spectra are modeled using blast-wave fits [29].

This model can be implemented in two statistical ensembles: grand-canonical ensemble (GCE) and canonical ensemble (CE). While GCE enforces conservation of electric charge, baryon number, and strangeness only on average across the whole system, the CE enforces exact conservation of these charges within a defined correlation volume V_c [33, 34]. In this CE framework, V_c is often expressed as a multiple of the system’s volume per unit rapidity, dV/dy , such that $V_c = k \times dV/dy$. This construction effectively restricts the system to a rapidity interval of size k centered around midrapidity, i.e., $|y| < k/2$, thus approximating a scenario of global charge conservation limited to a reduced rapidity range [35]. The finite size and shape of this correlation volume inherently limit fluctuation measurements:

for fluctuations observed within a rapidity window $|y| < y_{\text{cut}}$, reliable descriptions are possible when the cut satisfies $|y_{\text{cut}}| \lesssim k/4$, and beyond such limits, the model's applicability becomes compromised [35]. Alternative approaches exist that characterize local charge conservation through correlation lengths between produced particles and their corresponding antiparticles in rapidity space [35–37]. In this work, the CE results are obtained using $V_c = 3dV/dy$ (unless otherwise specified), following prior parametrizations [34] that describe light-flavor hadron yields across collision systems.

Modeling of resonance decays

Although all three models include resonance decays, they differ significantly in the way these decays are implemented. In HIJING, resonances emerge from string fragmentation and decay promptly through fixed branching ratios, without any subsequent interaction with the hadronic medium [17, 25]. This treatment assumes that the decay products freely stream out without undergoing rescattering or regeneration processes. In contrast, EPOS LHC adopts a more dynamic scenario, where resonances are generated both during the early string fragmentation and at the freeze-out surface of the hydrodynamic-like core [23, 38]. These resonances decay according to their lifetimes and branching ratios, but no rescattering after decay is included. Thermal-FIST, on the other hand, samples resonances from a static thermal ensemble at chemical freeze-out and applies a full probabilistic decay chain based on branching ratios, that allows event-by-event fluctuation of the actual number of decay products [24, 39]. Two- and three-body decays are modeled isotropically in the resonance rest frame, while many-body channels are approximated [24, 39]. As in the other models, no rescattering or regeneration is considered once the decay has taken place.

These differences likely reflect the varying degrees of dynamical complexity included in resonance decay modeling, which may influence how well each model reproduces

experimental data.

6.4 Results and discussions

In this section, we present the centrality dependence of the second-order cumulants of net-proton, net-kaon, net-pion, and net-electric charge distributions, together with their off-diagonal correlations. The corresponding ratios, $C_{p,K}$, $C_{Q,K}$, and $C_{Q,p}$, which serve as experimental proxies for BS, QS, and QB correlations respectively, are discussed in detail. The measurements are performed for two independent choices of p_T intervals, denoted as Set 1 and Set 2, to investigate the sensitivity of the observables to kinematic acceptance effects. All observables have been carefully corrected for detector inefficiencies in tracking and particle identification as described in the previous section. For Set 1, positively- and negatively-charged pions and kaons are included within the range $0.2 < p_T < 2.0$ GeV/ c , while protons and antiprotons are selected with $0.4 < p_T < 2.0$ GeV/ c . In contrast, Set 2 applies a narrower acceptance window of $0.4 < p_T < 1.6$ GeV/ c uniformly to all three particle species. The full set of diagonal and off-diagonal cumulants, including κ_π^2 , κ_K^2 , κ_p^2 , κ_Q^2 , $\kappa_{p,K}^{11}$, $\kappa_{\pi,K}^{11}$, and $\kappa_{\pi,p}^{11}$, are presented in Figure 6.10 for both acceptance sets.

The observed dependence of cumulants on centrality reflects their extensive property, which causes them to grow roughly in proportion to the system volume. Both the diagonal cumulants of individual species and net-electric charge, as well as the off-diagonal cumulants among protons, pions, and kaons, show a clear sensitivity to the chosen p_T interval. This arises from acceptance effects, since the selected phase-space window directly impacts the number of particles and their correlations included in the measurement [40]. It is also important to clarify here that the measurements are not corrected for the kinematic acceptance on p_T and η . This is because the dependence of fluctuation observables on kinematic

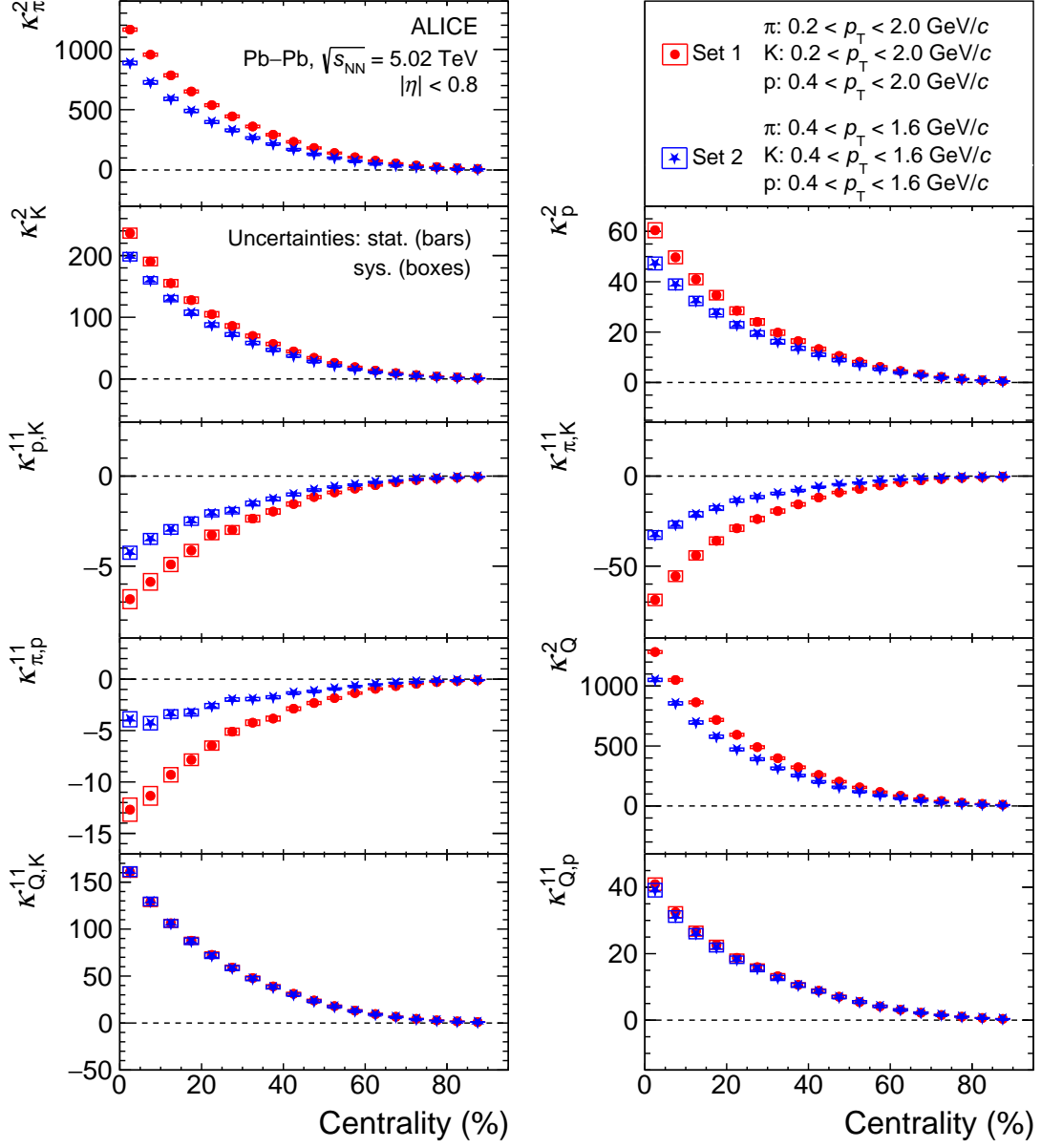


FIGURE 6.10: The second-order diagonal cumulants, κ_{α}^2 , and off-diagonal cumulants, $\kappa_{\alpha,\beta}^{11}$, for net-pion, net-kaon, net-proton, and net-electric charge distributions measured in Pb–Pb collisions at $\sqrt{s_{NN}} = 5.02$ TeV. Results are displayed as a function of centrality for two distinct p_T ranges, referred to as Set 1 and Set 2 (refer to text for details). Statistical uncertainties are indicated by vertical error bars, while systematic uncertainties are shown as open boxes. The figure is taken from Ref. [22].

intervals represents a genuine physical feature, that reflects both the sampled phase-space region and the underlying system dynamics. The considered approach is consistent with that of prior studies on fluctuations [36, 41].

In contrast to the pronounced p_T -dependent changes seen in most cumulants, the off-diagonal cumulants involving net-electric charge and kaons or protons— $\kappa_{Q,K}^{11}$ and $\kappa_{Q,p}^{11}$ —remain stable within uncertainties across both p_T selections. This effect arises from the composite nature of these cumulants, which can be expressed as sums of constituent terms:

$$\kappa_{Q,K}^{11} = \kappa_{p,K}^{11} + \kappa_{\pi,K}^{11} + \kappa_K^2 \quad \kappa_{Q,p}^{11} = \kappa_{p,K}^{11} + \kappa_{\pi,p}^{11} + \kappa_p^2. \quad (6.31)$$

The interdependence of these components leads to partial cancellations of acceptance-driven changes, resulting in overall variations smaller than those observed for individual diagonal or simpler off-diagonal cumulants.

Figure 6.11 shows the centrality dependence of the ratio observables $C_{Q,p}$, $C_{Q,K}$, and $C_{p,K}$ in the top, middle, and bottom panels respectively. Results for the broader p_T acceptance (Set 1) are shown in the left column, while those for the narrower p_T acceptance (Set 2) appear on the right. Across both p_T selections, these ratios reveal only modest variation with centrality. The relatively weak dependence on centrality aligns with the intensive nature of these ratios, which suppresses sensitivity to the system size of the collision. Intriguingly, $C_{p,K}$ remains negative across all centralities, in contrast to $C_{Q,p}$ and $C_{Q,K}$, which stay positive. This distinction follows directly from their underlying definitions, given in Eqs. 6.9 and 6.10. All off-diagonal cumulants among individual particle species exhibit a similar trend, i.e., they become increasingly negative from peripheral to central collisions, while diagonal cumulants grow more positive. Consequently, $C_{p,K}$ takes negative values. On the other hand, since $C_{Q,p}$ and $C_{Q,K}$ contain a constant unity term that offsets the negative contributions from the ratio terms, their values remain positive. Observed

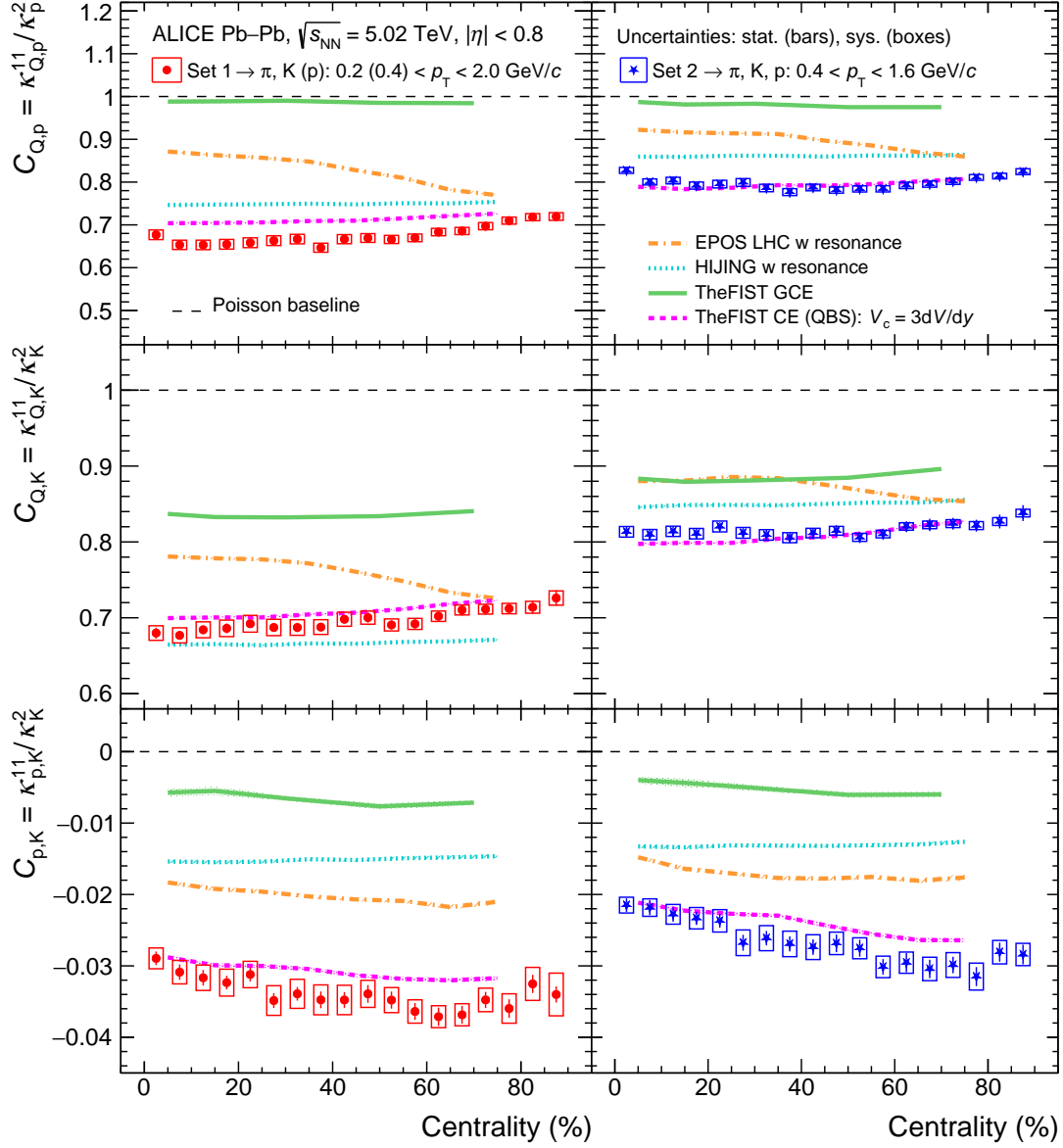


FIGURE 6.11: The cumulant ratios $C_{Q,p}$ (top panel), $C_{Q,K}$ (middle panel), and $C_{p,K}$ (bottom panel) in Pb-Pb collisions at $\sqrt{s_{NN}} = 5.02$ TeV is shown as a function of centrality, with left and right columns corresponding to two distinct p_T intervals, referred to as Set 1 and Set 2, respectively. Model predictions from HIJING [17], EPOS LHC [23], and Thermal-FIST [24] are shown as colored lines. The Thermal-FIST calculations are presented within both the grand canonical (GCE) and canonical ensemble (CE) frameworks. The CE calculations impose exact conservation of electric charge, baryon number, and strangeness within a correlation volume defined as $V_c = 3dV/dy$. Statistical uncertainties are represented by vertical bars, systematic uncertainties by open boxes, and the dashed line indicates the Poisson baseline expectation. The figure is taken from Ref. [22].

deviations from the Poisson baseline expectations—which are unity for $C_{Q,p}$ and $C_{Q,K}$, and zero for $C_{p,K}$, as expected for statistically uncorrelated particle production—are attributed to non-trivial physical effects such as collective flow, resonance decay contributions, and constraints from global charge conservation [9, 10, 13, 14, 42].

The HIJING model predictions are closer to the measured values of $C_{Q,p}$ and $C_{Q,K}$, but it struggles to reproduce the trends and magnitude of the $C_{p,K}$. This discrepancy arises likely because of incomplete modeling of resonance decays in HIJING [17, 25]. The model shows almost no change with centrality, as a consequence of its neglect of collective flow and medium effects. In comparison, the EPOS LHC model exhibits a distinct dependence on centrality, which results from the relative contributions of the dense "core" versus the less dense "corona" in its framework. While the decreasing trend of $C_{p,K}$ with centrality is successfully reproduced by the model, its predictions for $C_{Q,p}$ and $C_{Q,K}$ differ from the experimental observations. The Thermal-FIST model, when used in the GCE setup, fails to describe the data for both p_T ranges (Set 1 and Set 2) considered. However, within the CE framework—which enforces exact local conservation of charges—the model provides a significantly better match to the observed data. Notably, the CE formulation reproduces both the magnitude and centrality dependence of the correlations, especially for the narrower p_T range of Set 2. This suggests that accounting for local charge conservation is crucial for accurately modeling the measured fluctuations and correlations. Fine-tuning parameters such as the size of the correlation volume v_c in the CE framework could further improve agreement between model and data.

6.4.1 Effect of Q, B, S conservation

This section explores the role of conserved quantum numbers—Q, B, and S—in shaping the correlation observables $C_{p,K}$, $C_{Q,p}$, and $C_{Q,K}$. Figure 6.12 presents a comparison between

the experimental measurements and predictions from the Thermal-FIST model in the CE with $V_c = 3dV/dy$. Different scenarios are considered by imposing exact conservation of

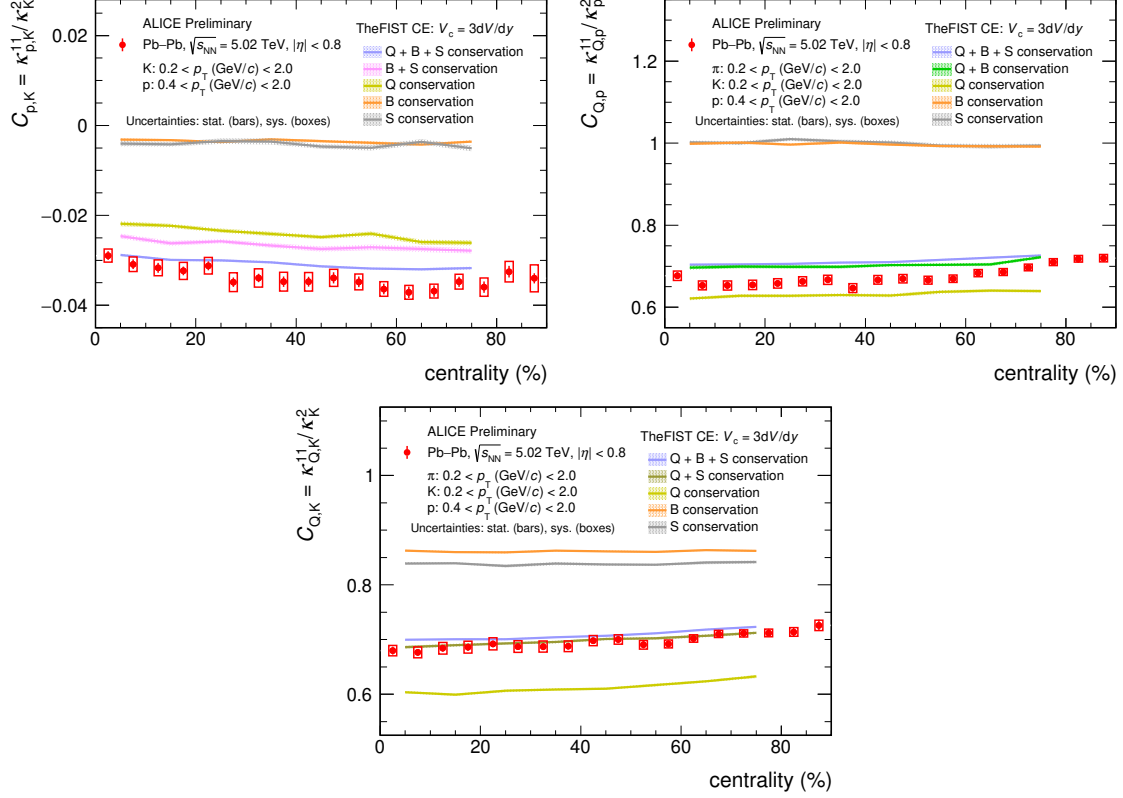


FIGURE 6.12: The centrality dependence of $C_{p,K}$ (top-left), $C_{Q,p}$ (top-right), and $C_{Q,K}$ (bottom) is presented for Pb–Pb collisions at $\sqrt{s_{NN}} = 5.02$ TeV for Set 1 p_T acceptance (π^\pm , K^\pm : $0.2 < p_T < 2.0$ GeV/c, and $p(\bar{p})$: $0.4 < p_T < 2.0$ GeV/c). The colored lines represent predictions from the Thermal-FIST (TheFIST) model in the canonical ensemble (CE), calculated with a correlation volume of $V_c = 3dV/dy$, under various conservation scenarios for Q, B, and S. Statistical uncertainties are displayed as vertical bars, while systematic uncertainties are indicated by boxes. These figures are taken from Ref. [43].

selected combinations of Q, B, and S. This study shows that the strength and shape of these correlations depend strongly on which quantum numbers are conserved. In the left panel, the data for $C_{p,K}$ are compared with CE calculations enforcing conservation of Q only, S only, B only, both B and S (B+S), and all three combined (Q+B+S). The results indicate that

enforcing Q-only conservation yields effects that are nearly indistinguishable from those obtained with B+S conservation. Similarly, the data for $C_{Q,p}$ ($C_{Q,K}$) are compared to CE predictions conserving Q only, S only, B only, Q+B (Q+S), and Q+B+S. While $C_{Q,K}$ exhibits more sensitivity to conservation of both Q and S, $C_{Q,p}$ can be described qualitatively with both Q only, and Q+B conservation. Taken together, the results suggest that Q conservation plays the most dominant role in driving the deviations of these observables from their Poissonian baselines (0 for $C_{p,K}$, 1 for $C_{Q,p}$ and $C_{Q,K}$). The best overall description of all three ratios is achieved when the CE model simultaneously enforces the conservation of Q, B, and S.

6.4.2 Estimation of CE correlation volume

This section focuses on how the observables $C_{p,K}$, $C_{Q,p}$, and $C_{Q,K}$ vary with the correlation volume in the CE framework. The V_c determines the spatial domain over which exact conservation of quantum numbers is enforced, and therefore plays a crucial role in governing the fluctuations and correlations of conserved charges. A smaller V_c corresponds to stronger local conservation effects, leading to more pronounced deviations from the Poissonian baseline, while larger values effectively weaken these constraints and bring the observables closer to the grand-canonical expectation. By performing a systematic comparison of model predictions with data across a range of V_c values, it is possible to quantitatively determine the effective correlation volume that best describes the experimental results.

In Fig. 6.13, the measurements of $C_{p,K}$, $C_{Q,p}$, and $C_{Q,K}$ (for Set 1 p_T acceptance) as a function of centrality are compared to the Thermal-FIST model calculations with V_c varying incrementally from $2dV/dy$ to $4dV/dy$. The T_{chem} is fixed at 155 MeV and the γ_s is set to unity consistently across all centrality intervals [44]. To quantify the agreement between data and model, a combined chi-squared value, χ_{combined}^2 , is calculated for each

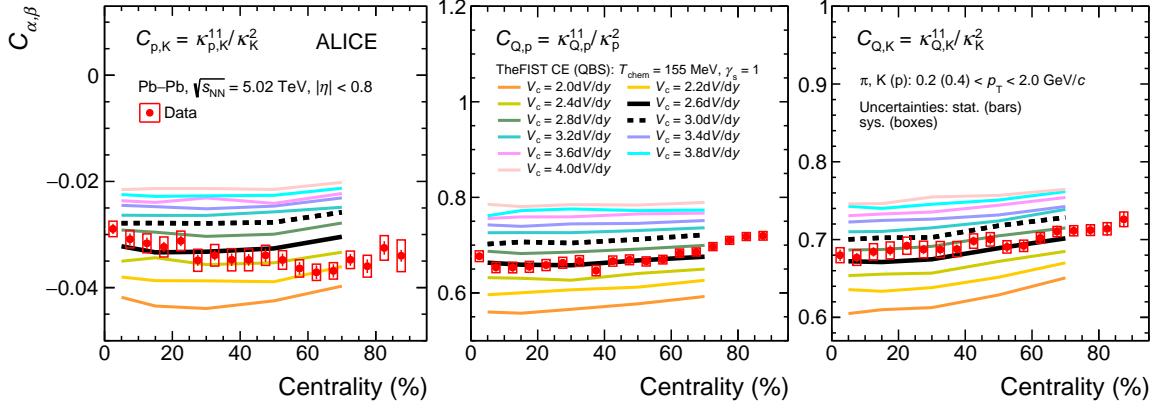


FIGURE 6.13: The centrality dependence of $C_{p,K}$, $C_{Q,p}$, and $C_{Q,K}$ is displayed for Pb–Pb collisions at $\sqrt{s_{NN}} = 5.02$ TeV is presented in the left, middle, and right panels, respectively. Model predictions from Thermal-FIST (TheFIST) [24], calculated within the canonical ensemble (CE) framework with exact conservation of Q , B , and S in a correlation volume (V_c), are superimposed as colored lines for different values of V_c . Vertical bars denote statistical errors, whereas systematic uncertainties are indicated by boxes. The figure is taken from Ref. [22].

V_c , incorporating contributions from all three correlation observables:

$$\chi_{\text{combined}}^2 = \chi_{C_{Q,p}}^2 + \chi_{C_{Q,K}}^2 + \chi_{C_{p,K}}^2. \quad (6.32)$$

The distributions of χ_{combined}^2 for both Set 1 and Set 2 p_T acceptances are shown in panel (a) of Figs. 6.14 and 6.15, respectively. The optimal V_c is identified as the value at which χ_{combined}^2 reaches its minimum. This minimum is obtained by fitting the χ_{combined}^2 distribution with a fourth-order polynomial and identifying its minimum point.

The associated statistical uncertainty is estimated from the range of V_c values over which χ_{combined}^2 increases by one unit above this minimum. Lets say, the V_c values for which $\chi_{\text{combined}}^2 = \text{MIN}(\chi_{\text{combined}}^2 + 1)$ are $V_{c,1}$ and $V_{c,2}$ in left and right of optimum V_c , then the statistical uncertainty on V_c , i.e., $\sigma_{V_c}^{\text{stat}}$ is given by

$$\sigma_{V_c}^{\text{stat}} = \frac{V_{c,2} - V_{c,1}}{2}. \quad (6.33)$$

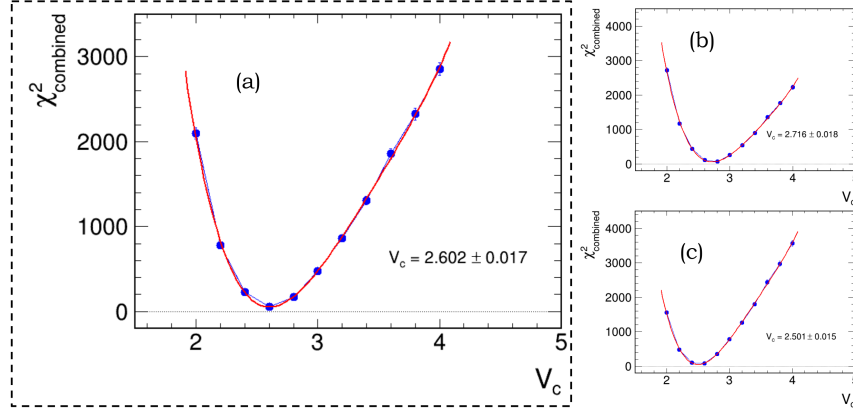


FIGURE 6.14: Dependence of the combined chi-squared, χ^2_{combined} on the correlation volume V_c for Set 1 p_T acceptance (π^\pm, K^\pm : $0.2 < p_T < 2.0$ GeV/c, and $p(\bar{p})$: $0.4 < p_T < 2.0$ GeV/c). Panel (a) presents the χ^2_{combined} distributions from fits of the observables $C_{p,K}$, $C_{Q,p}$, and $C_{Q,K}$ to the model. Panel (b) presents the χ^2 distributions obtained when the data are shifted upward by their systematic uncertainties, while panel (c) shows the corresponding case for a downward shift. The minima of χ^2_{combined} distributions in each case, which correspond to the best-fit values of V_c , are obtained by fitting the distributions with a fourth-order polynomial. The resulting minima and their associated uncertainties are marked in each panel.

To estimate the systematic uncertainty on V_c , we adopt the method used in Ref. [45], where the χ^2_{combined} values are recalculated after shifting the data points up and down by their respective systematic uncertainties. For each shifted dataset, the value of V_c that minimizes the respective χ^2_{combined} is extracted, as shown in panels (b) and (c) of Figs. 6.14 and 6.15. Half of the difference between these two V_c values is then assigned as the systematic uncertainty, $\sigma_{V_c}^{\text{sys}}$. The total uncertainty on V_c is obtained by taking quadrature sum of the statistical and systematic uncertainties, i.e., $\sigma_{V_c}^{\text{total}} = \sigma_{V_c}^{\text{stat}} + \sigma_{V_c}^{\text{sys}}$. Using this approach, the V_c is determined to be $(2.60 \pm 0.11)\text{dV/dy}$ and $(2.82 \pm 0.14)\text{dV/dy}$ for Set 1 and Set 2 p_T acceptances respectively. The extracted values provide a useful characterization of the effective correlation volume related to charge conservation; however, they should be interpreted with care. They may be affected by limitations in the current treatment of

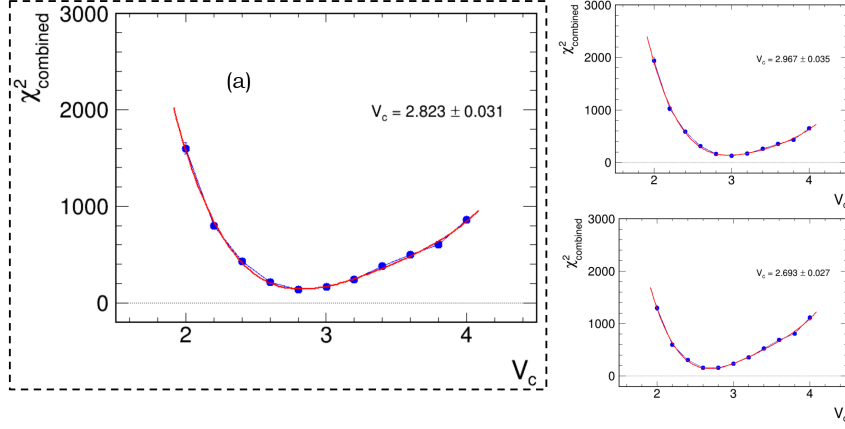


FIGURE 6.15: Dependence of the combined chi-squared, χ^2_{combined} on the correlation volume V_c for Set 2 p_T acceptance (π^\pm , K^\pm , $p(\bar{p})$): $0.4 < p_T < 1.6$ GeV/ c). Panel (a) presents the χ^2_{combined} distributions from fits of the observables $C_{p,K}$, $C_{Q,p}$, and $C_{Q,K}$ to the model. Panel (b) presents the χ^2 distributions obtained when the data are shifted upward by their systematic uncertainties, while panel (c) shows the corresponding case for a downward shift. The minima of χ^2_{combined} distributions in each case, which correspond to the best-fit values of V_c , are obtained by fitting the distributions with a fourth-order polynomial. The resulting minima and their associated uncertainties are marked in each panel.

resonance decays, assumptions inherent in the V_c parametrization [35], and the absence of certain dynamic phenomena such as initial-state fluctuations and final-state interactions.

6.4.3 Effect of resonance decays

Figure 6.16 presents a comparison between the measurements of $C_{p,K}$, $C_{Q,p}$, and $C_{Q,K}$ for the Set 1 p_T acceptance, and the Thermal-FIST CE model predictions. The calculations are performed with fixed parameters $T_{\text{chem}} = 155$ MeV, $\gamma_s = 1$, and $V_c = 2.6dV/dy$, and are presented both with and without the contribution from resonance decays. Resonance decays are found to play a crucial role in shaping these observables, since they naturally introduce correlations between different particle species. Their inclusion enhances the magnitude of all three correlation measures across the full centrality range, moving them

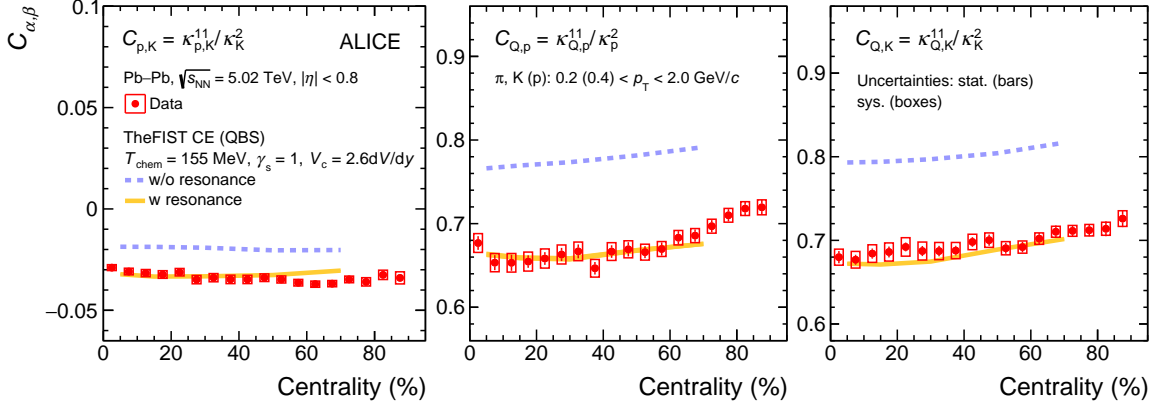


FIGURE 6.16: The centrality dependence of $C_{p,K}$, $C_{Q,p}$, and $C_{Q,K}$ is displayed in the left, middle, and right panels, respectively, for Pb–Pb collisions at $\sqrt{s_{NN}} = 5.02$ TeV. The curves correspond to predictions from the Thermal-FIST (TheFIST) [24] framework within the canonical ensemble (CE), shown both with (w) and without (w/o) the inclusion of resonance decays. Statistical uncertainties are indicated by vertical error bars, while systematic uncertainties are shown as open boxes. The figure is taken from Ref. [22].

further away from the Poisson baseline and bringing the model into close agreement with the experimental data. In contrast, when resonances are neglected, the predicted correlations are significantly underestimated, highlighting the importance of hadronic decay contributions in the fluctuations and correlations of conserved charges.

6.4.4 Collision energy dependence

Figure 6.17 illustrates the behavior of $C_{p,K}$, $C_{Q,p}$, and $C_{Q,K}$ as a function of $\sqrt{s_{NN}}$ for both central and peripheral collisions. The comparison combines ALICE measurements in Pb–Pb collisions at $\sqrt{s_{NN}} = 5.02$ TeV with results from the STAR experiment for Au+Au collisions over the range $\sqrt{s_{NN}} = 7.7$ –200 GeV [8]. While the STAR analysis uses $|\eta| < 0.5$, the ALICE data are shown for both $|\eta| < 0.5$ and $|\eta| < 0.8$. A smooth decrease of all three observables is observed when moving from RHIC to LHC energies. At the same time, the departure from the Poisson expectation becomes more pronounced at higher energies, for

both central and peripheral events.

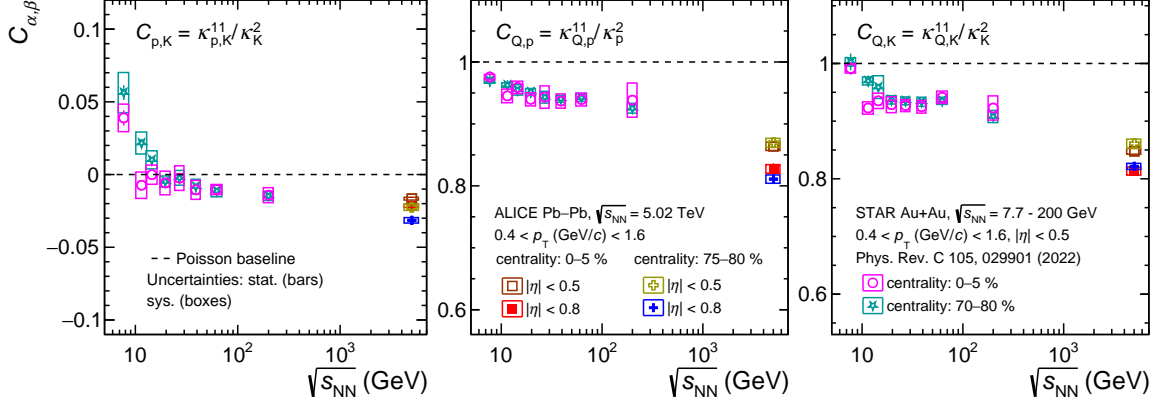


FIGURE 6.17: The collision-energy dependence of $C_{p,K}$ (left), $C_{Q,p}$ (middle), and $C_{Q,K}$ (right). Results for central and peripheral Au+Au collisions at lower beam energies ($\sqrt{s_{NN}} = 7.7\text{--}200$ GeV) from the STAR experiment [8] are compared to that of Pb–Pb collisions at LHC energies ($\sqrt{s_{NN}} = 5.02$ TeV). The dashed line marks the expectation from an uncorrelated (Poisson) baseline. Vertical error bars indicate statistical uncertainties, whereas the systematic effects are shown as surrounding boxes. The figure is taken from Ref. [22].

This energy-dependent behavior reflects the evolving nature of particle production mechanisms and the interplay of conservation laws. At lower collision energies, the larger beam rapidity leads to substantial baryon stopping, which causes an increased number of protons to fall within the detector’s acceptance window. This enhanced baryon density makes charge conservation effects even stronger, increasing their impact on the measured correlations. In contrast, at higher collision energies, the system achieves a more extended longitudinal expansion with greater particle multiplicities and reduced net-baryon density at midrapidity [46], modifying the strength of these correlations. Moreover, the production of hadronic resonances is significantly enhanced at LHC energies compared to RHIC, and the decay of this increased resonance population can further influence the correlations, as discussed in the previous section.

6.4.5 Testing the LQCD predictions with magnetic field

Theory expectations:

Recent lattice QCD studies by Ding et al. [47, 48] investigate fluctuations and correlations among conserved charges in the presence of uniform external magnetic fields. They observe that specific combinations of second-order thermodynamic susceptibilities associated with Q, B, and S are altered compared to the case without a magnetic field [47]. Since the isospin symmetry between up (u) and down (d) quarks is broken in the presence of magnetic field, their individual susceptibilities, χ_u^2 , χ_d^2 are modified. This effect propagates into the full second-order susceptibility matrix involving Q, B, and S [47] and as a result, significant modifications are observed in ratios such as $(2\chi_{Q,S}^{11} - \chi_{B,S}^{11})/\chi_S^2$, $(2\chi_{Q,B}^{11} - \chi_{B,S}^{11})/\chi_B^2$ (as shown in Fig. 6.18), and $\chi_{Q,B}^{11}/\chi_Q^2$ [47, 48]. In particular, the scaled

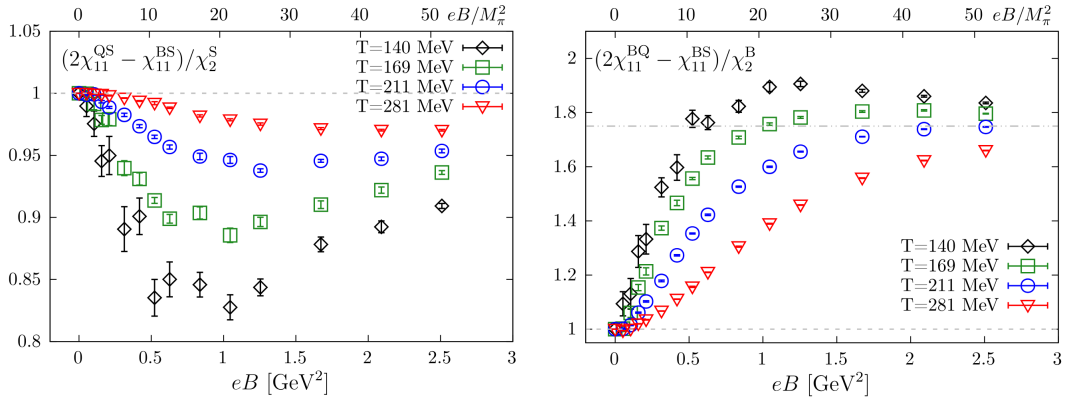


FIGURE 6.18: Lattice QCD simulation results with non-zero magnetic field: $(2\chi_{Q,S}^{11} - \chi_{B,S}^{11})/\chi_S^2$ (left) and $(2\chi_{B,Q}^{11} - \chi_{B,S}^{11})/\chi_B^2$ (right) shown as a function of eB . Different colored markers correspond to various temperatures spanning the range $140 < T < 281 \text{ MeV}$. The figure is taken from Ref. [47].

ratio $[\chi_{Q,B}^{11}/\chi_Q^2(eB)]/[\chi_{Q,B}^{11}/\chi_Q^2(eB=0)]$ (shown in Fig. 6.19) exhibits notable deviations from unity that could be interpreted as indicative of the magnetic field's effect, as discussed in Ref. [48].

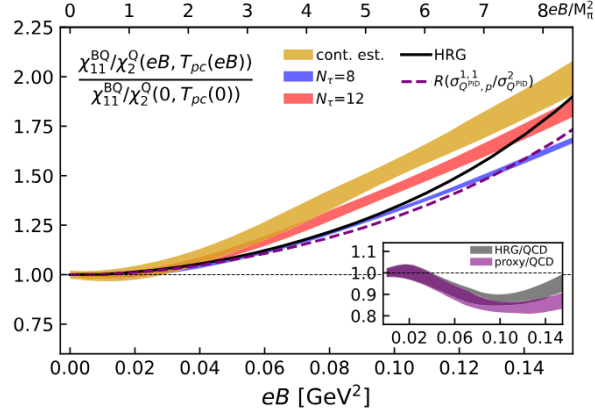


FIGURE 6.19: The dependence of $[\chi_{Q,B}^{11}/\chi_Q^2(eB)]/[\chi_{Q,B}^{11}/\chi_Q^2(eB=0)]$ on the strength of the magnetic field eB at the pseudocritical temperature, T_{pc} , as obtained from lattice QCD simulations. The black curve indicates the prediction from the HRG model, while the dashed-purple line represents an experimentally accessible proxy $[\sigma_{Q,p}^{1,1}/\sigma_Q^2(eB)]/[\sigma_{Q,p}^{1,1}/\sigma_Q^2(eB=0)]$. The yellow band denotes the QCD continuum estimate, with results for different lattice spacings indicated by blue ($N_\tau=8$) and red ($N_\tau=12$) bands. The inset illustrates the ratios of the HRG and proxy results to those from lattice QCD. The figure is taken from Ref. [48].

In experiments, these quantities are accessed using proxies such as $(2\kappa_{Q,K}^{11} - \kappa_{p,K}^{11})/\kappa_K^2$, $(2\kappa_{Q,p}^{11} - \kappa_{p,K}^{11})/\kappa_p^2$, and $(\kappa_{Q,p}^{11}/\kappa_Q^2)/(\kappa_{Q,p}^{11}/\kappa_Q^2)^{0-5\%}$. The last expression denotes the ratio of $\kappa_{Q,p}^{11}/\kappa_Q^2$ to its value in the most central (0–5%) collisions. It is generally expected that the magnetic field strength increases as collisions become more peripheral because the larger impact parameter leads to more spectator protons generating stronger electromagnetic fields. Hence, investigating how these observables vary with centrality could provide valuable insight into the influence of the magnetic field on the final-state hadrons in heavy-ion collisions.

We now explore these theoretical predictions in the experimental data to assess the influence of magnetic fields on relevant conserved charge correlations.

Experimental measurements:

Figure 6.20 presents the centrality dependence of the observables $(2\kappa_{Q,K}^{11} - \kappa_{p,K}^{11})/\kappa_K^2$ and $(2\kappa_{Q,p}^{11} - \kappa_{p,K}^{11})/\kappa_K^2$ for Set 1 p_T acceptance. Both quantities show a modest upward trend

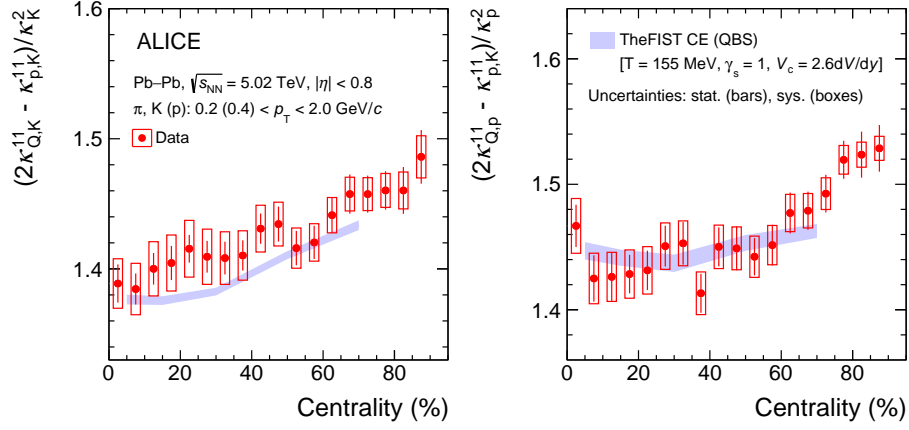


FIGURE 6.20: The ratios $(2\kappa_{Q,K}^{11} - \kappa_{p,K}^{11})/\kappa_K^2$ (left) and $(2\kappa_{Q,p}^{11} - \kappa_{p,K}^{11})/\kappa_K^2$ (right) measured as a function of centrality in Pb-Pb collisions at $\sqrt{s_{NN}} = 5.02$ TeV. The colored band shows the expectations from the Thermal-FIST (TheFIST) [24] framework within the canonical ensemble (CE), obtained using a correlation volume of $V_c = 2.6, dV/dy$. Statistical errors are indicated by vertical lines, and systematic uncertainties are displayed as boxes. The figure is taken from Ref. [22].

moving from semi-central to peripheral collisions. Specifically, the value of $(2\kappa_{Q,K}^{11} - \kappa_{p,K}^{11})/\kappa_K^2$ demonstrates an approximate 4% increase between the 50–55% and 85–90% centrality intervals, while $(2\kappa_{Q,p}^{11} - \kappa_{p,K}^{11})/\kappa_K^2$ rises by around 5%, corresponding to statistical significances of 2.1σ and 2.8σ , respectively. The measurements are compared to Thermal-FIST model calculation with CE, using the same parameters as discussed in earlier sections. It is found that although the Thermal-FIST CE model does not incorporate magnetic field effects, it reproduces the experimental results within statistical uncertainties. The findings are similar also for Set 2 p_T acceptance.

In Fig. 6.21, the normalized ratio $(\kappa_{Q,p}^{11}/\kappa_Q^2)/(\kappa_{Q,p}^{11}/\kappa_Q^2)^{0-5\%}$ is shown as a function

of centrality. For both Set 1 and Set 2 p_T acceptances, the ratio increases steadily with

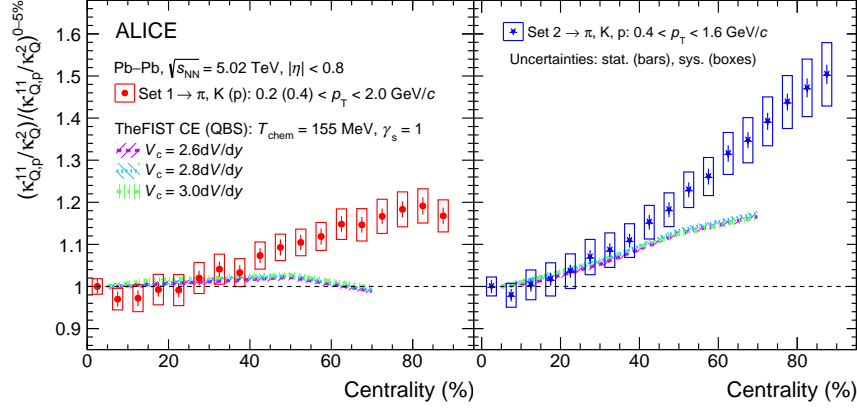


FIGURE 6.21: Variation of the normalized ratio $(\kappa_{Q,p}^{11}/\kappa_Q^2)/(\kappa_{Q,p}^{11}/\kappa_Q^2)^{0-5\%}$ as a function of collision centrality in Pb–Pb collisions at $\sqrt{s_{NN}} = 5.02$ TeV. Results are shown for two p_T acceptances: Set 1 and Set 2 (refer to text for details) in left and right panels, respectively. The shaded bands correspond to predictions from the Thermal-FIST (TheFIST) [24] framework within the canonical ensemble (CE), evaluated for different choices of correlation volume V_c . Statistical errors are indicated by vertical bars, while systematic uncertainties are depicted as boxes. The figure is taken from Ref. [22].

centrality. For Set 1, the ratio starts to differ from one (dashed line) after 40% centrality and grows to about 20% higher by the 85–90% centrality interval. In Set 2, the deviation sets in earlier, near ~25% centrality, and reaches almost 50% in the most peripheral collisions. The measurements are also compared to Thermal-FIST CE model calculations performed without including magnetic field effects, for V_c ranging from 2.6 dV/dy to 3.0 dV/dy. Across this range, the model predictions remain nearly unchanged, reflecting limited sensitivity to the precise choice of V_c . However, the model fails to describe the increasing trend observed in data beyond ~50% centrality. This discrepancy may point to incomplete treatment of resonance decays, missing physical ingredients, or potentially a contribution from the initial magnetic field. Further detailed studies are required to disentangle whether these deviations are driven by magnetic field effects or by other unaccounted mechanisms.

6.5 Summary

This work investigates second-order fluctuations and correlations among conserved charges by using event-by-event net-particle numbers. Specifically, we analyzed how the correlations between net-charged particles, net-protons, and net-kaons—denoted as $C_{p,K}$, $C_{Q,p}$, and $C_{Q,K}$, which are ratios of cumulants—depend on collision centrality and also on p_T acceptance in Pb–Pb collisions at $\sqrt{s_{NN}} = 5.02$ TeV. The net-charged particle, net-proton, and net-kaon numbers are considered as proxies of net-electric charge, net-baryon number, and net-strangeness, respectively. All three correlators exhibit significant deviations from the Poisson expectation, which corresponds to independent particle emission. These deviations mainly reflect correlations introduced by resonance decays and by conservation of the quantum numbers Q , B , and S . Theoretical predictions from event generators HIJING and EPOS LHC, as well as the Thermal-FIST model in the grand canonical ensemble, fail to fully reproduce the observed results. In contrast, the Thermal-FIST model implemented within the canonical ensemble framework, which enforces exact conservation of electric charge, baryon number, and strangeness within a correlation volume of $3.0dV/dy$, achieves a better match to experimental data across all centralities. Further comparison with Thermal-FIST CE model for different correlation volumes and combined χ^2 fit to the data, allows to estimate the optimum value of correlation volume. This volume is also found to depend on the p_T acceptance, underscoring the importance of kinematic selections in interpreting fluctuation and correlation measurements. The measurements of $C_{p,K}$, $C_{Q,p}$, and $C_{Q,K}$ show a monotonically decreasing trend from lower energies at RHIC to higher energies at the LHC; concurrently, the deviation from Poisson baseline increases with collision energy. This energy dependence likely arises from multiple physics mechanisms: baryon stopping is more relevant at lower energies, whereas resonance production

is expected to contribute more strongly at higher energies, together shaping the observed correlations.

6.6 Outlook

Future measurements in LHC Runs 3 and 4 will benefit from the upgraded ALICE detector, providing significantly higher statistics along with improved tracking and PID performance. These advances will enable more precise and differential studies of conserved-charge fluctuations, including higher-order and mixed cumulants, thereby increasing sensitivity to critical phenomena and QCD phase structure. Complementary measurements in the lower-energy regime at RHIC Beam Energy Scan Phase II, as well as future experiments at FAIR [49] and NICA [50], will be essential to map the evolution of conserved charge fluctuations and correlations across a wider range of μ_B . Additionally, improved PID will allow the inclusion of strange and multi-strange baryons in the study of conserved charge correlations, enabling more direct comparisons with LQCD predictions. Together, these efforts will enable a more comprehensive characterization of the QCD phase structure across energies and system sizes.

Bibliography

- [1] Sourendu Gupta et al. “Scale for the Phase Diagram of Quantum Chromodynamics”. *Science* 332 (2011), pp. 1525–1528. arXiv: [1105.3934 \[hep-ph\]](#).
- [2] A. Bazavov et al. “Fluctuations and Correlations of net baryon number, electric charge, and strangeness: A comparison of lattice QCD results with the hadron resonance gas model”. *Phys. Rev. D* 86 (2012), p. 034509. arXiv: [1203.0784 \[hep-lat\]](#).

- [3] Heng-Tong Ding, Frithjof Karsch, and Swagato Mukherjee. “Thermodynamics of strong-interaction matter from Lattice QCD”. *Int. J. Mod. Phys. E* 24.10 (2015), p. 1530007. arXiv: [1504.05274 \[hep-lat\]](#).
- [4] H. T. Ding et al. “Chiral Phase Transition Temperature in (2+1)-Flavor QCD”. *Phys. Rev. Lett.* 123.6 (2019), p. 062002. arXiv: [1903.04801 \[hep-lat\]](#).
- [5] Szabolcs Borsanyi et al. “Higher order fluctuations and correlations of conserved charges from lattice QCD”. *JHEP* 10 (2018), p. 205. arXiv: [1805.04445 \[hep-lat\]](#).
- [6] Rene Bellwied et al. “Off-diagonal correlators of conserved charges from lattice QCD and how to relate them to experiment”. *Phys. Rev. D* 101.3 (2020), p. 034506. arXiv: [1910.14592 \[hep-lat\]](#).
- [7] V. Koch, A. Majumder, and J. Randrup. “Baryon-strangeness correlations: A Diagnostic of strongly interacting matter”. *Phys. Rev. Lett.* 95 (2005), p. 182301. arXiv: [nucl-th/0505052](#).
- [8] Jaroslav Adam et al. “Collision-energy dependence of second-order off-diagonal and diagonal cumulants of net-charge, net-proton, and net-kaon multiplicity distributions in Au + Au collisions”. *Phys. Rev. C* 100.1 (2019). [Erratum: *Phys.Rev.C* 105, 029901 (2022)], p. 014902. arXiv: [1903.05370 \[nucl-ex\]](#).
- [9] Volodymyr Vovchenko and Volker Koch. “Particlization of an interacting hadron resonance gas with global conservation laws for event-by-event fluctuations in heavy-ion collisions”. *Phys. Rev. C* 103.4 (2021), p. 044903. arXiv: [2012.09954 \[hep-ph\]](#).
- [10] Peter Braun-Munzinger, Anar Rustamov, and Johanna Stachel. “The role of the local conservation laws in fluctuations of conserved charges” (July 2019). arXiv: [1907.03032 \[nucl-th\]](#).
- [11] Xiaofeng Luo et al. “Volume fluctuation and auto-correlation effects in the moment analysis of net-proton multiplicity distributions in heavy-ion collisions”. *J. Phys. G* 40 (2013), p. 105104. arXiv: [1302.2332 \[nucl-ex\]](#).
- [12] P. Braun-Munzinger, A. Rustamov, and J. Stachel. “Bridging the gap between event-by-event fluctuation measurements and theory predictions in relativistic nuclear collisions”. *Nucl. Phys. A* 960 (2017), pp. 114–130. arXiv: [1612.00702 \[nucl-th\]](#).

- [13] P. Garg et al. “Conserved number fluctuations in a hadron resonance gas model”. *Phys. Lett. B* 726 (2013), pp. 691–696. arXiv: [1304.7133 \[nucl-ex\]](#).
- [14] D. K. Mishra et al. “Effect of resonance decay on conserved number fluctuations in a hadron resonance gas model”. *Phys. Rev. C* 94.1 (2016), p. 014905. arXiv: [1607.01875 \[hep-ph\]](#).
- [15] Chun Shen and Björn Schenke. “Dynamical initial state model for relativistic heavy-ion collisions”. *Phys. Rev. C* 97.2 (2018), p. 024907. arXiv: [1710.00881 \[nucl-th\]](#).
- [16] Yutaro Ohnishi, Masakiyo Kitazawa, and Masayuki Asakawa. “Thermal blurring of event-by-event fluctuations generated by rapidity conversion”. *Phys. Rev. C* 94.4 (2016), p. 044905. arXiv: [1606.03827 \[nucl-th\]](#).
- [17] Xin-Nian Wang and Miklos Gyulassy. “HIJING: A Monte Carlo model for multiple jet production in p p, p A and A A collisions”. *Phys. Rev. D* 44 (1991), pp. 3501–3516.
- [18] René Brun et al. “GEANT Detector Description and Simulation Tool”. *CERN-W5013* (Oct. 1994).
- [19] Toshihiro Nonaka, Masakiyo Kitazawa, and Shinichi Esumi. “More efficient formulas for efficiency correction of cumulants and effect of using averaged efficiency”. *Phys. Rev. C* 95.6 (2017). [Erratum: *Phys. Rev. C* 103, 029901 (2021)], p. 064912. arXiv: [1702.07106 \[physics.data-an\]](#).
- [20] Adam Bzdak and Volker Koch. “Local Efficiency Corrections to Higher Order Cumulants”. *Phys. Rev. C* 91.2 (2015), p. 027901. arXiv: [1312.4574 \[nucl-th\]](#).
- [21] “Centrality determination in heavy ion collisions”. *ALICE-PUBLIC-2018-011* (Aug. 2018).
- [22] Shreyasi Acharya et al. “Measurement of correlations among net-charge, net-proton, and net-kaon multiplicity distributions in Pb–Pb collisions at $\sqrt{s_{NN}} = 5.02$ TeV”. *JHEP* 08 (2025), p. 210. arXiv: [2503.18743 \[nucl-ex\]](#).
- [23] T. Pierog et al. “EPOS LHC: Test of collective hadronization with data measured at the CERN Large Hadron Collider”. *Phys. Rev. C* 92.3 (2015), p. 034906. arXiv: [1306.0121 \[hep-ph\]](#).

- [24] Volodymyr Vovchenko and Horst Stoecker. “Thermal-FIST: A package for heavy-ion collisions and hadronic equation of state”. *Comput. Phys. Commun.* 244 (2019), pp. 295–310. arXiv: [1901.05249 \[nucl-th\]](#).
- [25] V. Topor Pop et al. “Baryon junction loops and the baryon-meson anomaly at high energies”. *Phys. Rev. C* 70 (2004), p. 064906. arXiv: [nucl-th/0407095](#).
- [26] T. Pierog and K. Werner. “EPOS Model and Ultra High Energy Cosmic Rays”. *Nucl. Phys. B Proc. Suppl.* 196 (2009). Ed. by Jean-Noël Capdevielle, Ralph Engel, and Bryan Pattison, pp. 102–105. arXiv: [0905.1198 \[hep-ph\]](#).
- [27] P. Koch, Berndt Muller, and Johann Rafelski. “Strangeness in Relativistic Heavy Ion Collisions”. *Phys. Rept.* 142 (1986), pp. 167–262.
- [28] Johann Rafelski. “Strange anti-baryons from quark - gluon plasma”. *Phys. Lett. B* 262 (1991), pp. 333–340.
- [29] Shreyasi Acharya et al. “Production of charged pions, kaons, and (anti-)protons in Pb-Pb and inelastic pp collisions at $\sqrt{s_{NN}} = 5.02$ TeV”. *Phys. Rev. C* 101.4 (2020), p. 044907. arXiv: [1910.07678 \[nucl-ex\]](#).
- [30] Betty Bezverkhny Abelev et al. “ $K^*(892)^0$ and $\phi(1020)$ production in Pb-Pb collisions at $\sqrt{s_{NN}} = 2.76$ TeV”. *Phys. Rev. C* 91 (2015), p. 024609. arXiv: [1404.0495 \[nucl-ex\]](#).
- [31] Betty Bezverkhny Abelev et al. “ K_S^0 and Λ production in Pb-Pb collisions at $\sqrt{s_{NN}} = 2.76$ TeV”. *Phys. Rev. Lett.* 111 (2013), p. 222301. arXiv: [1307.5530 \[nucl-ex\]](#).
- [32] Betty Bezverkhny Abelev et al. “Multi-strange baryon production at mid-rapidity in Pb-Pb collisions at $\sqrt{s_{NN}} = 2.76$ TeV”. *Phys. Lett. B* 728 (2014). [Erratum: *Phys.Lett.B* 734, 409–410 (2014)], pp. 216–227. arXiv: [1307.5543 \[nucl-ex\]](#).
- [33] F. Becattini. “An Introduction to the Statistical Hadronization Model”. In: *International School on Quark-Gluon Plasma and Heavy Ion Collisions: past, present, future*. Jan. 2009. arXiv: [0901.3643 \[hep-ph\]](#).
- [34] Volodymyr Vovchenko, Benjamin Dönigus, and Horst Stoecker. “Canonical statistical model analysis of p-p , p -Pb, and Pb-Pb collisions at energies available at the CERN Large Hadron Collider”. *Phys. Rev. C* 100.5 (2019), p. 054906. arXiv: [1906.03145 \[hep-ph\]](#).

- [35] Volodymyr Vovchenko. “Density correlations under global and local charge conservation”. *Phys. Rev. C* 110.6 (2024), p. L061902. arXiv: [2409.01397 \[hep-ph\]](#).
- [36] Shreyasi Acharya et al. “Closing in on critical net-baryon fluctuations at LHC energies: Cumulants up to third order in Pb–Pb collisions”. *Phys. Lett. B* 844 (2023), p. 137545. arXiv: [2206.03343 \[nucl-ex\]](#).
- [37] Peter Braun-Munzinger et al. “The imprint of conservation laws on correlated particle production”. *JHEP* 08 (2024), p. 113. arXiv: [2312.15534 \[nucl-th\]](#).
- [38] A. G. Knospe et al. “Hadronic resonance production and interaction in p-Pb collisions at LHC energies in EPOS3”. *Phys. Rev. C* 104.5 (2021), p. 054907. arXiv: [2102.06797 \[nucl-th\]](#).
- [39] Marlene Nahrgang et al. “Impact of resonance regeneration and decay on the net-proton fluctuations in a hadron resonance gas”. *Eur. Phys. J. C* 75.12 (2015), p. 573. arXiv: [1402.1238 \[hep-ph\]](#).
- [40] Bo Ling and Mikhail A. Stephanov. “Acceptance dependence of fluctuation measures near the QCD critical point”. *Phys. Rev. C* 93.3 (2016), p. 034915. arXiv: [1512.09125 \[nucl-th\]](#).
- [41] J. Adam et al. “Nonmonotonic Energy Dependence of Net-Proton Number Fluctuations”. *Phys. Rev. Lett.* 126.9 (2021), p. 092301. arXiv: [2001.02852 \[nucl-ex\]](#).
- [42] Marcus Bluhm et al. “Dynamics of critical fluctuations: Theory – phenomenology – heavy-ion collisions”. *Nucl. Phys. A* 1003 (2020), p. 122016. arXiv: [2001.08831 \[nucl-th\]](#).
- [43] Swati Saha. “Investigating baryon-strangeness and charge-strangeness correlations in Pb–Pb collisions at $\sqrt{s_{\text{NN}}} = 5.02$ TeV with ALICE”. *PoS ICHEP2024* (2025), p. 598. arXiv: [2409.10939 \[nucl-ex\]](#).
- [44] Anton Andronic et al. “Decoding the phase structure of QCD via particle production at high energy”. *Nature* 561.7723 (2018), pp. 321–330. arXiv: [1710.09425 \[nucl-th\]](#).
- [45] Shreyasi Acharya et al. “Probing strangeness hadronization with event-by-event production of multistrange hadrons” (May 2024). arXiv: [2405.19890 \[nucl-ex\]](#).

- [46] Oscar Garcia-Montero and Sören Schlichting. “Baryon stopping and charge deposition in heavy-ion collisions due to gluon saturation”. *Phys. Rev. C* 111.2 (2025), p. 024912. arXiv: [2409.06788 \[hep-ph\]](#).
- [47] H. T. Ding et al. “Fluctuations and correlations of net baryon number, electric charge and strangeness in a background magnetic field”. *Eur. Phys. J. A* 57.6 (2021), p. 202. arXiv: [2104.06843 \[hep-lat\]](#).
- [48] Heng-Tong Ding et al. “Baryon Electric Charge Correlation as a Magnetometer of QCD”. *Phys. Rev. Lett.* 132.20 (2024), p. 201903. arXiv: [2312.08860 \[hep-lat\]](#).
- [49] Facility for Antiproton and Ion Research (FAIR). *Nuclear Matter Physics – Experiments*. <https://fair-center.eu/user/experiments/nuclear-matter-physics>.
- [50] Nuclotron-based Ion Collider Facility (NICA). *Physics program*. <https://nica.jinr.ru/physics.php>.

Conclusions

This thesis provides a detailed study of the properties of strongly interacting matter created in ultra-relativistic heavy-ion collisions, through systematic analyses of higher-order fluctuations of the mean transverse momentum $\langle p_T \rangle$, differential radial flow via $v_0(p_T)$, and correlations among conserved charges. Using data collected by the ALICE experiment at the LHC, measurements were carried out in Pb–Pb, Xe–Xe, and pp collision systems.

The investigation of higher-order moments of $\langle p_T \rangle$ fluctuations—standardized skewness, intensive skewness, and kurtosis—revealed systematic trends as functions of system size. Standardized skewness was observed to decrease with increasing multiplicity, while intensive skewness remained positive and larger than baseline expectations, consistent with state-of-the-art relativistic hydrodynamic model predictions. These results underscore the sensitivity of skewness observables to the earliest stages of collision dynamics and fluctuations in the initial geometry. Notably, an increase in skewness and convergence of kurtosis toward Gaussian values in the most central collisions suggests the onset of local thermal equilibrium in the evolving medium, a fundamental criterion for the formation of quark–gluon plasma. Complementary measurements in pp collisions showed qualitatively

similar behaviors in $\langle p_T \rangle$ fluctuations as observed in heavy-ion collisions. Comparisons with PYTHIA8 highlighted the role of color reconnection and final-state effects in shaping these fluctuations in small collision systems.

A novel differential observable of radial flow, $v_0(p_T)$, introduced and measured for identified hadrons in Pb–Pb collisions, revealed similar features as observed for anisotropic flow. The results demonstrate characteristic mass ordering at low p_T , baryon–meson splitting at intermediate p_T , and approximate scaling with the number of constituent quarks—all hallmarks of partonic collectivity and quark coalescence–driven hadronization. The sensitivity of $v_0(p_T)$ to the bulk viscosity and the equation of state, as confirmed by comparisons with hydrodynamic models, allows for new insights into the properties of the medium beyond traditional characterization of radial flow. These findings firmly establish $v_0(p_T)$ as a valuable addition to the suite of observables employed in Bayesian analyses to extract the transport properties of the quark–gluon plasma. To further unravel the implications of these measurements, $v_0(p_T)$ distributions were modeled using a blast-wave framework that incorporates event-by-event fluctuations of both the radial flow velocity and the freeze-out temperature. The Bayesian-extracted parameters obtained by fitting the data are consistent with those obtained from traditional p_T spectra analyses, and importantly, this approach enables the quantification of fluctuations in radial flow and freeze-out temperature themselves. Collectively, these studies underscore $v_0(p_T)$ as a sensitive and complementary observable, for studying collectivity, freeze-out dynamics, and hadronization mechanisms of the QCD medium.

Investigations of net-proton, net-kaon, and net-charge correlations extended this comprehensive study into the domain of conserved charge fluctuations, pivotal for elucidating the QCD phase structure and freeze-out conditions at baryon-chemical potential close to zero. Significant deviations from Poisson baselines and agreement with hadron resonance

gas models incorporating local charge conservation affirm the complex interplay of conservation laws, resonance decays, and medium-induced correlations. Furthermore, hints of effects potentially related to the strong magnetic fields generated in peripheral collisions open exciting avenues for future investigations.

Overall, these combined analyses deepen our understanding of the quark–gluon plasma’s initial state fluctuations, its collective expansion, and the QCD phase structure at temperatures and densities accessible at the LHC energies. Looking ahead, continuing advancements in experimental precision and theoretical modeling will further elucidate the detailed mechanisms governing strongly interacting matter under extreme conditions. The methodologies developed and the findings obtained in this thesis lay groundwork for future studies with LHC Run 3 data, especially for the small-ion collisions (oxygen-oxygen and neon-neon collisions) promising further insight into the emergence of collectivity and the fundamental properties of strongly interacting matter.